University of Southampton Research Repository

Copyright © and Moral Rights for this thesis and, where applicable, any accompanying data are retained by the author and/or other copyright owners. A copy can be downloaded for personal non-commercial research or study, without prior permission or charge. This thesis and the accompanying data cannot be reproduced or quoted extensively from without first obtaining permission in writing from the copyright holder/s. The content of the thesis and accompanying research data (where applicable) must not be changed in any way or sold commercially in any format or medium without the formal permission of the copyright holder/s.

When referring to this thesis and any accompanying data, full bibliographic details must be given, e.g.

Thesis: Author (Year of Submission) "Full thesis title", University of Southampton, name of the University Faculty or School or Department, PhD Thesis, pagination.

Data: Author (Year) Title. URI [dataset]

UNIVERSITY OF SOUTHAMPTON

Faculty of Engineering and Physical Sciences
School of Engineering

Duct effects on acoustic source radiation

by

Ben Baddour
MEng

A thesis for the degree of
Doctor of Philosophy

May 30, 2023

University of Southampton

Abstract

Faculty of Engineering and Physical Sciences
School of Engineering

Doctor of Philosophy

Duct effects on acoustic source radiation

by Ben Baddour

This thesis details an investigation into the effect of a duct on acoustic source radiation. The duct is assumed to be hard-walled, hollow, have a constant cross-section and have no axial flow. This study was motivated by the increasing tendency for ducted propellers to be located close to the open end relative to the acoustic wavelength.

Investigations are conducted using the widely accepted semi-infinite duct model, formed from the Wiener–Hopf technique, as well as a new finite length duct formulation. In this study, the conditions are established under which duct effects on source radiation are considerable, and the duct plays a governing role on the overall acoustic radiation of the source.

The duct acoustic model assumes the acoustic pressure field can be reconstructed from a summation of propagating cut-on and evanescent cut-off modes, which have largely been unstudied. Systematic studies of the radiation characteristics of cut-off modes are documented in this thesis, detailing properties such as their modal directivity and radiation efficiency. It is found that cut-off modal radiation is predominantly directed towards the rear-arc with an effect of up to 5 dB at certain angles and a more general increase of 3 dB in the rear-arc far-field radiation.

In many cases, sources close to the duct open end relative to the acoustic wavelength are shown to be largely unaffected by the duct, causing equal free-field and ducted radiation. The effect of source axial position and varying duct length are shown to have a diminishing effect on the ducted source radiation as frequency is increased. At high frequency the duct has a relatively small effect on the acoustic radiation.

Dipole sources located near the duct rim are shown to have a significant increase in ducted radiation, causing an omni-directional directivity – which can largely be attributed to cut-off modal radiation. Dipole sources located exactly on the duct rim are shown to have directivity characteristics solely governed by modes which are cut-off and have almost all radiation directed towards the rear-arc.

Contents

List of Figures

List of Tables

Declaration of Authorship

I declare that this thesis and the work presented in it is my own and has been generated by me as the result of my own original research.

I confirm that:

1. This work was done wholly or mainly while in candidature for a research degree at this University;
2. Where any part of this thesis has previously been submitted for a degree or any other qualification at this University or any other institution, this has been clearly stated;
3. Where I have consulted the published work of others, this is always clearly attributed;
4. Where I have quoted from the work of others, the source is always given. With the exception of such quotations, this thesis is entirely my own work;
5. I have acknowledged all main sources of help;
6. Where the thesis is based on work done by myself jointly with others, I have made clear exactly what was done by others and what I have contributed myself;
7. Parts of this work have been published as:
   Baddour et al. (2020)
   Baddour et al. (2021)
   Baddour et al. (2022a)
   Baddour et al. (2022b)
   Baddour et al. (2022c)

Signed:..... Date:.....

Acknowledgements

I would first like to thank my two supervisors Phil Joseph and Alan McAlpine, and the considerable effort of my industrial supervisor Ronnie Leung. Ronnie attended almost every meeting and was present during every technical aspect of the work, much of this he did of his own accord. I would also like to express gratitude to my internal examiners, Alec Wilson, Rui Sugimoto and Brian Tester, who's feedback at the progression milestones helped shape and guide the project.

The most complicated aspect of the project was the experimental work, which would not have been possible without the significant time and effort put in by the post-doctoral researcher Sergi Palleja-Cabre and Royal Academy of Engineering Research Fellow and lecturer Chaitanya Paruchuri, who not only advised me, but instructed on setting up and calibrating the microphone array. I would also like to express gratitude to fellow students Ellie Kattenhorn, Amin Karimian, Enrico Degregori and Suresh Palani, who helped with the running of the experiments. Collectively these individuals voluntarily contributed hours of their time on my behalf.

Several pieces of the apparatus for the experiment required assembly, for this I would like to thank workshop staff Andrea and Clive, who oversaw and participated in manufacture of the apparatus. I would like to express thanks to Jack Lawrence for aiding in the 3 dimensional printing required to modify the Speaker. For the equipment supplied for the experiments I would like to thank Jacob Hollebon, who advised and assisted.

I would like to thank the admin staff Sue Brindle and Rodger Hunns who helped not only me with this work but also ensured the smooth running of operations of the institute of sound and vibration.

Funding for this work was gratefully received from the Engineering and Physical Sciences Research Council and the Defence Science and Technology Laboratory. Gratitude is expressed to Gwenael Gabard for supplying the program to calculate the directivity function for the un-flanged duct theoretical model.

Definitions and Abbreviations

Commonly used symbols

a	duct radius
a_{mn}, b_{mn}	modal pressure amplitudes
c	ambient speed of sound
D, d	polar directivity and scaled directivity
E_m	propagation factor
F	fluctuating force per cross sectional area
f	fluctuating force source strength
G	Green's function
h	distance between field point and source point
K^+, K^-	Wiener–Hopf Kernel functions
k	acoustic wavenumber
k_z	axial wavenumber
$\mathcal{M}, \mathcal{N}$	modal index's corresponding to cut-on modes
p	acoustic pressure
P_m	sum of propagation factors
Q	Polar directivity factor (non-dimensional)
$\mathcal{Q}$	Fluctuating volume velocity per cross sectional area
q	volume velocity source strength
$\boldsymbol{R}_{mnl}$	reflections matrix
r_{mn}	reflection of a single mode neglecting scattering
s	source term
S	cross sectional area
t	time
t_0	retarded time
$\mathcal{T}$	open-to-ducted transfer function (ratio)
v_{mn}	acoustic velocity amplitude
u	acoustic velocity
W	acoustic power
Z	radiation impedance

Commonly used coordinates

(R, ϕ, θ)	spherical polar coordinates
(r, θ, z)	cylindrical polar coordinates
(x, y, z)	Cartesian coordinates
$\boldsymbol{X}$	vector of cylindrical polar coordinates

Commonly used Greek symbols

η	sound power split ratio between forward and rear-arcs
κ	transverse wavenumber component
λ	wavelength
ρ	mean density
Π	free-field to ducted power ratio
τ	power efficiency
χ	phase factor
Ψ_{mn}, ψ_{mn}	mode shape functions
Ω	rotational frequency
ω	angular frequency
ζ, ξ	modal cut-off ratios

Commonly used subscripts

F	flanged duct
l	scattered radial modal index
m	azimuthal modal index
n	radial modal index
off	cut-off modes
on	cut-on modes
S	source plane
0	source location

Commonly used superscripts

^{D}	Ducted
^{ff}	free-field
^{R}	radiating components
^{r}	right
^{l}	left
$^{+}, ^{-}$	forward incident/ reflected wave

Chapter 1

Introduction

A relatively large amount of work has been done to mathematically and experimentally investigate propagating acoustic, cut-on, modes. However, there is very little published work on the radiation of non-propagating waves. In marine ducted propellers and more recently, the ducted rotors of quadcopters the noise sources are very close to the openings. Thus, a better understanding of the significance of far-field radiation from cut-off modes is required.

Most of the previous work on the radiation from ducts assume either, a source buried deep inside the duct (where cut-off modes can be neglected) or, for a short duct, omit the duct in the modeling. Consequently, there is a very limited understanding of the radiation from sources located near the duct open end.

1.1 Aims and objectives

The aim of this thesis is to investigate the effect on the far-field acoustic radiation due to locating a free-field source inside a duct. This aim is comprised of three main objectives, which are:

1. To understand the far-field acoustic radiation characteristics of cut-off modes highlighting the differences between propagating acoustic cut-on and cut-off modes.
2. To identify the significance of cut-off modes in calculations of multi-modal acoustic radiation from sources close to the open end of a duct.
3. Compare the ducted radiation prediction to an equivalent free-field source radiation prediction, to identify the effect of ducts.

1.2 Motivation and applications

Many submarines, ships, aircraft and drones use ducted rotors for propulsion. This section discusses these applications, as well as a discussion of the broader applications relevant to this work.

1.2.1 Submarine, ship and marine engines

This project is part funded by the defence science and technology laboratory, whose primary interest is to model radiation from marine ducted propellers where the propeller is close to the duct open end relative to the wavelength.

An important aspect of marine warfare is the ability to detect other marine vehicles whilst remaining undetected. Therefore to predict and reduce acoustic radiation from marine engines is highly desirable to the defence industry. *Figure 1.1* shows examples of marine propellers.

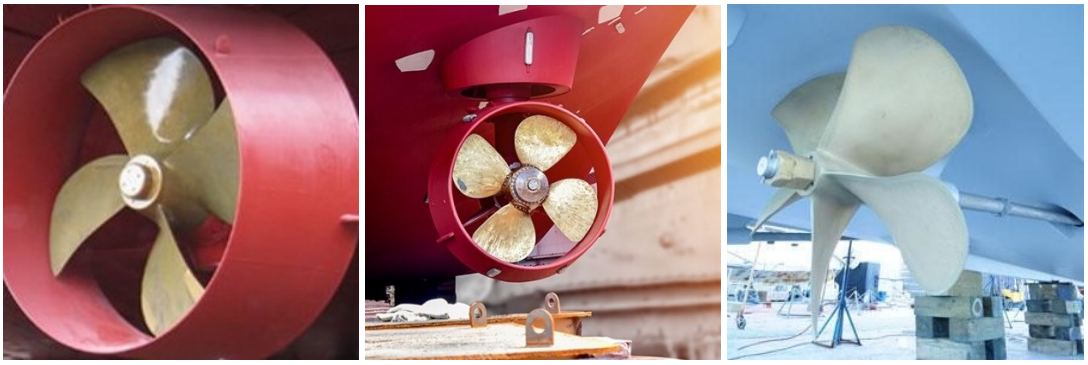

(A) Gunjan and Sonia (2013) (B) Promain UK LTD (2020) (C) Edwards (2020)

FIGURE 1.1: Example of marine propellers

Figure 1.1 shows that some marine propellers are ducted, but not all. Furthermore the ducts can be very short, with the propeller located relatively close to both duct open ends which limits the use of current modelling techniques. For a submarine or ship engine, the main purposes of including a duct are to improve and condition the flow around the propeller which can be achieved by a short duct.

1.2.2 Drones, small unmanned aerial vehicles and quad-copters

Drones or unmanned aerial vehicles are of major research interest due to their potential. For example, drones could drastically decrease regional and international shipping costs, Drive (2020). Small scale drones are of interest to online delivery companies such as Amazon, who could potentially reduce delivery times to as short as a few hours, if drones can be proven to be cost effective and environmentally sustainable.

One major obstacle for drones is the noise annoyance they produce. Regional transportation drones are often small in size implying the need for short small ducts. This work could prove beneficial to drone design engineers. Drones also have use in the leisure industry. Quiet, recreational drones are of interest to companies such as Hamleys, where superior acoustic properties could create a great financial benefit. A common drone is the quad-copter (or multi-copter) as shown in *figure 1.2*.

(A) Throneberry et al. (2021) (B) Cheap Drones (2022) (C) Technology Co (2020)

FIGURE 1.2: Example of drone quad-copters

Figure 1.2 confirms some drones utilise ducts. Owing to the size of the drone, the fan is located close to the duct open ends, where this work necessary may be improtant.

1.2.3 Aircraft and large aerial vehicles

A major application for the use of ducts is to control and condition the air flow in aircraft engines. Aircraft generate significant noise annoyance both for a passenger on-board and communities on the ground. Due to this annoyance, aircraft are governed by stringent international standards for the maximum levels of noise they can produce, such as those set by Europa (2021). To better understand the acoustic radiation from aircraft is highly desirable for companies such as Rolls-Royce. *Figure 1.3* shows examples of ducted turbines of aircraft.

(A) Nathan (2018) (B) Duivis (2020) (C) Cutler (2020)

FIGURE 1.3: Example of ducted turbines from aircraft engines

Figure 1.3 shows the location between the turbine and the inlet of the duct can vary for turbofan aero-engines. This work aims to analyze the influence on the distance between a noise source, such as a rotor, and the duct open end which may influence the design of future aircraft.

1.2.4 Domestic and industrial appliances

Noise generating compressor fans located in ducts are required in many household domestic appliances such as vacuum cleaners, hair dryers. Similarly, many industrial applications use ducted fans such as heating, ventilation and air conditioning systems. For these applications, a compressor fan is required to pump fluid from one reservoir to another, and the component requires a casing, which can be modelled as a duct.

The sound produced from these components is inconvenient for the consumer. Quieter domestic appliances are of prime interest to companies such as Dyson, who design and manufacture appliances such as their silent hairdryer, IBTimes (2021), which makes use of a ducted noise source with several quietening techniques. Before a reduction of noise can be achieved, a better understanding of the underlying physics of the radiation from short ducts is required. *Figure 1.4* shows examples of household appliances that utilize ducted fans.

(A) IBTimes (2021) (B) A Limited (2021) (C) Baddour (2022)

FIGURE 1.4: Examples of typical household appliances

1.2.5 Direct applications

In this section the applications of this work are analysed to determine the most directly relevant to the findings presented in this thesis, where ideal sources are considered such as dipoles and monopoles. A dipole noise source is created from a fluctuating unsteady force such as can be generated by propellers. A monopole source is generated from an unsteady volume velocity such as can be observed from cavitation noise from underwater propellers. This work does not include flow, hence if the Mach number is relatively high, further investigation is required to incorporate this into the models presented here.

The potential increase of the far-field pressure as a result of cut-off modes is dependent on the distance between the source and the open end relative to the acoustic wavelength. Consequently, low frequencies are most significantly affected by cut-off modes. Low frequency radiation can be a significant feature of the acoustic radiation from marine applications, where the high impedance of water causes large wavelengths, leading to potential for cut-off modes to radiate efficiently.

The small size of some aerial vehicles such as drones create a high frequency of noise, due to the relative high rotational speeds of the rotor. For high frequencies cut-off modes have a limited effect on the far-field radiation as at high frequencies cut-off modes decay over relatively short distances. However, the ducts are likely to be relatively short, which may result in cut-off modes having strong radiation from drone engines, potentially making this work useful to drone designers.

Aircraft typically have longer ducts than the previous applications discussed, particularly at the outlet, and the rotor's generate noise over a large frequency range. Furthermore, the use of ducts in aircraft engines is often to accelerate the flow, this is achieved by decreasing the cross sectional area downstream. The acoustic radiation of ducts with a varying cross section was not investigated in this project. The results presented in this thesis are more directly applicable to the inlet, than the outlet of an aircraft, if the distance to the open end is short. The Mach number for this type of applications is often non-trivial, requiring extra study to apply results discussed in this thesis for these cases. Consequently, the major findings of this work are not directly relevant to aircraft, but with additional study could become very important to aircraft design.

1.3 Literature review

This section is a review of the previous research that is relevant to the work presented in this thesis. The important topics developed in this thesis are identified in the graphic of *figure 1.5*, along with there hierarchical dependencies.

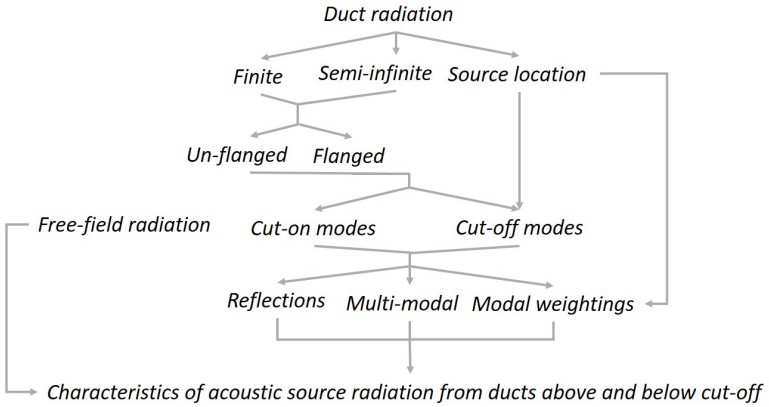

FIGURE 1.5: Structure of the literature review

1.3.1 Free-field sources and transfer functions

This section provides a brief overview of the radiation of free-field sources to characterise the effect of ducts on acoustic source radiation

The free-field radiation of propeller noise has been a topic of interest for almost a century. The first study, was an experimental investigation conducted by Ernsthausen (1937), who identified that blade shape plays a governing role in the radiated noise produced from rotating propellers. It was also noted that obstacles near the blade increase the measured noise level.

Gutin (1948) derived radiation expressions for distributions of dipole sources, as a first attempt to model noise radiated by propeller blades. Early work regarding propeller noise modelled the noise sources as ideal dipole sources, which is still a method widely used in early approximations of propeller noise. Several others have investigated noise radiation of free-field dipole sources, for example Garrick and Watkins (1953), Hanson (1983), Schulten (1988), Parry and Crighton (1989) and Peake and Crighton (1991). These research papers may present the formulation and theoretical model slightly differently, but the major concepts are the same.

More recently, a theoretical expression for the acoustic radiation from point rotating dipole sources was derived by Mao Y and Tang (2012), using spherical harmonics. Mao and Tang investigated the effect of rotational speed on the acoustic radiation of tones and was able to provide directivity patterns of dipole sources at tonal frequencies.

McAlpine and Kingan (2012) also derived an expression for the rotating dipole sources, alongside an equivalent expression for monopole sources. Their theoretical model was used to give practical examples showing how the effect of rotational direction and location relative to a rigid body, representing a fuselage, affects the acoustic radiation.

The work on free-field simple source radiation was extended by McAlpine et al. (2015) to consider distributions of sources. They used this source distribution model to predict the near field radiation tones of a rotor. In their paper, they validated their results using experiments. Their work quantitatively identified the effect of a rigid cylinder, representative of a aircraft fuselage, on the radiated noise of a rotor. Blade passing frequencies were considered as well as supersonic operating conditions.

The only study aimed at characterising the differences between free-field and ducted radiation was conducted by Chapman (1996). Chapman identified the 'nil-shielding' directions, which are particular angles that the duct does not influence the radiation of the mode, causing equal free-field and ducted acoustic source radiation for modes of consistent azimuthal mode order.

Chapman (1996) considered the radiation of multiple radial mode orders but was restricted to investigations of a single azimuthal order, which is not likely representative of a radiated pressure field from a ducted source, limiting it's applicability. Additionally, Chapman restricted his analysis to dipole sources. A development of Chapman's findings is presented in this thesis, which allows for multiple azimuthal orders to be incorporated, as well as the location of the source to be considered, better representing source radiation.

1.3.2 Modal radiation from a semi-infinite flanged duct

This section reviews the theoretical models for modal radiation from a semi-infinite flanged duct. The first prediction of the acoustic radiation from a flanged duct was conducted using the flanged duct model. Nomura et al. (1960) formulated a prediction for the far-field radiation from a flanged duct assuming plane wave excitation i.e. a spatially independent pressure distribution on the duct cross section. Their model was used to predict the radiation impedance, transmission coefficient, power gain function and end correction for the plane wave mode radiating from a flanged duct.

The Rayleigh integral was used by Tyler and Sofrin (1962) to predict the modal radiation from a flanged duct for higher mode orders. Rayleigh (1945) developed a relationship between the velocity of a vibrating surface inside a rigid body, in principal extending to infinity, and the associated radiated acoustic field - which is now known as the Rayleigh integral. Tyler and Sofrin represented the vibrating surface as a duct mode shape in the Rayleigh integral. This enabled the forward-arc radiation from a single duct mode to be predicted for cut-on modes.

A more recent use of Tyler and Sofrin's work was undertaken by McAlpine et al. (2012) who inferred the radiated pressure field from an inclined duct by solving the Rayleigh integral in an inclined coordinate system. They found that the acoustic field was essentially radiated by an angle equal to the inclination angle of the duct.

Chapman (1994) used the flanged duct model to identify some features of modal duct radiation directivity patterns for cut-on modes. One such feature discussed is known as the 'quiet zone', a region of relatively low radiation caused by sub-sonic radiating components. The region of the quiet zone extends from the duct axis to some angle governed by the modes azimuthal order and excitation frequency.

The mode-ray angles were also identified in Chapman (1994), which represent the location of the maximum radiation due to cut-on modes. The mode-ray angles are governed solely by mode cut-on ratio. Alongside the mode-ray angle, Chapman identified the presence of side-lobes in cut-on mode directivity patterns. These features of cut-on mode radiation have not been investigated for cut-off modes.

1.3.3 Modal radiation from a semi-infinite un-flanged duct

The first attempt at predicting the characteristics of ducted radiation from an un-flanged duct was by Levine and Schwinger (1948), who developed the solution for the far-field acoustic pressure due to plane wave radiation from a cylindrical hard-walled un-flanged duct. This enabled the first comparisons between the flanged and un-flanged duct models, which revealed the flanged model has modal radiation similar to the un-flanged, but is typically higher in the sideline directions (perpendicular to the duct axis), the radiation near the flange. Furthermore the first indication of rear-arc radiation from ducted sources was obtained.

The more general solution for the radiation from higher order modes for un-flanged ducts was obtained by Weinstein (1969) using the Wiener–Hopf method whose solution was expressed in terms of complex contour integrals. The formulation presented by Weinstein was difficult to interpret due to the complexity of the contour integrals, making predictions difficult for the modal radiation.

Homicz and Lordi (1975) also developed an expression for the far-field modal pressure from a semi-infinite hard-walled un-flanged duct using the Wiener–Hopf technique but in a form much more amenable to computation. Mean flow effects were included by the use of a Lorenz transformation. Homicz and Lordi's model was found to be in good agreement with the flanged model of Tyler and Sofrin (1962) matching exactly at the region of highest radiation (which are now known as the mode ray-angles), as well as the location of the nulls (angles of no radiation). The models deviated somewhat in the sideline direction - highlighting the limits of approximating a duct with a flange, which also cannot predict rear-arc radiation. Homicz and Lordi's model agreed with the findings of the plane wave mode radiation model from Weinstein (1969).

The theoretical model of Homicz and Lordi (1975) was compared to experimental data by Snakowska et al. (1996). Comparisons were made for the far-field modal directivity factor using the mathematical model and experimental data. Snakowska found that the experimental data matched well the theoretical model, although at certain angles the directivity was seen to under-predict the theoretical results.

Munt (1977) obtained a more general formulation for the modal radiation from circular ducts in the presence of realistic flow profiles in the duct, such as a radially varying mean flow, density and temperature. Munt showed that mean flow increases the acoustic radiation upstream, which was supported by experimental data.

The effects on the radiation due to a centre body were included in the analysis by Gabard and Astley (2006). These additional features improved the practical capability of the un-flanged duct model making it more directly applicable to aircraft engine bypass ducts. Gabard and Astley used their theoretical model to predict modal and multi-modal far-field radiation directivity patterns, considering cut-on modes only.

By increasing the practical capabilities of the un-flanged duct radiation model, the model first derived by Munt (1977) enabled the pressure radiation from cut-off modes to be predicted, in it's presented form, where the solution of Homicz and Lordi (1975) did not.

More recently, the semi-infinite duct radiation model was studied by Peake and Abrahams (2020), who modeled liners in a duct with an annulus, which led to a matrix Wiener-Hopf problem. They went on to use their model to identify the effect of varying the properties of the wall lining, comparing results to the hard walled solution.

1.3.4 Modal radiation from a finite length duct

The calculation of the far-field modal radiation from a finite length duct terminated at both open ends with a spherical flange was conducted by Doak (1973a) and Doak (1973b). An exact method of calculating the near, and far-field pressure radiation due to an acoustic source distribution inside a duct with a spherical flange was derived. Doak presented multi-modal calculations for the radiated power at different frequencies and found that relative maxima and minima occur at modal cut-on frequencies, identifying modes are most significant just as they become cut-on, at their respective cut-on frequencies.

An approximate formulation for the modal pressure radiation from a finite length duct was derived by Johnston and Ogimoto (1980a), who validated their theoretical pressure radiation formulae considering plane waves with experimental results, Johnston and Ogimoto (1980b). Using their formulations, they found axial standing waves are generated inside the duct causing peaks in the far-field radiation spectra at specific frequencies.

Hamdi and Ville (1982) presented an exact formulation for the radiation from a finite length duct of variable cross section valid for propagating modes. They used a variational formulation by integral equations, in place of the Wiener–Hopf technique, to avoid the explicit evaluation of the duct termination at the second open end.

It was found by Hamdi and Ville (1982) that, due to interference between the radiation of the forward and rear-arc, modal radiation from a finite duct gives an increased number of lobes in the far-field directivity than the semi-infinite duct case. This was shown to potentially cause the maximum radiation to not be on the duct axes, even for the plane wave mode. The formulation proposed by Hamdi and Ville is invalid for modes excited below cut-off. Therefore, their model cannot be used to accurately predict the acoustic radiation from a finite length duct of a small length relative to the wavelength of the source radiation.

1.3.5 Multi-modal radiation, modal amplitudes and reflections at the open end of ducts

This section is a review of work regarding multi-modal radiation from ducted sources. To obtain a multi-modal solution using the flanged duct expression, an understanding of the reflection at the open end of the duct is required. Zorumski (1973) used a matrix formulation to infer the effect of reflection at the open end of the duct in terms of an impedance scattering matrix. Zorumski found that the reflection coefficients are a complex quantity that, at cut-off, are purely real with a value of 1. The effect of reflections diminishes as the mode becomes increasingly cut-on, as the frequency is increased. Although some figures in Zorumski (1973) presented data for the reflections and radiation impedance for modes below cut-off, no detailed analysis was discussed.

One of the first studies that considered multi-modal ducted radiation was by Rice and Prydz (1978). The cut-off ratio was used to approximate the modal relative source amplitude (which Rice described as a biasing function). Rice used this biasing function to add modes incoherently (neglecting the relative phase of the modes) to infer the multi-modal radiation from a flanged duct. Rice used this model to predict the radiated power and found that local minima and maxima in the power spectra occur at modal cut-on frequencies.

The first multi-modal radiation calculations using the un-flanged duct model were conducted by Joseph and Morfey (1999), who presented radiation patterns for incoherent monopole, axial dipole and equal energy per mode source radiation models. The modal amplitude functions were restricted to cut-on modes assuming the sources were buried deep inside the duct, using the theoretical model of Homicz and Lordi (1975). Furthermore, they went on to form high frequency, asymptotic approximate relations.

The effects of modal reflection due to propagating duct modes incident upon the duct open end considering an un-flanged duct was analysed by Snakowska and Jurkiewicz (2010). They found relative minimum appear in the modal power spectra at the cut-on frequencies of modes of a difference radial order.

Hewlett et al. (1997) derived an approximate solution for the radiation from a finite length duct, terminated at both open ends with an infinite flange. Using the semi-infinite duct radiation theoretical model of Tyler and Sofrin (1962) and accounting for reflection at both open ends, using Zorumski (1973) they were able to predict the far-field radiation from a point monopole source in a finite length duct. Hewlett et al did not expand their work to other source types, limiting it's applicability. Furthermore their work considered a flanged duct only, meaning the interaction of the effective rear-arcs with the forward-arcs were not investigated. Only cut-on modes were included in their calculations.

1.3.6 Radiation of cut-off modes from ducts

This section is a review of the few research papers that discuss the radiation of cut-off modes from ducts and a discussion of the only research paper that has investigated the radiation of sources close to the open end of ducts.

The effect on acoustic radiation due to locating a source close to the open end of ducts was briefly investigated by Howe (1992), and is the only published study that specifically looks into this effect. Howe derived expressions for the radiated pressure field for blade vortex interaction tones of rotors. Asymptotic approximations for the high and low frequency acoustic radiation cases were formulated. It was found that for sources located close to the open end of the duct the sound power radiated is increased, which is predominantly observed at the lower frequencies. Howe did not break the source into cut-on and cut-off modal components, meaning his approach is difficult to generalize.

Morfey (1969) has studied directly the radiation behaviour of cut-off modes which was confined to an analysis of their radiation efficiencies from a flanged duct. He found that cut-on modes radiate with near perfect (unity) radiation efficiency that decreases as the excitation frequency is reduced below their cut-on frequency, at a rate that is predominantly determined by the modes azimuthal order.

Doak (1973a) developed the findings of Morfey (1969) by repeating the analysis regarding modal radiation efficiency above and below cut-off for a finite length duct with a spherical flange. Doak found oscillatory behavior of the radiation efficiency of modes excited below cut-off. Neither Doak nor Morfey, investigated the radiation efficiency of modes using the un-flanged duct model and their analysis was restricted to modes a relatively short way below cut-off.

Wang and Tszeng (1984) predicted the effect of reflections due to cut-off modes incident upon the open end of the duct. They identified that the reflection of modes approaches 1 from above *and* below cut-on. The range of frequencies investigated was restricted to just below cut-off.

Cut-off modes were recently studied by Snakowska and Jurkiewicz (2021) who analysed the multi-modal sound field in a duct. They studied the propagation and transmission loss from cut-on and cut-off modes, which can be used in muffler design. Their formulation presented a new scattering matrix computational method and incorporate near-field effects. Their predictions of the scattering matrix were compared against published results to find good agreement.

1.4 Scope of this Thesis

This section details the original contributions in this thesis.

In *Chapter 3*, the study of modal efficiencies is extended by using the un-flanged duct model. An approximate expression for the modal efficiency from a flanged duct is derived, which is in good agreement at low frequencies with the un-flanged modal efficiency, and at nearly all frequencies for the first radial order mode. Also included in *Chapter 3* is an analysis of the effect of modal reflections below cut-off, which reinforces and develops the conclusions of Wang and Tszeng (1984), who identified characteristics of the effect of reflection just below cut-off. In this chapter the asymptotic behavior of the effect of reflection far below cut-off is investigated.

The polar directivity factors, for cut-on modes is well understood, for example Tyler and Sofrin (1962), Chapman (1994) and Gabard and Astley (2006). Features such as the location of the mode ray angle (region of maximum directivity) and nulls (location of no radiation) are easily predictable. For cut-off modes these features are largely unknown, an investigation for such features is presented in *Chapter 3*. The properties of the cut-off modes, such as the efficiency and directivity are found to be weakly dependent on the radial mode order, which is shown mathematically in *Appendix A* from analysis of the Wiener–Hopf kernel function.

Based on the theoretical models of McAlpine and Kingan (2012) and McAlpine et al. (2015) for the acoustic radiation from free-field point sources and source distributions, *Chapter 5* and *7* predict the effect of placing a duct around free-field sources. There is a particular emphasis on sources with axial planes close to the open ends of the duct, where cut-on and cut-off modes have the potential to radiate strongly.

Joseph and Morfey (1999) derived some modal amplitudes for duct modes, based on the earlier work of Rice and Prydz (1978), for source distributions valid for cut-on modes. In *Chapter 4*, an alternative derivation is shown with extended validity to cut-off modes. Modal amplitudes are derived for point sources as well as source distributions.

Chapter 5 presents predictions of the multi-modal acoustic radiation from sources close to the open end of semi-infinite ducts, including radiation from cut-on and cut-off modes. These predictions are compared to the radiation of equivalent free-field sources to identify the effect of the duct.

Based on the model of Hewlett et al. (1997), an approximate finite length duct radiation model is derived. The derivation, presented in *Chapter 6*, uses the un-flanged, semi-infinite duct polar directivity factor which, accounting for modal reflections at both open ends of the duct, is used to approximate a finite length duct. Predictions are compared to the radiation of equivalent free-field sources.

The free-field and ducted theoretical radiation predictions are validated via means of numerical simulations. The simulations were conducted using COMSOL Multiphyics, comparisons between the theoretical and numerical predictions are presented in *Chapter 1* for the semi-infinite duct case and *Chapter 7* for the finite length duct case.

Additional means of validation of the conclusions from the theoretical duct radiation models are presented via results of an experiment. The experiment comprised a relatively large pipe blocked at one end to represent a semi-infinite duct. A broadband driven loudspeaker was used as the source and thirteen microphones were used to measure the far-field directivity. The experimental results are compared to the theoretical duct radiation model in *Chapter 8*.

1.4.1 Publications

In production of this thesis, 4 conference proceedings and 1 journal paper have been published, a second journal paper has been submitted for publication.

Findings from *Chapter 3*, regarding the characteristics of cut-off modes where presented at the international conference of underwater acoustics 2020 and published in Baddour et al. (2020) and have been published as a full length Journal article in Baddour et al. (2022a).

The modal source amplitude formulations from *Chapter 4* were presented at the Aero-acoustics conference 2021 and published in Baddour et al. (2021). Additionally, at that conference, multi-modal directivity patterns, highlighting the influence of cut-off modes were presented, which are detailed in *Chapter 5*.

The comparisons between free-field and ducted sources, considering a semi-infinite duct shown in *Chapter 5* were presented at the Aero-acoustics conference 2022 and published in Baddour et al. (2022c). A Journal paper has been submitted for publication to the American Institute of Aero-acoustics Journal, which further develops these findings.

The comparisons between free-field and ducted sources, considering a finite length ducts were presented at the international conference of acoustics 2022 and published in Baddour et al. (2022b). These findings are detailed in *Chapter's 6* and *7*.

Chapter 2

Acoustic radiation from a semi-infinite duct

In this section a theoretical model to predict the far-field acoustic radiation due to arbitrary source distributions inside un-flanged and flanged semi-infinite hard-walled ducts is developed. The axial flow speed (mach number) is assumed trivial, which is likely representative of the case for marine ducted propellers. This model is extended to a finite duct radiation model in *Chapter 6*, based on the findings presented here.

Consider an arbitrary source distribution located a distance z_0 from the open end of a semi-infinite duct of radius a. The source is made of infinitesimal source elements each located at $\boldsymbol{X_0}$ with radial position r_0 and azimuthal angle θ_0. In-duct observers are located at $\boldsymbol{X}$ with a single radial position r, azimuthal angle θ and axial position z. Far-field observers are located outside the duct at a single radius R, polar angle ϕ and azimuthal angle θ. A sketch of the ducted source and associated coordinates is shown in *figure 2.1*.

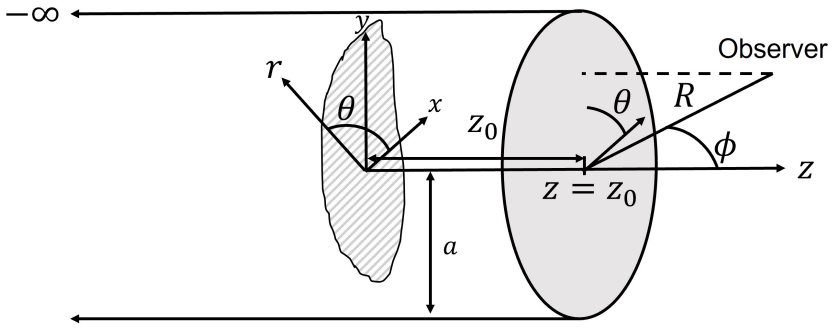

FIGURE 2.1: Sketch of source distribution inside a semi-infinite duct and associated coordinates

2.1 Acoustic pressure inside an infinite duct

To obtain expressions for the acoustic pressure both inside and radiated from semi-infinite ducts first consider the harmonic solution to the sound field inside an infinite duct. It is assumed a pressure field $\hat{p}$ is harmonic in time t, at a single frequency ω of the form,

$$\hat{p}(\boldsymbol{X}, t) = p(\boldsymbol{X}, \omega)\mathrm{e}^{j\omega t}. \tag{2.1}$$

The pressure field inside an infinite, hard-walled, cylindrical duct, in cylindrical polar coordinates, $p^{(D)}(r, \theta, z, \omega)$, can be found from solution of the Helmholtz equation,

$$\frac{\partial^2 p^{(D)}}{\partial r^2} + \frac{1}{r}\frac{\partial p^{(D)}}{\partial r} + \frac{1}{r^2}\frac{\partial^2 p^{(D)}}{\partial \theta^2} + \frac{\partial^2 p^{(D)}}{\partial z^2} + k^2 p^{(D)} = 0, \tag{2.2}$$

where k is the acoustic wavenumber, which for medium speed of sound c, is computed $k = \omega/c$. Furthermore, the pressure must satisfy the hard-walled boundary condition at the wall of the duct $r = a$, of the form,

$$\left.\frac{\partial p^{(D)}}{\partial r}\right|_{r=a} = 0. \tag{2.3}$$

Using the method of separation of variables, the acoustic pressure field inside the duct can be constructed from a modal sum of the form,

$$p^{(D)}(r, \theta, z, \omega) = \sum_{m=-\infty}^{\infty}\sum_{n=1}^{\infty} p_{mn}^{(D)}(r, \theta, z, \omega), \tag{2.4}$$

where each modal term has azimuthal order m and a radial order n, of the form

$$p_{mn}^{(D)}(r, \theta, z, \omega) = a_{mn}(\omega)\Psi_{mn}(r, \theta)\mathcal{Z}(z), \tag{2.5}$$

where $\Psi_{mn}(r, \theta)$ is the normalised mode shape function and $a_{mn}(\omega)$ is the modal pressure amplitude.

Substituting *Eq. 2.5* into *Eq. 2.2* and solving for the axial z component reveals,

$$\mathcal{Z}(z) = e^{-jk_{z,mn}z} \tag{2.6}$$

where $k_{z,mn}$ is the axial wavenumber. Similarly, substituting *Eq. 2.5* into *Eq. 2.2* and solving for the azimuthal θ dependence is of the form,

$$\Psi_{mn}(r,\theta) = \psi_{mn}(r)\mathrm{e}^{-jm\theta}. \tag{2.7}$$

Finally, to obtain the radial r variation, *Eqs. 2.5, 2.6* and *2.7* are substituted into *Eq. 2.2* to give,

$$\frac{\partial^2}{\partial r^2}\psi_{mn}(r) + \frac{1}{r}\frac{\partial}{\partial r}\psi_{mn}(r) + \left(k^2 - k_{z,mn}^2 - \frac{m^2}{r^2}\right)\psi_{mn}(r) = 0. \tag{2.8}$$

Equation 2.8 is Bessel's differential equation and is assumed to have solution,

$$\psi_{mn}(r) = \frac{J_m(\kappa_{mn}r)}{N_{mn}}, \tag{2.9}$$

where N_{mn} is the normalization factor, J_m is the Bessel function of the first kind of order m and κ_{mn} is the radial wavenumber, obtained by applying the hard-walled boundary condition of *Eq. 2.3*. The radial wavenumber κ_{mn} is calculated by considering the n^{th} turning point of the Bessel function of order m.

The relationship between the radial, axial and acoustic wavenumbers, known as the Dispersion relationship, is of the form,

$$k_{z,mn}^2 + \kappa_{mn}^2 = k^2. \tag{2.10}$$

This result delineates the range of propagating modes $k > \kappa_{mn}$ (for which $k_{z,mn}$ is purely real) from non-propagating cut-off modes $k < \kappa_{mn}$ (for which $k_{z,mn}$ is purely imaginary. Applying these conditions to *Eq. 2.6* identifies that cut-off modes exhibit evanescent decay along the duct axis, where cut-on exhibit a phase change.

Two non-dimensional measures of the degree to which a mode is cut-on or cut-off is adopted here, one is the modal cut-off ratio ζ_{mn} defined,

$$\zeta_{mn} = \frac{ka}{\kappa_{mn}a}. \tag{2.11}$$

Cut-on modes are therefore associated with $\zeta_{mn} > 1$, while cut-off modes are associated with $\zeta_{mn} < 1$. Another non-dimensional index of the degree to which a mode is cut-off is defined,

$$\xi_m = \frac{ka}{m}. \tag{2.12}$$

Noting that $\kappa_{m,1} \approx m$ (for large m), by estimation of the first turning point of the Bessel function, the two modal indices are approximately related by $\xi_m \approx \zeta_{m,1}$.

The mode shape function is chosen to satisfy the normalisation property,

$$\int_S |\Psi_{mn}(r,\theta)|^2 dS = S, \tag{2.13}$$

where S is the cross sectional area of the duct. Substituting the mode shape function $\Psi_{mn}(r,\theta)$ of *Eq. 2.7* and *2.9* into *Eq. 2.13*, noting that $dS = rdrd\theta$, gives

$$N_{mn}^2 = \frac{1}{S}\int_0^{2\pi}\int_0^a J_m^2(\kappa_{mn}r)rdrd\theta. \tag{2.14}$$

The integral across r in *Eq. 2.14* is solved using the orthogonality property of the Bessel function, the azimuthal integral is solved simply as $\int_0^{2\pi} d\theta = 2\pi$. Combining these results reveal N_{mn} is of the form,

$$N_{mn}^2 = \left[\left(\frac{r^2}{a^2} - \frac{m^2}{(\kappa_{mn}a)^2}\right)J_m^2(\kappa_{mn}r) - \left(\frac{r}{a}J'_m(\kappa_{mn}r)\right)^2\right]_{r=0}^{r=a}. \tag{2.15}$$

Substituting the normalisation factor of *Eq. 2.15* into the mode shape function of *Eq. 2.7*, inserting the limits and noting the hard-walled boundary condition of *Eq. 2.3*, leading to $J'_m(\kappa_{mn}a) = 0$, reveals,

$$\psi_{mn}(r) = \frac{J_m(\kappa_{mn}r)}{\sqrt{(1-\frac{m^2}{\kappa_{mn}^2a^2})}J_m(\kappa_{mn}a)}. \tag{2.16}$$

Note in *Eq. 2.9* for $(m,n) = (0,1)$, the plane wave, $N_{01} = 1$. The mode shape function represents the spacial pressure distribution inside a duct. *Figure 2.2* shows the first few modes of varying m and n with the lines of zero pressure shown as black lines.

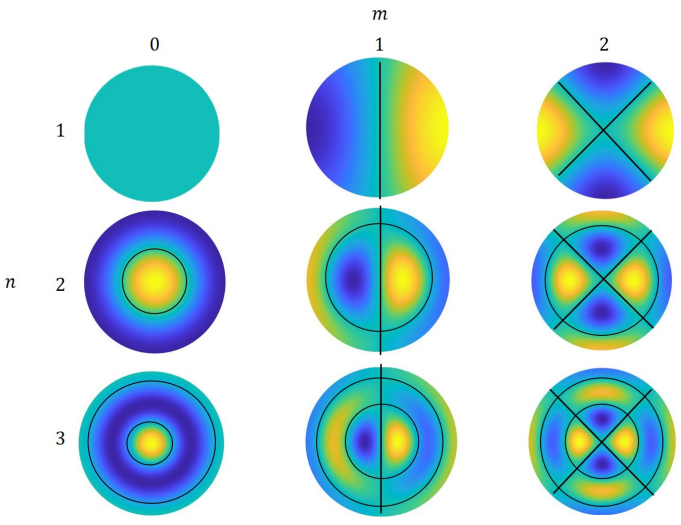

FIGURE 2.2: Duct mode shapes with lines of zero pressure indicated by black lines.

Figure 2.2 shows the azimuthal order m governs the number of radial lines and radial order n governs the number of nodal circles in the mode shape function $\Psi_{mn}(r,\theta)$ of *Eq. 2.16*.

2.1.1 Green's function

This section derives an expression for the pressure radiated from an arbitrary source distribution, such as the sketch shown in *figure 2.1*, to an observer *inside* the duct.

Consider the modal Green's function that relates the acoustic pressure released from a source element inside a duct at location $\boldsymbol{X}_0(r_0,\theta_0,z_0)$ at retarded time t_0 to an observer inside the duct at location $\boldsymbol{X}(r,\theta,z)$ at observer time t. The frequency domain Greens function, $G_{mn}(\boldsymbol{X}|\boldsymbol{X_0},\omega)$, obeys the inhomogeneous Helmholtz equation,

$$\frac{\partial^2 G_{mn}}{\partial r^2}+\frac{1}{r}\frac{\partial G_{mn}}{\partial r}+\frac{1}{r^2}\frac{\partial^2 G_{mn}}{\partial \theta^2}+\frac{\partial^2 G_{mn}}{\partial z^2}+k^2 G_{mn}=\delta(\boldsymbol{X}-\boldsymbol{X}_0), \tag{2.17}$$

where δ is the Dirac delta function. The Green's function allows the pressure to be computed for any arbitrary source distribution using,

$$\hat{p}^{(D)}_{mn}(r,\theta,z,t)=\int_S\int_{-\infty}^{\infty}\hat{s}(r_0,\theta_0,t_0)\hat{G}_{mn}(\boldsymbol{X},t|\boldsymbol{X_0},t_0)dtdS(r_0,\theta_0), \tag{2.18}$$

where $\hat{s}(r_0,\theta_0,t_0)$ is the source term and $S(r_0,\theta_0)$ is the cross sectional area of the source. The time domain Green's function $\hat{G}_{mn}(\boldsymbol{X},t|\boldsymbol{X_0},t_0)$ can be determined by inverse Fourier transform of $G_{mn}(\boldsymbol{X}|\boldsymbol{X_0},\omega)$,

$$\hat{G}_{mn}(\boldsymbol{X},t|\boldsymbol{X}_0,t_0)=\frac{1}{2\pi}\int_{-\infty}^{\infty}G_{mn}(\boldsymbol{X}|\boldsymbol{X_0},\omega)\mathrm{e}^{j\omega(t-t_0)}d\omega. \tag{2.19}$$

To obtain the frequency domain Green's function for a hard-walled infinite duct, a separable solution is assumed, with radial r and azimuthal θ dependence's of the form of the normalised mode shape function $\Psi(r,\theta)$ of *Eq. 2.7*. The Green's function is of the form,

$$G_{mn}(\boldsymbol{X}|\boldsymbol{X_0},\omega)=\mathcal{A}_{mn}(\boldsymbol{X_0},\omega)\Psi_{mn}(r,\theta)\mathcal{Z}(z), \tag{2.20}$$

assuming separation of variables (r,θ) and z and $\mathcal{A}_{mn}(\boldsymbol{X_0},\omega)$ is the modal amplitude.

Substituting *Eq. 2.20* into *Eq. 2.17* shows,

$$\mathcal{G}_{mn}(\boldsymbol{X_0},\omega)\Psi_{mn}(r,\theta)\left(\frac{\partial^2}{\partial z^2}\mathcal{Z}(z)+k^2_{z,mn}\mathcal{Z}(z)\right)=\delta(\boldsymbol{X}-\boldsymbol{X}_0), \tag{2.21}$$

Multiplying *Eq. 2.21* by $\Psi^*_{mn}(r,\theta)$ and integrating across the cross sectional area of the duct S,

$$\mathcal{A}_{mn}(\boldsymbol{X_0},\omega)\frac{1}{S}\int_S \Psi_{mn}(r,\theta)\Psi^*_{mn}(r,\theta)dS\left(\frac{\partial^2}{\partial z^2}\mathcal{Z}(z)+k^2_{z,mn}\mathcal{Z}(z)\right)=\frac{1}{S}\int_S \Psi^*_{mn}(r,\theta)\delta(\boldsymbol{X}-\boldsymbol{X_0})dS(r_0,\theta_0). \tag{2.22}$$

To solve the integrals over S in *Eq. 2.22*, the normalisation property of the mode shape functions, *Eq. 2.13*, is used, as well as the sifting property of the Dirac delta function,

$$\mathcal{A}_{mn}(\boldsymbol{X_0},\omega)\left(\frac{\partial^2}{\partial z^2}\mathcal{Z}(z)+k^2_{z,mn}\mathcal{Z}(z)\right)=\frac{1}{S}\Psi^*_{mn}(r_0,\theta_0)\delta(z-z_0). \tag{2.23}$$

Noting the delta function in *Eq. 2.23*, the solution for $\mathcal{Z}(z)$ is required everywhere, including at $z=z_0$. To examine $\mathcal{Z}(z_0)$ an integral from $z_0-\epsilon$ to $z_0+\epsilon$ is performed and again using the sifting property of the delta function,

$$\mathcal{A}_{mn}(\boldsymbol{X_0},\omega)\left(\frac{\partial}{\partial z}\mathcal{Z}(z_0+\epsilon)-\frac{\partial}{\partial z}\mathcal{Z}(z_0-\epsilon)\right)+\mathcal{G}_{mn}(\boldsymbol{X_0},\omega)k^2_{z,mn}\int_{z_0-\epsilon}^{z_0+\epsilon}\mathcal{Z}(z)dz=\frac{1}{S}\Psi^*(r_0,\theta_0). \tag{2.24}$$

As $\epsilon\to 0$, the solution to the integral in *Eq. 2.24* also tends to zero. Assuming only forward propagating waves in the region $z>z_0$, c.f. *figure 2.1*, a function that satisfies *Eq. 2.24* is of the form,

$$\mathcal{Z}(z)=e^{-jk_{z,mn}(z-z_0)}. \tag{2.25}$$

Substituting *Eq. 2.25* into *Eq. 2.24*, solving for $\mathcal{A}_{mn}(\boldsymbol{X_0},\omega)$, reveals the frequency domain Green's function is of the form,

$$G_{mn}(\boldsymbol{X}|\boldsymbol{X_0},\omega)=\frac{j}{2S}\Psi_{mn}(r,\theta)\Psi^*_{mn}(r_0,\theta_0)\frac{\mathrm{e}^{jk_{z,mn}(z_0-z)}}{k_{z,mn}},\quad z>z_0, \tag{2.26}$$

as derived by, for example McAlpine (2018).

2.2 Far-field acoustic pressure radiation from a duct

This section derives the far-field modal acoustic radiation from a flanged duct and presents the formulation for un-flanged duct. A flange represents a rigid surface at the open end of a duct, extending in principal to infinity. The flanged model gives an approximate formulation for the forward-arc of the far-field acoustic radiation from ducted sources.

The un-flanged duct model requires numerical solution to the the Wiener-Hopf equation, making the radiation from an un-flanged duct drastically more complicated to derive and compute. The derivation and solution of the radiation from a flanged duct provides insight into duct radiation.

2.2.1 Far-field pressure radiation from a flanged duct

This section derives the far-field acoustic radiation from a flanged duct. Consider a circular axial velocity distribution of radius a and cross sectional area S inside an infinite hard-walled flange shown in *Figure 2.3*.

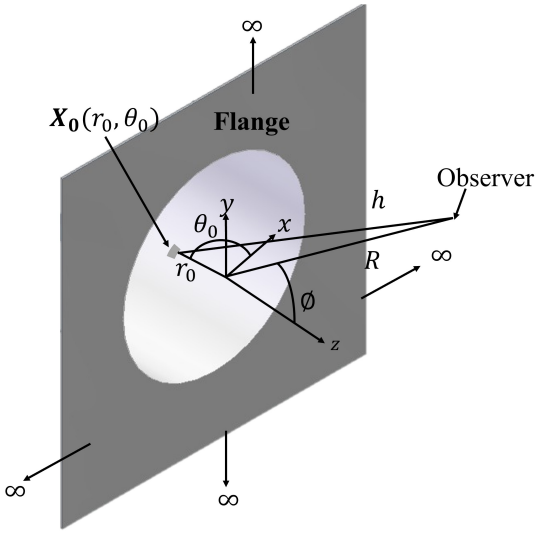

FIGURE 2.3: Semi-infinite, hard-walled flanged duct and associated coordinate system

The axial vibrating surface may be represented as a continuum of infinitesimal source elements located on the flange, each at position (r_0, θ_0). The distance between a given source element and the observer point is h.

The acoustic pressure of a harmonic, outgoing spherical wave, or monopole, of volume velocity q, in a medium of density ρ following Rienstra and Hirschberg (2004) is given by,

$$p(\boldsymbol{X}, \omega) = \frac{jk\rho cq(\omega)}{4\pi h} \mathrm{e}^{-jkh} \tag{2.27}$$

The volume velocity of each source element of the vibrating surface in *figure 2.3* is equal to the product of the axial velocity $u_z(r_0, \theta_0, \omega)$ on the surface and the elemental area, δS. Therefore, the contribution to the pressure $p_F^{(D)}(R, \phi, \theta, \omega)$ at the observer from each source element on the vibrating surface is of the form

$$\delta p_F^{(D)}(R, \phi, \theta, \omega) = \frac{jk\rho c}{2\pi h} u_z(r, \theta, \omega) \delta S(r_0, \theta_0) \mathrm{e}^{-jkh}. \tag{2.28}$$

The factor of 2 in *Eq. 2.28* is required to restrict the radiation forward $z > 0$, amounting to a pressure doubling, i.e. the flange doubles the pressure field. The pressure at the field point is formed from a sum of the contributions, $\delta p_F^{(D)}(R, \phi, \theta, \omega)$, from all source elements. In the limit as $\delta S(r_0, \theta_0) \to 0$, this becomes,

$$p_F^{(D)}(R, \phi, \theta, \omega) = \frac{jk\rho c}{2\pi} \int_S u_z(r, \theta) \frac{\mathrm{e}^{-jkh}}{h} dS(r_0, \theta_0) \tag{2.29}$$

Equation 2.29 is known as the Rayleigh integral. From *figure 2.3*, it can be shown that

$$h = \sqrt{R^2 + r_0^2 - 2Rr_0 \sin\phi \cos(\theta - \theta_0)}. \tag{2.30}$$

Considering the far-field, $R \to \infty$, approximations for h can be formed. Using the first term of the binomial expansion it can be shown in *Eq. 2.30*, $h \approx R - r_0 \sin\phi \cos(\theta - \theta_0)$ and $1/h \approx 1/R$. Substituting these approximations for h into the Rayleigh integral of *Eq. 2.29* shows the radiated pressure $p_F^{(D)}(R, \phi, \theta, \omega)$ is of the form,

$$p_F^{(D)}(R, \phi, \theta, \omega) \approx \frac{jk\rho c \mathrm{e}^{-jkR}}{2\pi R} \int_S u_z(r, \theta, \omega) \mathrm{e}^{jkr_0 \sin\phi \cos(\theta - \theta_0)} dS(r_0, \theta_0). \tag{2.31}$$

The velocity $u_z(r_0, \theta_0, \omega)$ in *Eq. 2.31* can be represented by the axial modal velocity distribution of a duct mode $u_{z,mn}(r, \theta, z, \omega)$. The axial modal velocity $u_{z,mn}(r, \theta, z, \omega)$ at a given axial position z inside an infinite duct is related to the pressure from the momentum equation in the axial dimension, the momentum equation is of the form,

$$u_z(\boldsymbol{X}, \omega) = -\frac{j}{\rho c k} \frac{\partial}{\partial z} p(\boldsymbol{X}, \omega). \tag{2.32}$$

Substituting the pressure of *Eq. 2.5* into the momentum equation of *Eq. 2.32* and computing the differentiation shows the modal velocity is of the form,

$$u_{z,mn}(r, \theta, z) = v_{mn}(\omega) \Psi_{mn}(r, \theta) \mathrm{e}^{-jk_{z,mn}z}. \tag{2.33}$$

where $v_{mn}(\omega)$ is the velocity modal amplitude of the form,

$$v_{mn}(\omega) = -a_{mn}(\omega)\frac{k_{z,mn}}{\rho c k} \tag{2.34}$$

Substituting the modal velocity of *Eq. 2.33* for $z = 0$, and the mode shape function $\Psi(r,\theta)$ of *Eq. 2.7* into the radiated pressure of *Eq. 2.31*, noting $dS = r_0 dr_0 d\theta_0$ reveals,

$$\begin{aligned} p^{(D)}_{F,mn}(R,\phi,\theta,\omega) \approx -\frac{jk_{z,mn}a_{mn}(\omega)\mathrm{e}^{-jkR}}{2\pi R\sqrt{(1-\frac{m^2}{\kappa^2_{mn}a^2})}J_m(\kappa_{mn}a)}\int_0^a J_m(\kappa_{mn}r_0)r_0 \\ \int_0^{2\pi}\mathrm{e}^{j(kr_0\sin\phi\cos(\theta-\theta_0)-m\theta_0)}d\theta_0 dr_0. \end{aligned} \tag{2.35}$$

To accurately relate the incident modal pressure distribution excited from a source inside the duct requires the effect of reflections to be incorporate. To simplify this analysis, the effect of reflections are initially neglected, although the effect of reflections are discussed later in this section and are included in the subsequent plots of this chapter.

The integral across θ_0 in *Eq. 2.35* is evaluated using the identity $\int_0^{2\pi}\mathrm{e}^{jX\cos(\Theta)+jm\Theta}d\Theta = 2\pi j^m J_m(X)$, to give

$$p^{(D)}_{F,mn}(R,\phi,\theta,\omega) \approx \frac{j^{m-1}k_{z,mn}a_{mn}(\omega)\mathrm{e}^{-j(kR+m\theta)}}{R\sqrt{(1-\frac{m^2}{\kappa^2_{mn}a^2})}J_m(\kappa_{mn}a)}\int_0^a J_m(\kappa_{mn}r_0)J_m(kr_0\sin\phi)r_0 dr_0. \tag{2.36}$$

From the classical solution to the radiation from a flanged duct, the integral across r_0 in *Eq. 2.36* is solved using the orthogonality of the Bessel function, showing the far-field pressure is of the form

$$p^{(D)}_{F,mn}(R,\phi,\theta,\omega) \approx a_{mn}(\omega)\left(\frac{a}{R}\right)D_{F,mn}(\phi,ka)\,\mathrm{e}^{-j(kR+m\theta)} \tag{2.37}$$

where $D_{F,mn}(\phi,ka)$ is the far-field modal non-dimensional polar directivity factor from a flanged duct of the form,

$$D_{F,mn}(\phi,ka) = j^{m-1}\frac{k_{z,mn}}{k}\frac{\sin\phi J'_m(ka\sin\phi)}{(\frac{\kappa^2_{mn}}{k^2}-\sin^2\phi)\sqrt{1-\frac{m^2}{\kappa^2_{mn}a^2}}}, \tag{2.38}$$

which was first derived by Tyler and Sofrin (1962). In *Chapter 3*, an alternative derivation of *Eq. 2.38* is shown by considering the radiating velocity components and neglecting those which only contribute to the near-field.

The flanged directivity expression of *Eq. 2.38* is not valid at,

$$\sin\phi_{mn} = \frac{\kappa_{mn}}{k}, \tag{2.39}$$

where the term $J'_m(ka\sin\phi_{mn})/(\frac{\kappa_{mn}^2}{k^2} - \sin^2\phi_{mn})$ becomes singular. Using L'Hôpital's rule and the Wronksian Bessel identity function from Rienstra and Hirschberg (2004), it can be shown,

$$D_{F,mn}(\phi_{mn}, ka) = \frac{1}{2} j^{m-1} k_{z,mn} a J_m(\kappa_{mn} a)\sqrt{1 - \frac{m^2}{\kappa_{mn}^2 a^2}}, \tag{2.40}$$

The radiation at the mode ray angle ϕ_{mn} of *Eq. 5.1*, corresponds to the location of maximum directivity for well cut-on modes. The significance of this angle to free-field and ducted radiation is explored in *Chapter 5*.

Equations 2.37 and *2.38* for the flanged duct radiation neglect the effect of reflections at the open end of the duct. However, the effect of reflections was first obtained by Zorumski (1973). A summary of the formulae is presented here, and full derivation is provided in Zorumski (1973). Consider a duct mode reaching the open end of the duct. As the mode experiences the change in boundary between the duct hard wall and free-field, the mode experiences reflections and is scattered into modes of different radial orders l. The effect of reflections is determined by the modal impedance $z_{mnl}(ka)$. The modal impedance and modal reflections $r_{mnl}(ka)$ are defined,

$$z_{mnl}(ka) = \frac{p_{mn}(\boldsymbol{X}, \omega)}{u_{mn}(\boldsymbol{X}, \omega)}, \tag{2.41}$$

$$r_{mnl}(ka) = \frac{p_{ml}^{(D)-}(\boldsymbol{X}, \omega)}{p_{mn}^{(D)+}(\boldsymbol{X}, \omega)}, \tag{2.42}$$

where $p^{(D)+}(\boldsymbol{X}, \omega)$ and $p^{(D)-}(\boldsymbol{X}, \omega)$ denote the forward incident and reflected waves respectively. For a hollow flanged duct, with no flow, Zorumski (1973) showed that the scattering impedance matrix $\boldsymbol{Z}_{mnl}(ka)$ is given by,

$$\boldsymbol{Z}_{mnl}(ka) = \begin{bmatrix} z_{m11} & \cdots & z_{m1l'} \\ \vdots & \ddots & \\ z_{mn'1} & & z_{mn'l'} \end{bmatrix}, \tag{2.43}$$

where the matrix is truncated at $(mn'l')$ but in principal these terms continue to infinity. Each term of the matrix is of the form,

$$z_{mnl}(ka) = \int_0^{\frac{\pi}{2}} \sin\phi d_{F,mn}(\sin\phi) d_{F,ml}(\sin\phi) d\phi - j\int_0^{\infty} \cosh\eta d_{F,mn}(\cosh\eta) d_{F,ml}(\cosh\eta) d\eta, \tag{2.44}$$

$$d_{F,mn}(\Theta) = \frac{\Theta J'_m(ka\Theta)}{(\frac{\kappa_{mn}^2}{k^2} - \Theta^2)\sqrt{1 - \frac{m^2}{\kappa_{mn}^2 a^2}}}. \tag{2.45}$$

Note $d_{F,mn}(\sin\phi)$ is the flanged directivity factor of *Eq. 2.38*. In *Eq. 2.44* n and l denote the row and column of the matrix element respectively. Combining *Eqs 2.43*, *2.44* and *2.45* allows the reflection matrix $\boldsymbol{R}_{mnl}(ka)$ to be computed using,

$$\boldsymbol{R}_{mnl}(ka) = \text{Inv}\left\{\left[ka\boldsymbol{I} + \boldsymbol{Z}_{mnl}(ka)\boldsymbol{K}_{z,mnl}\right]\right\} \times \left[ka\boldsymbol{I} - \boldsymbol{Z}_{mnl}(ka)\boldsymbol{K}_{z,mnl}\right], \tag{2.46}$$

where $\boldsymbol{I}$ is the identity matrix, Inv is the matrix inverse and $\boldsymbol{K}_{z,mnl}(ka)$ is a diagonal matrix of the axial wavenumbers,

$$\boldsymbol{K}_{z,mnl} = \begin{bmatrix} k_{z,m11}a & \dots & 0 \\ \vdots & k_{z,m22}a & \\ 0 & & k_{z,mn'l'}a \end{bmatrix}. \tag{2.47}$$

Combining *Eq. 2.46* and *Eq. 2.37* reveals the far-field multi-modal pressure radiation from a flanged duct $p_F^{(D)}(R,\phi,\theta,ka)$ is of the form,

$$p_F^{(D)}(R,\phi,\theta,\omega) = \left(\frac{a}{R}\right)\mathrm{e}^{-jkR}\sum_{m=-\infty}^{\infty}\boldsymbol{D}_m^{\boldsymbol{T}}(\phi,ka)\left(\boldsymbol{I} - \boldsymbol{R}_{mnl}(ka)\right)\boldsymbol{a}_m(\omega)\mathrm{e}^{-jm\theta}, \tag{2.48}$$

where $\boldsymbol{D}_m^{\boldsymbol{T}}(\phi,ka)$ is row vector (denoted by superscript $^{\boldsymbol{T}}$) of the modal directivity at one angle ϕ of the same azimuthal order m for each radial mode n,

$$\boldsymbol{D}_m^{\boldsymbol{T}}(\phi,ka) = \begin{bmatrix} D_{m1}(\phi,ka) & D_{m1}(\phi,ka) & \dots & D_{mn'}(\phi,ka) \end{bmatrix} \tag{2.49}$$

The modal amplitude vector $\boldsymbol{a}_m$ is of the form,

$$\boldsymbol{a}_m(\omega) = \begin{bmatrix} a_{m1}(\omega) \\ a_{m2}(\omega) \\ \vdots \\ a_{mn'}(\omega) \end{bmatrix}. \tag{2.50}$$

2.2.2 Far-field pressure radiation from an un-flanged duct

Consider a semi-infinite un-flanged hollow duct as shown in *figure 2.4*.

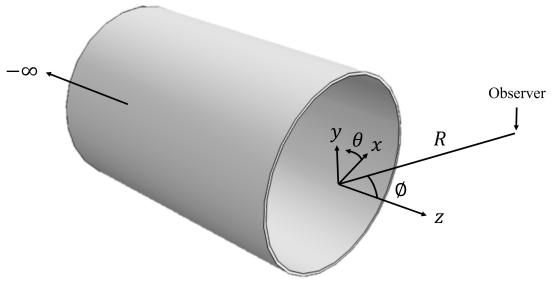

FIGURE 2.4: Semi-infinite, hard-walled un-flanged duct and associated coordinates

From solution of the Weiner-Hopf equation Gabard and Astley (2006) showed that with no flow, a hollow, un-flanged duct has far-field pressure of the form,

$$p_{mn}^{(D)}(R,\phi,\theta,\omega) = a_{mn}(\omega)\left(\frac{a}{R}\right)D_{mn}(\phi,ka)\mathrm{e}^{-j(kR+m\theta)}, \tag{2.51}$$

with modal directivity factor of the form,

$$D_{mn}(\phi,ka) = \frac{(1-\cos\phi)}{\pi ka\sin\phi H_m'(ka\sin\phi)}\frac{(ka+k_{z,mn}a)}{(k_{z,mn}a-ka\cos\phi)\sqrt{1-\frac{m^2}{\kappa_{mn}^2a^2}}}\frac{K_m^-(\kappa_{mn}a)}{K_m^+(ka\sin\phi)}, \tag{2.52}$$

where H_m is the Hankel function of the first kind of order m. The positive and negative Kernel functions $K_m^+(ka\sin\phi)$ and $K_m^-(\kappa_{mn}a)$ are discussed in *Appendix A*. Unlike the flanged directivity $D_{F,mn}(\phi,ka)$ of *Eq. 2.38*, *Eq. 2.52* includes the effect of reflections, therefore the radiated pressure $p(R,\phi,\theta,\omega)$ is of the form,

$$p^{(D)}(R,\phi,\theta,\omega) = \sum_{m=-\infty}^{\infty}\sum_{n=1}^{\infty}p_{mn}^{(D)}(R,\phi,\theta,\omega). \tag{2.53}$$

Gabard and Astley (2006) showed, that the reflection matrix $\boldsymbol{R}_{mnl}(ka)$ is of the form,

$$\boldsymbol{R}_{mnl}(ka) = \begin{bmatrix} r_{m11} & \dots & r_{m1l'} \\ \vdots & \ddots & \\ r_{mn'1} & & r_{mn'l'} \end{bmatrix}, \quad \text{where,} \tag{2.54}$$

$$r_{mnl}(ka) = \frac{J_m(\kappa_{mn}a)(ka+k_{z,mn}a)(ka+k_{z,ml}a)}{ka(k_{z,mn}a+k_{z,ml}a)J_m''(\kappa_{ml}a)k_{z,ml}a}\frac{K_m^-(\kappa_{mn}a)}{K_m^+(\kappa_{ml}a)}. \tag{2.55}$$

2.2.3 Modal efficiency

Each mode arriving at the duct open end radiates acoustic power with an efficiency, first investigated by Morfey (1969), that depends predominantly on how well it is cut-on or cut-off, as shall be explored in *Chapter 3*. The modal radiation efficiency τ_{mn} is defined for an un-flanged duct as the non-dimensional ratio of total radiated acoustic power $W_{mn}(\omega)$ to the mean square axial velocity modal amplitude, $1/2$ $|v_{mn}(\omega)|^2$, incident on the duct open end,

$$\tau_{mn} = \frac{W_{mn}(\omega)}{\rho c \frac{1}{2} |v_{mn}(\omega)|^2 S}, \tag{2.56}$$

where the radiated power $W_{mn}(\omega)$ can be determined by integrating the intensity,

$$W_{mn}(\omega) = \frac{2\pi}{\rho c} R^2 \int_0^{\pi} |p_{mn}^{(D)}(R, \phi, \theta, \omega)|^2 \sin\phi d\phi. \tag{2.57}$$

Note that this definition of radiation efficiency is fundamentally different from that investigated by Morfey (1969) for flanged ducts, which was defined with respect to the modal velocity amplitude *before* reflection. The modal radiation efficiency $\tau_{F,mn}$ from a flanged duct was defined,

$$\tau_{F,mn} = \frac{W_{F,mn}(\omega)}{\rho c \frac{1}{2} |v_{mn}(\omega)|^2 S}, \tag{2.58}$$

where,

$$W_{F,mn}(\omega) = \frac{2\pi}{\rho c} R^2 \int_0^{\pi/2} |p_{F,mn}^{(D)}(R, \phi, \theta, \omega)|^2 \sin\phi d\phi, \tag{2.59}$$

and does not include the effect of reflection at the open end of the duct. In his investigation Morfey (1969) was able to specify a single modal velocity component at the open end, which was then radiated to the far-field to compute the radiated sound power using the Kirchhoff approximation. This modal amplitude is therefore the velocity distribution that occurs *before* modal scattering has occurred at the open end. By contrast the radiation efficiency considering un-flanged ducts, however, specifies a single modal velocity component at the open end *after* reflection, as the effect of reflection is included in the directivity factor $D_{mn}(\phi, ka)$.

The modal radiation efficiencies investigated by Morfey (1969) and those for an un-flanged duct therefore differ by a factor relating to the modal scattering coefficients at the open end. It is therefore not possible to compare them directly although as will be explored, they share a number of common characteristics.

2.3 Comparison between predictions of the flanged and un-flanged duct models

This section compares the effect of reflections at the open of the duct and radiation directivity computed using the un-flanged and flanged theoretical duct models. The un-flanged duct radiation model, detailed in *Section 2.2.2* is relatively complicated. To obtain parameters such as the radiated pressure field requires numerical solution to the Wiener-Hopf equation. However, a much simpler model by comparison, is the flanged duct model, discussed in *Section 2.2.1*. Using the flanged duct model, the radiated pressure field can be approximated in the far-field without numerical integration, therefore it is advantageous to use when possible.

2.3.1 Reflection coefficient

This section compares the effect of reflections at the open end of the duct for the flanged and un-flanged duct models. To conduct these comparisons the effect of modal scattering is neglected, comparing only the diagonal terms in the reflection matrix $\boldsymbol{R}_{mn}(ka)$, i.e. $n = l$, which are the dominant terms. In this thesis, the reflection coefficient $r_{mn}(ka)$ is defined the magnitude the mode is reflected into a mode of the *same* order, and consequently can be calculated from *Eq. 2.55* for the un-flanged duct model and *Eq. 2.44* and *Eq. 2.46*, for the flanged duct model setting $n = l$. By neglecting the effect of modal scattering, and using $r_{mn}(ka)$ comparisons can be made without prescribing a modal amplitude $a_{mn}(\omega)$, required for use in *Eq. 2.42*. Therefore this analysis is independent of source type.

Figure 2.5 compares the effect of reflections $|r_{mn}(ka)|$ at the duct open end above and below cut-off calculated using the un-flanged and the flanged duct model. The analysis is presented for the typical modes of azimuthal index $m = 10$ and 20 and the same radial index $n = 3$ and the modes of the same azimuthal index $m = 2$ and radial indices $n = 10$ and 20, plotted against ζ_{mn}

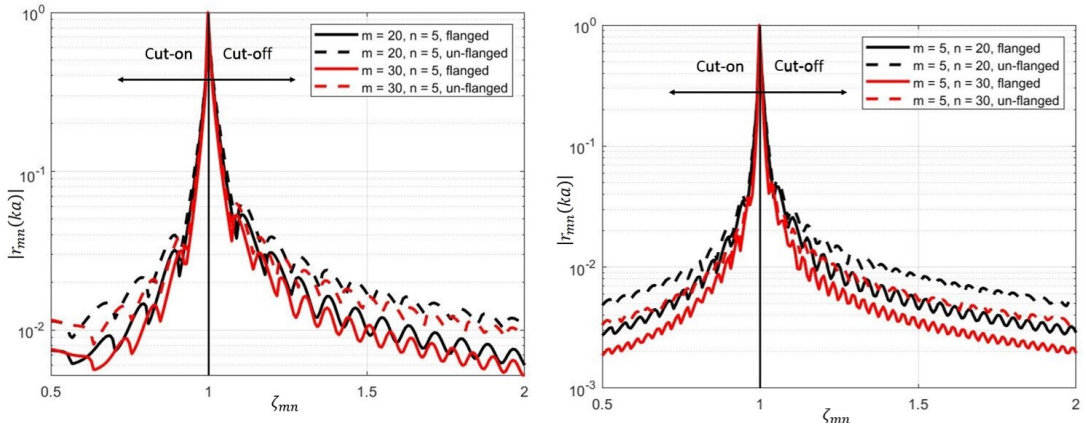

(A) Modes of diferent m (B) Modes of different n

FIGURE 2.5: Comparison between prediction of the reflection at the open end calculated using the flanged and un-flanged duct theoretical models.

Figure 2.5 shows good agreement between the methods of calculating $r_{mn}(ka)$, although the reflections computed using the flanged duct model appear to be consistently lower than that from the un-flanged duct by typically a factor of 2. This discrepancy appears independent of mode index (m,n) and frequency ka, and consistent for cut-on $\zeta_{mn} > 1$ and cut-off $\zeta_{mn} < 1$ modes. Although very close to cut-off, the agreement is excellent, matching exactly at cut-off where both methods indicate $|r_{mn}(ka)| = 1$.

2.3.2 Directivity

This section investigates the validity of approximating the flanged duct directivity factor of *Eq. 2.38* as the un-flanged directivity factor of *Eq. 2.52*, $D_{F,mn}(\phi, ka) \approx D_{mn}(\phi, ka)$. As previously noted the un-flanged directivity factor incorporates the effect of reflections at the duct open end where the flanged expression does not. To conduct this comparison, the effect of reflections is now incorporated in the flanged model, neglecting scattering using the method described above in *Section 2.3.1*.

Figure 2.6 shows a comparison between the directivities for the un-flanged and flanged duct models in dB $10\log(|D_{mn}(\phi, ka)|^2)$ and $10\log(|D_{F,mn}(\phi, ka)|^2)$ respectively, for a mode (m,n) = (10,10) excited at $\zeta_{mn} = 1.2$ (cut-on), 0.8 (cut-off), 0.4 and 0.01 corresponding to non-dimensional frequencies 52.3, 34.9, 17.4 and 0.4.

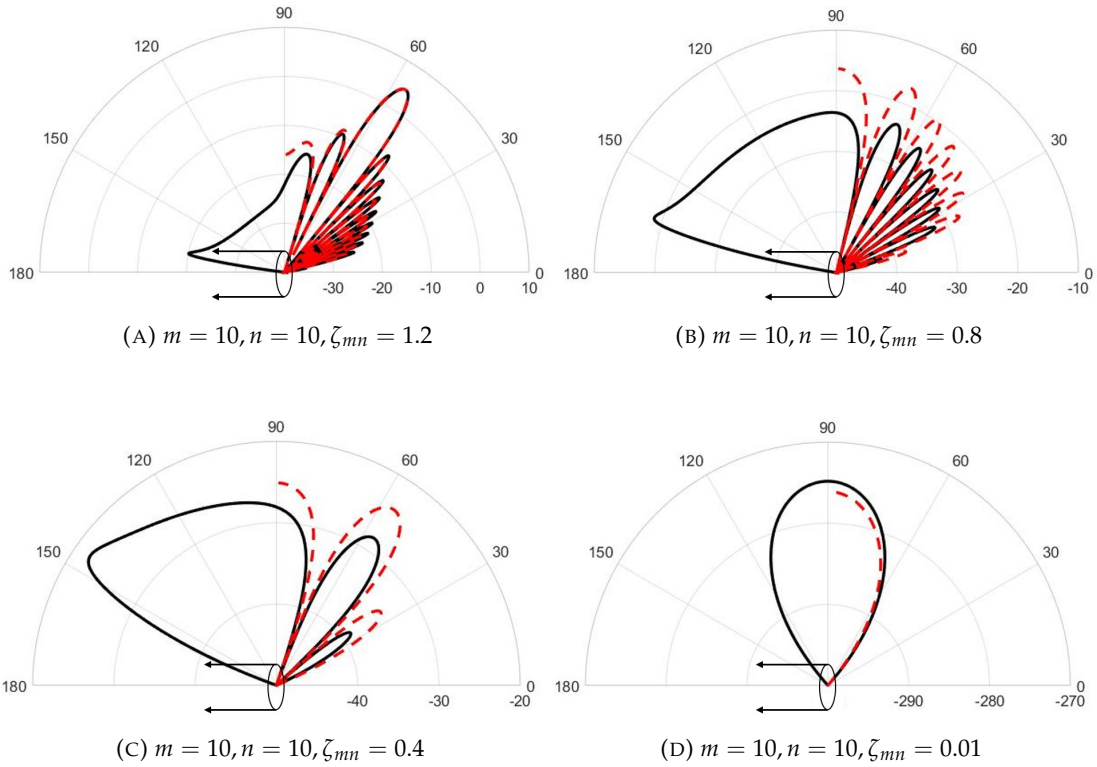

(A) $m = 10, n = 10, \zeta_{mn} = 1.2$ (B) $m = 10, n = 10, \zeta_{mn} = 0.8$

(C) $m = 10, n = 10, \zeta_{mn} = 0.4$ (D) $m = 10, n = 10, \zeta_{mn} = 0.01$

FIGURE 2.6: Comparison between directivities of the un-flanged (solid black line) and flanged (red dashed line) duct models. In dB re 1.

For modes excited above their cut-on frequency the flanged and un-flanged directivities have good agreement not too close to the sideline directions $60^\circ \lesssim \phi < 90^\circ$. In the sideline directions the models typically agree to within 3 dB, and elsewhere the agreement is considerably better. For cut-off modes the agreement is typically to within 5 dB everywhere and deviation between the directivity factors is not limited to the sideline directions. Despite these discrepancies the location of the lobes (region of relatively large radiation) and nulls (region of zero radiation) is consistent, and the relative shape of the directivities is very similar.

It has been found that cut-off modes of high radial orders n have extremely poor agreement between the flanged and un-flanged directivities, conversely, this is not the case for modes of high m but low n, indicating disagreement is not solely determined by modal cut-off ratios ζ_{mn} and ξ_m.

Considering very cut-off modes of relative high radial order n, but low azimuthal order m and high azimuthal order m but low radial order n, *figure 2.7* shows plots of the un-flanged and flanged directivity factor for the modes (m, n) = (0,50) and (50,1) at $\zeta_{mn} = 0.01$, corresponding to non-dimensional frequencies $ka = 1.5$ and 0.5 respectively.

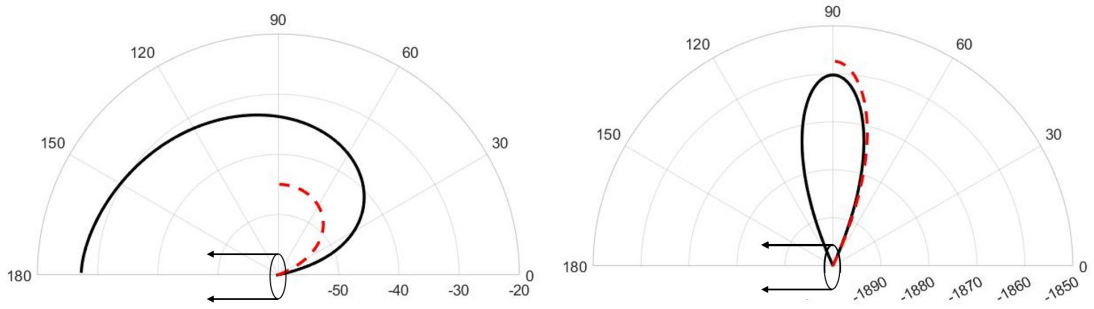

(A) $m = 0, n = 50, \zeta_{mn} = 0.01$ (B) $m = 50, n = 1, \zeta_{mn} = 0.01$

FIGURE 2.7: Comparison between directivities of the un-flanged (solid black line) and the flanged(red dashed line) duct models. In dB re 1.

Figure 2.7a identifies disagreement between the un-flanged and flanged duct models to be as much as 10 dB, although the relative shape of the directivity factors are similar. This difference has been shown to increase with n. The relatively large difference between the directivity factors is not observed for modes of large mode index m, but relatively small index n as indicated by *figure 2.7b*, where agreement can be observed to within 3 dB. This behavior confirms the modal cut-off ratio ζ_{mn}, does not solely govern the behavior of cut-off modes. Note the level of the directivity factors at all polar angles ϕ shown in *figure 2.7b* differ largely from that in *figure 2.7a*. This feature of cut-off mode radiation is a property of the radiation efficiency τ_{mn} and is explored in *Chapter 3*. The disagreement between the flanged and un-flanged directivities for cut-off modes of large n is investigated in *Appendix A*, where it is shown the square directivities differ by a factor proportional to $\sqrt{\kappa_{mn}}$.

Chapter 3

Radiation characteristics of cut-off modes from ducts

This chapter concerns the modal radiation characteristics of cut-off modes to determine their behaviour, and their likely influence in the far-field directivity for sources close to the duct open end. It is shown that cut-off modes are an essential contributor for the radiation in the rear-arc. A numerical study on the radiation characteristics of cut-off modes from semi-infinite, hard-walled, circular ducts in the absence of mean flow is presented.

The aim is to better understand the behaviour of cut-off modes, and to highlight their fundamental differences from cut-on propagating modes. The far-field modal directivity predicted using the mathematical formulation due to Gabard and Astley (2006) is used as the basis for this investigation, which readily allows the prediction of the radiation from cutoff modes unlike that due to Homicz and Lordi (1975) which explicitly assumes cut-on modes.

Analysis of cut-off mode behavior commences with a study of the factors that determine the angular location of the mainlobes and sidelobes of radiation directivity patterns. This leads to an investigation into the radiation efficiency of cut-off modes. A physical interpretation of the radiation characteristics of cut-off modes is provided utilising particle velocity source reconstructions. The final issue addressed is the effect of reflections at the duct open end.

3.1 Directivity characteristics of cut-off modes

In this section the directivity function $D_{mn}(\phi, ka)$ of modes excited at frequencies below the cut-off frequencies is investigated for un-flanged semi-infinite ducts. Whilst the characteristics of the directivity for cut-on modes is well established by for example Chapman (1994), a systematic study of its behaviour for cut-off modes remains to be performed.

3.1.1 Modal directivity of cut-off modes

Figure 3.1 shows the modal directivity in dB, $10\log_{10}(|D_{mn}(\phi, ka)|^2)$, for an arbitrary mode (m, n) = (10,2), at six non-dimensional frequencies ka between 1 and 16, for which the mode is cut-off with modal cut-off ratios equal to ζ = 0.97, 0.79, 0.61, 0.43, 0.24 and 0.06. The modal directivities under investigation, for which the modes are cut-off, have been divided into two groups, for which $\xi_m > 1$, as shown in *figure 3.1a* and $\xi_m < 1$ as shown in *figure 3.1b*.

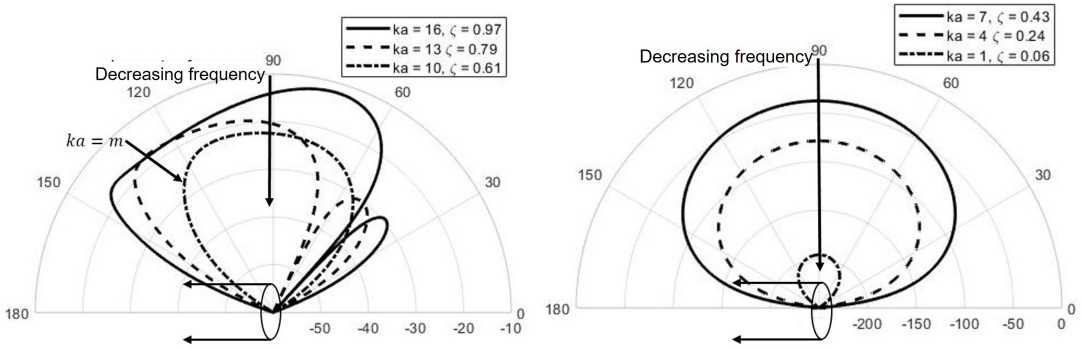

(A) $\xi_m \geq 1$ (B) $\xi_m < 1$

FIGURE 3.1: Modal directivity for six frequencies between ka = 16 and 1. In dB re 1.

The directivity patterns in *figure 3.1a* are of relatively similar level (when compared to *figure 3.1b*) and characterised by a number of sidelobes. An important feature of these directivities is that the main radiation lobe can be directed towards the rear-arc, which is contrary to the behaviour of cut-on modes. For a mode just below cut-off, the main radiation lobe can be observed in the forward-arc near $\phi = 90°$. As the mode becomes more cut-off the region of largest directivity can be observed in the rear-arc radiation to move towards the sideline direction $\phi = 90°$ as the frequency is reduced below cut-off. These behaviours will be explored further in *Section 3.1.2*.

In *figure 3.1b* the most striking feature is the absence of sidelobes with a main radiation lobe directed close to $\phi = 90°$. *Figure 3.1b* also indicates that modes excited in the range $\xi_m < 1$ exhibit forward and rear-arc symmetry. However, the main feature of this figure is the significant level of reduction with decreasing frequency below cut-off. The frequency $\xi_m = 1$ therefore marks the delineation for the the presence of sidelobes.

For both cut-on and cut-off modes the location of the nulls are at angles given by *Eq. 3.2*. Following the 'interlacing' property of the Bessel function (Chapman (1994)), the angular location of the main lobe of a given radial order n corresponds to the same location for the nulls of a different order n', for modes of the same azimuthal order m.

The angular location ϕ_{mn} of the nulls in the far-field directivity are associated with the angles for which the Kernel function $K_m^+(\cos\phi_{mn})$ in the denominator of the directivity function of *Eq. 2.52* tends to infinity. Inspection of *Eqs. A.2* and *A.4* shows that this occurs where

$$J'_m(ka\sin\phi_{mn}) = 0\,. \tag{3.1}$$

Equation 3.1 for the angular location of the directivity nulls is satisfied at locations

$$\phi_{mn} = \sin^{-1}(1/\zeta_{mn})\,. \tag{3.2}$$

For cut-on modes $\zeta_{mn} > 1$, which applied to *Eq. 3.2* identifies that $0^\circ \leq \phi_{mn} \leq 90^\circ$. By contrast, cut-off modes are characterised by $\zeta_{mn} < 1$, and hence no real solutions exists for ϕ_{mn}.

Another feature of these directivity functions, which are also observed in *figure 3.1*, is the presence of a range of angles of very weak radiation close to the duct axis, which are identical in the front and rear-arcs in *figure 3.1*. These are commonly referred to as the 'quiet zone'. Chapman Chapman (1994) has investigated in detail the characteristics of this zone and provides a physical interpretation for the reason why the angle of the quiet zone ϕ_m is independent of radial mode order and is given by,

$$\phi_m = \sin^{-1}(1/\xi_m). \tag{3.3}$$

The angle of the quiet zone of *Eq. 3.3* is particularly important for cut-off modes since it is shown later in *figure 3.2* that it closely corresponds to the angle of maximum radiation in the rear-arc. Chapman (1994) provides a physical argument of *Eq. 3.3* for the quiet zone based on the circumferential phase speed c_θ of the mode, given by $\omega a/m$, which is independent of the radial mode order. It is well established that the angle of maximum radiation occurs when the phase speed in the direction of the observer is sonic. Chapman demonstrates that this polar angle for a far-field observer, which delineates the transition between subsonic and supersonic phase speeds, and hence efficient and inefficient radiation, occurs at the quiet zone angle ϕ_m of *Eq. 3.3*.

3.1.2 Angle of maximum radiation for cut-off modes

In this section, an investigation is presented for the relationship between the angle of maximum radiation for cut-off modes and the modal cut-off ratios ζ_{mn} and ξ_m, the latter of which is shown to govern the location of the quiet zone.

The angle of maximum radiation is presented in *figure 3.2* for three modes with azimuthal orders $m = 0, 1$ and 2, each with the the radial order $n = 10$. The angles are plotted against ζ_{mn} by varying frequency from below cut-off, $\zeta_{mn} \approx 0$, to above cut-off, $\zeta_{mn} = 1.2$. Also plotted in this figure for cut-off modes, $\zeta_{mn} < 1$, is the curve $\sin^{-1}(1/\xi_m)$ (red dashed lines) representing the quiet zone angle, and for cut-on modes $\zeta_{mn} > 1$, the curve $\sin^{-1}(1/\zeta_{mn})$ for the main lobe angle (red solid line).

To illustrate this general behaviour some representative directivity plots for mode $(m, n) = (1, 10)$ are included with $\zeta_{mn} = 0.01$ (well below cut-off), $\zeta_{mn} = 0.95$ (just below cut-off), and $\zeta_{mn} = 1.05$ (just above cut-off). These directivity plots highlight the sudden transition between the angle of maximum radiation in the rear-arc for the mode just below cut-off to the forward-arc just above cut-off.

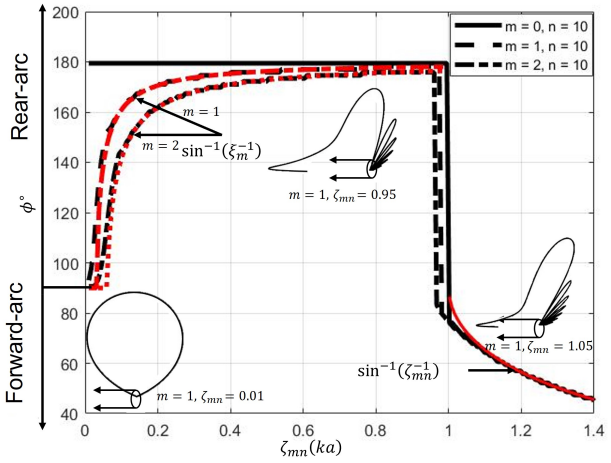

FIGURE 3.2: Angle of the major lobe plotted against ζ_{mn} for modes (m, n) = (0,10) (1,10) (2,10). For $\zeta_{mn} > 1$, the curve $\sin^{-1}(1/\zeta_{mn})$ is shown (solid red line) and for $\zeta_{mn} < 1$ the shadow zone region ϕ_m, $\sin^{-1}\xi_{mn}$ for the azimuthal orders $m = 1$ and 2 is shown (dashed red lines). The directivity of the mode (m, n) = (1,10) is shown at three frequencies corresponding to $\zeta_{mn} = 1.05, 0.95$ and 0.01

The angle of maximum radiation can be clearly seen to closely match the quiet zone angle for cut-off modes in *figure 3.2*. As the frequency is increased, $\zeta_{mn} \to 1$ the angle of maximum radiation tends to 180°. At frequencies just below cut-off, $\zeta_{mn} \approx 0.95$, the angle of maximum radiation shifts towards the sideline direction at 90°. At frequencies above the cut-off frequency, $\zeta_{mn} > 1$, the angle of maximum radiation then shifts towards the forward-arc and closely follows the angle $\sin^{-1}(1/\zeta_{mn})$. This figure makes clear that cut-off modes contribute most significantly to the radiation in the rear-arc and as will become clear from the next section, this angle is determined solely by the azimuthal mode order m. By contrast, cut-on modes radiate most strongly in the forward-arc whose angle of maximum radiation is determined by both m and n through the cut-off ratio. Finally, it is noted that the angle of maximum radiation is at $\phi = 180^\circ$ for the axi-symmetric $m = 0$ mode, consistent with *Eq. 3.3*.

3.1.3 Scaling law for the directivity of cut-off modes

This section highlights the small effect of varying radial mode order n on the directivity of cut-off modes. *Figure 3.3* shows the variation in directivity factor $|D_{mn}(\phi, ka)|^2$ of *Eq. 2.52* in dB plotted against ζ_{mn} for three circumferential mode orders m = 1, 2, 3 for their first 100 radial modes n = 1 to 100. Results are given at the two representative rear-arc angles of $\phi = 120°$ and 150°. Note that in this figure the frequency is kept constant at ka = 1, while κ_{mn} varies according to the different mode indices, which in turn, varies ζ_{mn}. Also shown in this figure, for reference purposes, is the line $10 \log \zeta_{mn}$.

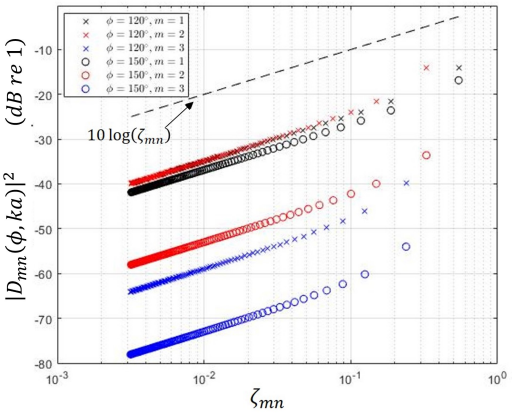

FIGURE 3.3: Directivity at representative far-field angles ϕ = 120° and 150° for modes $m = 0, 1$ and 2, n = 1 to 100, plotted against ζ_{mn}, excited at ka = 1.

Figure 3.3 shows the far-field radiation at a single radiation angle can be observed to be a smoothly varying, monotonically increasing function of ζ_{mn}. More significantly, for the modes that are sufficiently cut-off, the directivity factor closely follows the slope of the curve ζ_{mn}. Therefore, for sufficiently cut-off modes,

$$D_{mn}(\phi, ka) \propto \frac{1}{\sqrt{\kappa_{mn}}} \qquad (\text{for} \quad \text{constant } m \text{ and } ka). \tag{3.4}$$

Further analysis of this function is presented in *Appendix A*, where a mathematical explanation is provided. The radiation efficiency, discussed in *Section 3.2*, must vary as $1/\kappa_{mn}$ for fixed m and ka. For cut-off modes, the shape of the modal directivity only depends on m and ka, but for fixed m, the magnitude of the directivity is only dependent on $\kappa_{mn}a$. A clear demonstration of this phenomenon is shown in *figure 3.4* which compares the directivity factor scaled by the inverse of the cut-off ratio, $|D_{mn}(\phi, ka)|^2/\zeta_{mn}$, plotted in dB. The comparisons are shown for four cut-off modes with the same azimuthal order $m = 0$ and $ka = 50$, but with the different radial orders $n = 20, 30, 40$ and 50, corresponding to cut-off ratio ζ_{mn} of 0.83, 0.54, 0.41 and 0.32.

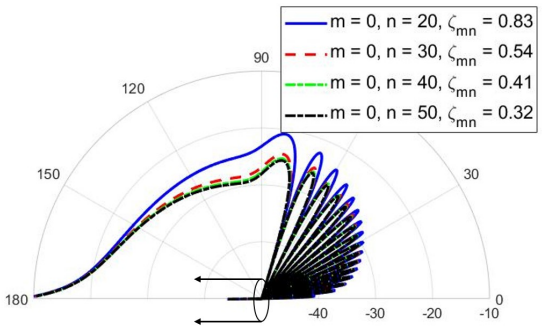

FIGURE 3.4: Polar directivity factor $|D_{mn}(\phi, ka)|^2/\zeta_{mn}$ for four modes with azimuthal order $m = 0$ and radial orders $n = 20, 30, 40$ and 50, at $ka = 50$. In dB re 1.

Excellent agreement is obtained for the three most well cut-off modes $\zeta_{mn} = 0.32, 0.41$ and 0.54, but with poorer agreement observed for the mode $\zeta_{mn} = 0.83$ that is closer to cut-on, thereby confirming the relationship in *Eq. 3.4*. Note as suggested by *figure 3.2* the major lobe can be observed to be located at $\phi = 180°$.

3.2 Radiation efficiency of cut-off modes

In this section, the radiation efficiencies of cut-off modes is investigated. Radiation efficiency for cut-off modes was first investigated by Morfey (1969) for flanged ducts, which included the effect on radiation due to a centre body. In this section the un-flanged solution given by *Eq. 2.52* is used to compute the radiation efficiency defined by *Eq. 2.56*. Morfey's main result was to show that the frequency dependence of the radiation efficiency of cut-off modes varies as

$$\tau_{mn} \propto (ka)^{2m+2}, \qquad |m| > 0\,, \tag{3.5}$$

which only depends on the azimuthal order m. No physical explanation was provided in this early paper, or any limit of the frequency range over which this result is valid.

As mentioned in the introduction it is not possible to compare directly the efficiencies of the flanged and un-flanged solutions, as the former investigated by Morfey is based on the modal velocity amplitudes at the end of the duct *following* reflection, while in the current investigation the modal velocity amplitude is that of the incident mode *before* reflection has occurred at the open end. However, this difference is not anticipated to affect the main frequency dependence identified by Morfey, but only affect the magnitude.

Figure 3.5 shows the radiation efficiency τ_{mn} plotted against ka, computed from *Eqs. 2.51*, *2.52* and *2.56*. The figure also shows results for radial orders $n = 1, 2$ and 3 with the same azimuthal order $m = 1$. A plot of $(ka)^{2m+2}$ evaluated for $m = 1$ is shown for comparative purposes.

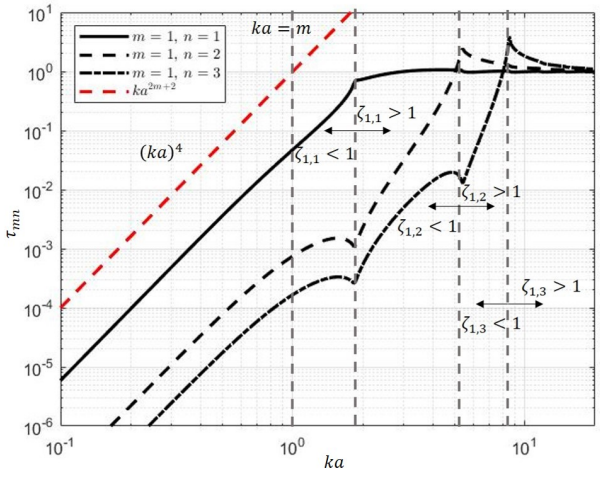

FIGURE 3.5: Modal efficiency for azimuthal order $m = 1$ and radial order $n = 1, 2$ and 3.

Figure 3.5 mostly confirms the prediction made by Morfey (1969) that the overall trend of the radiation efficiencies varies with frequency as $\tau_{mn} \propto (ka)^{2m+2}$. The general trend in the variation of radiation efficiency with frequency of these cut-off modes is therefore predominantly independent of n. However, it is observed that Morfey's result begins to deviate from the exact behaviour at frequencies $\xi_m > 1$. Following the analysis from *Section 3.1.1*, Morfey's result is therefore confined to the frequency range where sidelobes are completely absent, such as for those shown in *figure 3.1b*, which are excited at $\xi_m < 1$. This behavior will be investigated further in *Section 3.3* for modes excited in this region, where the radiating velocity components are investigated and found to be relatively weak inside the duct.

Similar to Morfey, in this new work it is observed that maximum radiation efficiency occurs at cut-off $\zeta_{mn} = 1$, where τ_{mn} slightly exceeds unity, since it is not a true measure of energy efficiency. However, a number of features not apparent in Morfey's results are observed, principally the appearance of a number of peaks and dips. For the mode (m, n) these may be shown to occur at the cut-off frequencies of (m, n'), where $n' < n$. The radiation efficiency of the $(m, n)^{th}$ mode therefore has (n-1) dips, where the radiation efficiency is relatively poor. This phenomenon can be attributed to peaks in the reflection coefficient at these frequencies caused by strong scattering of the mode (m, n) into (m, n') modes at their cut-off frequencies.

The general result of *Eq. 3.5* has been found to provide a good fit to the frequency dependence of τ_{mn} for nearly all azimuthal orders m for modes excited below their cut-off frequency. A physical explanation for this finding will be presented in *Section 3.3*. However, *Eq. 3.5* breaks down for the axi-symmetric $m = 0$ modes, which may be shown to have the same radiation efficiency as the $m = 1$ mode, and hence vary as $\tau_{mn} \propto (ka)^4$. This behavior is also discussed in *Section 3.4*.

3.2.1 Sound power split between forward and rear-arcs

It is shown in *figs 3.1–3.4* that cut-off modes radiate significantly to the rear-arc. In this section, the division in the total radiated sound power between the forward and rear-arcs is investigated in more detail.

The power split ratio η_{mn} is defined as the ratio between the sound power radiated to the forward-arc $0^\circ \leq \phi \leq 90^\circ$ to the total power radiated defined in *Eq. 2.57*. The ratio of sound power radiated to the rear-arc is therefore $1 - \eta_{mn}$. In *figure 3.6* the cut-off frequencies of the modes of lower radial order are identified to highlight the significant behavior observed for modes at that frequency. Appearance of dips is consistent with the so-called power reflection/ transmission coefficient presented by Snakowska and Jurkiewicz (2010).

Figure 3.6 shows the power split ratio η_{mn} plotted against ζ_{mn} computed for the modes of constant radial order $n = 1$, and azimuthal order $m = 1, 2$ and 3. Also shown in the figure is the corresponding result for modes of constant azimuthal order $m = 1$ with $n = 1, 2$ and 3.

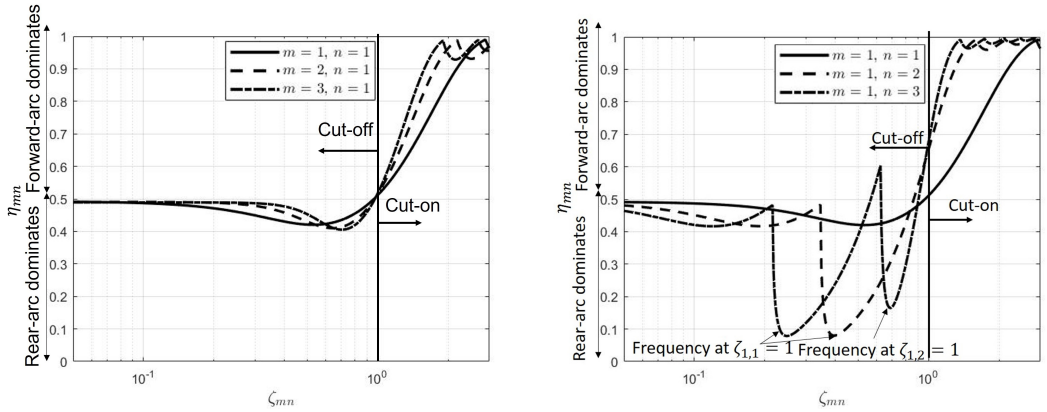

(A) $m = 1, 2$ and 3 $n = 1$ (B) $m = 1$ and $n = 1, 2$ and 3

FIGURE 3.6: Comparison of radiation efficiency in forward-arc to total radiation.

Both figures reveal the existence of well defined low frequency and high frequency asymptotes for which the power split ratio tends to 0.5 and 1.0 respectively. The low frequency asymptote is a direct consequence of the symmetry of the directivity function about $\phi = 90°$ in the lower frequency limit. The high frequency asymptote provides evidence that the degree of diffraction of the acoustic mode around the duct opening becomes progressively weaker, and sound increasingly beams directly in the forward-arc. It is worthy of note that the transition between equal energy split between the forward and rear-arcs, $\eta_{mn} = 0.5$, and dominance in the forward-arc occurs close to the the cut-off frequency $\zeta_{mn} = 1$.

In *figure 3.6b* showing the power split ratio for the different radial mode orders, distinct dips in η_{mn} can be observed, corresponding to frequencies at which the sound power is considerably greater in the rear-arc, $\eta_{mn} < 0.5$. The frequencies that this effect is maximum coincides with the cut-off frequencies of the lower radial orders $n' < n$.

3.2.2 Approximate modal radiation efficiency using the flanged duct formulation

The flanged directivity, first derived by Tyler and Sofrin (1962), can be used to approximate the efficiency from an un-flanged duct, as was the process used by Morfey (1969). By forming the efficiency in this, approximations can be made to form a relatively simple expression that does not require numerical integration, which for modes excited in the region $\xi_m \lesssim 1$ is very accurate.

An approximate expression for the modal efficiency from a flanged duct was shown in Morfey (1969), although this expression is restricted to modes of radial order $n = 1$ and was only investigated a short way below the cut-off frequency; far below Morfey's expression has limited accuracy.

Consider the pressure from a flanged duct of *Eq. 3.25*, but the far-field angle ϕ has been replaced by the radial wavenumber components κ using the relationship of *Eq. 3.23* ($\kappa = k \sin\phi$), to aid the following analysis. The pressure $p^{(D)}_{F,mn}(R, \kappa, \theta, \omega)$ is of the form,

$$p^{(D)}_{F,mn}(R, \kappa, \theta, \omega) \approx j^{m-1} a_{mn}(\omega) \mathrm{e}^{-j(kR+m\theta)} \frac{k_{z,mn}}{k} \frac{a}{R} \frac{\kappa J'_m(\kappa a)}{(\kappa^2_{mn} - \kappa^2)\sqrt{(1 - \frac{m^2}{\kappa^2_{mn} a^2})}}. \tag{3.6}$$

To calculate the power, the radial intensity across a hemisphere enclosing the duct opening of radius R is integrated using *Eq. 2.57*. Using the relationship of *Eq. 3.23* to replace the integral over ϕ by an integral over κ, using the substitution $d\kappa = \sqrt{k^2 - \kappa^2} d\phi$, and substituting $p_{F,mn}(R, \kappa, \theta, ka)$ of *Eq. 3.6* into $W_{F,mn}(\omega)$ of *Eq. 2.57* gives,

$$W_{F,mn}(\omega) = \frac{\pi}{\rho c} R^2 \int_0^k |p^{(D)}_{F,mn}(R, \kappa, \theta, \omega)|^2 \sqrt{\frac{\kappa^2}{k^4 - (k\kappa)^2}} d\kappa. \tag{3.7}$$

Note that the integrand has a singularity at $\kappa = k$, but later analysis shows this does not affect the accuracy of this work. The modal radiation efficiency $\tau_{F,mn}$ is calculated by substituting the pressure of *Eq. 3.6* and the power of *Eq. 3.7* into the efficiency of *Eq. 2.56*, which shows,

$$\tau_{F,mn} = \frac{2}{(1 - \frac{m^2}{\kappa^2_{mn} a^2})} \int_0^k \left(\frac{J'_m(\kappa a)}{(1 - \frac{\kappa^2_{mn}}{\kappa^2})} \right)^2 \frac{1}{\kappa} \sqrt{\frac{1}{1 - \left(\frac{\kappa}{k}\right)^2}} d\kappa. \tag{3.8}$$

A simple analytic approximate expression can be formed by representing the Bessel function in terms of an infinite series defined by,

$$J_m(\kappa a) = \sum_{s=0}^{\infty} \frac{-1^s (\kappa a)^{(m+2s)}}{2^{(m+2s)} v! (m+s)!}. \tag{3.9}$$

Taking the differential of *Eq. 3.9* and substituting into *Eq. 3.8* gives

$$\tau_{F,mn} = \frac{2}{(1 - \frac{m^2}{\kappa^2_{mn} a^2})} \int_0^k \sum_{s=0}^{\infty} \sum_{s'=0}^{\infty} B_{mss'} (\kappa a)^{(2m+2s+2s'-2)} \left[\frac{1}{(1 - \frac{\kappa^2_{mn}}{\kappa^2})^2} \right] \frac{1}{\kappa} \sqrt{\frac{1}{1 - \left(\frac{\kappa}{k}\right)^2}} d\kappa, \tag{3.10}$$

where for brevity the function $B_{mn}(ka)$ is defined as

$$B_{mss'} = \frac{-1^{(s+s')}(m+2s)(m+2s')}{2^{(2m+2s+2s')}s!s'!(m+s)!(m+s')!}. \tag{3.11}$$

The radiation efficiency has its most interesting properties at low frequencies corresponding to small κ, noting that κ is bounded by 0 and k. For small κa the approximation $\kappa a << \kappa_{mn} a$ can be made. Multiplying numerator and denominator by $(\kappa a)^4$ for the fraction in the square bracket allows $(\kappa_{mn} a)^4$ to be taken out of the integrand. Note that to absorb $1/\kappa$ into $(\kappa a)^{2m+1}$ requires multiplication by a, giving

$$\tau_{F,mn} \approx \frac{2a}{(\kappa_{mn}a)^4\left(1-\frac{m^2}{\kappa_{mn}^2 a^2}\right)} \sum_{s=0}^{\infty}\sum_{s'=0}^{\infty} B_{mss'} \int_0^{k-\epsilon} (\kappa a)^{(2m+2s+2s'+1)} \sqrt{\frac{1}{1-\left(\frac{\kappa}{k}\right)^2}}\, d\kappa. \tag{3.12}$$

From Gradshteyn et al. (Section 3.248, p 294, 1980), $\int_0^1 s^{(2b+1)}(1-s^2)^{-1}/2ds = (2b)!!/(2b+1)!!$, where $b!! = b \times (b-2) \times (b-4)...$ and the last multiplier is 1 for odd or 2 for even b. Notice that the integrand is singular at the upper limit but the integral has an exact solution. Solving the integral across κ in *Eq. 3.12* shows the radiation efficiency from a flanged duct is approximately of the form

$$\tau_{F,mn} \approx \frac{2B_{mn}(ka)}{(\kappa_{mn}a)^4\left(1-\frac{m^2}{\kappa_{mn}^2 a^2}\right)} \sum_{s=0}^{\infty}\sum_{s'=0}^{\infty} (ka)^{(2(m+s+s')+2)} \frac{(2(m+s+s'))!!}{(2(m+s+s')+1)!!} \tag{3.13}$$

The number of terms required in the summations used is investigated. The special case of only considering the first term (zeroth term) in the summation ($s = s' = 0$), gives the simplest case showing the efficiency $\tau_{F,mn}$ can be approximated as,

$$\tau_{F,mn}(ka) \approx (ka)^{2m+2} \frac{(2m)!!}{\kappa_{mn}^4 a^4 (1-\frac{m^2}{\kappa_{mn}^2 a^2}) 2^{2m-1}(m-1)!^2(2m+1)!!}, \qquad |m| > 0, \tag{3.14}$$

which is valid at sufficiently low frequency. *Figure 3.7* shows the radiation efficiency for the flanged formulation computed from *Eq. 2.58*, the efficiency for the un-flanged formulation from *Eq. 2.56* and the approximation from *Eq. 3.14* for the modes (m,n) = (1,1) and (1,5) plotted against ζ_{mn}.

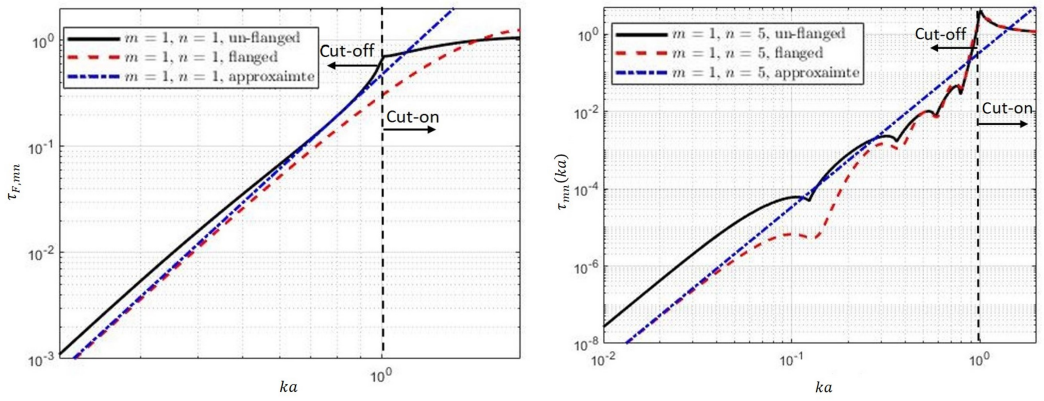

(A) $m = 1, n = 1$ and $m = 2, n = 1$ (B) $m = 1, n = 1$ and $m = 1, n = 5$

FIGURE 3.7: Comparison between radiation efficiency and approximation described by *Eq. 3.14*.

For modes of $n = 1$, the approximation described by *Eq. 3.14* has best agreement with the flanged efficiency, which is very good for $\zeta_{mn} \lesssim 0.5$, for the mode $(m, n) = (1, 1)$. However, for a mode of $n > 1$, agreement between the flanged efficiency and approximation of *Eq. 3.14* is poor for $\xi_m > 1$, which can be seen from *figure 3.7b* to have differences up to a factor of 10. The general trend of the decrease in radiation efficiency with decreasing frequency ka is matched by the approximation $\tau_{mn} \propto (ka)^{2m+2}$ for almost the entire frequency range for which the mode is cut-off, $\zeta \lesssim 0.95$, which is also noted in *figure 3.5*. In the region $\xi_m > 1, \zeta_{mn} < 1$ the un-flanged and flanged radiation efficiencies are seen to have a number of oscillations, which are not matched by the approximation of *Eq .3.14*.

Finally, it can be noted from *figure 3.7* that the un-flanged efficiency of *Eq. 2.56* is consistently higher than the flanged of *Eq. 2.58*. This is unsurprising for cut-off modes as the flanged directivity factor is limited to the forward-arc, $\phi \leq 90°$. However, it is shown by *figs 3.1* and *3.6* that for the region $\xi_m 1$ the un-flanged directivity exhibits forward and rear-arc symmetry about $\phi = 90°$. For this region the flanged efficiency is seen to consistently differ from the un-flanged by a factor of 2 (for the $n = 1$ mode). Combining these results, the relatively simple approximation of *Eq. 3.14* can be used to accurately predict approximately half the un-flanged efficiency, which requires relatively complicated numerical integration to obtain.

3.3 Equivalent far-field source distribution

In this section the equivalent source distribution for cut-off modes is investigated in order to assist in the interpretation of the radiation characteristics presented above. By way of simplification, introduce an infinite rigid flange onto the end of the duct. According to the Rayleigh integral the source distribution is now completely specified by the axial particle velocity everywhere at the exit plane $z = 0$ and is equal to zero on the flange $r > a$.

The radial variation of axial velocity for the $(m,n)^{\text{th}}$ mode incident at the exit plane of a flanged duct is given by,

$$u_{mn}(r,\omega) = \begin{cases} v_{mn}(\omega)\,\psi_{mn}(r) & r \leq a \\ 0 & r > a, \end{cases} \tag{3.15}$$

This is now decomposed into its wavenumber spectral components by use of the Hankel transform, i.e.

$$\widetilde{u}_{mn}(\kappa,\omega) = \int_0^\infty u_{mn}(r,\omega) J_m(\kappa r) r dr \tag{3.16}$$

where $\widetilde{u}_{mn}(\kappa,\omega)$ is the modal velocity wavenumber spectrum. Substituting *Eq. 5.4* into *Eq. 3.16*, and replacing the upper limit of integration by $r = a$, gives the equivalent radiating velocity distribution. The integral can be evaluated analytically to give

$$\widetilde{u}_{mn}(\kappa,\omega) = v_{mn}(\omega) \frac{\kappa a}{\kappa_{mn}^2 - \kappa^2} \frac{J_m'(\kappa a)}{\sqrt{\left(1 - \frac{m^2}{\kappa_{mn}^2 a^2}\right)}}. \tag{3.17}$$

The radial velocity distribution can be recovered from the spectrum by the inverse Hankel transform,

$$u_{mn}(r,\omega) = \int_0^\infty \widetilde{u}_{mn}(\kappa,\omega) J_m(\kappa r) \kappa d\kappa. \tag{3.18}$$

The dispersion relation in *Eq. 2.10* suggests that the equivalent radiating velocity distribution $u_{mn}^{(R)}(r,\omega)$ is associated with the range of spectral wavenumber components in the range $0 < \kappa < k$, of the form

$$u_{mn}^{(R)}(r,\omega) = \int_0^k \widetilde{u}_{mn}(\kappa,\omega) J_m(\kappa r) \kappa d\kappa, \tag{3.19}$$

while non-radiating components are due to the high 'frequency' components of the spectrum $k < \kappa < \infty$.

3.3.1 Far-field radiation

The velocity components of *Eq. 3.19* are now radiated. The radiation due to this equivalent perfectly radiating velocity distribution $u_{mn}^{(R)}(r,\omega)\,e^{jm\theta}$ may be estimated by substituting *Eq. 3.19* into the Rayleigh integral. The Rayleigh integral involves integration over all source positions, denoted by (r_0,θ_0). Following the approach by Tyler and Sofrin (1962), the expression for the far-field acoustic pressure is of the form,

$$p_F^{(D)}(R,\phi,\theta,\omega) \approx \frac{jk\rho c e^{-jkR}}{2\pi R}\int_S u_z(r_0,\theta_0)e^{jkr_0\sin\phi\cos(\theta-\theta_0)}dS(r_0,\theta_0). \tag{3.20}$$

Substituting *Eq. 3.19* into *3.20*, and solving the integral across θ_0 is solved using standard identities of the Bessel function, as is shown in *Chapter 2*,

$$p_{F,mn}^{(D)}(R,\phi,\theta,\omega) = j^{m+1}v_{mn}(\omega)\rho ck\frac{e^{-j(kR+m\theta)}}{R}\int_0^k \widetilde{u}_{mn}(\kappa,\omega)\kappa\int_0^\infty J_m(\kappa r_0)J_m(kr_0\sin\phi)r_0dr_0d\kappa. \tag{3.21}$$

The integral over r_0 is evaluated using the orthogonality property of the Bessel function,

$$p_{F,mn}^{(D)}(R,\phi,\theta,\omega) = j^{m+1}v_{mn}(\omega)\rho ck\frac{e^{-j(kR+m\theta)}}{R}\int_0^k \widetilde{u}_{mn}(\kappa,\omega)\left(\frac{\kappa}{k\sin\phi}\right)^{\frac{1}{2}}\delta(\kappa-k\sin\phi)d\kappa, \tag{3.22}$$

The sifting property of the delta function applied to the term $\delta(\kappa - k\sin\phi)$ implies that each spectral component κ radiates only to a single polar radiation angle,

$$\phi = \sin^{-1}\left(\frac{\kappa}{k}\right), \tag{3.23}$$

and is zero everywhere else. After integration over κ, and assuming that reflections can be neglected so that the velocity amplitude $v_{mn}(\omega)$ is assumed to be solely due to the incident mode with pressure amplitude $a_{mn}(\omega)$, the expression for the far-field directivity may be directly related to the velocity wavenumber spectrum,

$$D_{F,mn}(\phi,ka) = j^{m+1}\frac{k_{z,mn}}{k}\frac{1}{v_{mn}(\omega)}\widetilde{u}_{mn}(k\sin\phi). \tag{3.24}$$

Substituting $\kappa = k\sin\phi$ in *Eq. 3.24* gives the classical solution deduced by Tyler and Sofrin (1962), given by

$$D_{F,mn}(\phi,ka) = j^{m+1}\frac{k_{z,mn}}{k}\frac{\sin\phi J_m'(ka\sin\phi)}{(\frac{\kappa_{mn}^2}{k^2}-\sin^2\phi)\sqrt{(1-\frac{m^2}{\kappa_{mn}^2a^2})}}, \tag{3.25}$$

which can be used to approximate the far-field pressure radiated from a duct in the forward-arc ($0 < \phi < 90°$) using *Eq. 2.37*. The velocity spectrum at $\kappa = k$ therefore radiates solely in the sideline direction at 90° to the duct axis, while $\kappa = 0$ radiates only on-axis at 0°.

3.3.2 Radiating velocity components of cut-off modes

This theoretical framework can be used to identify the essential differences between the radiation due to cut-on and cut-off modes. *Figure 3.8* shows a plot of the modulus of the wavenumber velocity spectrum $\widetilde{u}_{mn}(\kappa, \omega)$, normalised to the maximum value, for a typical mode $(m, n) = (9, 6)$ excited below its cut-off frequency $\zeta_{mn} = 0.8$, plotted against κ/κ_{mn}. The vertical line indicates the frequency of excitation $k/\kappa_{mn} = 0.8$. Clearly, the range of velocity components responsible for far-field radiation in the forward-arc $0° < \phi < 90°$ now lies below the peak in the spectrum at $\kappa = \kappa_{mn}$, and therefore radiation to the far-field is comparatively weak and absent of a main radiation lobe, as discussed above.

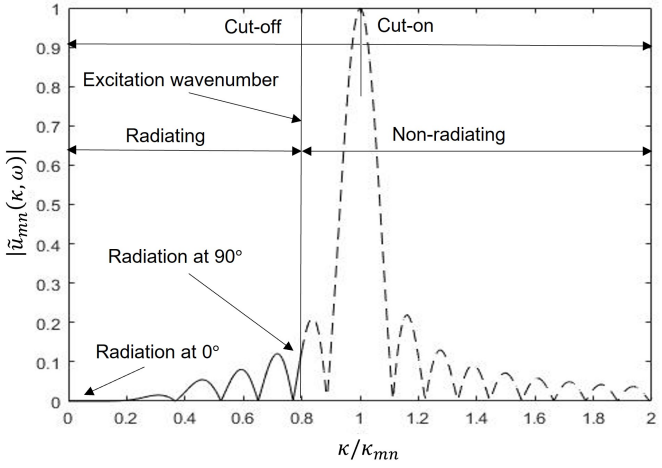

FIGURE 3.8: Wavenumber spectrum for the cut-off mode $(m, n) = (9, 6)$, $\zeta_{mn} = 0.8$

In this example, since the mode is excited below its cut-on frequency, and is therefore cut-off, the range of radiating wavenumbers κ therefore all occur below the cut-on wavenumber $\kappa = \kappa_{mn}$. When the mode is excited exactly at the cut-on frequency, therefore, the maximum radiating wavenumber component κ is equal to the cut-on wavenumber.

3.3.3 Radiating velocity distribution for cut-on modes

First the radiating velocity distribution, $u_{mn}^{(R)}(r, \omega)$ of *Eq. 3.19*, for three high-order cut-on modes with the same azimuthal order $m = 10$ and radial orders $n = 1, 5$ and 10, excited at the same frequency corresponding to modal cut-off ratios $\zeta_{mn} = 4.24$, 1.84 and 1.15, is investigated. The velocity distributions are plotted in *Figure 3.9*.

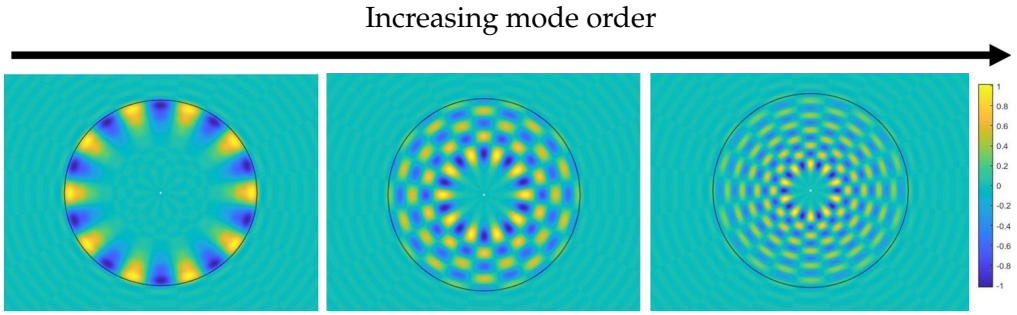

(A) $n = 1$ (B) $n = 5$ (C) $n = 10$

FIGURE 3.9: Radiating velocity distribution at the open end of the duct for varying cut-on modes for modes of azimuthal order $m = 10$, excited at non-dimensional frequency $ka = 10$. The duct is denoted by the black circle.

The equivalent perfectly radiating velocity distribution can be observed to extend beyond the duct $r > a$. This is to be expected as its wavenumber spectrum from *Eq. 3.16* is strictly band-limited in the wavenumber domain to $0 < \kappa < k$, which from elementary theory suggests that it must be unbounded in the space domain.

The equivalent radiating velocity distributions for these three cut-on modes can be observed to closely match the mode shape functions $\Psi_{mn}(r, \theta)$ of *Eq. 2.16*. It is now shown by numerical example that the radial variation in the equivalent perfectly radiating velocity tends exactly to the mode shape function $\psi_{mn}(r)$ in the high frequency limit $k \to \infty$. Note that attempts to prove this formally from solutions of *Eq. 3.19* for $k = \infty$ were unsuccessful and integrals of this type do not appear in literature.

Figure 3.10 shows a comparison of the result computed from *Eq. 3.19* for the mode $(m, n) = (10, 5)$ at the frequency of $\zeta_{mn} = 10$ with the exact mode shape function $\psi_{mn}(r)$. Note that both results have been normalised to their maximum value.

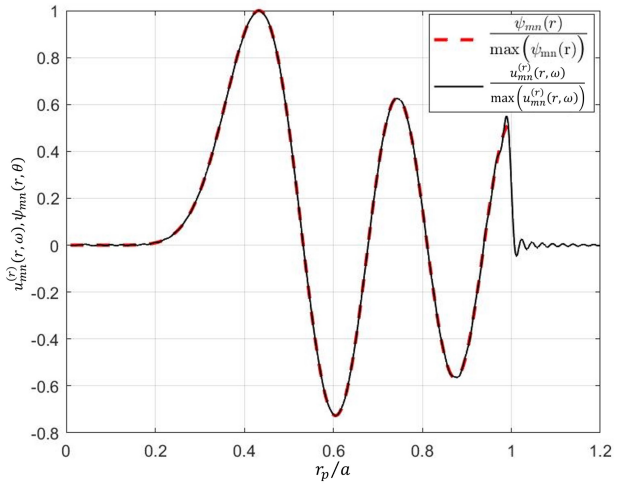

FIGURE 3.10: Comparison between radial variation of radiating velocity distribution and mode shape function for the mode $(m, n) = (10, 5), \zeta_{mn} = 10$.

Near perfect agreement between the two curves is observed, with the greatest deviation occurring near the wall $r/a = 1$ where small rapidly decaying oscillations are present. Note that these oscillations become progressively smaller as the frequency is increased further. This figure provides clear evidence that in the high frequency limit the entire modal velocity radiates to the far-field, and this is the reason why the radiation efficiency tends to unity in the high-frequency limit.

3.3.4 Radiating velocity distribution for cut-off modes

Equation 3.19 is used to compute the equivalent radiating velocity, shown in *figure 3.11*, for three typical cut-off modes of different azimuthal order $m = 0, 1$ and 2, for the same radial order $n = 2$, and three typical cut-off modes of different radial order $n = 2, 3$ and 4, for the same azimuthal order $m = 1$ all excited at $ka = 1$.

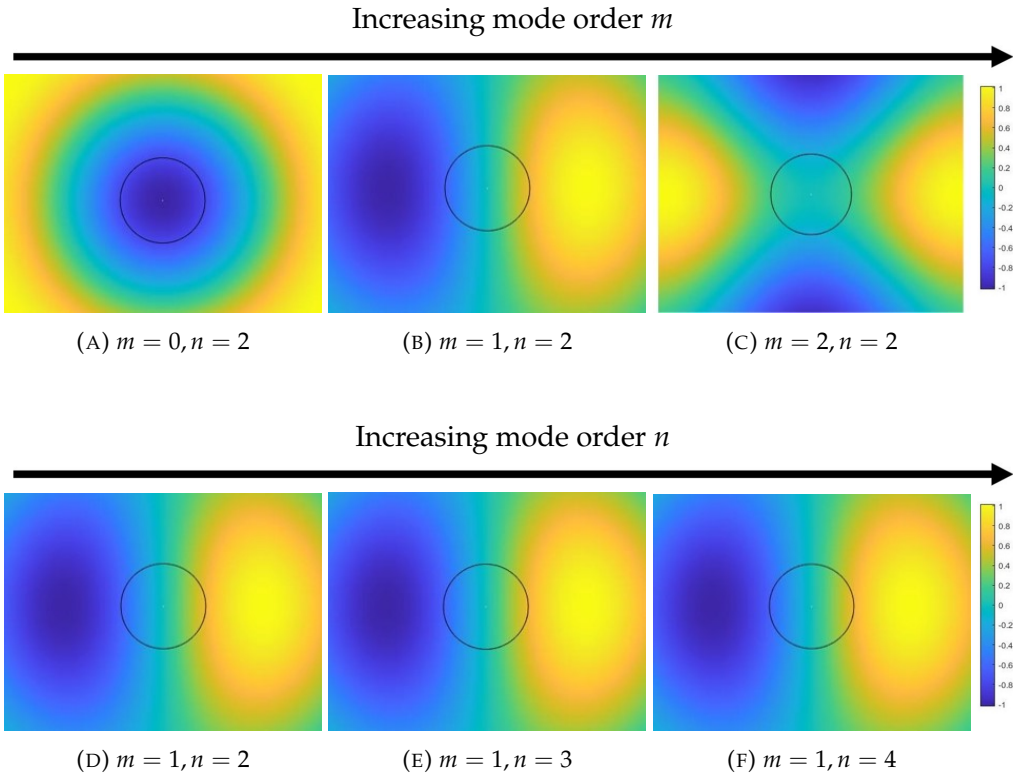

(A) $m = 0, n = 2$ (B) $m = 1, n = 2$ (C) $m = 2, n = 2$

(D) $m = 1, n = 2$ (E) $m = 1, n = 3$ (F) $m = 1, n = 4$

FIGURE 3.11: Radiating velocity distribution at the open end of the duct for different modes. The duct is denoted by the black circle.

Figure 3.11 shows that the equivalent velocity distribution is dominated by the azimuthal order m of the mode with no apparent dependence on n. These velocity distributions for $m = 1$ and 2 can be observed to have dipole and quadrupole type behaviours respectively, which explains their frequency dependencies of $(ka)^4$ and $(ka)^6$, which are well established results from classical radiation theory Rienstra and Hirschberg (2004). Clearly, destructive interference increases with m and hence is the reason for the reduction in radiation efficiency.

Note that the velocity distribution for $m = 0$ modes are a special case for which the general formula by Morfey (1969) $\tau_{mn} = (ka)^{2m+2}$ breaks down. A cut-off mode with $m = 0$ has the same frequency dependence as for $m = 1$ modes and therefore does not radiate with monopole type ((ka^2)) efficiency. This is evident from the velocity distribution of *figure 3.11a* which shows a concentric series of pressures of oscillating phase. These phase variations result in destructive interference leading to less efficient radiation than if the velocity was all radiating in phase. This velocity may therefore be interpreted as an 'azimuthal dipole'.

Figure 3.11 shows clearly that the effective normalised radiating velocity distribution is independent of n. This behavior helps provides further evidence that the behaviour of the radiation of cut-off modes is only weakly affected by the radial order n, and hence why their directivities and efficiencies are very similar.

3.3.5 Sonic radius

In this section the radiating velocity distributions for cut-on and cut-off modes is contrasted, in order to highlight the fundamental difference in the radiation characteristics when the mode becomes cut-off. Previous sections in this chapter have shown that, for cut-off modes, the radiation efficiency and modal directivity are predominantly governed by the azimuthal order m, with very weak dependence on the radial order n.

The expression for the equivalent perfectly radiating velocity distribution, after substituting *Eq. 3.16* into *Eq. 3.19* comprises three terms. However, only the third term $J_m(\kappa r)$ varies with radius r. The Bessel function $J_m(\Theta)$ is known to exhibit exponential-type behaviour for $\Theta < m$ with its first maxima at $\Theta \approx m$. The equivalent radiating velocity distribution is therefore relatively small for $r/a < \xi_m$, peaking at $r = r_s$ and then oscillates at radial positions beyond this,

$$\frac{r_s}{a} \approx \xi_m^{-1}. \tag{3.26}$$

Demonstration of this behaviour is provided in *figure 3.12*, which shows plots of the equivalent velocity distribution computed from *Eq. 3.19* for the high order cut-off mode (m, n) = (50,5) excited at the three different frequencies corresponding to cut-off ratios $\zeta_{mn} = 0.90, 0.67$ and 0.54. Their corresponding values of ξ_m^{-1} are equal to 0.75, 1.00 and 1.25. In each plot the radial location $r/a = \xi_m^{-1}$ is indicated as a white dashed circle while the duct radius is indicated a solid black circle.

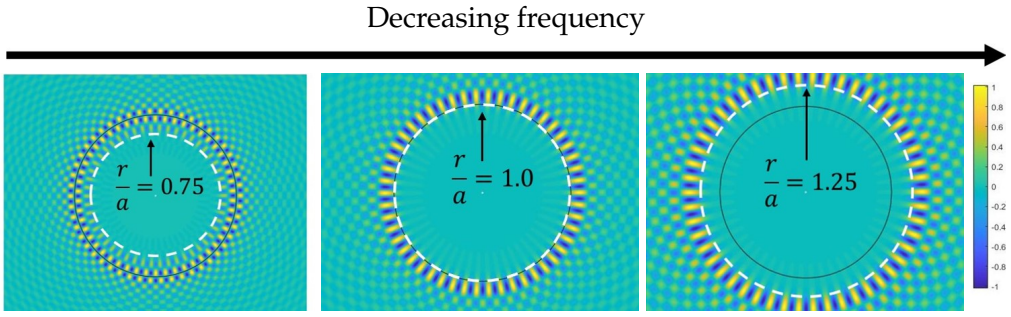

(A) $\xi_m^{-1} = 0.75$ (B) $\xi_m^{-1} = 1.05$ (C) $\xi_m^{-1} = 1.25$

FIGURE 3.12: Radiating velocity distribution at the open end of the duct for varying frequencies ka for the mode $(m, n) = (50, 5)$. The duct is denoted by the black circle.

In the first example in *figure 3.12a*, relating to the least cut-off mode, $\xi_m < 1$. In this case the radiating velocity distribution can be observed to be negligible for $r/a < 0.75$, and reaches its maximum value at the duct radius $r/a = 1$. The results from other calculations have shown this to be generally true for all the cases for which $\xi_m \geq 1$. As the frequency is reduced, the mode becomes more cut-off. When the critical frequency is reached, $\xi_m = 1$, and the radiating velocity becomes negligible within the duct $r/a < 1$. At this frequency, the maximum velocity is observed at the duct radius $r/a = 1$, which coincides with the sonic radius $r_s/a = 1$. All three plots in *figure 3.12* show the radiating velocity is outside the sonic circle. As the frequency is reduced further, the mode becomes increasingly cut-off, and significant radiating velocity now only occurs outside the sonic radius $r_s/a > 1$, and is negligible within it, according to *Eq. 3.26*. Note this behavior is not visible from *figure 3.11* as the azimuthal order of $m = 1$ is too low for this phenomenon to be observed.

In all examples in *figure 3.12*, $r/a = \xi_m^{-1}$ marks the transition radially between high and low velocity. This radial location is also shown by *Eq. 3.26* to represent the location for which the azimuthal phase speed becomes sonic. At radii smaller than the sonic radius the azimuthal phase speed is subsonic and is therefore weakly radiating while at greater distances the phase is supersonic and is hence efficiently radiating. In the previous section, the radius r_s delineating the region of significant radiating velocity was identified from its maximum value, however, here it is demonstrated that the radius r_s has a more fundamental interpretation as the sonic radius.

To establish this principle more clearly consider a point on the modal wavefront of constant phase $\chi(z, \theta, t)$, such that the mode propagates along the duct as $e^{j\chi(z,\theta,t)}$, where $\chi = \omega t - k_{z,mn} z - m\theta$. The azimuthal phase speed at a fixed radial and axial position r and z is given by $c_\theta(r) = r\partial\theta/\partial t$. Solving the expression for θ in the expression above for χ and differentiate with respect to time, the expression for the azimuthal phase speed becomes $c_\theta(r) = \omega r/m$. Classical radiation theory Rienstra and Hirschberg (2004) dictates that radiation to the far-field can only occur if the phase speed in the direction of the observer exceeds the speed of sound.

Only velocity components at radii r corresponding to $c_\theta(r) \geq c$ can therefore radiate. The transition between radiating and non-radiating components therefore occurs at the sonic radius at which the azimuthal phase speed equals the sound speed, which from the argument above is identical to *Eq. 3.26* above obtained from the first maxima of the Bessel function $J_m(\kappa r)$. *Equation 3.26* therefore has the simple physical interpretation as the sonic radius, which is determined completely by m, providing further evidence for why many of the characteristics of cut-off modal radiation is predominantly only a function of the azimuthal order m, and which only has a negligible dependence on radial order n, except when excited close to their cut-on frequencies.

3.3.6 Energy interpretation of the radial mode n weak dependencies for cut-off modes

Further insight into the dependence of the radiation directivity and efficiency for cut-off modes predominantly on m can be obtained by examining the behaviour of its sound intensity propagating towards the open end. The acoustic intensity $\boldsymbol{I}_{mn}(r,\theta,z)$, inside the duct, is given by

$$\boldsymbol{I}_{mn}(r,\theta,z) = \frac{1}{2} Re\{p_{mn}^{(D)}(r,\theta,z,\omega)\boldsymbol{u}_{mn}^{*}(r,\theta,z,\omega)\}, \tag{3.27}$$

where the incident particle velocity $\boldsymbol{u}_{mn}$ is found via the the momentum equation,

$$\boldsymbol{u}(\boldsymbol{X},\boldsymbol{\omega}) = \frac{-j}{\rho c k}\nabla p(\boldsymbol{X},\omega)\,. \tag{3.28}$$

Substituting *Eq. 3.28* and *Eq. 2.5* into *Eq. 3.27* leads to an expression for the intensity of the form

$$\boldsymbol{I}_{mn}(r,\theta,\phi) = \left(\frac{m}{kr}\vec{\theta} - \frac{Re\{k_{z,mn}\}}{k}\vec{z}\right)\frac{|p_{mn}^{(D)}(r,\theta,z)|^2}{2\rho c}\,, \tag{3.29}$$

where $\vec{\theta}$ and $\vec{z}$ are unit vectors in the θ and z directions.

This result suggests that for cut-on modes, $Re\{k_{z,mn}\} \neq 0$, and hence its sound intensity has components in both azimuthal and axial directions. For cut-off modes, however, $Re\{k_{z,mn}\} = 0$ and hence its sound intensity incident upon the open end is solely in the azimuthal direction. Radiation to the far-field is therefore only possible through the interaction of the incident field with the open end, which has the effect of altering the phase relationship between the acoustic pressure and particle velocity. The radiation directivity and associated efficiency must therefore be predominantly governed by the azimuthal mode index m as verified by *figure 3.4* and *3.5*. Radiation efficiency intensity is dependent on both modal indices m and n, however for cut-off modes the axial wavenumber $k_{z,mn}$ is imaginary, which removes the axial component from the intensity.

Physically this represents the power of cut-off modes rotating around the duct instead of propagating axially. The azimuthal dependence of cut-on and cut-off modes varies as $\exp(-jm\theta)$ and does not depend on radial mode index n, therefore by extension the far-field directivity is also independent of n. However, *figure 3.4* indicates that modes excited just below cut-off have a weak dependence on n, which is likely a result of the effect of reflection at the open end, which is a large effect for modes excited just below cut-off.

3.4 Reflections at the open end for cut-off modes

This section investigates the effect of reflections due to cut-off modes incident open the open end of the duct, to determine how efficiently they can radiate to the far-field. A cut-off mode in an infinite duct has pressure and axial velocity out of phase, meaning cut-off modes do not transmit power along the duct axis. It is only as a result of reflections at the open end of the duct modifying the phase of the mode that causes power to radiate to the far-field. This can be seen from *Eqs 2.33* and *2.5*, noting power inside the duct is computed with the intensity $1/2\,\mathrm{Re}\{p_{mn}(\boldsymbol{X},\omega)u^*_{z,mn}(\boldsymbol{X},\omega)\}$.

The effect of reflections due to cut-on modes is well understood, by for example Snakowska and Jurkiewicz (2010), which approach a value -1 as the mode becomes closer to cut-off $\zeta_{mn} \to 1$ from above. As the mode becomes more cut-on and the excitation frequency is increased, the effect of reflections becomes insignificant as $\zeta_{mn} \to \infty$.

The only observation previously, regarding the effect of reflections due to cut-off modes incident open the duct open end, was made by Wang and Tszeng (1984). They noted that the effect of reflections for modes excited just below their cut-on frequency ($0.95 < \zeta_{mn} < 1$) approach a value of -1 at cut-off from below. In this section their analysis is extended to cut-off modes both just below and well below cut-off, $\zeta_{mn} \to 0$.

The effect of modal scattering is neglected in this analysis. This assumption allows the effective reflection at the open end to be represented by the reflection coefficient $r_{mn}(ka)$, which can be computed from *Eq. 2.55* for $n = l$, in place of the more complicated matrix term $\boldsymbol{R}_{mnl}(ka)$. *Figure 3.13* shows $|r_{mn}(ka)|$ for three modes of the same azimuthal order $m = 5$ and different radial orders n = 1, 2 and 3, and three modes of the same radial order $n = 1$ and azimuthal orders $m = 5, 10$ and 15, plotted against ζ_{mn}.

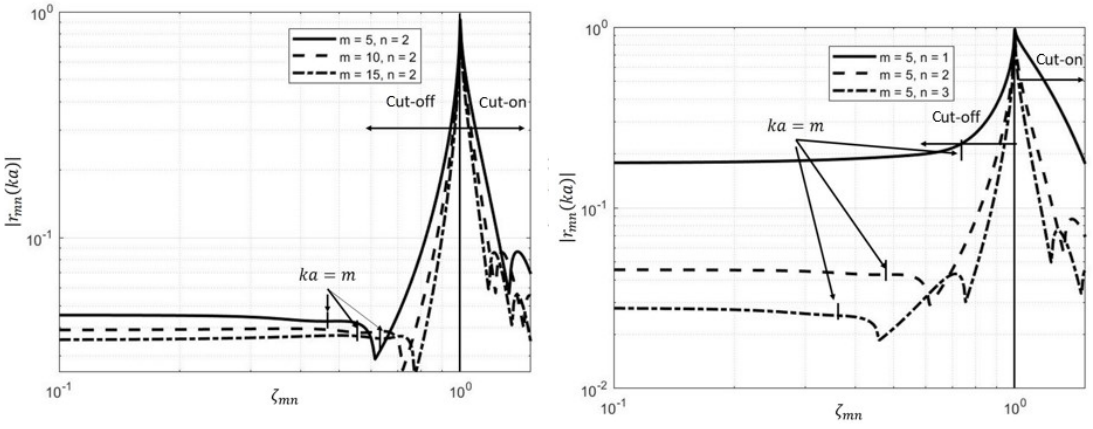

FIGURE 3.13: Effect of reflections ignoring scattering for several modes excited above and below cut-off.

Figure 3.13 shows different behavior of the reflection coefficient $|r_{mn}(ka)|$ for modes excited just below cut-off $\zeta_{mn} \lesssim 1$ and those excited well below their cut-off frequency $\zeta_{mn} \to 0$. Just below cut-off, $n-1$ turning points are observed between $\zeta_{mn} = 1$ and $\xi_m = 1$. This behavior is identical to what is observed for the modal efficiency τ_{mn} as shown in *figs 3.5* and *3.7b*. Considering the low frequency behavior for the region $\xi_m < 1$, the modal reflection coefficient $|r_{mn}(ka)|$ appears to approach a constant value. This value varies with both modal index m and n, and increases as $m \to 0$, $n \to 1$.

The region $\xi_m < 1$, where *figure 3.13* shows $|r_{mn}(ka)|$ approaches a constant is now investigated. *Figure 3.14* shows the reflection coefficient $|r_{mn}(ka)|$ plotted against ζ_{mn}, where the frequency is kept constant at $ka = 1$ and the radial wavenumbers κ_{mn} varies with the modal index m and n. Modes are investigated with constant azimuthal order $m = 0$, 1 and 2 for all radial modes between $n = 5$ and 50. Also shown is the modes of radial order $n = 1$, 2 and 3, for all azimuthal modes of order $m = 5$ to 50. For comparisons a plot of $\zeta_{mn}^{-(1/3)}$ and ζ_{mn}^{-1} are also shown.

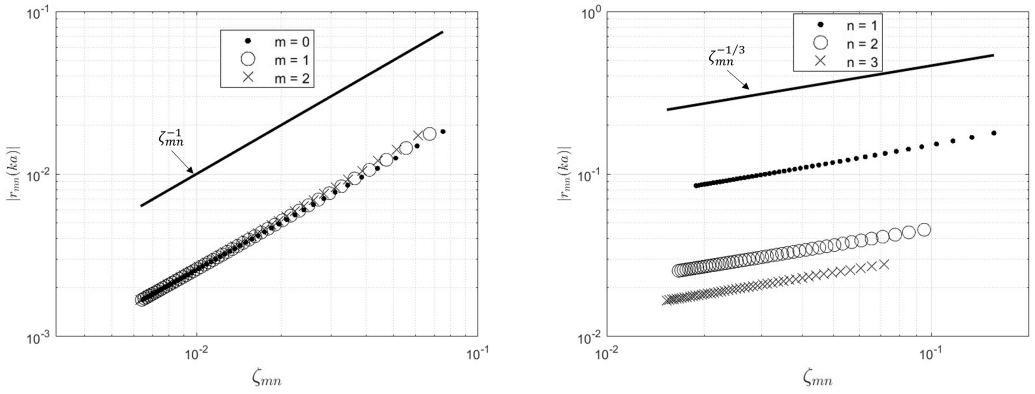

(A) Constant m (B) Constant n

FIGURE 3.14: Reflection coefficient for modes excited well below their cut-off frequency, $\xi_m < 1$, for the frequency $ka = 1$

Figure 3.14 shows that the reflection coefficient for cut-off modes excited in the region $\xi_m < 1$, is a monotonically decreasing function of ζ_{mn} for constant ka. Noting comparisons with the gradients of the curves ζ_{mn}^{-1} and $\zeta_{mn}^{-1/3}$ to the computed values, *figure 3.30* clearly identifies the relationships,

$$\begin{aligned} |r_{mn}(ka)| &\propto \zeta_{mn}^{1/3}, \quad \text{varying } m, \quad \xi \lesssim 1, \\ |r_{mn}(ka)| &\propto \zeta_{mn}^{-1}, \quad \text{varying } n, \quad \xi \lesssim 1. \end{aligned} \tag{3.30}$$

Contrary to the previous parameters discussed in this chapter, *Eq. 3.30* identifies the reflection coefficient $r_{mn}(ka)$ for modes excited in the region $\xi_m < 1$ is much more sensitive to the radial index n and varies much more slowly with azimuthal order m.

3.5 Summary

This chapter has identified characteristics of modes excited below their cut-off frequency. Cut-off modes have been shown to radiate more strongly into the rear-arc than the forward-arc, which is different to the radiation of cut-on modes. The location of maximum radiation for sufficiently cut-off modes has been shown to be determined solely by the azimuthal order m. Modal directivity patterns of those modes have been found to exhibit a number of side lobes above a threshold frequency of $\xi_m > 1$, below this frequency the directivity of cut-off modes is approximately symmetric about $\phi = 90°$.

A scaling law for modes excited below their cut-off frequency has been identified such that the directivity of cut-off modes approximately obeys $D_{mn}(\phi, ka) \propto \sqrt{1/\kappa_{mn}}$. This allows the level of the directivity patterns of cut-off modes to be predicted from the directivity of a different mode, providing the azimuthal mode m and excitation frequency ka are the same for both modes considered.

The radiation efficiency τ_{mn} for sufficiently cut-off modes is predominantly dependent on the azimuthal order m and has been shown to have dependency $\tau_{mn} \propto (ka)^{2m+2}$, agreeing with the flanged formulation first investigated by Morfey (1969).

Chapter 4

Acoustic radiation from free-field sources and sources inside semi-infinite ducts

In this chapter theoretical expressions are developed to compute the radiation from in duct and free-field sources for the purposes of establishing the similarities and differences between them. These models will be applied to the following four source distributions:

1. Incoherent distribution of axial dipole sources.
2. Incoherent distribution of monopole sources.
3. Rotating point dipole sources.
4. Rotating point monopole sources.

The derivation for the radiation from free-field steady sources has been studied by a number of authors, for example Garrick and Watkins (1953), Hanson (1983), Parry and Crighton (1989), Schulten (1988), Peake and Crighton (1991), Mao Y and Tang (2012), McAlpine and Kingan (2012), McAlpine et al. (2015) and Blake (2017). In this chapter the free-field radiation of sources with an arbitrary time dependence is derived using classical methods and new identities of the Bessel function.

The radiation of cut-on modes from ducted sources has been studied by a number of authors, for example Tyler and Sofrin (1962), Homicz and Lordi (1975), Joseph and Morfey (1999) and Gabard and Astley (2006). In this chapter a derivation is provided for the acoustic radiation of cut-on *and* cut-off modes excited by the four mentioned ducted sources, the latter of which has not been published before. A convergence study is presented to determine the number of cut-off modes required to ensure an accurate solution to within 0.5 dB is obtained.

4.1 Free-field radiation of sources

In this section free-field source radiation of rotating point dipole and monopole sources are derived, as well as a circular distribution (disc) of incoherent, axial dipole and monopole sources. The derivations for the free-field rotating point dipole and monopole source radiation is based on the work of McAlpine and Kingan (2012). The derivations for the free-field source distributions is loosely based on the work of McAlpine et al. (2015).

4.1.1 Incident field for rotating point dipole sources

As sketched in *figure 4.1* an unsteady force with arbitrary time dependence $\hat{f}(r, \theta, t_0)$ is assumed to rotate at angular velocity Ω around the z axis with radius of rotation r_0, at retarded time t_0. The dipole source is assumed to be orientated at angle γ in the $z - \theta$ plane. The observer position is assumed to be located at position (R, ϕ, θ) in the far-field .

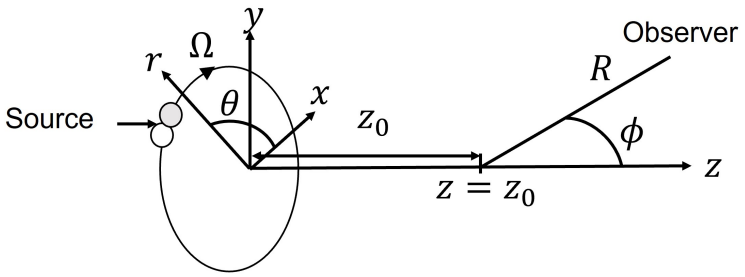

FIGURE 4.1: coordinate system of a rotating point source in free-field

The in-homogeneous wave equation to obtain the pressure field $\hat{p}^{(ff)}(r, \theta, z, t)$ in cylindrical polar coordinates defined in *figure 4.1* for an arbitrary fluctuating force or dipole source distribution is of the form,

$$\frac{\partial^2 \hat{p}^{(ff)}}{\partial r^2} + \frac{1}{r}\frac{\partial \hat{p}^{(ff)}}{\partial r} + \frac{1}{r^2}\frac{\partial^2 \hat{p}^{(ff)}}{\partial \theta^2} + \frac{\partial^2 \hat{p}^{(ff)}}{\partial z^2} - \frac{1}{c^2}\frac{\partial^2 \hat{p}^{(ff)}}{\partial t^2} = \hat{s}(r_0, \theta_0, t_0)\delta(z - z_0), \quad (4.1)$$

The general case of a rotating point dipole has source term of the form,

$$\hat{s}(r_0, \theta_0, t_0) = \left[\frac{1}{r}\frac{\partial}{\partial \theta}\sin\gamma + \frac{\partial}{\partial z}\cos\gamma\right] \cdot \hat{f}(t_0)\frac{\delta(r - r_0)}{r}\delta(\theta - \hat{\theta}_0), \quad (4.2)$$

where $\hat{f}(t_0)$ is the magnitude of the fluctuating force. The solution of *Eq. 4.1* is found using Fourier methods. Introduce the Fourier transform in z and t_0, and a Fourier series in θ,

$$\tilde{p}_m^{(ff)}(r, k_z, \omega) = \int_{-\infty}^{\infty} \int_0^{2\pi} \int_{-\infty}^{\infty} \hat{p}^{(ff)}(r, \theta, z, t) \mathrm{e}^{j(m\theta + k_z z - \omega t_0)} dz d\theta dt_0. \tag{4.3}$$

The transforms derivatives of *Eq. 4.3* are as follows

$$\frac{\partial}{\partial z} \rightarrow -jk_z \qquad \frac{\partial}{\partial \theta} \rightarrow -jm \qquad \frac{\partial}{\partial t} \rightarrow j\omega, \tag{4.4}$$

note $t = t_0 - R/c$. Fourier transforming the in-homogeneous wave equation of *Eq. 4.1* as in *Eq. 4.3* leads to,

$$\frac{\partial^2 \tilde{p}_m^{(ff)}}{\partial r^2} + \frac{1}{r}\frac{\partial \tilde{p}_m^{(ff)}}{\partial r} + \left(\kappa^2 - \frac{m^2}{r^2}\right)\tilde{p}_m^{(ff)} = -j\frac{\delta(r - r_0)}{r} \int_{-\infty}^{\infty} \mathrm{e}^{jk_z z} \delta(z - z_0) dz \int_{-\infty}^{\infty} \int_0^{2\pi} \left(\frac{m}{r}\sin\gamma + k_z \cos\gamma\right) \hat{f}(t_0) \mathrm{e}^{j(m\theta - \omega t_0)} \delta(\theta - \hat{\theta}_0) d\theta dt_0, \tag{4.5}$$

The integrals across z and θ in *Eq. 4.5* are evaluated using the sifting property of the delta function,

$$\frac{\partial^2 \tilde{p}_m^{(ff)}}{\partial r^2} + \frac{1}{r}\frac{\partial \tilde{p}_m^{(ff)}}{\partial r} + \left(\kappa^2 - \frac{m^2}{r^2}\right)\tilde{p}_m^{(ff)} = -j\mathrm{e}^{jk_z z_0} \frac{\delta(r - r_0)}{r_0} \left(\frac{m}{r}\sin\gamma + k_z \cos\gamma\right) \int_{-\infty}^{\infty} \hat{f}(t_0) \mathrm{e}^{j(m\hat{\theta}_0 - \omega t_0)} dt_0. \tag{4.6}$$

It is convenient to introduce the local coordinate system rotating with the dipole $\tilde{\theta}_0$, defined as,

$$\tilde{\theta}_0 = \Omega t_0 - \hat{\theta}_0, \tag{4.7}$$

The location $\tilde{\theta}_0$ represents the azimuthal location of the point source at time $t_0 = 0$. Substituting *Eq. 4.7* into *Eq. 4.5* gives,

$$\frac{\partial^2 \tilde{p}_m^{(ff)}}{\partial r^2} + \frac{1}{r}\frac{\partial \tilde{p}_m^{(ff)}}{\partial r} + \left(\kappa^2 - \frac{m^2}{r^2}\right)\tilde{p}_m^{(ff)} = -j\mathrm{e}^{j(k_z z_0 + m\tilde{\theta}_0)} \frac{\delta(r - r_0)}{r} \left(\frac{m}{r}\sin\gamma + k_z \cos\gamma\right) \int_{-\infty}^{\infty} \hat{f}(t_0) \mathrm{e}^{-j(\omega - m\Omega)t_0} dt_0. \tag{4.8}$$

The integral across t_0 in *Eq. 4.8*, is the inverse Fourier transform, which is readily evaluated to give,

$$\frac{\partial^2 \tilde{p}_m^{(ff)}}{\partial r^2} + \frac{1}{r}\frac{\partial \tilde{p}_m^{(ff)}}{\partial r} + \left(\kappa^2 - \frac{m^2}{r^2}\right)\tilde{p}_m^{(ff)} = -je^{j(k_z z_0 + m\tilde{\theta}_0)}\frac{\delta(r-r_0)}{r}\left(\frac{m}{r}\sin\gamma + k_z\cos\gamma\right)f(\omega - m\Omega). \tag{4.9}$$

Equation 4.9 is solved using the method of variation of parameters. Taking the right hand side to be 0, reveals Bessel's differential equation, it is convenient to take the linear solutions to be,

$$A(\kappa,\omega)J_m(\kappa r) + B(\kappa,\omega)H_m^{(2)}(\kappa r) = 0, \tag{4.10}$$

where $H_m^{(2)}(\kappa r)$ is the Hankel function of the second kind,
$H_m^{(2)}(\kappa r) = J_m(\kappa r) - jY_m(\kappa r)$, and $Y_m(\kappa r)$ is the Bessel function of the second kind.
Equation 4.8 is of the form,

$$\begin{aligned}\tilde{p}_m^{(ff)}(r,\theta,k_z,\omega) = &\frac{\pi}{2}f(\omega - m\Omega)\\ &\left(H_m^{(2)}(\kappa r)\int_0^r J_m(\kappa r)\delta(r-r_0)\left(\frac{m}{r}\sin\gamma + k_z\cos\gamma\right)dr - \right.\\ &\left. J_m(\kappa r)\int_0^r H_m^{(2)}(\kappa r)\delta(r-r_0)\left(\frac{m}{r}\sin\gamma + k_z\cos\gamma\right)dr\right),\end{aligned} \tag{4.11}$$

solving the integral using the sifting property of the delta function for $r > r_0$,
assuming far-field observers shows the pressure is of the form,

$$\tilde{p}_m^{(ff)}(r,k_z,\omega) = \frac{\pi}{2}\left(H_m^{(2)}(\kappa r)J_m(\kappa r_0) - J_m(\kappa r)H_m^{(2)}(\kappa r_0)\right)f(\omega - m\Omega)\left(\frac{m}{r_0}\sin\gamma - k_z\cos\gamma\right). \tag{4.12}$$

To ensure only outward propagating cylindrical waves are considered, it is assumed $J_m(\kappa r) \to 0$, *Eq. 4.12* becomes

$$\tilde{p}_m^{(ff)}(r,k_z,\omega) = \frac{\pi}{2}f(\omega - m\Omega)\left(\frac{m}{r_0}\sin\gamma - k_z\cos\gamma\right)J_m(\kappa r_0)H_m^{(2)}(\kappa r). \tag{4.13}$$

Applying the inverse Fourier transform in z and inverse Fourier series in θ shows the pressure is of the form,

$$p^{(ff)}(r,\theta,z,\omega) = \frac{1}{(2\pi)^2}\sum_{m=-\infty}^{\infty} \mathrm{e}^{-jm\theta}\int_{-\infty}^{\infty}\tilde{p}_m(r,k_z,\omega)\mathrm{e}^{-jk_z z}dk_z. \tag{4.14}$$

Substituting *Eq. 4.13* into *Eq. 4.14* noting cylindrical to spherical coordinate transformations, the far-field pressure is of the form

$$\begin{aligned} p^{(ff)}(R,\phi,\theta,\omega) =& \frac{1}{8\pi}\sum_{m=-\infty}^{\infty} \mathrm{e}^{-jm(\theta-\tilde{\theta}_0)} f(\omega - m\Omega) \\ & \int_{-\infty}^{\infty}\left(\frac{m}{r_0}\sin\gamma - k_z\cos\gamma\right) J_m(\kappa r_0) H_m^{(2)}(\kappa R\sin\phi)\mathrm{e}^{-jk_z(R\cos\phi - z_0)}dk_z, \end{aligned} \tag{4.15}$$

which is now evaluated using the method of stationary phase. The Hankel function is broken down into it's large argument approximation which is of the form,

$$H_m^{(2)}(\Theta) \approx j^m\sqrt{\frac{2}{\pi\Theta}}\mathrm{e}^{j(\frac{\pi}{4}-\Theta)} \tag{4.16}$$

following Rienstra and Hirschberg (2004) and substituted into *Eq. 4.15* to give,

$$\begin{aligned} p^{(ff)}(R,\phi,\theta,\omega) =& \frac{\mathrm{e}^{j\frac{\pi}{4}}}{8\pi}\sqrt{\frac{2}{\pi R\sin\phi}}\sum_{m=-\infty}^{\infty} j^m\mathrm{e}^{-jm(\theta-\tilde{\theta}_0)} f(\omega - m\Omega) \\ & \int_{-\infty}^{\infty}\left(\frac{m}{r_0}\sin\gamma - k_z\cos\gamma\right) J_m(\kappa r_0)\sqrt{\frac{1}{\kappa}}\mathrm{e}^{-jk_z(R\cos\phi - z_0)}\mathrm{e}^{-j\kappa R\sin\phi}dk_z. \end{aligned} \tag{4.17}$$

The variable of integration across k_z in *Eq. 4.17* is changed to κ, to aid subsequent comparisons to the ducted case, using

$$\kappa = \sqrt{k^2 - k_z^2} \tag{4.18}$$

$$\frac{d\kappa}{dk_{z,mn}} = -\frac{k_{z,mn}}{\sqrt{k^2 - k_{z,mn}^2}}, \tag{4.19}$$

leading to,

$$p^{(ff)}(R,\phi,\theta,\omega) = -\frac{e^{j\frac{\pi}{4}}}{8\pi}\sqrt{\frac{2}{\pi R\sin\phi}}\sum_{m=-\infty}^{\infty} j^m e^{-jm(\theta-\tilde{\theta}_0)} f(\omega - m\Omega) \int_{-\infty}^{\infty}\left(\frac{m}{r_0}\sin\gamma - k_z\cos\gamma\right) J_m(\kappa r_0)\sqrt{\frac{\kappa}{k^2-\kappa^2}} e^{-j\sqrt{k^2-\kappa^2}(R\cos\phi - z_0)} e^{-j\kappa R\sin\phi} d\kappa. \tag{4.20}$$

Following the method of stationary phase, the derivative of the imaginary part of the exponent in Eq. 4.20 is equated to 0 at the point of stationary phase, computed to be $\kappa = k\sin\phi$, assuming far-field observers $R >> z_0$. This result is noted from *Chapter 3 Eq. 3.23* to denote the radiation location of each ducted spectral component of the radial wavenumber, κ and is shown in *Chapter 5 Eq. 5.1* to represent the nil-shielding directions. The theoretical duct radius a is introduced to provide direct comparisons with the duct radiation equations. Solving the integral in *Eq. 4.20* and substituting into *Eq. 4.14* shows the far-field pressure is of the form,

$$p^{(ff)}(R,\phi,\theta,\omega) = \sum_{m=-\infty}^{\infty} p_m^{(ff)}(R,\phi,\theta,\omega), \tag{4.21}$$

$$p_m^{(ff)}(R,\phi,\theta,\omega) = j^{m-1}\frac{1}{4S}\frac{a}{R} e^{-jk(R-z_0\cos\phi)-jm(\theta-\tilde{\theta}_0)} J_m(kr_0\sin\phi) f(\omega - m\Omega) \left(\frac{a}{r_0}m\sin\gamma + ka\cos\phi\cos\gamma\right). \tag{4.22}$$

The expression for the mean squared pressure due to free-field rotating sources, with all possible azimuthal modes included, may be obtained by evaluating $\overline{p^2}^{(ff)} = 1/2E\{pp^*\}$, where $E\{\cdot\}$ denotes the Expectation. This procedure results in the cross spectral term $E\{f(\omega - m\Omega)f^*(\omega - m'\Omega)\}$. In this thesis frequency incoherence is assumed in the source cross spectrum, i.e.,

$$E\{f(\omega - m\Omega)f^*(\omega - m'\Omega)\} = \overline{f^2}(\omega - m\Omega)\delta_{mm'}, \tag{4.23}$$

where $\delta_{mm'}$ is the Knonecker delta function and ensures the source spectrum at different frequencies are incoherent. The far-field mean square pressure radiation from a point rotating dipole source is of the form,

$$\overline{p^2}^{(ff)}(R,\phi,\omega) = \frac{1}{2}\left(\frac{1}{4S}\frac{a}{R}\right)^2 \sum_{m=-\infty}^{\infty} J_m^2(kr_0\sin\phi)\overline{f^2}(\omega - m\Omega)\left(\frac{a}{r_0}m\sin\gamma + ka\cos\phi\cos\gamma\right)^2. \tag{4.24}$$

Equation 4.24 is a standard result for steady forces, Blake (2017), however it may be developed further for the case of unsteady forces. Expanding the term $(m/r_0 \sin\gamma + k\cos\phi\cos\gamma)^2$ and assuming a 'flat' source spectrum $\overline{f^2}(\omega) = \overline{f^2}$ (i.e., independent of frequency) *Eq. 4.24* may be simplified by noting the following Bessel function identities;

$$\sum_{m=-\infty}^{\infty} J_m^2(\Theta) = 1, \quad (4.25) \qquad \sum_{m=-\infty}^{\infty} m J_m^2(\Theta) = 0, \quad (4.26) \qquad \sum_{m=-\infty}^{\infty} m^2 J_m^2(\Theta) = \frac{1}{2}\Theta^2, \quad (4.27)$$

which upon substitution into *Eq. 4.24* gives,

$$\overline{p^2}^{(ff)}(R,\phi,\omega) = \frac{1}{2}\left(\frac{ka}{4S}\frac{a}{R}\right)^2 \left(\frac{1}{2}\sin^2\gamma\sin^2\phi + \cos^2\gamma\cos^2\phi\right)\overline{f^2} \qquad (4.28)$$

Equation 4.25 is a standard result, while *Eq. 4.26* arises since $mJ_m^2(\Theta)$ is an odd function in m. A reference to *Eq 4.27* cannot be found and has only been proven numerically. The final result of *Eq. 4.28* is particularly simple. It reduces to standard results for the axial and transverse dipole orientations of $\gamma = 0°$ and $\gamma = 90°$. Note that $\overline{p^2}^{(ff)}(R,\phi,\omega)$ of *Eq. 4.28* is independent of the radius of rotation r_0.

4.1.2 Free-field radiation of incoherent axial dipole source distributions

In this section the free-field radiation of a distribution (thin disc) of incoherent axial dipole sources is derived as sketched in *figure 4.2*. The free-field radiation of source distributions is formed by integration across a cross section of source elements, each of the form of the point source radiation of *Eq. 4.22*, .

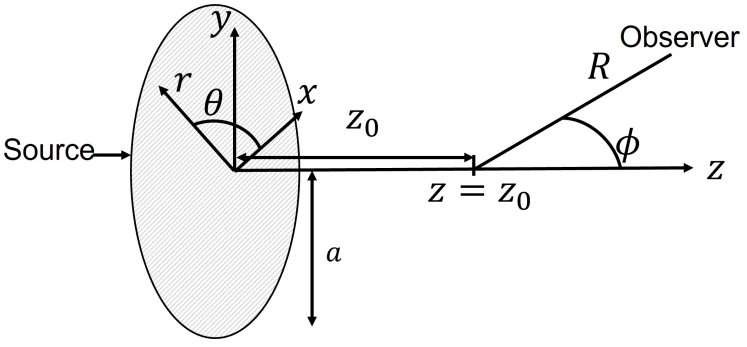

FIGURE 4.2: Coordinate system of an incoherent source distribution of radius a in free-field

Setting the rotation speed to 0, $\Omega = 0$, assuming the axial condition, $\gamma = 0^\circ$ and performing an integral across a circular cross sectional area S of radius a in *Eq. 4.22* gives,

$$p_m^{(ff)}(R,\phi,\theta,\omega) = j^{m-1}\frac{1}{4S}\frac{a}{R}\mathrm{e}^{-jk(R-z_0\cos\phi+m\theta)}ka\cos\phi\int_S \mathrm{e}^{jm\theta_0}F(r_0,\theta_0,\omega)J_m(kr_0\sin\phi)dS(r_0,\theta_0), \tag{4.29}$$

where the magnitude of the fluctuating force f has been replaced by the term $F(r_0,\theta_0,\omega)$ and represents the fluctuating force per unit area. The mean square acoustic pressure is formed by,

$$\overline{p^2}_m^{(ff)}(R,\phi,\omega) = \left(\frac{1}{4S}\frac{a}{R}\right)^2(ka\cos\phi)^2\int_S\int_{S'}F(r_0,\theta_0,\omega)F(r_0',\theta_0',\omega)\mathrm{e}^{jm\theta_0}\mathrm{e}^{-jm\theta_0'} J_m(kr_0\sin\phi)J_m(kr_0'\sin\phi)dSdS'. \tag{4.30}$$

In practise $F(r_0,\theta_0,\omega)$ is a random quantity. For simplicity it is assumed that the source elements are mutually incoherent and uniformly distributed over the cross section, the mean square source strength per unit surface area, $\overline{F^2}(\omega)$, representing a spacial average, is introduced and defined as,

$$E\{F(r_0,\theta_0,\omega)F'^*(r_0',\theta_0',\omega)\} = 4S\overline{F^2}(\omega)\frac{\delta(r_0'-r_0)}{r_0'}\delta(\theta_0'-\theta_0). \tag{4.31}$$

Substituting *Eq. 4.31* into *Eq. 4.30* shows,

$$\overline{p^2}_m^{(ff)}(R,\phi,\omega) = \frac{1}{4S}\left(\frac{a}{R}\right)^2(ka\cos\phi)^2\overline{F^2}(\omega)\int_{S'}\int_S\frac{\delta(r_0'-r_0)}{r_0'}\delta(\theta_0'-\theta_0)\mathrm{e}^{-jm\theta_0}\mathrm{e}^{jm\theta_0'} J_m(kr_0\sin\phi)J_m(kr_0'\sin\phi)dSdS'. \tag{4.32}$$

By using $dS' = r_0'd\theta_0'dr_0'$ the integral across S' is solved using the sifting property of the delta function in *Eq. 4.32* to give,

$$\overline{p^2}_m^{(ff)}(R,\phi,\omega) = \frac{1}{4S}\left(\frac{a}{R}\right)^2(ka\cos\phi)^2\overline{F^2}(\omega)\int_0^{2\pi}\int_0^a J_m^2(kr_0\sin\phi)r_0dr_0d\theta_0. \tag{4.33}$$

The integral across θ_0 in *Eq. 4.33* is solved ($\int_0^{2\pi} d\theta = 2\pi$) and across r_0 using the orthogonality of the Bessel function to show the pressure is of the form,

$$\overline{p^2}_m^{(ff)}(R,\phi,\omega) = \left(\frac{1}{2}\frac{a}{R}\right)^2 (ka\cos\phi)^2 \overline{F^2}(\omega) \left[\left(1 - \frac{m^2}{(ka\sin\phi)^2}\right) J_m^2(ka\sin\phi) + J_m'^2(ka\sin\phi)\right]. \tag{4.34}$$

The total pressure field is predicted using

$$\overline{p^2}^{(ff)}(R,\phi,\omega) = \frac{1}{2}\sum_{m=-\infty}^{\infty} \overline{p^2}_m^{(ff)}(R,\phi,\omega). \tag{4.35}$$

Using identities of the Bessel function, *Eq. 4.25* and *4.27* and a similar result not found in literature, proven by numerical computation,

$$\sum_{m=-\infty}^{\infty} J_m'^2(\Theta) = 1/2, \tag{4.36}$$

shows the mean square far-field pressure is of the form.

$$\overline{p^2}^{(ff)}(R,\phi,\omega) = \frac{1}{2}\left(\frac{1}{2}\frac{a}{R}\right)^2 (ka\cos\phi)^2 \overline{F^2}(\omega). \tag{4.37}$$

4.1.3 Free-field radiation of rotating point monopole sources

The same analysis presented in *Sections 4.1* and *4.1.2* is now repeated for rotating point monopole sources. An unsteady volume velocity with arbitrary time dependence $\hat{q}(t_0)$ is assumed to rotate at angular velocity Ω around the z axis with radius of rotation r_0. The observer position is assumed to be located in the far-field (R,ϕ,θ), using the coordinate system sketched in *figure 4.1*.

The in-homogeneous wave equation to obtain the pressure field $\hat{p}(r,\theta,z,t)$ in cylindrical polar coordinates for an arbitrary monopole source distribution is described by *Eq. 4.1*. The general case of a rotating point monopole has source term of the form

$$\hat{s}(r_0,\theta_0,t_0) = -jk\rho c\hat{q}(t_0)\frac{\delta(r-r_0)}{r}\delta(\theta-\hat{\theta}_0), \tag{4.38}$$

Following the same procedure as for the dipole case, the mean square pressure radiated from a point rotating monopole source is a modal solution, where each azimuthal mode m radiates of the form,

$$p_m^{(ff)}(R,\phi,\theta,\omega) = j^{m-1}\frac{1}{4S}\frac{a}{R}ka\rho c\mathrm{e}^{-jk(R-z_0\cos\phi)-jm(\theta-\tilde{\theta}_0)}J_m(kr_0\sin\phi)q(\omega-m\Omega). \quad (4.39)$$

Following analysis from *Section 4.1.2*, for rotating point sources, the mean square pressure is of the form,

$$\overline{p^2}^{(ff)}(R,\phi,\omega) = \frac{1}{2}\left(\frac{1}{4S}\frac{a}{R}\right)^2(ka\rho c)^2\sum_{m=-\infty}^{\infty}J_m^2(kr_0\sin\phi)\overline{q^2}(\omega-m\Omega), \quad (4.40)$$

where $\overline{q^2}(\omega-m\Omega)$ is the mean square volume velocity. Assuming a 'flat spectrum' of volume velocities $\overline{q^2}=\overline{q^2}(\omega-m\Omega)$ and using the result of *Eq. 4.25*, *Eq. 4.40* becomes,

$$\overline{p^2}^{(ff)}(R,\phi,\omega) = \frac{1}{2}\left(\frac{1}{4S}\frac{a}{R}\right)^2(ka\rho c)^2\overline{q^2}. \quad (4.41)$$

4.1.4 Free-field radiation of distributions of incoherent monopole sources

In this section the free-field radiation of a distribution (thin disc) of incoherent monopole sources as sketched in *figure 4.2* is derived. The free-field radiation of source distributions is formed by integration across a cross section of source elements, each of the form of the point source derived in the previous section. Setting the rotational speed to 0, $\Omega=0$ and performing an integral across a circular cross sectional area S of radius a,

$$p_m^{(ff)}(R,\phi,\theta,\omega) = \frac{j^{m-1}}{4S}\frac{a}{R}ka\rho c\mathrm{e}^{-jk(R-z_0\cos\phi)+jm\tilde{\theta}_0}\int_S\mathcal{Q}(r_0,\theta_0,\omega)J_m(kr_0\sin\phi)\mathrm{e}^{-jm\theta}dS(r_0,\theta_0). \quad (4.42)$$

where the volume velocity q has been replaced by the term $\mathcal{Q}(r_0,\theta_0,\omega)$ and represents the fluctuating volume velocity per unit surface area. The mean square acoustic pressure is formed,

$$\overline{p^2}_m^{(ff)}(R,\phi,\theta,\omega) = \left(\frac{1}{4S}\frac{a}{R}\right)^2(ka\rho c)^2\int_{S'}\int_S\mathcal{Q}(r_0,\theta_0,\omega)\mathcal{Q}'^*(r_0,\theta_0,\omega)\mathrm{e}^{jm(\theta'-\theta)} J_m(kr_0\sin\phi)J_m(kr_0'\sin\phi)dSdS'. \quad (4.43)$$

In practise $\mathcal{Q}(r_0, \theta_0, \omega)$ is a random quantity. It is assumed that the source elements are mutually incoherent and uniformly distributed over the cross section, the mean square source strength, $\overline{\mathcal{Q}^2}(\omega)$, representing a spatial average, is defined,

$$E\{\mathcal{Q}(r_0, \theta_0, \omega)\mathcal{Q}'^*(r_0', \theta_0', \omega)\} = 4S\overline{\mathcal{Q}^2}(\omega)\frac{\delta(r_0' - r_0)}{r_0'}\delta(\theta_0' - \theta_0). \tag{4.44}$$

Substituting *Eq. 4.44* into the pressure of *Eq. 4.43* shows the integrals across S and S' are the same as in *Eq. 4.32*, for the dipole case, and can be solved to show the far-field mean square pressure is of the form,

$$\overline{p^2}_m^{(ff)}(R, \phi, \omega) = \frac{1}{2}\left(\frac{1}{2}\frac{a}{R}\right)^2 (ka\rho c)^2\overline{\mathcal{Q}^2}(\omega) \tag{4.45}$$

4.1.5 Summary of free-field source radiation

This section has derived the mean square pressure radiation $\overline{p^2}_m^{(ff)}(R, \phi, \omega)$ for free-field rotating point dipole and monopole sources, as well as incoherent source distributions. These results are summarised in *Table 4.1*

TABLE 4.1: Acoustic pressure radiated by free-field sources

	Rotating point sources
Dipole	$\overline{p^2}^{(ff)}(R, \phi, \omega) = \frac{1}{2}\left(\frac{ka}{4S}\frac{a}{R}\right)^2 \left(\frac{1}{2}\sin^2\gamma\sin^2\phi + \cos^2\gamma\cos^2\phi\right)\overline{f^2}$ (4.28)
Monopole	$\overline{p^2}^{(ff)}(R, \phi, \omega) = \frac{1}{2}\left(\frac{1}{4S}\frac{a}{R}\right)^2 (ka\rho c)^2\overline{q^2}$ (4.41)
	Distributions of incoherent sources
Axial Dipoles	$\overline{p^2}^{(ff)}(R, \phi, \omega) = \frac{1}{2}\left(\frac{1}{2}\frac{a}{R}\right)^2 (ka\cos\phi)^2\overline{F^2}(\omega)$ (4.37)
Monopoles	$\overline{p^2}^{(ff)}(R, \phi, \omega) = \frac{1}{2}\left(\frac{1}{2}\frac{a}{R}\right)^2 (ka\rho c)^2\overline{\mathcal{Q}^2}(\omega)$ (4.45)

4.1.6 Acoustic power radiated by free-field sources

In the next chapter, *Chapter 5*, the power radiated by free-field and ducted sources is compared. This section derives expressions for the power radiated by free-field sources. The far-field power radiated from free-field acoustic sources is calculated by integrating the far-field intensity,

$$W^{(ff)}(\omega) = \frac{2\pi}{\rho c} R^2 \int_0^{\pi} |p^{(ff)}(R, \phi, \omega)^2| \sin\phi d\phi. \tag{4.46}$$

The power radiated by free-field rotating point dipole and monople sources is formed by substitution of *Eq. 4.28* and *4.41* into *Eq. 4.46* respectively, note $\overline{p^2} = 1/2|p^2|$. Similarly the power radiated by distributions of incoherent axial dipole and monopole sources is formed by substituting *Eq. 4.37* and *4.45* into *Eq. 4.46* respectively.

The power radiated by free-field sources are shown in *Table* .

TABLE 4.2: Acoustic power radiated by free-field sources

Rotating point sources

Dipole	$W^{(ff)}(\omega) = \frac{1}{12S}\frac{1}{\rho c}(ka)^2\overline{f^2}$	(4.47)
Monopole	$W^{(ff)}(\omega) = \frac{1}{4S}\rho c(ka)^2\overline{q^2}$	(4.48)

Distributions of incoherent sources

Axial Dipoles	$W^{(ff)}(\omega) = \frac{S}{3}\frac{1}{\rho c}(ka)^2\overline{F^2}(\omega)$	(4.49)
Monopoles	$W^{(ff)}(\omega) = S\rho c(ka)^2\overline{\mathcal{Q}^2}(\omega)$	(4.50)

4.2 Modal amplitudes at the open end of a semi-infinite duct

This section derives the relative modal amplitude $a_{mn}(\omega)$ for rotating point dipole and monopole sources, and a distribution of incoherent axial dipole and monopole sources inside semi-infinite ducts. The modal amplitudes are required to predict the mean square pressure radiation of the ducted sources.

Some modal amplitude functions were derived for source distributions by Joseph and Morfey (1999) but constrained to propagating modes. This section derives the relative modal amplitudes, valid above and below cut-off, using a Green's function approach.

To derive the modal amplitude $a_{mn}(\omega)$, consider the pressure inside an infinite duct which is formed by substituting the Green's function of *Eq. 2.26* into the pressure of *Eq. 2.18*,

$$\begin{aligned}\hat{p}^{(D)}_{mn}(r,\theta,z,t) = &\frac{j}{4\pi S}\frac{e^{jk_{z,mn}(z-z_0)}}{k_{z,mn}}\Psi_{mn}(r,\theta)\int_S \Psi^*_{mn}(r_0,\theta_0)\\ &\int_{-\infty}^{\infty}\int_{-\infty}^{\infty}\hat{s}(r_0,\theta_0,t_0)e^{j\omega(t-t_0)}d\omega dt_0 dS(r_0,\theta_0),\end{aligned} \tag{4.51}$$

4.2.1 Rotating point dipole sources

This section derives the modal amplitude distribution $a_{mn}(\omega)$ at the open end of a semi-infinite duct for rotating point dipole sources. As sketched in *figure 4.3* an unsteady force with arbitrary time dependence $\hat{f}(r,\theta,t_0)$ is assumed to rotate at angular velocity Ω around the z axis with radius of rotation r_0, at retarded time t_0 inside a semi-infinite duct of radius a.

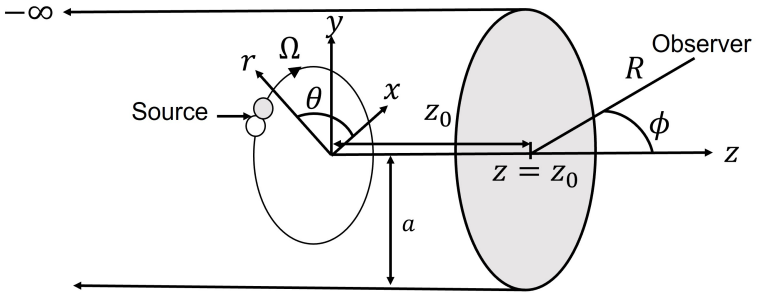

FIGURE 4.3: Coordinate system of a rotating point source inside a semi-infinite duct

A rotating point dipole has source term defined in *Eq. 4.2*, which is substituted into *Eq. 4.51* to show,

$$\hat{p}_{mn}^{(D)}(r,\theta,z,t) = \frac{j}{4\pi S}\int_S \Psi_{mn}(r,\theta)\frac{\delta(r-r_0)}{r_0}\int_{-\infty}^{\infty}\hat{f}(t_0)\delta(\theta-\hat{\theta}_0) \left[\frac{1}{r}\frac{\partial}{\partial\theta}\sin\gamma + \frac{\partial}{\partial z}\cos\gamma\right]\cdot\Psi_{mn}^*(r_0,\theta_0)\int_{-\infty}^{\infty}\frac{\mathrm{e}^{jk_{z,mn}(z_0-z)}}{k_{z,mn}}\mathrm{e}^{j\omega(t-t_0)}d\omega dt_0 dS(r,\theta), \tag{4.52}$$

Computing the integral across the surface area in *Eq. 4.52* utilizing the sifting property of the delta function,

$$\hat{p}_{mn}^{(D)}(r,\theta,z,t) = \frac{j}{4\pi S}\Psi_{mn}(r,\theta)\int_{-\infty}^{\infty}\left[\frac{1}{r}\frac{\partial}{\partial\theta}\sin\gamma + \frac{\partial}{\partial z}\cos\gamma\right]\cdot\hat{f}(t_0) \Psi_{mn}^*(r_0,\hat{\theta}_0)\int_{-\infty}^{\infty}\frac{\mathrm{e}^{jk_{z,mn}(z_0-z)}}{k_{z,mn}}\mathrm{e}^{j\omega(t-t_0)}d\omega dt_0. \tag{4.53}$$

The differentiation $\partial/\partial\theta$ and $\partial/\partial z$ in *Eq. 4.53* is computed using integration by parts which show,

$$\hat{p}_{mn}^{(D)}(r,\theta,z,t) = \frac{1}{4\pi S}\Psi_{mn}(r,\theta)\int_{-\infty}^{\infty}\frac{\mathrm{e}^{jk_{z,mn}(z_0-z)}}{k_{z,mn}}\left(\frac{m}{r_0}\sin\gamma + k_{z,mn}\cos\gamma\right) \int_{-\infty}^{\infty}\hat{f}(t_0)\Psi_{mn}^*\left(r_0,\hat{\theta}_0\right)\mathrm{e}^{j\omega(t-t_0)}dt_0 d\omega, \tag{4.54}$$

It is convenient to introduce the local coordinate system from *Eq. 4.7*, which is substituted into *Eq. 4.54*, noting $\Psi_{mn}^*(r_0,\hat{\theta}_0)$ has azimuthal dependence $\mathrm{e}^{jm\theta_0}$, as can be seen from *Eq. 2.16*, to give,

$$\hat{p}_{mn}^{(D)}(r,\theta,z,t) = \frac{1}{4\pi S}\Psi_{mn}(r,\theta)\Psi_{mn}^*(r_0,\tilde{\theta}_0)\int_{-\infty}^{\infty}\frac{\mathrm{e}^{jk_{z,mn}(z_0-z)}}{k_{z,mn}}\mathrm{e}^{j\omega t}\left(\frac{m}{r_0}\sin\gamma + k_{z,mn}\cos\gamma\right) \int_{-\infty}^{\infty}\hat{f}(t_0)\mathrm{e}^{-j(\omega-m\Omega)t_0}dt_0 d\omega. \tag{4.55}$$

The integral across t_0 in *Eq. 4.58* is the inverse Fourier transform and is readily evaluated to give,

$$\hat{p}_{mn}^{(D)}(r,\theta,z,t) = \frac{1}{4\pi S}\Psi_{mn}(r,\theta)\Psi_{mn}^{*}(r_0,\tilde{\theta}_0)\int_{-\infty}^{\infty}\frac{e^{jk_{z,mn}(z_0-z)}}{k_{z,mn}}\left(\frac{m}{r_0}\sin\gamma + k_{z,mn}\cos\gamma\right)f(\omega-m\Omega)e^{j\omega t}d\omega. \tag{4.56}$$

Comparison of the *Eq. 4.56* with the Fourier transform defined,

$$\hat{p}(\boldsymbol{X},t) = \frac{1}{2\pi}\int_{-\infty}^{\infty}p(\boldsymbol{X},\omega)e^{j\omega t}d\omega, \tag{4.57}$$

shows the frequency domain pressure is of the form,

$$p_{mn}^{(D)}(r,\theta,z,\omega) = \frac{1}{2S}\Psi_{mn}(r,\theta)\Psi_{mn}^{*}(r_0,\tilde{\theta}_0)\frac{e^{jk_{z,mn}(z_0-z)}}{k_{z,mn}}\left(\frac{m}{r_0}\sin\gamma + k_{z,mn}\cos\gamma\right)f(\omega-m\Omega). \tag{4.58}$$

Comparing the pressure of *Eq. 4.58* to the pressure inside an infinite duct in terms of the modal amplitude from *Eq. 2.5*, reveals $a_{mn}(\omega - m\Omega)$ is of the form,

$$a_{mn}(\omega-m\Omega) = a_{S,mn}(\omega-m\Omega)e^{jk_{z,mn}z_0} \tag{4.59}$$

where $a_{S,mn}(\omega - m\Omega)$ is the modal amplitude at the source plane, $z = 0$,

$$a_{S,mn}(\omega-m\Omega) = \frac{1}{2S}\Psi_{mn}^{*}(r_0,\tilde{\theta}_0)\frac{1}{k_{z,mn}a}\left(\frac{a}{r_0}m\sin\gamma + k_{z,mn}a\cos\gamma\right)f(\omega-m\Omega). \tag{4.60}$$

Consider the special case of $r_0/a = 0$, as the radius of rotation approaches zero, $r_0 \to 0$, the term $J_m(\kappa_{mn}r_0)$ in the mode shape function, $\Psi_{mn}^{*}(r_0,\tilde{\theta}_0)$, exhibits exponential decrease for modes of azimuthal order $|m| > 1$ and approaches 1 for the axi-symmetric modes $m = 0$. The term $1/r_0 \to \infty$, at a slower rate than the exponential decrease of the Bessel function. Therefore, as a result of these two effects, only the $m = 0$ modes radiate for a stationary source, $\Omega = 0$, located on the duct axis $r_0/a = 0$. The modal amplitude at the source plane $a_{S,mn}(\omega)$, for $r_0/a = 0$ is of the form,

$$a_{S,mn}(\omega) = \begin{cases} \frac{1}{2S}\frac{1}{J_m(\kappa_{mn}a)}f(\omega)\cos\gamma & m = 0, \\ 0 & m \neq 0, \end{cases} \tag{4.61}$$

4.2.1.1 Far-field mean square radiation from rotating ducted sources

The expression for the mean squared pressure due to free-field rotating sources, with all possible azimuthal m and radial n modes included, may be obtained by evaluating $\overline{p^2}^{(D)} = 1/2E\{pp^*\}$. This procedure results in the cross spectral term $E\{f(\omega - m\Omega)f^*(\omega - m'\Omega)\}$. In this thesis frequency incoherence is assumed in the source cross spectrum *Eq. 4.23*. The far-field mean square pressure radiation from a point rotating dipole source is of the form,

$$\overline{p^2}^{(D)}(R,\phi,\omega) = \frac{1}{2}\left(\frac{a}{R}\right)^2 \sum_{m=-\infty}^{\infty} E\left\{\left|\sum_{n=1}^{\infty} a_{mn}(\omega)D_{mn}(\phi,ka)\right|^2\right\}. \tag{4.62}$$

4.2.2 Distribution of incoherent axial dipole sources

This section derives the modal amplitude $a(\omega)$ at the open end of a semi-infinite duct for a distribution (thin disc) of incoherent axial dipole sources as sketched in *figure 4.4*.

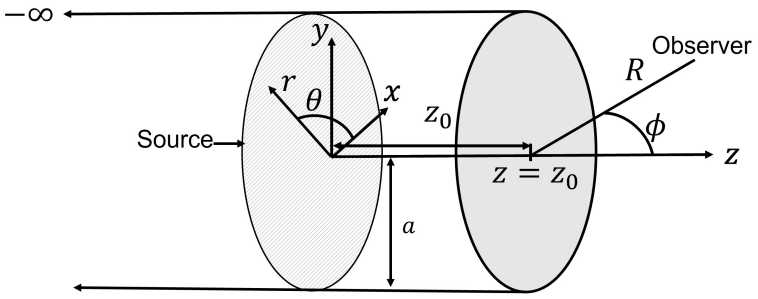

FIGURE 4.4: Coordinate system of an incoherent source distribution inside a semi-infinite duct

The modal amplitude for a rotating point source of *Eq. 4.59* and *4.60* can be extended to a distribution of incoherent axial dipole sources by setting the dipole orientation and rotation speed to 0, $\gamma = 0^\circ$, $\Omega = 0$ and performing an integral across the cross sectional area S. The modal amplitude for a distribution of incoherent axial dipole sources is of the form,

$$a_{mn}(\omega) = \frac{1}{2S}e^{jk_{z,mn}z_0}\int_S \psi^*_{mn}(r_0,\theta_0)F(r_0,\theta_0,\omega)dS, \tag{4.63}$$

where the source strength f has been replaced by the term $F(r_0,\theta_0,\omega)$ and represents the fluctuating force per unit surface area. The mean square acoustic pressure is obtained from,

$$E\{|a_{mn}(\omega)|^2\} = \frac{1}{4S}\left|e^{jk_{z,mn}z_0}\right|^2 \int_S \int_{S'} \psi^*_{mn}(r_0,\theta_0)\psi'_{mn}(r'_0,\theta'_0) \\ E\{F(r_0,\theta_0,\omega)F'^*(r'_0,\theta'_0,\omega)\}dSdS'. \tag{4.64}$$

In practise $F(r_0,\theta_0,\omega)$ is a random quantity. For simplicity it is assumed that the source elements are mutually incoherent and uniformly distributed over the cross section, the mean square source strength per unit surface area $\overline{F^2}(\omega)$ is introduced as defined in *Eq. 4.31* and substituted into *Eq. 4.64*,

$$E\{|a_{mn}(ka)|^2\} = \overline{F^2}(\omega)\left|e^{jk_{z,mn}z_0}\right|^2 \frac{1}{S}\int_S \int_{S'} \psi^*_{mn}(r_0,\theta_0)\psi'_{mn}(r'_0,\theta'_0)\frac{\delta(r'_0-r_0)}{r'_0}\delta(\theta'_0-\theta_0)dSdS'. \tag{4.65}$$

Performing the integrals across r'_0 and θ'_0 in *Eq. 4.65* using the sifting property of delta functions,

$$E\{|a_{mn}(\omega)|^2\} = \overline{F^2}(\omega)\left|e^{jk_{z,mn}z_0}\right|^2 \frac{1}{S}\int_S |\psi_{mn}(r_0,\theta_0)|^2 dS. \tag{4.66}$$

Utilizing the normalisation property of the mode shape function,
$\int_S |\psi_{mn}(r_0,\theta_0)|^2 dS = S$, the modal amplitude for a distribution of incoherent axial dipoles sources is of the form

$$E\{|a_{mn}(\omega)|^2\} = \left|e^{jk_{z,mn}z_0}\right|^2 E\{|a_{S,mn}(\omega)|^2\} \tag{4.67}$$

where,

$$E\{|a_{S,mn}(\omega)|^2\} = \overline{F^2}(\omega), \tag{4.68}$$

The mean square pressure radiated can be computed using a modal sum of the form,

$$\overline{p^2}^{(D)}(R,\phi,\omega) = \frac{1}{2}\left(\frac{a}{R}\right)^2 \sum_{m=-\infty}^{\infty}\sum_{n=1}^{\infty} E\{|a_{mn}(\omega)|^2\}|D_{mn}(\phi,ka)|^2. \tag{4.69}$$

4.2.3 Rotating point monopole sources

This section derives the modal amplitude $a_{mn}(\omega)$ at the open end of a semi-infinite duct for rotating point monopole sources. A rotating point monopole has source term of the from of *Eq. 4.38* which can be substituted into *Eq. 4.51*,

$$\begin{aligned}\hat{p}^{(D)}_{mn}(r,\theta,z,t) =& \frac{\rho c}{4\pi S}\Psi_{mn}(r,\theta)\int_S \Psi^*_{mn}(r_0,\theta_0)\frac{\delta(r_0-r_0)}{r_0}\int_{-\infty}^{\infty}\delta(\theta_0-\hat{\theta}_0)\hat{q}(t_0) \\ & \int_{-\infty}^{\infty}\frac{e^{jk_{z,mn}(z_0-z)}}{k_{z,mn}}e^{j\omega(t-t_0)}d\omega dt_0 dS(r_0,\theta_0).\end{aligned} \tag{4.70}$$

The integrals in *Eq. 4.70* are identical to *Eq. 4.52*, for the point dipole case, noting the different source strengths $\hat{q}(t_0)$ and $\hat{f}(t_0)$. Following the same procedure as for the dipole case as shown in *Section 4.2.1*, reveals the modal amplitude for rotating point monopole sources is of the form,

$$a_{mn}(\omega - m\Omega) = a_{S,mn}(\omega - m\Omega)e^{jk_{z,mn}z_0} \tag{4.71}$$

where,

$$a_{S,mn}(\omega - m\Omega) = \frac{1}{2S}\Psi^*(r_0,\tilde{\theta}_0)\frac{ka}{k_{z,mn}a}\rho c q(\omega - m\Omega), \tag{4.72}$$

Following the discussion in *Section 4.2.1*, for the $r_0/a = 0$ case,

$$a_{S,mn}(\omega) = \begin{cases} \frac{\rho c}{2S}\frac{k}{k_{z,mn}}\frac{1}{J_m(\kappa_{mn}a)}q(\omega) & m = 0, \\ 0 & m \neq 0. \end{cases} \tag{4.73}$$

The mean square pressure can then be computed from *Eq. 4.62*,

4.2.4 Distribution of incoherent monopole sources

This section derives the modal amplitude $a(\omega)$ at the open end of a semi-infinite duct for a distribution (thin disc) of incoherent monopole sources as sketched in *figure 4.4*. The modal amplitude for a point source of *Eq. 4.71* and *4.72* can be extended to a distribution of incoherent monopole sources by setting the rotational speed to 0, $\Omega = 0$ and performing an integration across the duct cross sectional area S. The modal amplitude for a distribution of incoherent monopole sources is of the form,

$$a_{mn}(\omega) = \frac{k\rho c}{2S}\frac{e^{jk_{z,mn}z_0}}{k_{z,mn}}\int_S \Psi^*(r_0,\theta_0)\mathcal{Q}(r_0,\theta_0,\omega)dS, \tag{4.74}$$

where the source strength q has been replaced by the term $\mathcal{Q}(r_0, \theta_0, \omega)$ and represents the fluctuating volume velocity per unit surface area. The mean square acoustic pressure is obtained from,

$$E\{|a_{mn}(\omega)|^2\} = \left(\frac{k\rho c}{2S}\right)^2 \left|\frac{e^{jk_{z,mn}z_0}}{k_{z,mn}}\right|^2 \int_S \int_{S'} \Psi^*(r_0, \theta_0)\Psi(r_0', \theta_0') E\{\mathcal{Q}(r_0, \theta_0, \omega)\mathcal{Q}'^*(r_0, \theta_0, \omega)\} dS dS'. \tag{4.75}$$

Following the same procedure as *Section 4.2.2*, and using *Eq. 4.44*, shows the modal mean square amplitude for a distribution of incoherent monopole sources is of the form,

$$E\{|a_{mn}(\omega)|^2\} = \left|e^{jk_{z,mn}z_0}\right|^2 E\{|a_{S,mn}(\omega)|^2\}, \tag{4.76}$$

where,

$$E\{|a_{S,mn}(\omega)|^2\} = \left|\frac{1}{k_{z,mn}a}\right|^2 (\rho cka)^2 \overline{\mathcal{Q}^2}(\omega), \tag{4.77}$$

from which the the mean square pressure can be computed using *Eq. 4.69*.

4.2.5 Summary

This section has derived the modal amplitudes $a_{mn}(\omega)$ for dipole and monopole sources. These can be used to predict the far-field acoustic radiation of ducted sources (using the polar directivity factor $D_{mn}(\phi, ka)$ of *Eq 2.52*. *Table 4.3* provides a summary of the acoustic radiation from ducted sources.

TABLE 4.3: Acoustic pressure radiated by sources inside a semi-infinite duct

Rotating point sources

$$\overline{p^2}^{(D)}(R,\phi,\omega) = \tfrac{1}{2}\left(\tfrac{a}{R}\right)^2 \sum_{m=-\infty}^{\infty} E\left\{\left|\sum_{n=1}^{\infty} a_{mn}(\omega) D_{mn}(\phi, ka)\right|^2\right\},$$

where,

Dipole $$a_{mn}(\omega) = \tfrac{1}{2S}\Psi^*_{mn}(r_0,\tilde{\theta}_0)\tfrac{e^{jk_{z,mn}z_0}}{k_{z,mn}a}\left(\tfrac{a}{r_0}m\sin\gamma - k_{z,mn}a\cos\gamma\right) f$$

Monopole $$a_{mn}(\omega) = \tfrac{1}{2S}\Psi^*_{mn}(r_0,\tilde{\theta}_0)\tfrac{e^{jk_{z,mn}z_0}}{k_{z,mn}a} ka\rho c q$$

Point source on axis $r_0/a = 0, m = 0$

$$\overline{p^2}^{(D)}(R,\phi,\omega) = \tfrac{1}{2}\left(\tfrac{a}{R}\right)^2 E\left\{\left|\sum_{n=1}^{\infty} a_{0n} D_{0n}(\phi, ka)\right|^2\right\},$$

where,

Dipole $$a_{mn}(\omega) = \tfrac{1}{2S}\tfrac{e^{jk_{z,mn}z_0}}{J_m(\kappa_{mn}a)}\cos\gamma\, f$$

Monopole $$a_{mn}(\omega) = \tfrac{1}{2S}\tfrac{e^{jk_{z,mn}z_0}}{k_{z,mn}aJ_m(\kappa_{mn}a)} ka\rho c q$$

Distributions of incoherent sources

$$\overline{p^2}^{(D)}(R,\phi,\omega) = \tfrac{1}{2}\left(\tfrac{a}{R}\right)^2 \sum_{m=-\infty}^{\infty}\sum_{n=1}^{\infty} E\left\{|a_{mn}(\omega)|^2\right\}|D_{mn}(\phi,ka)|^2,$$

where,

Axial dipoles $$E\{|a_{mn}(\omega)|^2\} = \left|\tfrac{e^{jk_{z,mn}z_0}}{k_{z,mn}a}\right|^2 |k_{z,mn}a|^2\overline{F^2}(\omega)$$

Monopoles $$E\{|a_{mn}(\omega)|^2\} = \left|\tfrac{e^{jk_{z,mn}z_0}}{k_{z,mn}a}\right|^2 (\rho c k a)^2\overline{\mathcal{Q}^2}(\omega)$$

4.3 Convergence of the acoustic pressure radiation solution from sources inside semi-infinite ducts

This section investigates the number of cut-off modes required to ensure the predictions for the radiated acoustic pressure field computed in the modal summation are converged. In principle an infinite number of cut-off modes can potentially radiate to the far-field. It therefore important to determine the number of modes required to ensure accurate predictions.

4.3.1 Modal convergence for monopole sources at the open end of semi-infinite ducts

This section examines the number of cut-off modes required to ensure that predictions of the mean square pressure $\overline{p^2}(R, \phi, \omega)$ for monopole sources is computed to within 0.5 dB of it's final value when converged.

The mean square pressure radiation due to a distribution of incoherent monopole sources inside a semi-infinite duct is formed by substituting the modal amplitude from *Eq. 4.76* and the un-flanged directivity of *Eq. 2.52* into *Eq. 4.69*. *Figure 4.5* shows a plot of the cumulative sum of the mean square pressure field $\overline{p^2}^{(D)}(R, \phi, \omega)$ for a distribution of incoherent monopole sources at the open end $z_0/\lambda = 0$ of a semi-infinite duct. The pressure is computed using a cumulative sum of modes across all cut-on and cut-off modes, plotted against ζ_{mn}, for two non-dimensional frequencies $ka = 5$ and 35, at the two representative rear-arc angles of $\phi = 120^\circ$ and 150°, where it is shown in *Chapter 3* that cut-off modes are most important in the rear-arc. The number of cut-off modes is determined by the minimum value of ζ_{mn} of the highest order mode included in the calculation of $\overline{p^2}^{(D)}(R, \phi, \omega)$, which satisfies,

$$\overline{p^2}^{(D)}(R, \phi, \omega) = \sum_{\zeta_{mn} \to \infty}^{\min\{\zeta_{mn}\}} \overline{p^2}^{(D)}_{mn}(R, \phi, \omega). \tag{4.78}$$

The source strength $\overline{Q^2}(\omega)$ and and far-field observer radial distance R are taken to be unity.

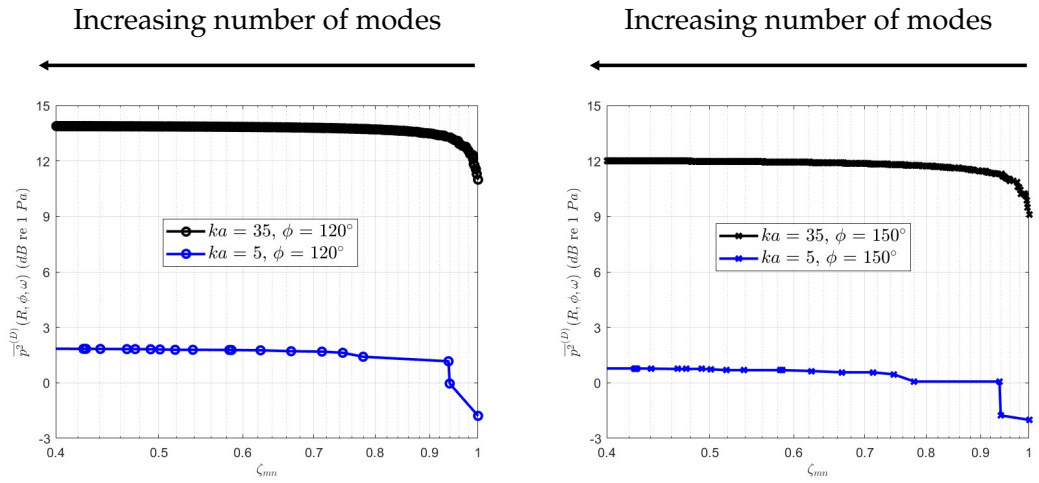

(A) $\phi = 120°$ (B) $\phi = 150°$

FIGURE 4.5: Radiated mean square pressure $\overline{p^2}^{(D)}(R, \phi, \omega)$, for a distribution of incoherent monopole sources at the open end $z_0/\lambda = 0$ of a semi-infinite duct, for a varying number of cut-off modes.

The prediction of the mean square pressure in *figure 4.5* is seen to converge to within 0.5 dB by including all modes with cut-off ratio $\zeta_{mn} > 0.75$.

The cumulative mean square pressure $\overline{p^2}^{(D)}(R, \phi, \omega)$ due to rotating point monopole sources inside a semi-infinite duct is formed by substituting the modal amplitude from *Eq. 4.71* and the un-flanged directivity of *Eq. 2.52* into *Eq. 4.62*. *Figure 4.6* shows a plot of the radiated pressure field for rotating point monopole sources at the open end $z_0\lambda = 0$ of a semi-infinite duct, plotted against ζ_{mn}, for two non-dimensional frequencies $ka = 5$ and 35, at the two representative rear-arc angles of $\phi = 120°$ and 150°. Three radii of rotation are investigated, $r_0/a = 0, 0.5$ and 1. The source strength $\overline{q^2}$ and far-field observer radial distance R are taken to be unity.

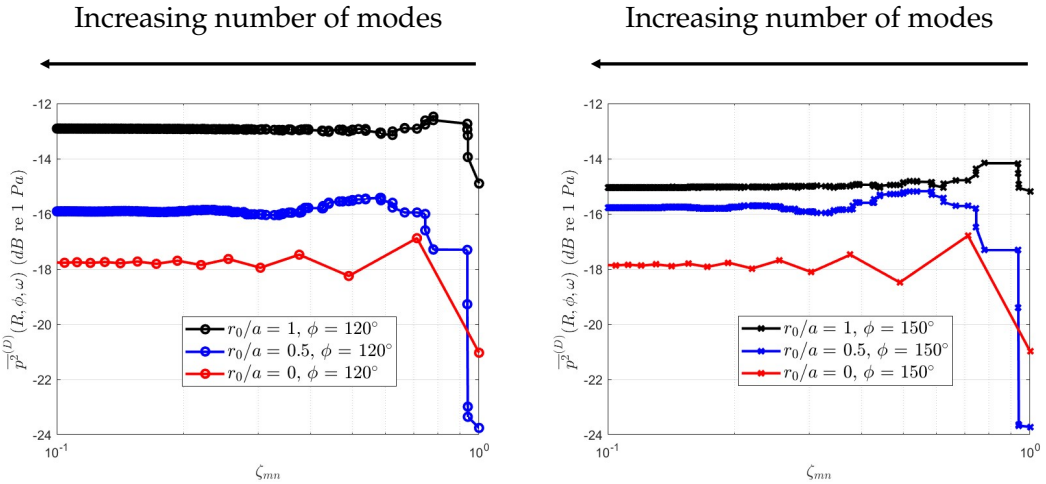

(A) $ka = 5, \phi = 120°$ (B) $ka = 5, \phi = 150°$

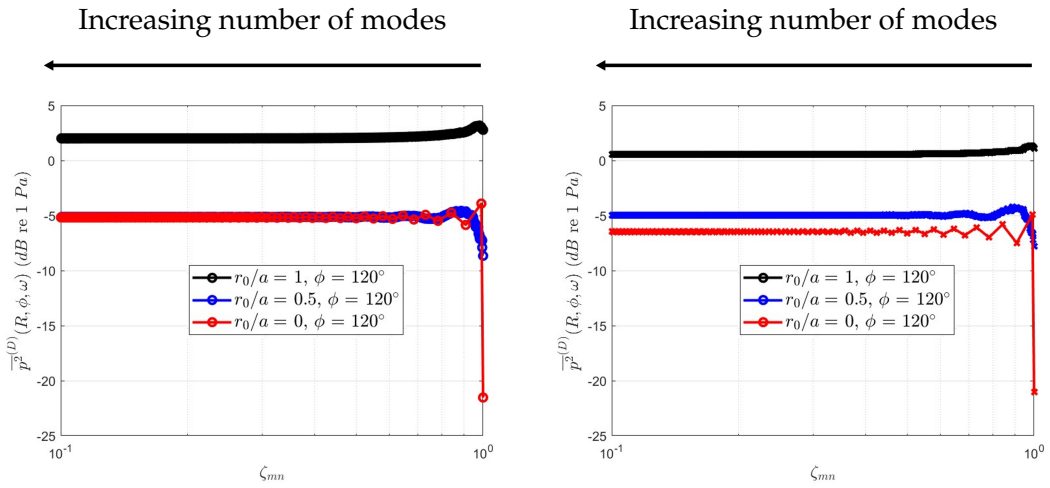

(C) $ka = 35, \phi = 120°$ (D) $ka = 35, \phi = 150°$

FIGURE 4.6: Radiated mean square pressure $\overline{p^2}^{(D)}(R,\phi,ka)$, for rotating point monopole sources at three radii of rotation $r_0/a = 0.0, 0.5$ and 1.0 at the open end of a semi-infinite duct $z_0/\lambda = 0$, for a varying number of cut-off modes.

For rotating point monopole sources, convergence to within 0.5 dB is achieved by including modes with cut-off ratio $\zeta_{mn} > 0.4$ for all cases investigated in *figure 4.6*.

4.3.2 Modal convergence for dipole sources at the open end of semi-infinite ducts

The same analysis in *Section 4.3.1* is now repeated for dipole sources. The mean square pressure $\overline{p^2}^{(D)}(R,\phi,\omega)$ radiated from a distribution of incoherent axial dipole sources inside a semi-infinite duct is formed by substituting the modal amplitude from *Eq. 4.67* and the un-flanged directivity of *Eq. 2.52* into *Eq. 4.69*.

Figure 4.7 shows a plot of the cumulative radiated acoustic pressure field $\overline{p^2}^{(D)}(R,\phi,\omega)$ for a distribution of incoherent axial dipole sources at the open end of a semi-infinite duct $z_0/\lambda = 0$. The source strength $\overline{F^2}(\omega)$ is taken to be unity. The remaining parameters are the same as in *figure 4.5*.

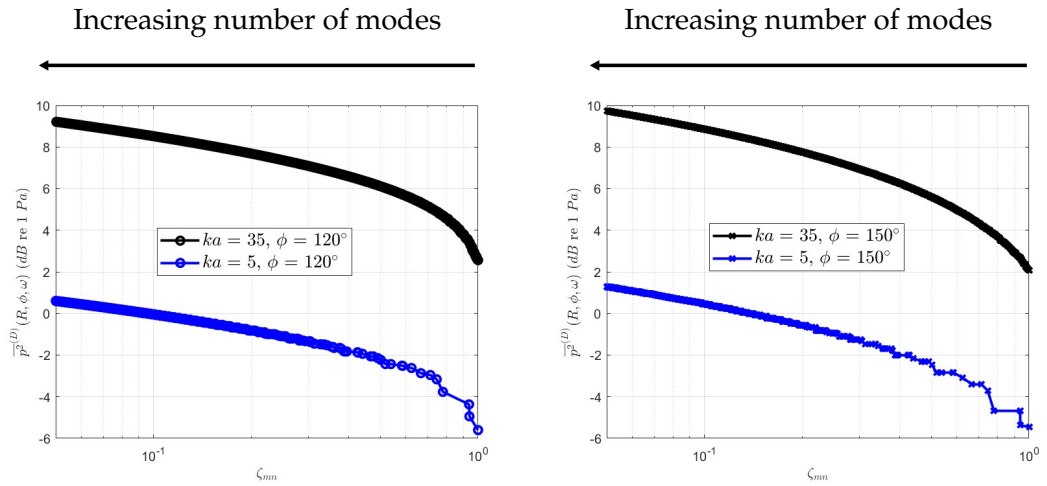

(A) $\phi = 120°$ (B) $\phi = 150°$

FIGURE 4.7: Radiated mean square pressure $\overline{p^2}^{(D)}(R,\phi,\omega)$, for a distribution of incoherent axial dipole sources at the open end $z_0/\lambda = 0$ of a semi-infinite duct, for a varying number of cut-off modes.

An unexpected finding from this convergence for dipole sources is that the solution does not converge when considering modes of cut-off ratio $\zeta_{mn} > 0.05$ for dipole radiation. For the $ka = 35$ case a summation of over 60,000 modes was included, with only 167 modes being cut-on. The cause of this lack of convergence behavior of dipole sources at the open end of ducts is investigated in the next section.

The mean square pressure $\overline{p^2}^{(D)}(R,\phi,\omega)$ radiated from a rotating point dipole source inside a semi-infinite duct is formed by substituting the modal amplitude of *Eq. 4.59* and the un-flanged directivity of *Eq. 2.52* into *Eq. 4.62*. *Figure 4.8* shows a plot of the cumulative radiated mean square pressure field $\overline{p^2}^{(D)}(R,\phi,\omega)$ for a rotating point dipole source at the open end of a semi-infinite duct $z_0/\lambda = 0$. The source strength $\overline{f^2}$ is taken to be unity. the remaining parameters are the same as in *figure 4.6*.

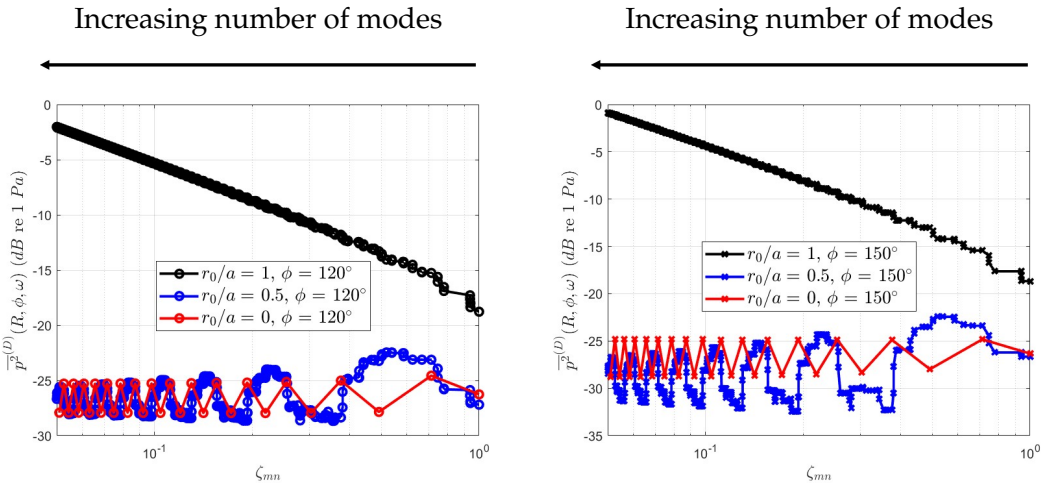

(A) $ka = 5, \phi = 120°$ (B) $ka = 5, \phi = 150°$

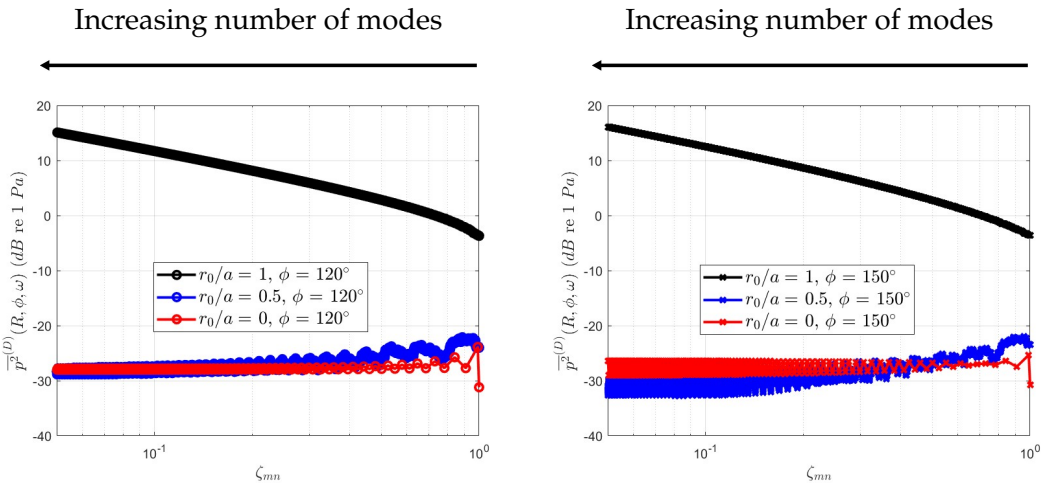

(C) $ka = 35, \phi = 120°$ (D) $ka = 35, \phi = 150°$

FIGURE 4.8: Radiated mean square pressure $\overline{p^2}^{(D)}(R,\phi,\omega)$, for rotating point dipole sources at the open end $z_0/\lambda = 0$ of a semi-infinite duct, for a varying number of cut-off modes.

Two distinct groups of convergence behavior can be identified from *figure 4.8*. The point sources at the wall of the duct $r_0/a = 1$ exhibit similar behavior to the source distributions shown in *figure 4.7*, where increasing the number of modes in the summation over m and n is seen to steadily increase the mean square pressure. For rotating point sources not at the wall $r_0/a < 1$, oscillations are observed by increasing the number of cut-off modes in the simulation. The convergence behavior of dipole sources at the open end of semi-infinite ducts is investigated in the next section.

4.3.3 Asymptotic prediction of dipole sources at the open end of semi-infinite ducts

The previous section has shown that radiation from dipole sources at the open end of ducts $z_0/\lambda = 0$ do not converge considering a summation of all cut-on and cut-off modes with $\zeta_{mn} > 0.05$. This section investigates the reason for this behavior of the radiated pressure. For dipole sources at the open end of the duct, three cases are investigated; incoherent distributions, rotating point sources $0 < r_p/a \leq 1$ and point sources on the duct axis $r_p/a = 0$.

Consider the polar directivity which has the normalisation property $\int_0^\pi Q(\phi, ka)d\phi = 1$, and represents the spatial distribution of power among the polar angles of the form,

$$Q(\phi, ka) = \frac{\overline{p^2}^{(D)}_{\text{cut-on}}(R,\phi,\omega) + \overline{p^2}^{(D)}_{\text{cut-off}}(R,\phi,\omega)}{\frac{1}{2}\int_0^\pi \left(\overline{p^2}^{(D)}_{\text{cut-on}}(R,\phi,\omega) + \overline{p^2}^{(D)}_{\text{cut-off}}(R,\phi,\omega)\right)\sin\phi d\phi}. \tag{4.79}$$

The contribution to the mean square pressure $\overline{p^2}^{(D)}(R,\phi,\omega)$ can be split into the contribution of the cut-on and cut-off modes defined respectively as,

$$\overline{p^2}^{(D)}_{\text{cut-on}}(R,\phi,\omega) = \sum_{(m,n)\in\{\mathcal{M},\mathcal{N}\}} \overline{p^2}^{(D)}_{mn}(R,\phi,\omega), \tag{4.80}$$

$$\overline{p^2}^{(D)}_{\text{cut-off}}(R,\phi,\omega) = \sum_{(m,n)\notin\{\mathcal{M},\mathcal{N}\}} \overline{p^2}^{(D)}_{mn}(R,\phi,\omega), \tag{4.81}$$

where $\{\mathcal{M},\mathcal{N}\}$ represent the modal indices (m,n) corresponding to the cut-on modes.

4.3.3.1 Incoherent distribution of axial dipole sources

In the evaluation of $\overline{p^2}^{(D)}_{\text{cut-off}}(R,\phi,\omega)$ of *Eq. 4.81* it can be shown ,

$$\overline{p^2}^{(D)}_{\text{cut-off}}(R,\phi,\omega) = \left(\frac{a}{R}\right)^2 \sum_{(m,n)\notin\{\mathcal{M},\mathcal{N}\}} E\{|a_{mn}(\omega)|^2\}|D_{mn}(\phi,ka)|^2. \tag{4.82}$$

Substituting the modal amplitude for a distribution of incoherent axial dipole sources of *Eq. 4.68* and *4.67* into *Eq. 4.82* for $z_0/\lambda = 0$ gives,

$$\overline{p^2}^{(D)}_{\text{cut-off}}(R,\phi,\omega) = \left(\frac{a}{R}\right)^2 \overline{F^2}(\omega) \sum_{(m,n)\notin\{\mathcal{M},\mathcal{N}\}} |D_{mn}(\phi,ka)|^2. \tag{4.83}$$

For sufficiently cut-off modes the scaling law discussed in *Appendix A*, $|D_{mn}(\phi,ka)|^2 \propto 1/\kappa_{mn}a$ will be introduced as the 'scaled' directivity $d_m(\phi,ka)$. The scaled directivity function $|d_m(\phi,ka)|^2$ is not sensitive to n providing the mode is sufficiently cut-off, $\zeta_{mn} \to 0$, as demonstrated by *figure 3.4*. The function $d_m(\phi,ka)$ is evaluated from *Eq. 4.84* using any sufficiently cut-off mode, which *Chapter 3* identified $\zeta_{mn} \lesssim 0.5$. The scaled directivity is of the form,

$$d_m(\phi,ka) = D_{mn}(\phi,ka)\,\sqrt{\kappa_{mn}a} \quad \text{as} \quad \zeta_{mn} \to 0. \tag{4.84}$$

Substituting *Eq. 4.84* into *Eq. 4.83* gives,

$$\overline{p^2}^{(D)}_{\text{cut-off}}(R,\phi,\omega) = \left(\frac{a}{R}\right)^2 \overline{F^2}(\omega) \sum_{(m,n)\notin\{\mathcal{M},\mathcal{N}\}} |d_m(\phi,ka)|^2 \frac{1}{\kappa_{mn}a}, \tag{4.85}$$

For sufficiently cut-off modes at a given frequency, $\kappa_{mn} \to \infty$, $\kappa_{mn}a$ can be representing the solution to $J'_m(\kappa_{mn}a) = 0$, can be approximated as,

$$\kappa_{mn}a \approx (n + \frac{1}{2}m - \frac{3}{4})\pi, \quad \kappa_{mn}a \to \infty, \tag{4.86}$$

from Rienstra and Hirschberg (2004). Substituting the approximation for $\kappa_{mn}a$ of *Eq. 4.86* into *Eq. 4.85* reveals that,

$$\overline{p^2}^{(D)}_{\text{cut-off}}(R,\phi,\omega) = \left(\frac{a}{R}\right)^2 \overline{F^2}(\omega) \sum_{(m,n)\notin\{\mathcal{M},\mathcal{N}\}} |d_m(\phi,ka)|^2 \frac{1}{(n+\frac{1}{2}m-\frac{3}{4})\pi}, \tag{4.87}$$

Equation 4.87 suggests that for any fixed value of m, the summation over n diverges as,

$$\sum_{n=n^*}^{\infty} \frac{1}{n} \to \infty, \tag{4.88}$$

where the lower limit of the summation of cut-off modes is taken such that $n^* >> m$. This implies that the contribution of cut-off modes to the directivity $Q(\phi,ka)$ and consequently the mean square pressure $\overline{p^2}^{(D)}(R,\phi,\omega)$ is infinite. Whilst $\overline{p^2}^{(D)}(R,\phi,\omega) \to \infty$ for $z_0/\lambda = 0$, it will be shown that $Q(\phi,ka)$ converges.

Substituting *Eq. 4.87* and *Eq. 4.80* into the directivity $Q(\phi,ka)$ of *Eq. 4.79*, shows that,

$$Q(\phi,ka) \approx \frac{\sum_{m=-m^*}^{m^*} |d_m(\phi,ka)|^2}{\frac{1}{2}\int_0^{\pi} \sum_{m=-m^*}^{m^*} |d_m(\phi,ka)|^2 \sin\phi d\phi}, \tag{4.89}$$

where m^* denotes the maximum value of the modal index m that contributes significantly to the far-field radiation. *Figure 4.9* shows the cumulative sum of $Q(\phi,ka)$ obtained from *Eq. 4.89*, calculated for a cumulative sum of azimuthal modes plotted against m^*/ka, at two non-dimensional frequencies ka = 5 and 35 and two representative rear-arc angles of $\phi = 120^\circ$ and $\phi = 150^\circ$. Note that $d_m(\phi,ka)$ was evaluated for all azimuthal modes with an arbitrary radial order $n = 250$.

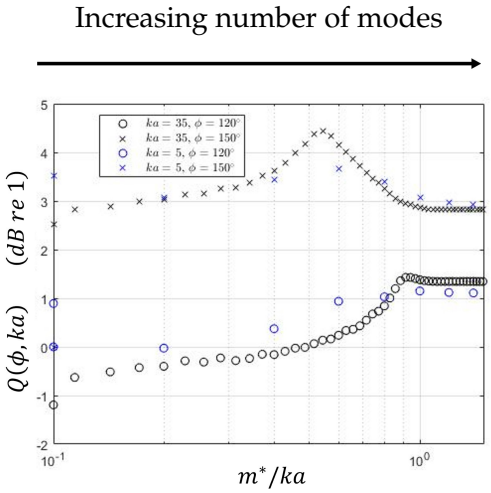

FIGURE 4.9: Directivity $Q(\phi, ka)$ for a distribution of incoherent axial dipole sources at two rear angles $\phi = 120°$ and $150°$ and at two non-dimensional frequencies $ka = 5$ and 35, plotted against m^*/ka.

Convergence of $Q(\phi, ka)$ in *figure 4.9* is achieved by the inclusion of all azimuthal modes with $m < ka$. This is likely due to the relatively low radiation efficiency of modes excited in that region as discussed in *Chapter 3*.

Figure 4.10 shows plots of the directivity computed using *Eq. 4.89* at ka = 5, 20 and 35. Also shown is an empirical approximate result that matches the solution given by $Q(\phi, ka) = 2\sin^2(\phi/2)$, where close agreement to the exact solution can be observed.

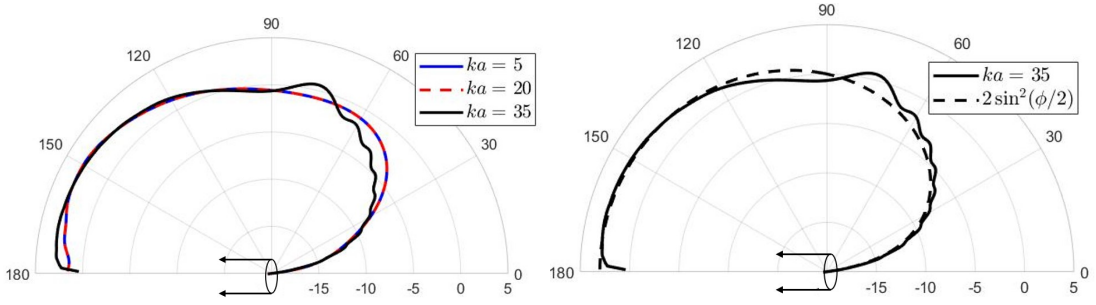

(A) $ka = 5, 20$ and 35 (B) $ka = 35$ and $2\sin^2(\phi/2)$

FIGURE 4.10: Normalized directivity for a distribution of incoherent axial dipole sources exactly at the duct open end at $z_0/\lambda = 0$, in dB.

One interpretation of the solutions shown in *figure 4.10* is that cut-off modes behave as edge scattering, which from Ffowcs Williams and Hawkings (1969) has directivity $\propto \sin^2 \phi/2$ and is the solution to Laplace's equation for in-compressible flow due to a sharp edge. Given that cut-off modes radiate most strongly in the rear-arc, it is unsurprising that in this limit the rear-arc radiation is highest.

4.3.3.2 Rotating point dipole sources

The previous section has demonstrated that for incoherent axial dipole source distributions exactly at the open end of semi-infinite ducts, all cut-off modes significantly contribute to the far-field radiation. The asymptotic behavior was investigated to predict the radiated field for this case, using asymptotic relationships such as those for the radial wavenumber κ_{mn} (*Eq. 4.86*) and the scaled directivity $d_m(\phi, ka)$ (*Eq. 4.84*). This section performs the same analysis for rotating point dipole sources, also at the open end of semi-infinite ducts.

Consider rotating point dipole sources at the open end $z_0/\lambda = 0$ of a semi-infinite duct. The pressure of the cut-off modes $\overline{p^2}^{(D)}_{\text{cut-off}}(R, \phi, \omega)$ of *Eq. 4.81*, is formed by substituting the modal amplitude of *Eq. 4.60* and is of the form,

$$\overline{p^2}^{(D)}_{\text{cut-off}}(R, \phi, \omega) = \left(\frac{a}{R}\frac{1}{2S}\right)^2 \overline{f^2} \sum_{m=-\infty}^{\infty} \left| \sum_{n=n^*(m)}^{\infty} \frac{J_m(\kappa_{mn} r_0)}{J_m(\kappa_{mn} a)} \frac{1}{\sqrt{1 - \frac{m^2}{(\kappa_{mn} a)^2}}} D_{mn}(\phi, ka) \frac{1}{k_{z,mn} a} \left(\frac{a}{r_0} m \sin\gamma + k_{z,mn} a \cos\gamma\right) \right|^2, \tag{4.90}$$

where $n^*(m)$ is the radial mode or lowest order that is cut-off for each azimuthal order m. For sufficiently cut-off modes, the Bessel function can be approximated by it's large argument approximation,

$$J_m(\Theta) \approx \left(\frac{\pi}{2}\Theta\right)^{-\frac{1}{2}} \cos(\Theta - \frac{1}{2} m\pi - \frac{1}{4}\pi), \tag{4.91}$$

from Rienstra and Hirschberg (2004). Substituting *Eq. 4.91* into *Eq. 4.90* shows that the pressure is of the form,

$$\overline{p^2}^{(D)}_{\text{cut-off}}(R, \phi, \omega) = \left(\frac{a}{R}\frac{1}{2S}\right)^2 \frac{a}{r_0}\overline{f^2} \sum_{m=-\infty}^{\infty} \left| \sum_{n=n^*(m)}^{\infty} \frac{\cos(\kappa_{mn} r_0 - \frac{1}{2} m\pi - \frac{1}{4}\pi)}{\cos(\kappa_{mn} a - \frac{1}{2} m\pi - \frac{1}{4}\pi)} \frac{1}{\sqrt{1 - \frac{m^2}{(\kappa_{mn} a)^2}}} D_{mn}(\phi, ka) \frac{1}{k_{z,mn} a} \left(\frac{a}{r_0} m \sin\gamma + k_{z,mn} a \cos\gamma\right) \right|^2, \tag{4.92}$$

Similar to the distributions of incoherent axial dipole sources, the scaled directivity, $d_m(\phi, ka)$ is introduced, substituting *Eq. 4.84* into *Eq. 4.92*, gives,

$$\overline{p^2}_{\text{cut-off}}(R,\phi,\omega) = \left(\frac{a}{R}\frac{1}{2S}\right)^2 \frac{a}{r_0}\overline{f^2} \sum_{m=-\infty}^{\infty} |d_m(\phi,ka)|^2 \left| \sum_{n=n^*(m)}^{\infty} \frac{\cos(\kappa_{mn} r_0 - \frac{1}{2}m\pi - \frac{1}{4}\pi)}{\cos(\kappa_{mn} a - \frac{1}{2}m\pi - \frac{1}{4}\pi)} \frac{1}{\sqrt{1-\frac{m^2}{(\kappa_{mn}a)^2}}} \frac{1}{\sqrt{\kappa_{mn}a}} \frac{1}{k_{z,mn}a} \left(\frac{a}{r_0} m \sin\gamma + k_{z,mn} a \cos\gamma\right) \right|^2, \tag{4.93}$$

From the dispersion relationship of *Eq. 2.10*, for sufficiently cut-off modes, $ka << \kappa_{mn}a$ the radial and axial wavenumber $k_{z,mn}$ are related by,

$$k_{z,mn} = j\kappa_{mn}, \qquad ka/\kappa_{mn}a \to 0. \tag{4.94}$$

Substituting *Eq. 4.94* into *Eq. 4.93*,

$$\overline{p^2}^{(D)}_{\text{cut-off}}(R,\phi,\omega) = \left(\frac{a}{R}\frac{1}{2S}\right)^2 \frac{a}{r_0}\overline{f^2} \sum_{m=-\infty}^{\infty} |d_m(\phi,ka)|^2 \left| \sum_{n=n^*(m)}^{\infty} \frac{\cos(\kappa_{mn} r_0 - \frac{1}{2}m\pi - \frac{1}{4}\pi)}{\cos(\kappa_{mn} a - \frac{1}{2}m\pi - \frac{1}{4}\pi)} \frac{1}{\sqrt{(\kappa_{mn}a)^2 - m^2}} \frac{1}{\sqrt{\kappa_{mn}a}} \left(\frac{a}{r_0} m \sin\gamma + j\kappa_{mn} a \cos\gamma\right) \right|^2, \tag{4.95}$$

For sufficiently cut-off modes, the radial wavenumber κ_{mn} can be approximated using *Eq. 4.86*, which after substituting for $\kappa_{mn}a$, *Eq. 4.95* becomes,

$$\overline{p^2}^{(D)}_{\text{cut-off}}(R,\phi,\omega) = \left(\frac{a}{R}\frac{1}{2S}\right)^2 \frac{a}{r_0}\overline{f^2} \sum_{m=-\infty}^{\infty} |d_m(\phi,ka)|^2 \left| \sum_{n=n^*(m)}^{\infty} \frac{\cos\left((n+\frac{1}{2}m-\frac{3}{4})\pi\frac{r_0}{a} - \frac{1}{2}m\pi - \frac{1}{4}\pi\right)}{\cos\left((n-1)\pi\right)} \frac{1}{\sqrt{\left((n+\frac{1}{2}m-\frac{3}{4})\,\pi\right)^2 - m^2}} \frac{1}{\sqrt{(n+\frac{1}{2}m-\frac{3}{4})\pi}} \left(\frac{a}{r_0} m \sin\gamma + j(n+\frac{1}{2}m-\frac{3}{4})\pi a \cos\gamma\right) \right|^2. \tag{4.96}$$

For radii of rotation not on the duct axis or at the wall, $0 < r_0/a < 1$, the two cosine terms in *Eq. 4.96* causes a periodicity with increasing the number of cut-off modes. These oscillations were shown in *figure 4.8* for the $r_0/a = 0.5$. Now consider dipole sources at the rim of the duct $(r_0/a, z_0/\lambda) = (1, 0)$, *Eq. 4.96* can be written,

$$\overline{p^2}^{(D)}_{\text{cut-off}}(R,\phi,\omega) = \left(\frac{a}{R}\frac{1}{2S}\right)^2 \overline{f^2} \sum_{m=-\infty}^{\infty} |d_m(\phi,ka)|^2 \left| \sum_{n=n^*(m)}^{\infty} \frac{1}{\sqrt{\left(\left(n+\frac{1}{2}m-\frac{3}{4}\right)\pi\right)^2 - m^2}} \right.$$
$$\left. \frac{1}{\sqrt{(n+\frac{1}{2}m-\frac{3}{4})\pi}} \left(m\sin\gamma + j\left(n+\frac{1}{2}m-\frac{3}{4}\right)\pi\cos\gamma \right) \right|^2, \tag{4.97}$$

Assuming a fixed value of m, such that the assumption $n >> m$ and $n \to \infty$ is met, *Eq. 4.97* for the dipole orientations $\gamma < 90^\circ$ is of the form,

$$\overline{p^2}^{(D)}_{\text{cut-off}}(R,\phi,\omega) = \left(\frac{a}{R}\frac{1}{2S}\cos\gamma\right)^2 \frac{1}{\pi}\overline{f^2} \sum_{m=-\infty}^{\infty} |d_m(\phi,ka)|^2 \left(\sum_{n=n^*(m)}^{\infty} \frac{1}{\sqrt{n}} \right)^2, \quad \gamma < 90^\circ \tag{4.98}$$

which tends to,

$$\overline{p^2}^{(D)}_{\text{cut-off}}(R,\phi,\omega) = \left(\frac{a}{R}\frac{1}{2S}\right)^2 \frac{1}{\pi^3}\overline{f^2} \sum_{m=-\infty}^{\infty} |d_m(\phi,ka)|^2 m^2 \left(\sum_{n=n^*(m)}^{\infty} \frac{1}{n^{\frac{3}{2}}} \right)^2, \quad \text{as } \gamma \to 90^\circ, \tag{4.99}$$

Both *Eq. 4.98* and *Eq. 4.99* lead to the conclusion that the contribution of cut-off modes to the directivity $Q(\phi,ka)$ leads to infinitely high pressure, and hence can be described by *Eq. 4.87*. Point sources rotating at the wall of the duct $r_0/a = 1$ at the open end $z_0/\lambda = 0$ radiate identically to incoherent distributions of axial dipoles sources, which gives the directivity shown in *figure 4.10*.

4.3.3.3 Point sources on the duct axis

Finally, this section predicts the radiation of point dipole sources on the duct axis at the open end $(r_0/a, z_0/\lambda) = (0,0)$ of a semi-infinite duct using asymptotic analysis discussed previously. Substituting the modal amplitude of *Eq. 4.61* into *Eq. 4.81* and setting $r_0/a = 0$ and $z_0/\lambda = 0$ gives,

$$\overline{p^2}^{(D)}_{\text{cut-off}}(R,\phi,\omega) = \left(\frac{1}{2S}\frac{a}{R}\right)^2 \overline{f^2}\cos^2\gamma \left| \sum_{(0,n)\notin\{0,\mathcal{N}\}} D_{mn}(\phi,ka)\frac{1}{J_0(\kappa_{0n}a)} \right|^2, \quad m = 0. \tag{4.100}$$

Substituting the scaled directivity $d_m(\phi,ka)$, of *Eq. 4.84* into *Eq. 4.100* gives,

$$\overline{p^2}^{(D)}_{\text{cut-off}}(R,\phi,\omega) \approx \left(\frac{1}{2S}\frac{a}{R}\right)^2 \overline{f^2}\cos^2\gamma\,|d_m(\phi,ka)|^2 \left(\sum_{(m,n)\notin\{0,\mathcal{N}\}} \frac{1}{J_0(\kappa_{0n}a)}\frac{1}{\sqrt{\kappa_{0n}a}}\right)^2, \quad m=0 \tag{4.101}$$

Assuming $\kappa_{mn}a \to \infty$, the Bessel function can be approximated by its large argument approximation. Substituting *Eq. 4.91* into *Eq. 4.101* shows that the pressure is of the form,

$$\overline{p^2}^{(D)}_{\text{cut-off}}(R,\phi,\omega) \approx \left(\frac{1}{2S}\frac{a}{R}\right)^2 \frac{\pi}{2}\overline{f^2}\cos^2\gamma\,|d_m(\phi,ka)|^2 \left(\sum_{(m,n)\notin\{0,\mathcal{N}\}} \frac{1}{\cos(\kappa_{0n}a-\frac{1}{4}\pi)}\right)^2, \quad m=0 \tag{4.102}$$

The large argument approximation of *Eq. 4.86* is substituted into *Eq. 4.102* to give,

$$\overline{p^2}^{(D)}_{\text{cut-off}}(R,\phi,\theta) = \left(\frac{1}{2S}\frac{a}{R}\right)^2 \frac{\pi}{2}\overline{f^2}\cos^2\gamma\,|d_m(\phi,ka)|^2 \left(\sum_{(m,n)\notin\{0,\mathcal{N}\}} \frac{1}{\cos\left((n-1)\pi\right)}\right)^2, \quad m=0 \tag{4.103}$$

The term $\cos\left((n-1)\pi\right)$ alternates between -1 and 1 for odd and even n respectively. This behavior can be observed in *figure 4.8* for the $r_0/a = 0$ case, as a relatively large order mode is shown to have the same contribution as a relatively low order mode, with each mode of adjacent radial order appearing with opposite sign.

This section has used asymptotic relationships to predict the behavior of the far-field radiation of axial dipole sources located at the duct open end. It has been shown that for incoherent distributions and rotating point sources at the duct rim, all cut-off modes cause $\overline{p^2}^{(D)}(R,\phi,\theta)$ to become infinitely large. For rotating sources not at the duct wall an expression has been derived that identifies periodicity with respect to increasing the number of cut-off modes in predictions $\overline{p^2}^{(D)}(R,\phi,\theta)$.

4.3.4 Convergence behavior for dipole sources near the open end of semi-infinite ducts

The remainder of this thesis considers sources located a small distance from the duct open end, to avoid the divergence behavior associated with dipole sources at $z_0/\lambda = 0$, discussed in detail in *section 4.3.3*. The sensitivity to z_0/λ is investigated in the next section.

The convergence study first shown in *Section 4.3.2* for dipole sources is now repeated considering a source location of $z_0/\lambda = 0.01$. *Figure 4.11* shows a plot of the cumulative radiated far-field mean square pressure $\overline{p^2}^{(D)}(R, \phi, \omega)$ for distributions of incoherent axial dipole sources with the same parameters as in *figure 4.7*.

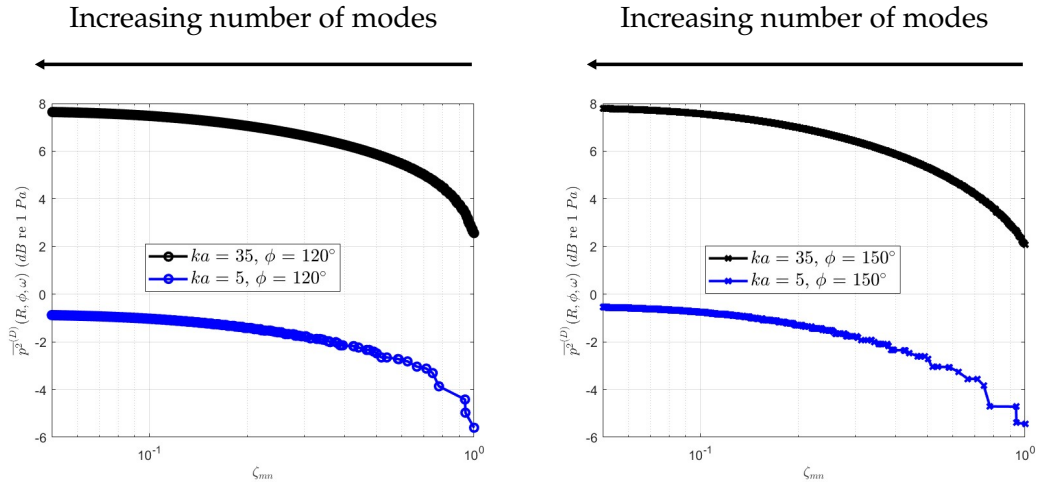

(A) $\phi = 120°$ (B) $\phi = 150°$

FIGURE 4.11: Radiated mean square pressure $\overline{p^2}^{(D)}(R, \phi, \omega)$, for a source plane a short distance inside a semi-infinite duct $z_0/\lambda = 0.01$ at two non-dimensional frequencies $ka = 5$ and 35, for a varying number of cut-off modes.

The solution for incoherent dipole sources can be observed to plateau faster for $z_0/\lambda = 0.01$ shown in *figure 4.11* than for $z_0/\lambda = 0.01$ *figure 4.7* but there is no certainty of convergence for this case by the inclusion of even more cut-off modes. For the remainder of this thesis all modes with $\zeta_{mn} > 0.05$ are included for the distributions of dipole source calculations, where *figure 4.7 implies* convergence is likely achieved to within at least 0.5 dB.

A convergence criteria is now established for rotating point dipole source a short distance inside a semi-infinite duct $z_0/\lambda = 0.01$. *Figure 4.12* shows a plot of the radiated pressure field $\overline{p^2}^{(D)}(R, \phi, \omega)$ for rotating point dipole sources just inside a semi-infinite duct plotted against ζ_{mn}. The remaining parameters are the same as in *figure 4.8*.

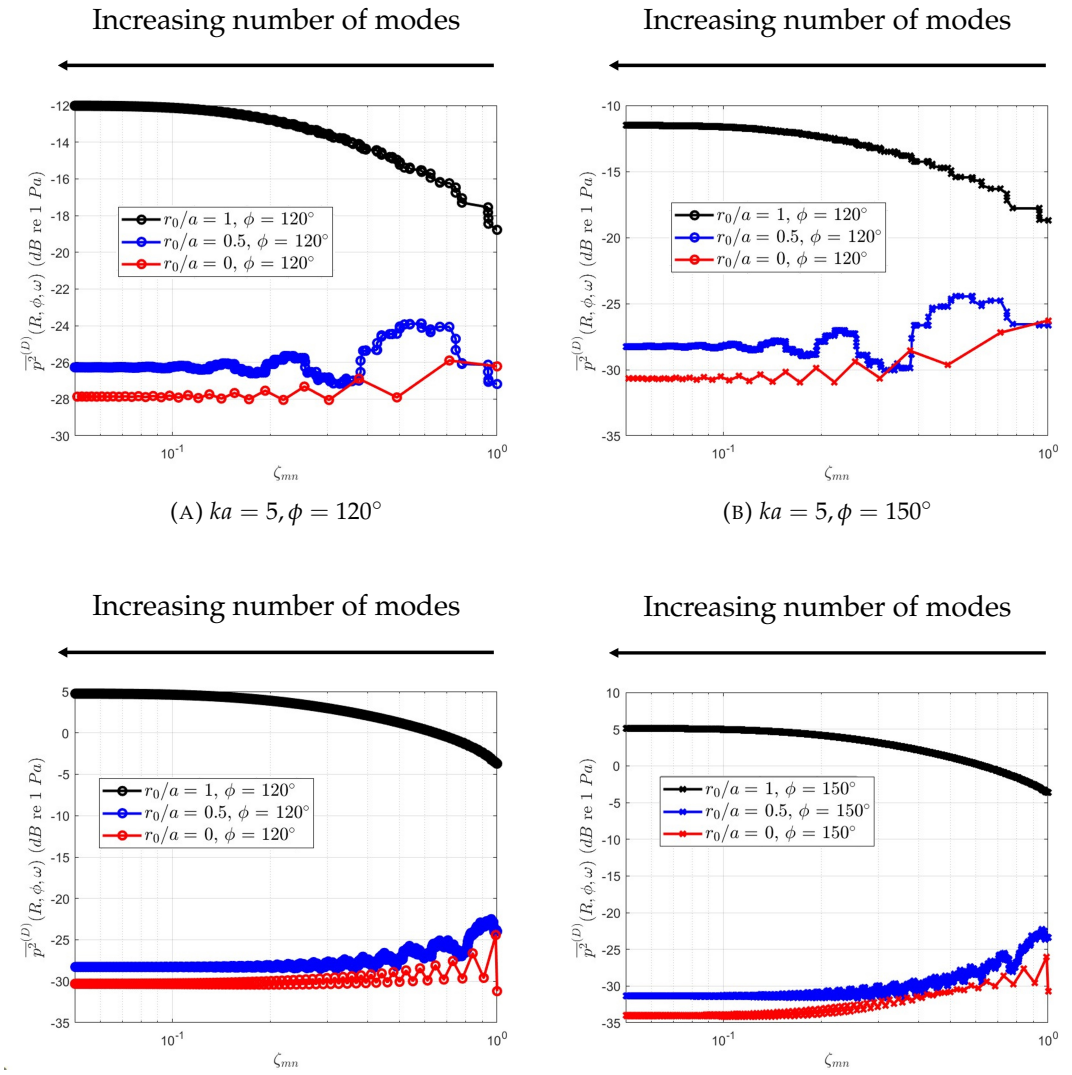

(A) $ka = 5, \phi = 120°$ (B) $ka = 5, \phi = 150°$

(C) $ka = 35, \phi = 120°$ (D) $ka = 35, \phi = 150°$

FIGURE 4.12: Radiated mean square pressure $\overline{p^2}^{(D)}(R,\phi,\omega)$, for rotating point dipole sources at three radii of rotation $r_0/a = 0.0, 0.5$ and 1.0 near the open end of a semi-infinite duct $z_0/\lambda = 0.01$, for a varying number of cut-off modes.

For rotating point dipole sources, convergence to within 0.5 dB is achieved by including modes with cut-off ratio $\zeta_{mn} > 0.2$ for all cases investigated in *figure 4.12*. For the higher frequency corresponding to $ka = 35$, this amounts to almost 100 times more cut-off modes than cut-on modes.

This section has shown that by considering dipole sources a short way inside a semi-infinite duct, a finite number of cut-off modes significantly radiate to the far-field. For the proceeding chapters of this thesis the source location will be limited to a minimum distance of 0.01λ inside the duct.

4.4 Sensitivity of sources to the axial location near the open end of ducts

The remainder of this thesis considers sources *near* the open end of the duct such that the source plane axial location investigated is $z_0/\lambda \to 0$. This section investigates the sensitivity of the radiation from sources inside ducts as they approach the open end.

Figure 4.13 shows the total mean square pressure from a semi-infinite duct, $\overline{p^2}^{(D)}(R, \phi, \omega)$, relative to the pressure due to the inclusion of the cut-on modes $\overline{p^2}^{(D)}_{\text{cut-on}}(R, \phi, \omega)$ only. Results are shown for distributions of incoherent axial dipole and monopole sources plotted against z_0/λ, at the polar angle $\phi = 150°$. The remaining parameters are the same as in *figure 4.7* and *figure 4.5* for the dipole and monopole sources respectively.

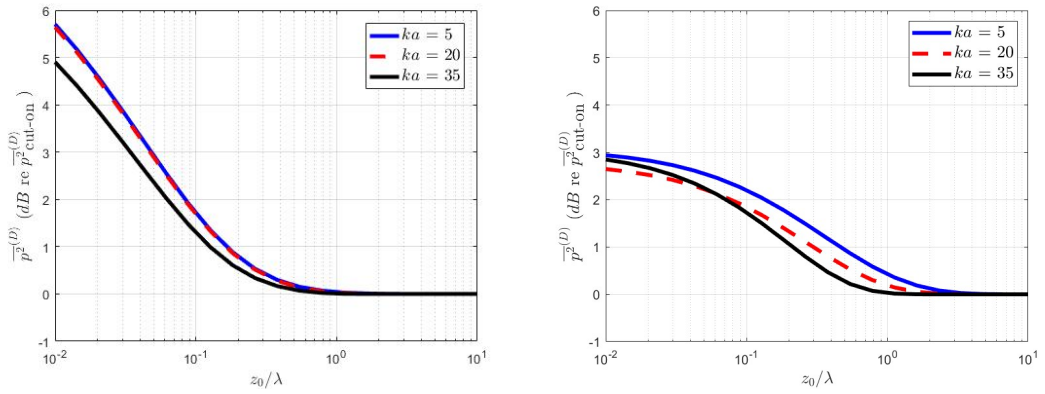

(A) Distribution of incoherent axial dipole sources

(B) Distribution of incoherent monopole sources

FIGURE 4.13: Radiated mean square pressure $\overline{p^2}^{(D)}(R, \phi, \omega)$, at two non-dimensional frequencies $ka = 5$ and 35 and far-field angle $\phi = 150°$ plotted against axial distance from the open end of a semi-infinite duct z_0/λ.

Two distinct regions can be identified in *figure 4.13*. Firstly as the source moves deeper inside the duct $z_0/\lambda \to \infty$, cut-off modes have negligible effect on the radiation. As the source is brought closer to the duct open end $z_0/\lambda \to 0$, cut-off modes are shown to radiate significantly at $\phi = 150°$, tending to infinity for dipole sources.

There is a critical distance above which the cut-off modes have negligible effect, this can be seen to be approximately $z_0/\lambda \gtrsim 1$. For monopole sources, increases in ducted radiation due to cut-off modes is observed to be less than 1 dB for sources located $z_0/\lambda > 0.5$ for the parameters investigated. For dipole sources, the range of z_0/λ for which cut-off modes are shown to increase the ducted radiation by less than 1 dB is $z_0/\lambda > 0.2$. Cut-off modes can be assumed to radiate more strongly due to monopole sources than dipole sources when sources are moderately close to the open end $1 < z_0/\lambda < 0.2$.

For the incoherent distribution of axial dipole sources, shown in *figure 4.13a*, the pressure radiated by the cut-off modes is shown to increase exponentially with reducing z_0/λ at a rate of approximately 1 dB for each halving of the axial distance between the source and the duct open end, for $z_0/\lambda < 0.1$. Furthermore this behavior has a low sensitivity to the excitation frequency, where the radiation for $ka = 20$ and 35 are almost indistinguishable. This finding suggests that source distance to the open end z_0 relative the λ is the key parameter in determining far-field radiation.

Clearly this divergence behavior for dipole sources is unrealistic. One possible explanation for this behavior is that for a source axial plane at the open end of the duct $z_0/\lambda = 0$, the boundary condition may not be properly defined. Approaching the open end of the duct z_0 from outside the duct (the right hand side of *figs 4.3* and *4.4*) implies the source is bounded by free-field. However, approaching z_0 from inside the duct (from the the left hand side in *figs 4.3* and *4.4*) implies a hard-walled boundary. The discontinuity therefore is associated with the assumption that the source can be located at a single axial plane z_0. A physical interpretation for this behavior associated with a point source is proposed in *Section 7.2.2*

Chapter 5

Comparison between free-field and semi-infinite ducted radiation

In this chapter the multi-modal acoustic radiation, apparent from a sum of cut-on and cut-off modes, is investigated and compared to the radiation from equivalent free-field sources. In *Chapter 3* a single cut-off mode was studied to identify several physical characteristics. In most practical situations many modes are excited simultaneously. This chapter considers the radiation from four source types:

1. Incoherent distribution of axial dipole sources.
2. Incoherent distribution of monopole sources.
3. Rotating point dipole sources.
4. Rotating point monopole sources.

which are investigated for varying axial locations including source locations close to the duct open end. Additionally, for the rotating sources, the radius of rotation is investigated, and for the point dipole, the dipole orientation between the axial and azimuthal directions is investigated. Before a full comparison of the radiated pressure fields are investigated, this chapter features a discussion on nil-shielding directions. First discovered by Chapman (1996) nil-shielding directions are particular far-field angles where free-field and ducted radiation equate for all sources.

The final part of this section investigates the differences in acoustic sound power radiated from free-field and ducted sources, to document the effect on the radiated power by shrouding a free-field source in a duct.

5.1 Nil-shielding directions

This section investigates the nil-shielding directions first discovered by Chapman (1996) and are defined,

$$\sin\phi_{mn} = \frac{\kappa_{mn}}{k}. \tag{5.1}$$

To identify the behavior of the directivity function at nil-shielding direction, *figure 5.1* compares the directivity factors computed using the un-flanged $D_{mn}(\phi, ka)$ and flanged $D_{F,mn}(\phi, ka)$ solutions of *Eq. 2.52* and *2.38* for a typical mode of azimuthal order $m = 9$ and radial order $n = 6$. Results are shown at two different frequencies representing cut-off ratios of $\zeta_{mn} = 1.5$ and 1.01 corresponding to a well cut-on mode and a mode just cut-on respectively.

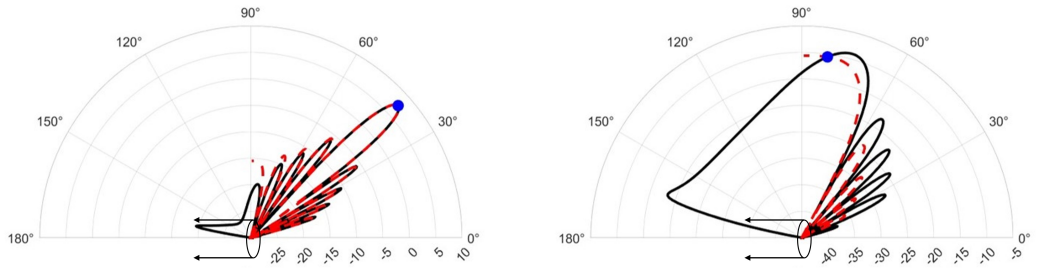

(A) $\zeta_{mn} = 1.50$ (B) $\zeta_{mn} = 1.01$

FIGURE 5.1: Far-field modal directivity factor for mode $(m,n) = (9,6)$ at two frequencies $\zeta_{mn} = 1.5$ and 1.01, computed using the un-flanged (solid black line) and the flanged directivity (red dashed line) factor. The nil-shielding direction is shown (blue circles). In dB re 1.

An intriguing observation from *figure 5.1*, commented on by Chapman (1996) but without providing examples, is that both flanged and un-flanged solutions agree exactly at nil-shielding direction, $D_{mn}(\phi_{mn}, ka) = D_{F,mn}(\phi_{mn}, \omega)$. For this angle therefore, the relatively complicated un-flanged directivity expression of *Eq. 2.52* may be replaced with the relatively simple flanged equivalent expression of *Eq. 2.38*.

The existence of nil-shielding directions is readily demonstrated from the flanged case by evaluating $p_{F,mn}(R, \phi, \theta, ka)$ of *Eq. 2.37* at $\phi = \phi_{mn}$ by the use of L'Hôpital's rule, for any of the source amplitudes previously discussed, but shown here for a point rotating dipole source. Substituting the modal amplitude of *Eq. 4.59* and the flanged directivity at the mode ray angles of *Eq. 2.40* into *Eq. 4.62* shows,

$$p_{F,mn}^{(D)}(R,\phi_{mn},\theta,\omega) = j^{m-1}\left(\frac{1}{4\pi R}\right)\left[\frac{m}{r_0}\sin\gamma + k\cos\phi_{mn}\cos\gamma f(\omega - m\Omega)\right.$$
$$\left. J_m(kr_0\sin\phi_{mn})\mathrm{e}^{-jk(R-z_0\cos\phi_{mn})-jm(\theta-\tilde{\theta}_0)}\right]. \tag{5.2}$$

This expression is identical to *Eq. 4.22* for the far-field pressure due to rotating dipole sources in free-field. Noting the result from *figure 5.1*, where it is shown $D_{F,mn}(\phi_{mn},ka) \approx D_{mn}(\phi_{mn},ka)$ and comparison of *Eq. 5.2* and *Eq. 4.22*, at these mode ray angles the rigid duct is effectively transparent to sound, i.e. $p_{mn}^{(D)}(R,\phi_{mn},\theta,\omega) = p_m^{(ff)}(R,\phi_{mn},\theta,\omega)$.

This property was first recognised and proven by Chapman (1996) who also stated that this behaviour was 'strikingly evident' from the predictions for free-field and ducted source radiation in Myers and Lan (1993). Attempts at proving the agreement between the expression for $p_m^{(ff)}(R,\phi_{mn},\theta,\omega)$ and $p_m^{(D)}(R,\phi_{mn},\theta,\omega)$ at $\phi = \phi_{mn}$ involving the un-flanged directivity expression of *Eq. 2.52* have been unsuccessful owing to the complexity of the Kernel function K.

5.1.1 Far-field directivities for single azimuthal modes due to sources deep inside the semi-infinite ducts

In the previous section, the characteristics of the far-field radiation for single acoustic duct modes have been shown which has verified the existence of nil-shielding directions, where they are in agreement with the free-field value.

Before comparing the directivities due to free-field and ducted sources for calculations involving multiple azimuthal m mode orders, directivities for some idealised cases involving only a single azimuthal mode order m are compared to highlight more clearly the role of nil-shielding directions in determining the overall directivity in the forward arc. The directivities between free-field and ducted sources is now investigated for a single azimuthal mode order m when the source plane is $z_0/\lambda = 5$ is now, i.e. well away from the duct open end such that cut-off modes can be neglected. Analysis is shown for rotating point dipole sources, however the behaviors discussed can be observed from all source types discussed.

Figure 5.2 shows a comparison between the free-field and ducted directivities for the single azimuthal mode $m = 0$ excited at $ka = 5$ and 35 respectively. The radius of rotation and dipole orientation are arbitrarily chosen to be $r_0/a = 0.5$ and $\gamma = 0°$ respectively. The source strength $f(\omega)$ and far-field observer distance R, throughout this section are taken to be unity. The nil-shielding directions at each constituent radial mode are represented by the blue circles.

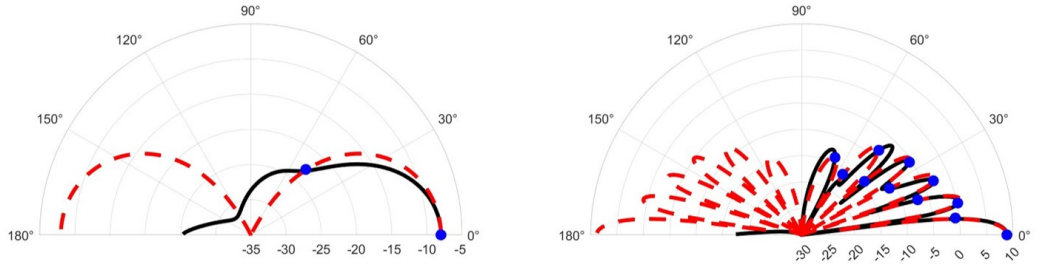

(A) $ka = 5$ (B) $ka = 35$

FIGURE 5.2: Free-field (red dashed line) and ducted (solid black line) directivity for rotating point dipole sources at a single azimuthal order $m = 0$ at two non-dimensional frequencies $ka = 5$ and 35, shown for a source radius of rotation $r_0/a = 0.5$, axial location, $z_0/\lambda = 5$ and dipole orientation $\gamma = 0°$. The nil-shielding directions are shown (blue circles). In dB re 1 Pa.

The important feature of *figure 5.2* is that, even when multiple radial modes are present with the same m value, very close agreement is observed between the un-flanged ducted solution and the free-field solution at the nil-shielding directions ϕ_{mn} (indicated by the blue circles in the figure). Clearly, therefore, the presence of additional radial modes do not disrupt the agreement between the two solutions at the nil-shielding directions.

This property was recognised by Chapman (1996) which he attributed to the 'interlacing' property of the Bessel function. Analysis of this property is presented in *Chapter 3* where single duct modes are considered. The interlacing property of the directivity function may be stated as,

$$\begin{aligned} D_{F,mn'}(\phi_{mn}, ka) &= 0, \qquad & n \neq n', \quad \forall ka \\ D_{F,mn'}(\phi_{mn}, ka) &\neq 0, \qquad & n = n', \quad ka < \kappa_{mn}a \end{aligned} \tag{5.3}$$

In *figure 5.2a* where $ka = 5$ and $m = 0$, only the plane wave and the $(m, n) = (0, 2)$ mode are cut-on, and hence only two nil-shielding directions occur at which the solutions can be observed to exactly match, with the former having $\phi_{mn} = 0°$. Deviations between the solutions of up to 2 dB can be observed at angles away from the nil-shielding directions.

At the much higher non-dimensional frequency of $ka = 35$, many more radial modes and hence nil-shielding directions therefore match, not only at the nil-shielding directions, but are also in close agreement at angles in-between. Naturally there is no agreement in the rear-arc $90° < \phi < 180°$ which is shielded by the duct unlike in free-field, which exhibits forward and rear-arc symmetry about $\phi = 90°$ in this example with $\gamma = 0°$ (axial dipole).

5.1.2 Far-field directivities for single azimuthal modes due to sources at the open end of semi-infinite ducts

As the source plane approaches the duct open end the contribution from cut-off modes become increasingly important to the far-field radiation. To illustrate the importance of the location of the source plane, *figure 5.3* shows the directivity when the source plane is now located approximately at the duct open end $z_0/\lambda = 0.01$ and $ka = 5$ for single azimuthal modes $m = 0, 1, 2$ and 3 respectively. Note the source cannot be located exactly at $z_0/\lambda = 0$, as is shown in *Chapter 4*, where the number of contributing cut-off modes to the far-field radiation is shown to be infinite. The free-field directivity for these modes is also shown. In each figure the directivity due to the ducted radiation is further broken into their contribution from cut-on modes and cut-off modes. The remaining parameters are the same as in *figure 5.2a*.

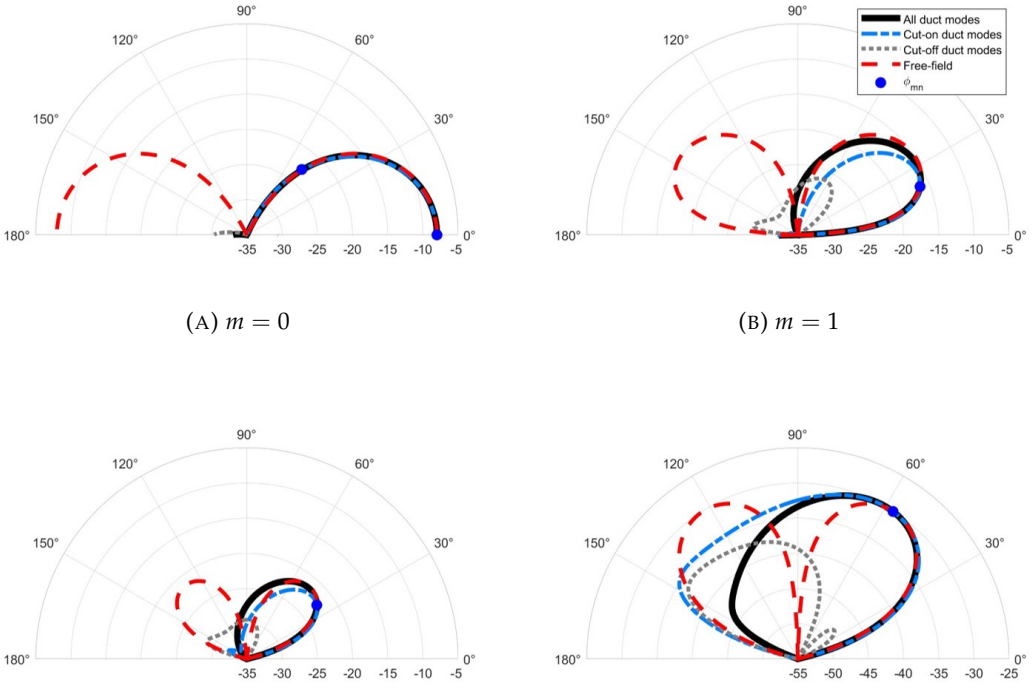

(A) $m = 0$ (B) $m = 1$

(C) $m = 2$ (D) $m = 3$

FIGURE 5.3: Free-field and ducted directivities for rotating point dipole sources at a single azimuthal order $m = 0, 1, 2$ and 3 at the non-dimensional frequency $ka = 5$. Shown for a source radius of rotation $r_0/a = 0.5$, dipole orientation $\gamma = 0°$ and axial location $z_0/\lambda = 0.01$. The contribution of cut-on and cut-off modes are highlighted and the nil-shielding directions are shown (blue circles). In dB re 1 Pa.

For the zero order mode, $m = 0$, only two radial modes are cut-on at this frequency whose nil-shielding directions can be seen at exactly $\phi_{mn} = 0°$ and approximately $\phi_{mn} = 50°$, where excellent agreement is obtained between the free-field and ducted solutions, not only at these angle, but at all angles in the forward-arc. Note that in this case there is negligible contribution from cut-off modes.

For the higher order mode $m = 1$, excellent agreement is limited to angles less than the first nil-shielding direction of $\phi_{mn} \approx 20^\circ$. Note that at this range of angles the contribution from cut-on modes is dominant. At angles greater than $\phi \approx 20^\circ$ the agreement between the free-field and ducted solution is less good but remains within 2 dB at all angles up to $\phi \approx 120^\circ$, which can be seen to be attributed to the presence of cut-off modes.

For azimuthal modes $m = 2$ and $m = 3$, good levels of agreement (less than 1 dB) persist at all angles up to approximately the first nil-shielding directions of $\phi_{mn} \approx 37^\circ$ and $\phi_{mn} \approx 57^\circ$ respectively, although the level of agreement can be seen to degrade with increasing m. At the higher angles, generally poor levels of agreement between the free-field and ducted solutions are observed, the contribution from cut-off modes becomes progressively weaker since their radiation efficiency has been shown to vary as $(ka)^{2m+2}$, c.f. *Chapter 3*. In summary, therefore, generally good agreement is observed in all cases for radiation angles close to the duct axis but the agreement is worse towards the sideline directions.

Significant deviations between the free-field and ducted directivities were observed in *figure 5.2a* at the comparatively low frequency of $ka = 5$ when the source plane was many wavelengths ($z_0/\lambda = 5$) from the duct open end, except at the nil-shielding directions where exact agreement was observed. The reason for the difference in levels of agreement for the two source planes can be attributed to the phase difference between different radial modes at the duct open end. *Equation 4.22* for the free-field radiation includes the phase term $e^{jkz_0 \cos\phi}$ (from Eq. 2.5), while for ducted sources the far-field pressure contains the phase term $e^{jk_{z,mn}z_0}$, *Eq. 4.59*. Clearly therefore, the phase difference between the various radial modes at the duct open end are equal:

1. At the nil-shielding directions $\phi = \phi_{mn}$.
2. At all radiation angles ϕ when the source plane is located, $z_0/\lambda = 0$.

This is an important result, which suggests that, for a single azimuthal mode, the far-field radiation due to free-field and ducted sources is identical at the nil-shielding directions and becomes almost identical over a large range of forward arc angles as the source plane is moved increasingly closer to the duct open end. Clearly therefore, for the source at the open end case, the duct has a relatively small effect on the radiation of the source in the forward arc.

The comparison between free-field and ducted source directivites presented above (for an axial location $z_0/\lambda = 0.01$) is now shown at the much higher non-dimensional frequency of $ka = 35$, for the azimuthal modes $m = 0, 10, 20$ and 30, whose results are shown in *figure 5.4*. The remaining parameters are the same as in *figure 5.2b*.

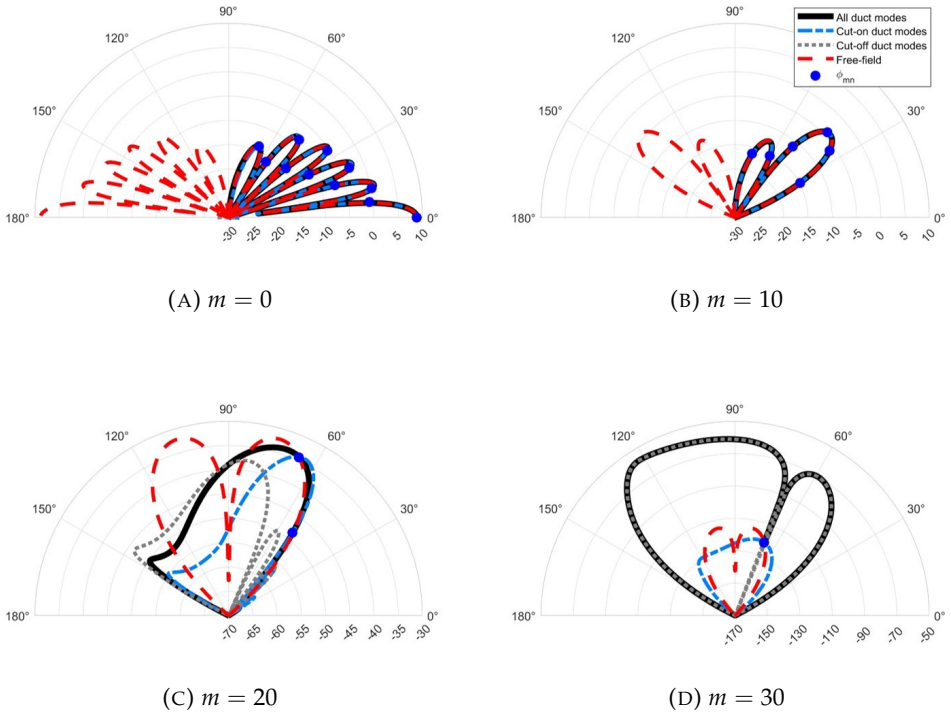

(A) $m = 0$ (B) $m = 10$

(C) $m = 20$ (D) $m = 30$

FIGURE 5.4: Free-field and ducted directivity of rotating point dipole sources at single azimuthal orders $m = 0, 10, 20$ and 30 at the non-dimensional frequency $ka = 35$. Shown for a source radius of rotation $r_0/a = 0.5$, dipole orientation $\gamma = 0^\circ$ and axial location $z_0/\lambda = 0.01$. The contribution of cut-on and cut-off modes are highlighted and the nil-shielding directions are shown (blue circles). In dB re 1 Pa.

By comparison with the previous results at $ka = 5$, in *figure 5.3*, the free-field and ducted solutions at this higher frequency are now in excellent agreement over a much larger range of angles owing to the higher number of nil-shielding directions present for $m = 0, 10$ and 20. At $m = 0$ and $m = 10$ contributions from cut-off modes can be observed to be negligible. However, at $m = 20$, the directivity levels can be observed to be significantly weaker than at the lower m modes by approximately 10 to 20 dB and hence the relative contribution from cut-off modes is more significant. For this mode the directivity is dominated by the cut-on modes at angles of up to the second nil-shielding direction at $\phi_{mn} \approx 65^\circ$, but then becomes dominated by the cut-off modes at higher angles.

At the highest azimuthal mode under investigation $m = 30$, overall directivity is many orders of magnitude smaller than for the lower order m modes by virtue of their intrinsic weaker radiation efficiency. The notable aspect of the directivity for this azimuthal mode is that cut-off modes completely dominate the overall response (gray curve hidden below the black curve) except at the single nil -shielding direction at $\phi_{mn} \approx 68^\circ$. Here, the contribution due to cut-off modes exhibits a null and the free-field and ducted solutions still agree.

Note that there exists a lower-bound frequency below which no nil-shielding directions can occur at which all radial order modes associated of the same azimuthal order m are cut-off.

5.1.3 High-ka limit, $ka \to \infty$

Following from the observations above, now consider the limiting behaviour of ducted source radiation in the high frequency limit, $ka \to \infty$. Irrespective of the source location relative to the duct open end, z_0, the existence of nil-shielding directions at the discrete mode-ray angles ϕ_{mn} is highlighted. In the high ka limit, the mode-ray angles associated with a particular value of m tend towards a continuum of values and the expression for the far-field radiation due to a ducted source must therefore tend to that of the free-field source for almost *all* radiation angles independent of its position relative to the duct open end. The radiation angles in the side-line directions however, will have a lower ducted than free-field radiation caused by reflections of the modes closest to cut-off.

5.1.4 Summary of radiation characteristics due to a single azimuthal order

By way of summary, for sources located close to the duct open end the radiation due to a single azimuthal mode m and its comparison with free-field radiation can be summarised as follows:

1. Ducted radiation is sensitive to source position relative to the duct open end at low frequencies where there are comparatively few nil-shielding directions. The sensitivity of the radiation to source position becomes much weaker as frequency is increased since there are a greater number of nil-shielding directions at which the ducted directivity matches the free-field solution.

2. For sources close to the duct open end there is close agreement between the free-field and ducted source radiation at polar angles from 0° (the duct axis) up to the highest nil-shielding direction associated with the least cut-on propagating mode.

3. For sources close to the duct open end, far-field radiation appears to be dominated by cut-on modes, with relatively small contribution due to cut-off modes over the range of angles specified above in 2.

4. Cut-off modes are generally important to the overall directivity for the higher order azimuthal modes m at radiation angles above the highest nil-shielding direction $\phi > \phi_{mn}$, including in the rear-arc. The contribution of cut-off modes appear to improve the agreement between the free-field and ducted radiation at the higher angles above the highest nil-shielding directions.

5.2 Comparison between the free-field and ducted directivities from semi-infinite ducts

The previous section has compared the directivity patterns for free-field and ducted rotating sources for a single azimuthal mode order m. In this section the directivities are compared, now with all possible modes are excited for the four source types; distribution of incoherent axial dipoles, distribution of incoherent monopoles, rotating point dipole and rotating point monopole. Comparisons are made for different axial locations from the open end z_0, radii of rotation r_0, and dipole orientations γ and non-dimensional frequencies ka.

5.2.1 Effect of axial distance from the open end of ducted radiation

This section investigates the effect of the axial distance of the ducted source z_0 from the duct open end on the multi-mode directivity patterns and these are compared to the free-field directivity.

An important feature of this study is to determine the effect of cut-off modes on the far-field radiation. This is first investigated by considering incoherent source distributions, where the only effect of source axial location is the significance of cut-off modal radiation from the duct. Consequently, incoherent source distributions are the most direct measure of the influence of cut-off modes in the far-field radiated noise for sources at varying axial locations.

This study also includes an investigation of the radiation from point sources, which excite coherent modes. The axial location of the point source will determine the significance of cut-off modal radiation in the same way as with the incoherent sources. Additionally, the phase of the cut-on modes is also determined by the sources axial location. The modal interference between the cut-on modes will be shown to be an important feature in ducted radiation, especially at low frequency. Therefore, for the coherent source case the axial location has two effects on the far-field acoustic radiation.

5.2.1.1 Incoherent source distributions

The significance of cut-off modes is now investigated for incoherent source distributions close to the open end of the duct. Predictions for the mean square pressure radiated from incoherent axial dipole and monopole sources in a semi-infinite duct are calculated by substituting *Eqs 4.67* or *4.76* respectively and *2.52* into *Eq. 2.51* and in free-field using *Eq. 4.37* or *4.45* respectively. *Figure 5.5* compares the mean square pressure $\overline{p^2}(R, \phi, \omega)$ for a source distribution of incoherent axial dipole and incoherent monopole sources inside a semi-infinite duct to the same source in free-field.

Investigations are conducted at the non-dimensional frequency ka = 5 and 35. The source plane is computed for three axial locations, $z_0/\lambda \to \infty$, where cut-off modes have no effect, $z_0/\lambda = 0.1$ and $z_0/\lambda = 0.01$, where cut-off modes have a maximum effect, following analysis in *Chapter 4*, the source plane at exactly the duct open end is avoided, where it was shown that all excited cut-off modes radiate significantly for $z_0/\lambda = 0$. Simulations are conducted for unit source strengths $\overline{F^2}(\omega)$ and $\overline{Q^2}(\omega)$ and observer radius R. Clearly, the far-field radiation of the free-field sources do not change with source axial location.

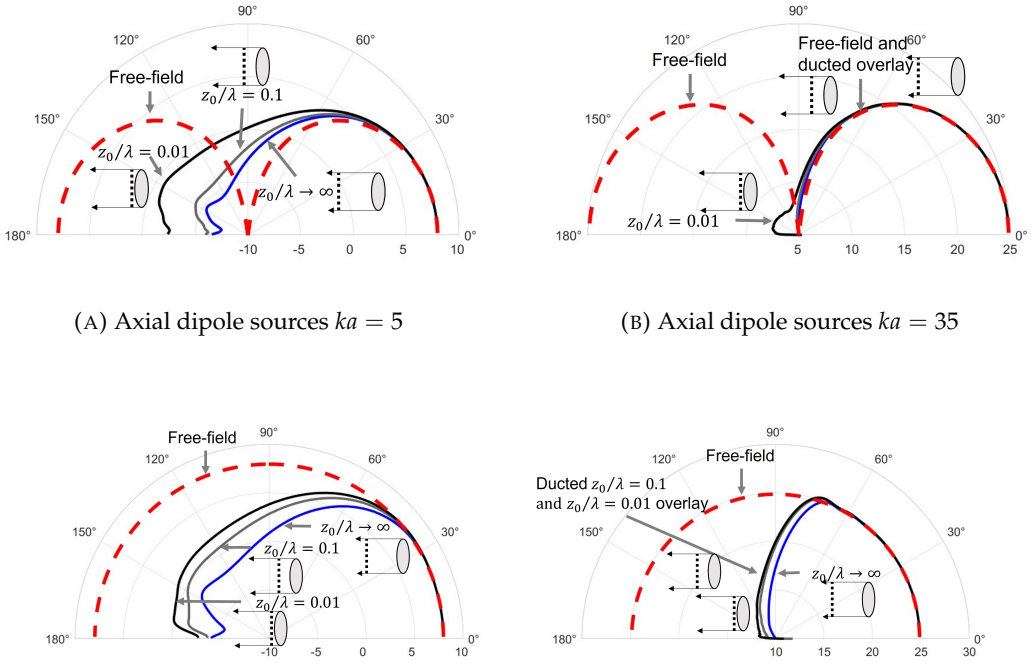

(A) Axial dipole sources $ka = 5$

(B) Axial dipole sources $ka = 35$

(C) Monopole sources $ka = 5$

(D) Monopole sources $ka = 35$

FIGURE 5.5: Directivity of distributions of incoherent axial dipole and monopole sources at varying axial locations inside a semi-infinite duct and in free-field. In dB re 1 Pa.

Cut-off modes can be assumed to increase the radiation in the rear-arc, $90° > \phi > 180°$ for sources close to the duct open end. Marginal increases of pressure to the rear-arc can be observed from *Figure 5.5a*, for the dipole case at $ka = 5$, for source locations at $z_0/\lambda > 0.1$ of up to 1 dB. For sources closer to the open end $z_0/\lambda < 0.1$, the pressure in the rear-arc is seen to increase significantly, peaking at a 5 dB increase at approximately $\phi = 170°$.

Figure 5.5b, for the dipole case at $ka = 35$, shows cut-off modes increase the radiation in the rear-arc, although for a much smaller range of angles than the $ka = 5$ case. An increase in radiation is observed to be up to 1.5 dB for sources located at $z_0/\lambda = 0.1$. This increase in ducted radiation is seen for far-field angles $150° > \phi > 180°$.

Distributions of incoherent monopole sources radiate cut-off modes to the rear-arc, similarly to the dipole case. For the $ka = 5$ case shown in *figure 5.5c* the cut-off modes are shown to change the shape of the directivity. For the source buried deep inside the duct, $z_0/\lambda \to \infty$ at the angles $150^\circ\phi < 180^\circ$ the directivity pattern can be observed to be similar to a sin wave. For the source at the open end $z_0/\lambda = 0.01$, the radiation is a similar level between $150^\circ\phi < 170^\circ$ and then decreases between $170^\circ\phi < 180^\circ$.

For distributions of incoherent monopole sources at $ka = 35$, shown in *figure 5.5d*, the cut-off modes are shown to generally increase the radiation equally at all rear-arc angles $90^\circ < \phi < 180^\circ$. For a source at the open end an increase of pressure to the rear-arc is seen to be as much as 4 dB due to cut-off modal radiation.

Dipole sources are assumed to be more sensitive to the axial location of the source, where a small difference in axial location is seen to significantly increase the pressure radiation in the rear-arc. The monopole case changes much more slowly, this is especially shown in *figure 5.5d* where a source location of $z_0/\lambda = 0.1$ and $z_0/\lambda = 0.01$ have almost indistinguishable directivities where *figure 5.5b*, for dipole sources, shows a much bigger increase for the ducted radiation at those locations.

The monopole modal amplitude of *Eq. 4.77* shows the cut-off modes closest to cut-on have the largest modal pressure amplitude. Therefore the contribution of the cut-off modes will have a relatively slow decay rate with axial distance, as the most contributing modes have the smallest axial wavenumber $k_{z,mn}$, signifying the slowest modal axial decay. Conversely, the dipole modal amplitude of *Eq. 4.77* shows a much more equal distribution of modal amplitudes, meaning it is the collective sum of the modes that cause the increase in far-field pressure. The pressure amplitude of the higher order modes decay quickly over short axial distances. This analysis explains why monopole source distributions are affected by cut-off modes for sources deeper inside the duct than dipole sources.

In nearly all cases presented in *figure 5.5* the effect of cut-off modes is shown to improve the similarity between free-field and ducted source radiation. This improved agreement identifies the decrease in shielding effect of the duct as $z_0/\lambda \to 0$.

5.2.1.2 Rotating point sources

In *Section 5.1* it is established that there is good agreement between the forward-arc of the directivity of free-field and ducted radiation for sources at the open end $z_0/\lambda = 0.01$ of the duct and in the high-frequency limit $ka \to \infty$ irrespective of source axial location. Since the contributions from individual azimuthal modes may be summed incoherently it therefore follows that the multi-mode radiation due to any arbitrary source distribution should also match the free-field directivity, (i) for all source positions from the open end at high frequencies, and (ii) at low frequencies for sources at the open end.

To confirm this hypothesis *figure 5.6* shows a comparison between the free-field and ducted directivity patterns for rotating point dipole and monopole sources. The mean square pressure for rotating point dipole and monopole sources inside a semi-infinite duct is formed by substituting *Eqs 4.59* or *4.71* respectively and *2.52* into *Eq. 2.5* and using *Eq. 4.28* and *4.41* respectively for the sources in free-field. Computations are conducted at two axial locations of $z_0/\lambda = 5$ and $z_0/\lambda = 0.01$. The radius of rotation is $r_0/a = 0.5$ and for the dipole source an orientation of $\gamma = 0$ (axial) is simulated. Simulations are conducted for unit source strengths $\overline{f^2}$ and $\overline{q^2}$ and observer radius R.

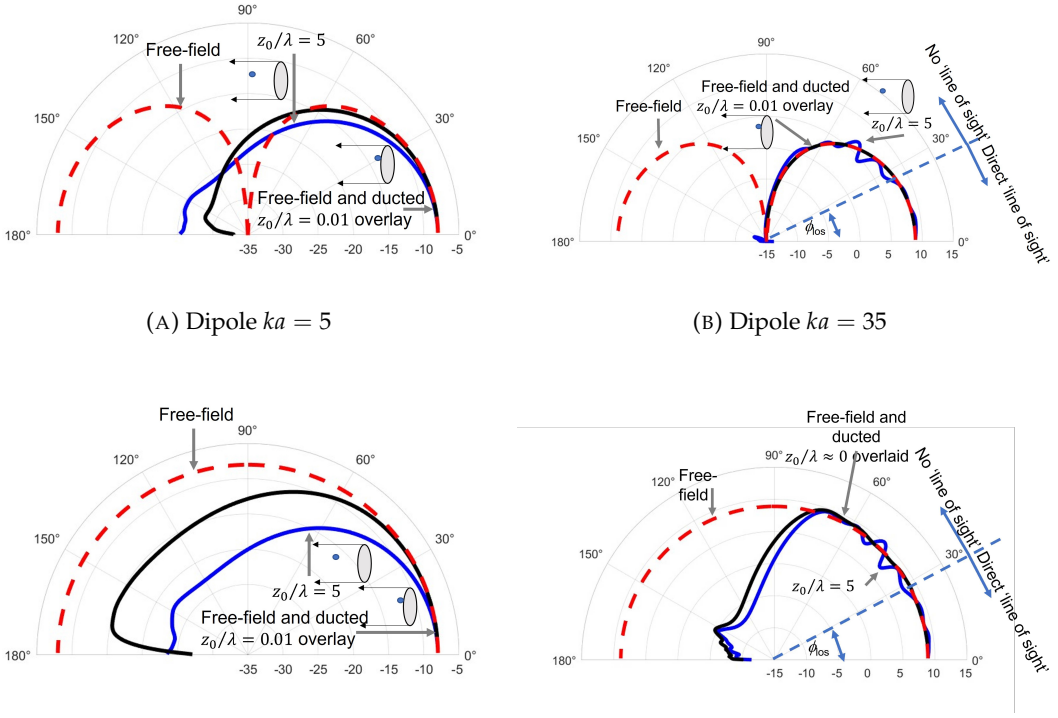

(A) Dipole $ka = 5$

(B) Dipole $ka = 35$

(C) Monopole $ka = 5$

(D) Monopole $ka = 35$

FIGURE 5.6: Free-field and ducted directivity for point rotating sources at two non-dimensional frequencies $ka = 5$ and 35, with a radius of rotation $r_0/a = 0.5$, for dipole sources the orientation is simulated to be $\gamma = 0^\circ$ (axial) and varying axial location. In dB re 1 Pa.

Figure 5.6 shows that, when the source plane is located at the duct open end (black curve), the free-field and ducted directivities generally agree to within 1 dB over a wide range of forward-arc angles at both frequencies. This result is consistent with the behaviour for individual modes m explored in *Section 5.1*.

The most striking effect of locating the source deep within the duct $z_0/\lambda = 5$ is the appearance of oscillations in the far-field radiation, which in *Section 5.1* has been found to be due to interference between different radial modes n within the same azimuthal mode m. As frequency is increased the number of oscillations increase and becomes smaller in amplitude such that the ducted radiated tends to that of the free-field source.

Although not seen explicitly in *figs 5.5* or *5.6*, deviations from free-field behavior is observed in the sideline directions, even in the high frequency limit due to significant reflections of near cut-off modes, and can be reasoned from the shielding effect of the duct.

5.2.2 Effect of far-field radiation due to source radius

This section investigates the effect on the far-field radiation due to source radius r_0/a from rotating point sources. Here, the same two axial locations investigated previously are used, of $z_0/\lambda = 5$, where the effect of cut-off modes is negligible, and $z_0/\lambda = 0.01$, where cut-off modes make most contribution. The behavior of dipole and monopole sources is shown to somewhat differ.

5.2.2.1 Point dipole sources

Figure 5.7 shows a comparison between the free-field and ducted directivities at $z_0/\lambda = 5$ and $z_0/\lambda = 0.01$ at the relatively low frequency of $ka = 5$ for an axial dipole ($\gamma = 0°$). In each figure, results are shown for the two source radii of $r_0/a = 0.0$ and 1.0, which only affects the ducted radiation and not the free solution of *Eq. 4.28*. which in this case reduces to $\overline{p^2}^{(ff)} = \overline{f^2}\left(k^2/4\pi R\right)^2 \cos^2\phi \cos^2\gamma$. The remaining parameters are the same as in *figure 5.6*.

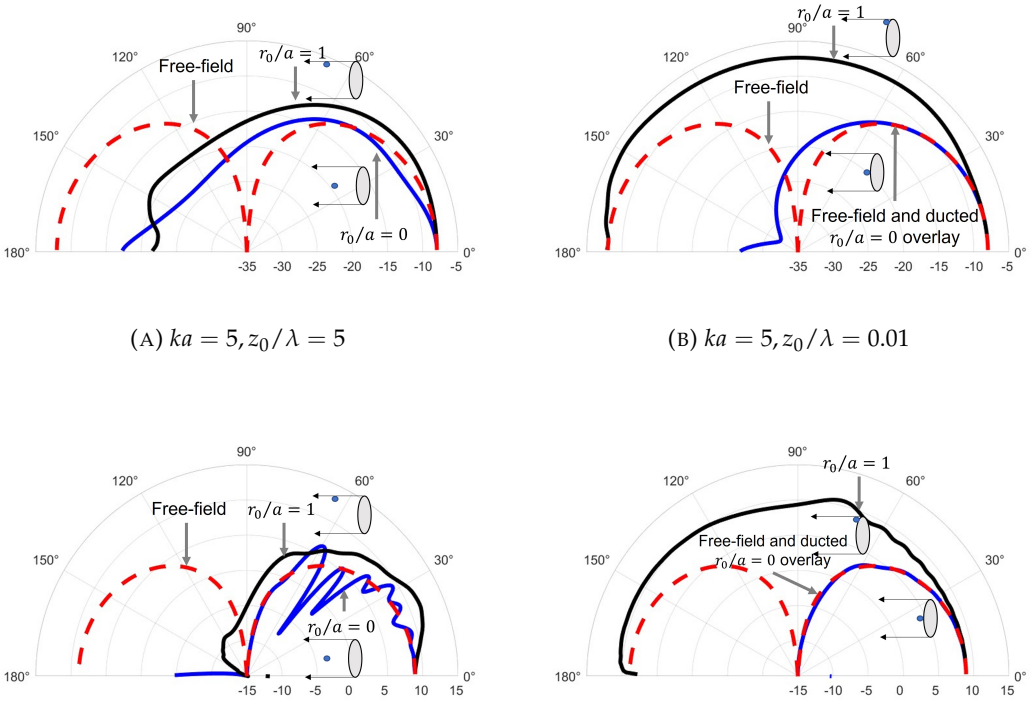

(A) $ka = 5, z_0/\lambda = 5$

(B) $ka = 5, z_0/\lambda = 0.01$

(C) $ka = 35, z_0/\lambda = 5$

(D) $ka = 35, z_0/\lambda = 0.01$

FIGURE 5.7: Free-field and ducted directivities for rotating axial dipole sources ($\gamma = 0°$) at two axial locations $z_0/\lambda = 5$ and $z_0/\lambda = 0.01$, two non-dimensional frequencies $ka = 5$ and 35 and two radii of rotation $r_0/a = 0$ and 1. In dB re 1 Pa.

Figure 5.7 illustrates clearly the influence of both the source radius r_0 and axial position z_0 on the far-field directivity of ducted sources. At the lowest frequency of interest, $ka = 5$, there is significant difference in level between the free-field and ducted solutions when the source is deep within the duct. This finding is a direct result of the effective doubling of the source strength that occurs when a source is located next to a hard boundary. When the source is located on axis far-field levels of radiation are similar.

However, when the source is located close to the open end, *figure 5.7b* and *5.7d* indicate that the far-field directivity varies between being of dipole radiation, when the source is on-axis $r_0/a = 0$, to being close to omni-directional when the source is located at the duct wall $r_0/a = 1$. Further investigation, shown in *Section 5.4.3*, where the power radiated is investigated, indicate that this monopole-type behaviour only occurs when the source is a very small fraction of a wavelength close to the duct wall. Clearly, this difference in the dipole behaviour of *figure 5.7a* and the monopole behaviour from dipole radiation in *figure 5.7b* is the now important contribution due to cut-off modes. The clear conclusion, therefore, is that locating the dipole source at the edge of a diffracting half-plane fundamentally alters the radiation to be similar to that of a monopole.

Very similar behaviour to *figures 5.7a* and *5.7b* can be observed in *5.7c* and *5.7d* at the much higher frequency of $ka = 35$. When the source is deep within the duct, evidence of strong interference between radial modes can be observed, which are absent when the source is located close to the duct open end, as discussed previously in *Section 5.2.1* above. Very close agreement is observed between the free-field and ducted source when the source is on the duct axis, $r_0/a = 0$, but differs significantly when the source is on the duct rim $r_0/a = 0, z_0/\lambda = 0.01$ which exhibits monopole radiation behavior.

Insight into the cause of the omni-directional behaviour for a source located at the duct rim observed in *figure 5.7b* and *5.7d* can be obtained by splitting this directivity into contributions due to cut-on and cut-off modes, as shown in *figure 5.8*.

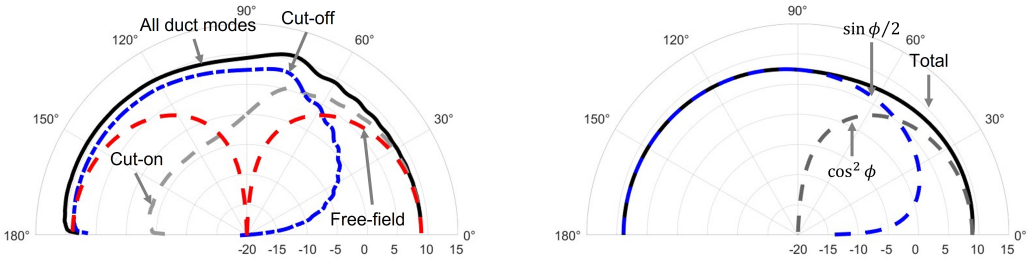

(A) Exact (B) Theoretical

FIGURE 5.8: Free-field and ducted directivities for a rotating axial dipole source on the duct rim $r_0/a = 1$, $z_0/\lambda = 0.01$ at the non-dimensional frequency $ka = 35$, highlighting the contribution of cut-on and cut-off modes. Also shown is a theoretical prediction of the cut-on modes $cos^2\phi$ and cut-off modes $\sin\phi/2$. In dB re 1 Pa.

Figure 5.8 demonstrates that the forward-arc is dominated by propagating modes as observed previously. However, for the axial dipole source at the duct rim, cut-off modes become dominant in the rear-arc. An intriguing finding is that the radiation at $\phi = 0°$ due to cut-on modes is equal to that at $\phi = 180°$ due to cut-off modes. When the pressure directivities from cut-on and cut-off modes are summed the resultant directivity is strongly omni-directional, as observed in the figure.

The forward-arc pressure closely follows the free-field directivity $\overline{p^2}_{\text{cut-on}} \approx \cos^2\phi$. The rear-arc directivity can be observed to closely follow $\overline{p^2}_{\text{cut-off}} = \sin\phi/2$. As noted in *Chapter 4*, which is characteristic of the radiation directivity at a distance R due to edge scattering of the form $R^{-1/2}\sin\phi/2$, and is the solution to Laplace's equation for in-compressible flow due to a sharp edge, see Ffowcs Williams and Hawkings (1969). The resultant directivity is therefore the incoherent sum of the forward and rear-arc directivities, i.e.,

$$\overline{p^2}^{(D)}(R,\phi,\omega) \approx \begin{cases} \cos^2\phi + \sin\phi/2, & 0° < \phi < 90°, \\ \sin\phi/2, & 90° < \phi < 180°. \end{cases} \tag{5.4}$$

These approximations are plotted in *figure 5.8b* with the level chosen to match the exact solution. Agreement can be observed to be within about 1 dB at all radiation angles.

5.2.2.2 Point monopole sources

The previous section has shown that dipole sources rotating near the wall of the duct $r_0/a \to 1$ exhibit a large increase in ducted radiation. This section continues this study but now for monopole sources. *Figure 5.9* shows a comparison between the free-field and ducted directivities for rotating point monopole sources at $z_0/\lambda = 5$ and $z_0/\lambda = 0.01$ for the non-dimensional frequency $ka = 5$ for the same two source radii of $r_0/a = 0.0$ and 1.0. The remaining parameters are the same as in *figure 5.6*.

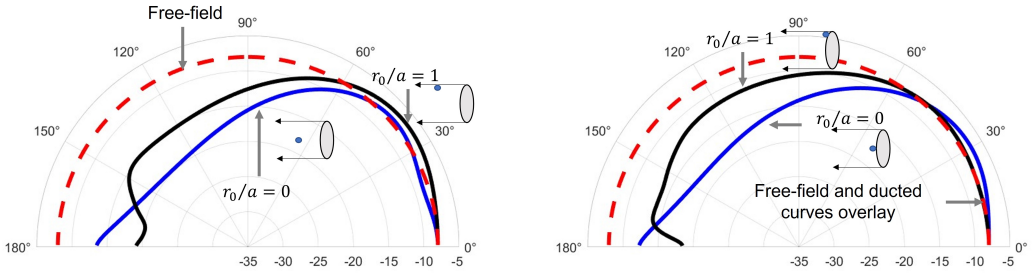

(A) $ka = 5, z_0/\lambda = 5$ (B) $ka = 5, z_0/\lambda = 0.01$

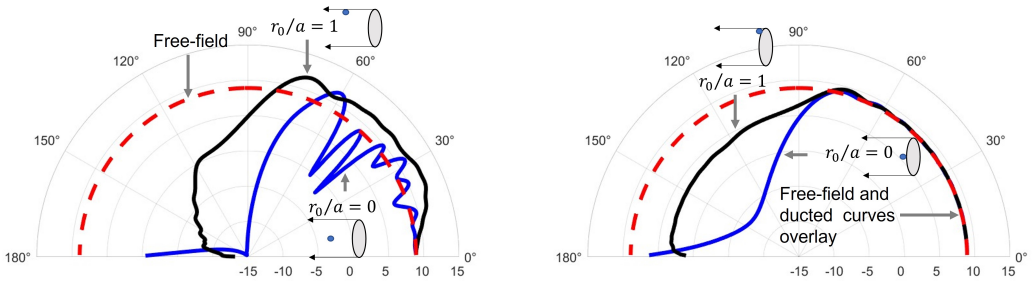

(C) $ka = 35, z_0/\lambda = 5$ (D) $ka = 35, z_0/\lambda = 0.01$

FIGURE 5.9: Free-field and ducted directivities for rotating monopole sources at two axial locations $z_0/\lambda = 5$ and $z_0/\lambda = 0.01$, two non-dimensional frequencies $ka = 5$ and 35 and two radii of rotation $r_0/a = 0$ and 1. In dB re 1 Pa.

Figure 5.9 illustrates that monopole sources at the wall of the duct $r_0/a = 1$ generally exhibit higher radiation than sources on the duct axis $r_0/a = 0$, at all angles except for $\phi \approx 180°$. The radiation of ducted sources is high at $\phi \approx 180°$ for sources on the duct axis $r_0/a = 0$, this is a property of the axi-symmetric ($m = 0$) modal radiation, which as discussed in *Chapter 3* region of high radiation for those modes. Note for $r_0/a = 0$, only the $m = 0$ modes radiate as discussed in *Chapter 4*.

Comparison between the ducted radiation at the duct wall $r_0/a = 1$ for the two source axial planes investigated, $z_0/\lambda = 5$ and $z_0/\lambda = 0.01$ reveal little difference considering the overall level. This behavior is contrary to that noted from *figure 5.7*, for the dipole sources, where increases in ducted radiation are observed as $z_0/\lambda \to 0$. Cut-off modes radiate with a weaker efficiency for monopole (than dipole) sources for $r_0/a = 1$. Further comparison between *figure 5.9* and *5.7* indicates that the increase in radiation due to sources near the wall of the duct, $r_0/a = 1$, particularly on the duct rim, $(r_0/a, z_0/\lambda)$ = (1,0), is much lower for monopole sources.

When the source plane is located near the rim of the duct $(r_0/a, z_0/\lambda) = (1, 0.01)$ the free-field and ducted radiation are shown to equate for monopole sources, which largely contrasts the dipole directivity (*figure 5.7d*). The strong radiation properties of cut-off modes excited by dipole sources can be attributed to their strong near field, which identifies the differences observed between *figure 5.7* and *5.9*.

5.2.3 Effect far-field radiation due to dipole orientation

Finally, for completeness, this section presents an investigation of dipole orientation on the acoustic radiation from free-field and ducted sources. *Figure 5.10* shows the free-field and ducted directivities, computed for $z_0/\lambda = 0.01$ at $ka = 5$ and 35, for the two dipole orientations of $\gamma = 45°$ and $90°$. The remaining parameters are the same as in *figure 5.6*.

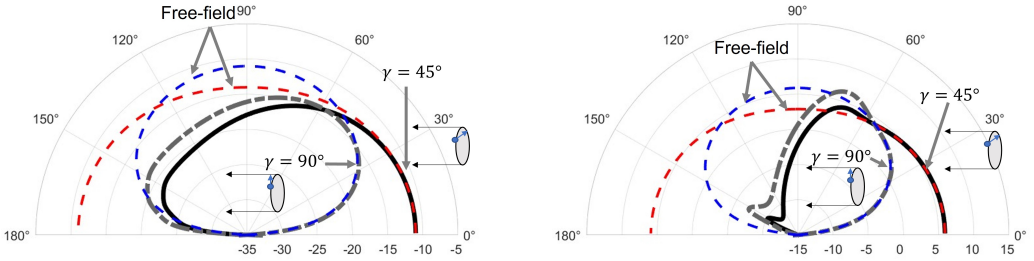

(A) $ka = 5$ (B) $ka = 35$

FIGURE 5.10: Free-field and ducted directivities for rotating dipole sources at the duct open end $z_0/\lambda = 0.01$, two non-dimensional frequencies $ka = 5$ and 35, radius of rotation $r_0/a = 0.5$ and two dipole orientations $\gamma = 45°$ and $90°$. In dB re 1 Pa.

Increasing the dipole orientation γ is shown to cause the main pressure lobe to approximately rotate towards the sideline directions with the maximum radiation occurring at $90°$ for the transverse dipole $\gamma = 90°$. The level of agreement between the free-field and ducted sources is approximately the same as for the axial dipole source shown in *figure 5.6c*, suggesting that dipole orientation has no significant effect on the difference between free-field and ducted radiation.

5.3 Physical interpretation

Figure 5.6 has indicated that the agreement between the free-field and ducted directivities tend to converge over all forward-arc angles as the source is moved closer to the duct open end. However, for sources well away from the duct open end, good agreement with the free-field solution is confined to a range of shallow angles up to some particular polar angle but then begins to oscillate at angles above this. Two interpretations of these results are now discussed. The first is a simple ray interpretation, valid in the high frequency $ka \to \infty$ limit. The second is based on a modal interpretation of the far-field radiation.

5.3.1 Ray theory interpretation

Simple physical reasoning can help to explain the reason why, for sources well away from the duct open end, close agreement between the free-field and ducted directivity patterns begins to deviate above some particular angle but agrees at all angles when the source is brought close to the duct open end, as observed in *figs 5.6c* and *5.6d*. Invoking a ray interpretation of the solution in the high-frequency limit, would suggest that the effect of the duct on the source radiation is negligible at all radiation angles for which there is a clear 'line of sight' between the source and the far-field observer. By simple geometry, for a point source at radial position r_0 and distance z_0 from the open end a clear line of sight exists at all polar angles up to some maximum angle ϕ_{los} given by,

$$\phi_{los} = \tan^{-1}(a - r_0)/z_0. \tag{5.5}$$

For the cases under investigation with source axial location $z_0/\lambda = 5$, in *figure 5.6c*, ϕ_{los} corresponds to approximately 29°, and for *figure 5.6d*, it is approximately 39°. These range of angles are indicated in *figure 5.6* and can be clearly seen to delineate the range of angles of good agreement and those where deviations begin to occur owing to to duct diffraction effects.

As the non-dimensional frequency *ka* is increased the influence on the forward-arc radiation due to the duct becomes increasingly weaker. This interpretation explains why the free-field and ducted solutions always agree on axis 0°. Note also that 0° represents the nil-shielding direction for the plane wave mode and this is the only mode that radiates at this angle. However, as the source is moved deeper within the duct, the 'line of sight' becomes closer to the duct rim, where diffraction of the duct modes starts to become significant.

5.3.2 Modal interpretation

An alternative interpretation to the ray theory model proposed in the previous section is now discussed based solely on the behaviour of individual modes. To present this, the relative contribution of cut-off modes to the total radiated field for the case considered in *figure 5.6a* is now shown.

Contribution due to cut-off modes

The radiated field from the rotating point dipole source inside the duct at non-dimensional frequency of $ka = 5$ for the rotating point dipole source located near the open end $z_0/\lambda = 0.01$ at a radial location of $r_0/a = 0.5$, and dipole orientation $\gamma = 0°$. The directivity is decomposed into its contributions from cut-on and cut-off modes, as shown in *figure 5.11*. The corresponding free-field result is also shown.

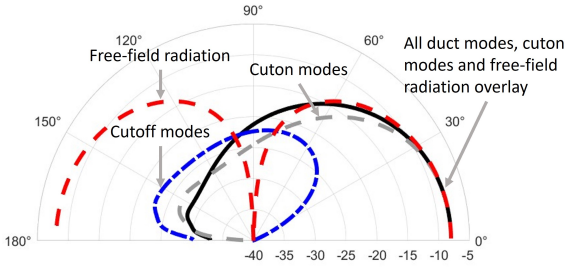

FIGURE 5.11: Free-field and ducted directivity from rotating point dipole sources at the non-dimensional frequency $ka = 5$, radius of rotation $r_0/a = 0.5$, dipole orientation $\gamma = 0°$, for the source plane near the open end of the duct, $z_0/\lambda = 0.01$. The contribution of cut-on and cut-off modes are isolated. In dB re 1 Pa.

Overall agreement between the free-field and ducted solution in the forward-arc is generally good, particularly at the radiation angles close to the duct axis. An intriguing observation is that the good levels of agreement observed at high angles above $\phi \approx 30°$ are only achieved because of the significant contribution due to cut-off modes. In their absence significant deviations between the free-field and ducted solutions would be observed. Moreover, the far-field radiation in the rear-arc, whilst being small compared to forward-arc radiation, is dominated by the cut-off modes. The corresponding decomposition into cut-on and cut-off modes at higher frequencies $ka > 10$ indicate similar behaviour, except that the level of agreement is better over a wider range of angles and the contribution to the far-field noise due to cut-off modes are weaker at all radiation angles but are still dominant in the rear-arc.

The close agreement between the free-field and ducted solutions at the higher non-dimensional frequency corresponding to $ka = 35$ in *figure 5.6* when the source is at the open end is therefore predominately due to contributions due to propagating modes with significant contributions due to cut-off modes being observed at the at the lowest frequency of interest $ka = 5$, as identified in *figure 5.11*.

Contribution due to cut-on modes

An alternative interpretation of the results in *figure 5.6* can be developed in terms of the directivity of individual cut-on modes. It is now assumed that the contribution to the forward-arc pressure due to cut-off modes can be neglected, which is realistic for sources well away from the duct open end and at high frequency.

A single mode propagating within the duct towards the open end at some axial location z from the source plane is of the form $e^{-jk_{z,mn}z}$. From the dispersion relation of *Eq. 2.10* and the relationship between κ_{mn} and the nil-shielding direction ϕ_{mn} of *Eq. 5.1*, modal propagation within the duct can be written as $p_{mn} \propto e^{-jk\cos\phi_{mn}z}$. The phase χ accumulated by the mode in propagating a unit axial distance $z = 1$ along the duct is therefore,

$$\chi_{mn} = k\cos\phi_{mn} \tag{5.6}$$

It is clear therefore that modes with nil-shielding directions close to the duct axis $\phi_{mn} \approx 0$ due to well cut-on modes accumulate greatest phase χ_{mn} with zero accumulated phase $\chi = 0$ for modes precisely at cut-off $\phi = 90$. Of interest here is the phase *difference* between modes with similar nil-shielding directions ϕ. The phase difference $\delta\chi$ between any two modes with nil-shielding directions separated by $\delta\phi$ is therefore approximately given by,

$$\delta\chi \approx -k\sin\phi\,\delta\phi \tag{5.7}$$

A number of modes with nil-shielding directions close to the duct axis therefore arrive at the duct open end with relatively small phase difference compared to cut-on modes with nil-shielding directions close to $\phi \approx 90^\circ$. This property is the cause of the oscillations observed in *figure 5.6* at high radiation angles.

Equation 5.7 suggests that the modes responsible for the radiation close to the duct axis arrive with relatively small phase difference $\delta\chi$ and therefore radiate approximately in phase. At high radiation angles, however, oscillations appear in the ducted directivity due to phase interference between the modes responsible for the radiation at these high angles. The degree of phase difference between the modes at the duct open end may be quantified by the use of *Eq. 5.7* to compute the phase difference $\delta\chi$ between successive modes with nil-shielding direction separated by $\delta\phi$. This phase difference is plotted in *figure 5.12* against ϕ_{mn} for the case considered in *figure 5.6c* where $z_0/\lambda = 5$ and $ka = 35$.

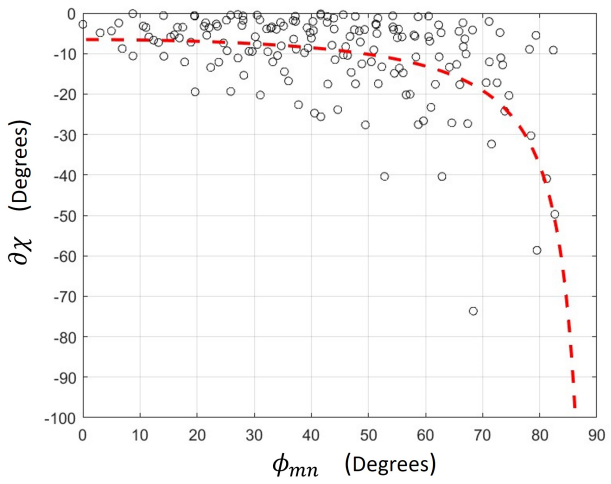

FIGURE 5.12: Change in phase $\delta\chi$ between successive modes with adjacent nil-shielding directions ϕ_{mn} for unit axial distance $z_p/a = 1.0$ and a non-dimensional frequency $ka = 35$

A general trend is clearly observed in which the phase difference between successive modes increases with increasing nil-shielding direction, although significant oscillations in the variation of χ with ϕ can be observed in *figure 5.12*. This oscillatory behaviour originates from the uneven and oscillatory values of $\delta\phi_{mn}$ between successive modes. This phase difference can be observed to be less than $\phi \approx 20^\circ$ for nil-shielding directions with angles below $\phi < 70^\circ$, which corresponding roughly to the range of radiation angles at which good agreement between the free-field and ducted solutions are observed in *figure 5.6c*. At high radiation angles, the phase difference between successive modes begins to increase, leading to significant oscillations in the far-field directivity caused by destructive interference between the modes arriving at the duct open end.

The phase differences plotted in *figure 5.12* above have been demonstrated to be the cause of oscillations in the directivities shown in *figures 5.6* when the source is deep within the duct. A simple analysis is now performed to quantify this phase difference between successive modes propagating along the duct.

An expression is now derived for the *average* phase difference $\delta\overline{\phi}$ between successive modes at any frequency ka with mean nil-shielding direction ϕ. In this analysis modes with negative m value (phase fronts spinning counter-clockwise) have been omitted since these will have identical nil-shielding direction to the corresponding mode with positive m value. Modes with azimuthal order m or $-m$ with the same radial order n arrive at the duct open end perfectly in phase. The number of modes $\delta N(ka, \phi)$ with nil-shielding directions per unit range of angles $\delta\phi$ is given by,

$$dN(ka, \phi)/d\phi = N(ka)\mathcal{N}(\phi), \tag{5.8}$$

where $N(ka)$ is the total number of propagating modes with $m \geq 0$ at frequency ka and $\mathcal{N}(\phi)$ is the modal density function, which specifies the relative number of modes with nil-shielding directions in a unit range of angles $\delta\phi = 1$, which has the normalisation property $\int_0^{\frac{\pi}{2}} \mathcal{N}(\phi)d\phi = 1$. Following Rice and Prydz (1978) $N(ka) \approx (12ka)^2$ and $\mathcal{N}(\phi) = \sin 2\phi$. The latter has been derived from the modal density function derived by Rice in terms of cut-off ratio and making a change of variable indicated in *Eq. 5.1* between cut-off ratio κ_{mn}/k and modal propagation angle ϕ. The average difference between successive nil-shielding directions $\overline{\delta\phi}$ is therefore given by $\overline{\delta\phi} = (dN(ka,\phi)/d\phi)^{-1}$. Substituting this expression into *Eq. 5.7* and substituting for $N(ka)$ and $\mathcal{N}(\phi)$ gives the following expression for the average difference in phase accumulated by successive modes in propagating unit length along the duct of the form,

$$\delta\chi = \frac{-k}{(\frac{1}{2}ka)^2 \cos\phi} \tag{5.9}$$

This equation is plotted in red in *figure 5.12*, which can be observed to provide a close fit to the general trend in the exact variation of phase difference between successive modes, with greatest phase difference being predicted for near cut-off modes.

5.4 Sound power radiation by free-field and ducted sources

Previous sections have investigated the difference in the directivities between free-field sources and those inside semi-infinite ducts. This has shown that the level of agreement between the two solutions is mostly determined from the number and density of nil-shielding directions. In this section, the acoustic power $W(\omega)$ radiated by free-field and ducted sources is investigated to assess the global effect on far-field radiation by the introduction of duct.

Computations of free-field and ducted power are presented for a distribution of incoherent axial dipole and monopole sources in a semi-infinite duct calculated by substituting *Eqs 4.67* or *4.76* respectively, *2.52* and *2.51* into *Eq. 2.57*, and in free-field using *Eq. 4.49* or *4.50* respectively. Computations are also presented for rotating point dipole and monopole sources inside finite ducts calculated by substituting *Eqs 4.59* or *4.71* respectively, *2.52*, and *2.51* into *Eq. 2.57* and in free-field calculated using *Eq. 4.47* or *4.48* respectively.

5.4.1 Effect of sound power due to dipole sources axial location

To begin this analysis, *figure 5.13* shows a plot of the free-field and ducted sound powers versus ka for $z_0/\lambda = 5$ and $z_0/\lambda = 0.01$ for an incoherent distribution of axial dipole sources and rotating point dipole sources with radius of rotation $r_0/a = 0.5$ and $\gamma = 0°$ (axial). Also shown is the free-field sound power. Simulations are conducted for unit source strengths $\overline{f^2}(\omega)$ and $\overline{F^2}$ and observer radius R.

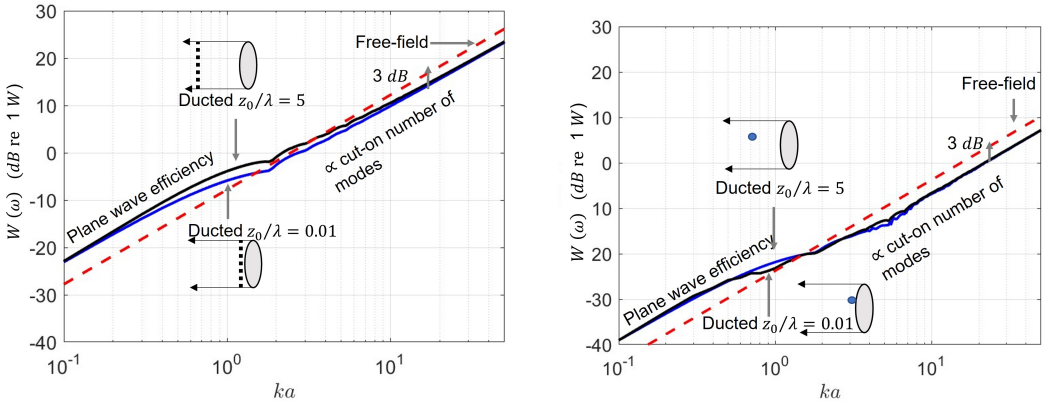

(A) Distribution of incoherent dipoles

(B) Rotating point dipole $r_0/a = 0.5$

FIGURE 5.13: Sound power radiated by free-field and ducted axial dipole sources ($\gamma = 0°$) for two axial locations $z_0/\lambda = 5$ and $z_0/\lambda = 0.01$.

The free-field and ducted sound powers can be observed to vary as $(ka)^2$ over most of the frequency range in *figure 5.13*. This dependence on frequency is seen explicitly in the free-field sound power expressions in *table 4.2*. The $(ka)^2$ frequency dependence for the ducted source has different interpretations at low and high frequencies.

At low frequency $ka < 1.84$ the $(ka)^2$ frequency dependence is a well-known classical result for the radiation efficiency of plane waves radiating from ducts, whose radiation efficiency for the un-flanged and flanged ducts approaches $1/2(ka)^2$ and $(ka)^2$ respectively as $ka \to 0$, Kinsler et al. (2000).

The approximate $(ka)^2$ dependence observed in *figure 5.13* at higher frequencies, $ka \gtrsim 5$, arises because the *relative* mode amplitude distribution is independent of ka, as demonstrated by Rice and Prydz (1978). Increasing frequency, therefore, only has the effect of increasing the number of propagating modes. The variation in total sound power radiation is therefore proportional to the number of modes, which varies as $(ka)^2$.

As the frequency increases a notable frequency is reached when the free-field and ducted sound powers are equal, which in this example is approximately $ka \approx 1.5$ and therefore close to the cut-on frequency of the first higher order duct modes $(m, n) = (1, 1)$. As the frequency is increased further the free-field sound power is greater than the ducted power by power by 3 dB, which as seen in *figure 5.6*, is due to shielding of the rear-arc radiation by the semi-infinite duct. In general there is negligible difference at almost all frequencies between the sound power radiation for when the source is at $z_0/\lambda = 5$ and when the source is at the open end $z_0/\lambda = 0.01$.

In the low frequency limit, in this example (*figure 5.6*) the ducted source radiates greater sound power than when in free-field by approximately 4.8 dB. For this region, only the plane wave radiates efficiently from within the duct, which clearly radiates more strongly than the free-field dipole source. This is likely due to the lack of a null in the plane wave directivity pattern radiating from the duct.

Comparison between *figs 5.13a* and *5.13b* identifies that the distributions of incoherent sources radiate power with the same frequency dependence (ka^2) as rotating point sources, but are consistently higher. From *Table 4.2*, which presents the free-field power radiation equations identifies this value to be $4\pi^2$.

5.4.2 Effect of sound power due to monopole sources axial distance from the open end

For monopole sources, finer details can be observed in the sound power spectra. To present this the sound power ratio of free-field to ducted power is defined,

$$\Pi(\omega) = \frac{W^{(D)}(\omega)}{W^{(ff)}(\omega)}, \tag{5.10}$$

Figure 5.14 shows a plot of the free-field ducted sound power ratio $\Pi(\omega)$ of *Eq. 5.10* for an incoherent distribution of monopole and point rotating monopole source with the same parameters as *figure 5.13*.

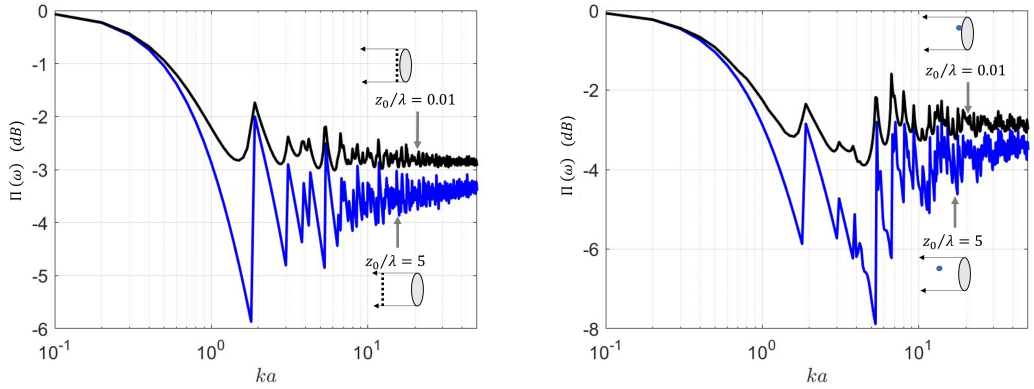

(A) Distribution of incoherent monopole (B) Rotating point monopole $r_0/a = 0.5$

FIGURE 5.14: Sound power ratio between free-field monopole sources and those inside semi-infinite ducts at two axial locations $z_0/\lambda = 5$ and $z_0/\lambda = 0.01$.

Most striking form *figure 5.14* is the 'spikey' behavior which can be seen to occur at the modal cut-on frequencies. This behavior has been noted for ducted sour power radiation spectra by several authors, for example Snakowska and Jurkiewicz (2010), who conduced a similar study assuming an equal energy per source. Unlike dipole sources, a clear difference is observed in *figure 5.14* between the radiation of ducted sources near the open end of the duct $z_0/\lambda = 0.01$ and for sources buried deep inside the duct $z_0/\lambda = 5$. This difference can be attributed to the radiation of cut-off modes and can be seen to be approximately 1 dB. Clearly this increase in ducted power is a result of the cut-off modes.

5.4.3 Effect of sound power due to source radii of rotation

Section 5.2.2 identified that ducted source located at the wall $r_0/a = 1$ exhibit a larger directivity than sources located elsewhere. This section further illustrates this phenomenon by studying the sound power of sources at varying radial location.

Figure 5.15a shows the sound power ratio $\Pi(\omega)$ of *Eq. 5.10* at three radii of rotation, $r_0/a = 0, 0.95$, and 1 for a point rotating axial dipole source ($\gamma = 0$) and monopole source deep within the duct, $z_0/\lambda = 5$ and near the open end $z_0/\lambda = 0.01$, as a function of non-dimensional frequency ka.

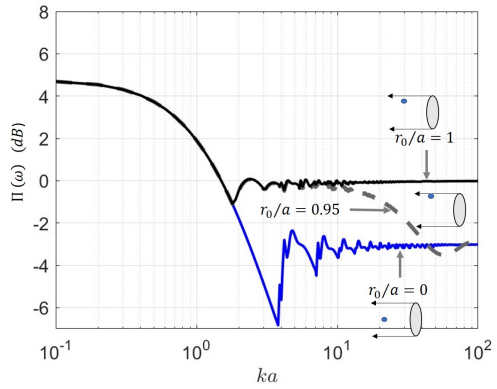

(A) Axial dipole $\gamma = 0°, z_0/\lambda = 5$

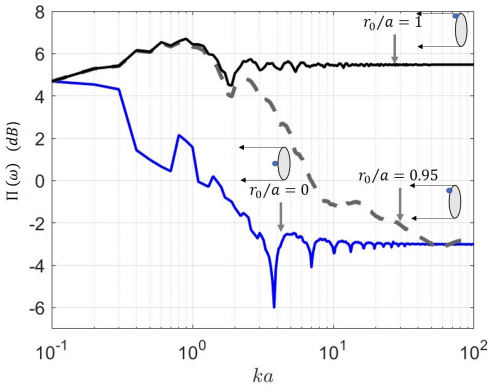

(B) Axial dipole $\gamma = 0°, z_0/\lambda = 0.01$

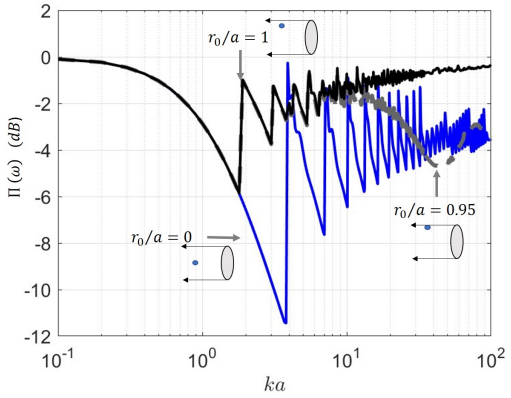

(A) Monopole $z_0/\lambda = 5$

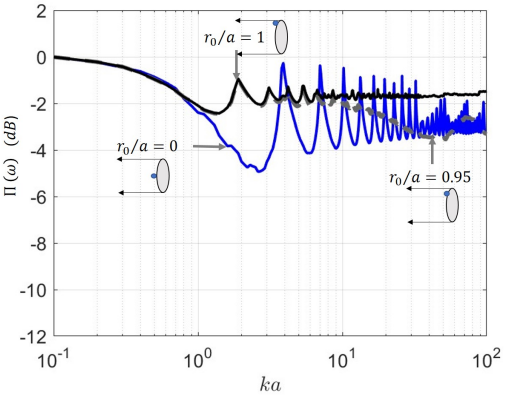

(B) Monopole $z_0/\lambda = 0.01$

FIGURE 5.16: Sound power ratio between free-field and ducted rotating point sources at varying radial and axial locations.

When the source is deep within the duct, as shown in *figure 5.16*, identical sound power is radiated at all three radial positions below the first duct cut-off frequency $ka = 1.84$ where only the plane wave is present. The same behavior is observed for the point monopole source at the open end of the duct, *figure 5.16b*, but not for the dipole source at the open end of the duct, *figure 5.15b*, where even at low frequencies the ducted radiation is seen to be high. Comparison between *figs 5.15a* and *5.15b* identifies this increase in radiation can be attributed to cut-off mode radiation. *Figure 5.16* identifies that even for sources with radius of rotation close to the wall, such as $r_0/a = 0.95$, the relatively large ducted radiation is not observed at high frequencies.

Clear high frequency asymptotes for the power ratio $\Pi(\omega)$ can be observed from *figure 5.16*, these are summarised in *Table 5.1* below.

Source \ Location	$z_0/\lambda = 5$	$z_0/\lambda = 0.01$
Dipole	$\approx 0\ dB$	$\approx 6\ dB$
Monopole	$\approx$ -1 dB	$\approx$ -2 dB

TABLE 5.1: High frequency free-field to ducted power ratios for sources at the duct wall $r_0/a = 1$

5.4.4 Effect of sound power due to source orientation

Finally, the variation in the sound power ratio between free-field and ducted dipole sources due to varying dipole orientation γ is investigated. *Figure 5.17* shows the power ratio $\Pi(\omega)$ of *Eq. 5.10* for a dipole source deep within the duct $z_0/\lambda = 5$, with radius of rotation $r_0/a = 0.5$ and for the three dipole orientations $\gamma = 0°, 45°$ and $90°$. Note that the free-field power of *Eq. 4.47* does not depend on dipole orientation.

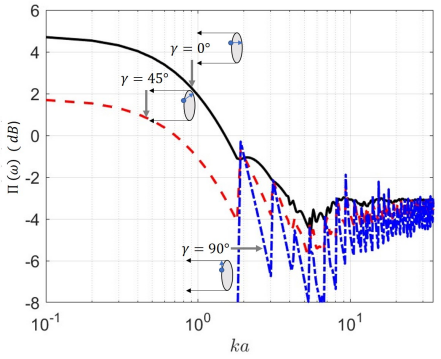

FIGURE 5.17: Ratio of free-field to ducted sound power radiated by rotating point dipole sources with source axial location $z_0/\lambda = 5$, radius of rotation $r_0/a = 0.5$ and varying dipole orientation.

In the plane wave frequency range $ka < 1.84$, the ducted sound power radiation varies proportional to $\cos^2\gamma$. Zero radiation is therefore produced for the transverse dipole ($\gamma = 90°$) whose dipole strength is normal to the particle velocity of the plane wave mode and hence is unable to couple into the mode. Furthermore the radiated power for this region can be seen to decrease with γ for the ducted source. Similarly to *figure 5.16*, *figure 5.17* identifies the modal cut-on frequencies as spikes in the power spectra.

At higher frequencies, the sound power generally reduces with increasing dipole orientation γ and becomes more oscillatory. The reasons for both behaviours can be found in the expression for the modal amplitude in the duct of *Eq. 4.54*. As γ is increased the relative contribution from the zero azimuthal order $m = 0$, which makes the largest overall contribution, becomes comparatively weaker compared to the $m \neq 0$, leading to weaker sound power. Furthermore, as the dipole orientation γ is increased the modal amplitudes of these non-axisymmetric modes increases, which increases the significance of the oscillations observed at the modal cut-on frequencies.

5.5 Numerical validation for the semi-infinite duct radiation model

This section details numerical simulations conducted using COMSOL Multiphysics predicting the far-field radiation from point sources inside semi-infinite ducts. The purpose of these simulations is to validate the theoretical results presented in the previous sections of this chapter. The free-field source is not validated here, as this formulation is mostly classical, and well validated in the literature by for example McAlpine et al. (2015). Comparisons are conducted using the directivity,

$$Q(\phi, ka) = \frac{\overline{p^2}^{(D)}(R, \phi, \theta, \omega)}{\frac{1}{2}\int_0^{\pi} \overline{p^2}^{(D)}(R, \phi, \theta, \omega) \sin\phi d\phi}. \tag{5.11}$$

Figure 5.18 presents a 2 dimensional axi-symmetric model, valid for sources on the duct axis $r_0/a = 0$, for a semi-infinite duct created using COMSOL Multiphysics.

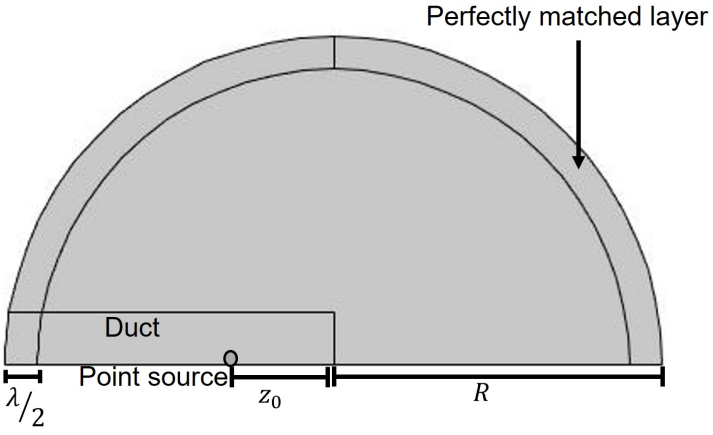

FIGURE 5.18: Geometry of the COMSOL 2 dimensional model

The 2 dimensional numerical model was made from an oblong and a semi-circle, which when revolved represent the duct and computational domain respectively. A point source is modeled in the duct at a distance z_0 from the open end. The axial radiation inwards from the duct open end is absorbed into a perfectly matched layer, representing a semi-infinite duct. Similarly the edge of the domain at R is also terminated in a perfectly matched layer, modeling a free-field. The perfectly matched layer was arbitrarily chosen to have a thickness of $\lambda/2$, although sensitivity to this parameter was confirmed to be minimal.

A convergence study is now conducted to determine the number of points per wavelength and radial distance R required to ensure the simulation does not change to within 0.5 dB.

Figure 5.19 shows a plot of the directivity $Q(\phi, ka)$ of *Eq. 5.11* for a point axial dipole source $\gamma = 0°$, on the duct axis $r_0/a = 0$ computed using COMSOL Multiphysics for non-dimensional frequency $ka = 5$, $z_0 = 2\lambda$ and 2, 3, 4 and 5 points per wavelength at a far-field distance $R = 5\lambda$ and at a far-field radiated distance $R = 3\lambda, 4\lambda, 5\lambda$ and 6λ for a mesh density of 8 points per wavelength. Note due to the normalisation property of $Q(\phi, ka)$ the distance R, does not change the directivity.

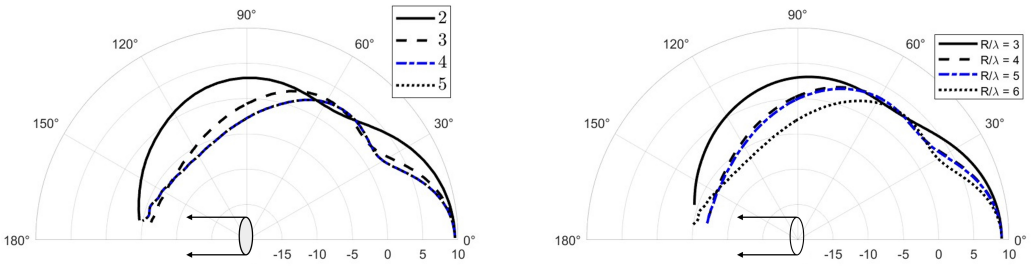

(A) Mesh study (B) Domain study

FIGURE 5.19: Directivity $Q(\phi, ka)$ computed using COMSOL Multiphysics for a point dipole source on the axis $r_0/a = 0$ of a semi-infinite duct at non-dimensional frequency $ka = 5$, for a source axial location $z_0/\lambda = 2$, varying points per wavelength and far-field radial distances, in dB.

Figure 5.19 identifies the model is sufficiently converged, to within 0.5 dB for a far-field distance of $R/\lambda = 5$ and 4 points per wavelength.

5.5.1 Comparison between theoretical and numerical model

Using the COMSOL Multiphysics numerical model, simulations were conducted to predict the directivity of a point dipole and monopole source at two non-dimensional frequencies $ka = 5$ and 35 on the duct axis at two axial locations $z_0/\lambda = 2$ and 0.1. A comparison between the theoretical and numerical directivity $Q(\phi, ka)$ of *Eq. 5.11* are shown in *figure 5.20*.

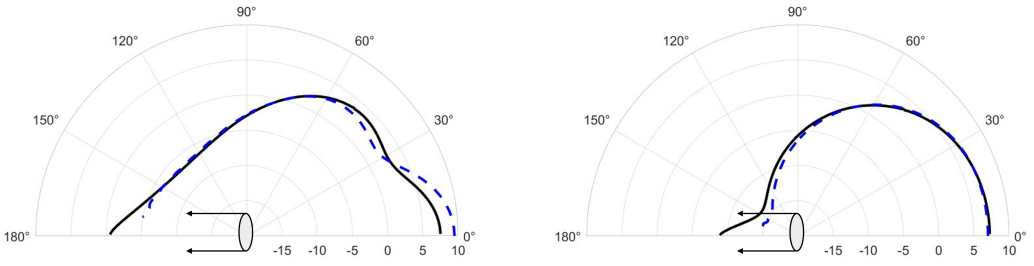

(A) Dipole $ka = 5, z_0/\lambda = 2$ (B) dipole $ka = 5, z_0/\lambda = 0.1$

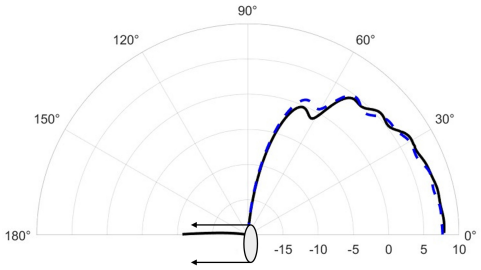

(C) Dipole $ka = 35, z_0/\lambda = 2$

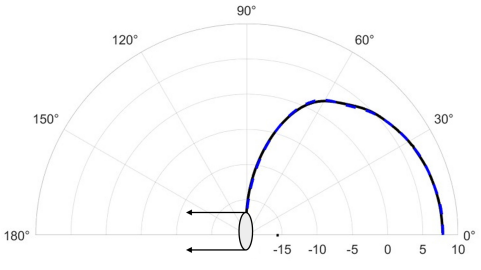

(D) Dipole $ka = 35, z_0/\lambda = 0.1$

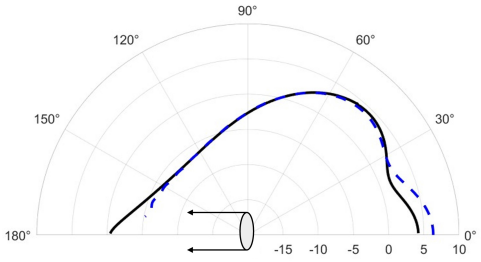

(E) Monopole $ka = 5, z_0/\lambda = 2$

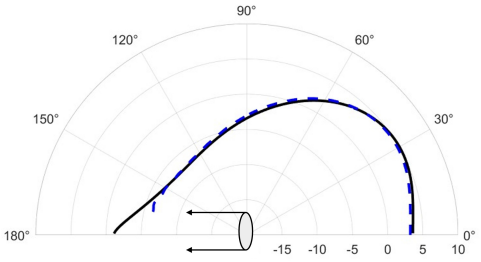

(F) Monopole $ka = 5, z_0/\lambda = 0.1$

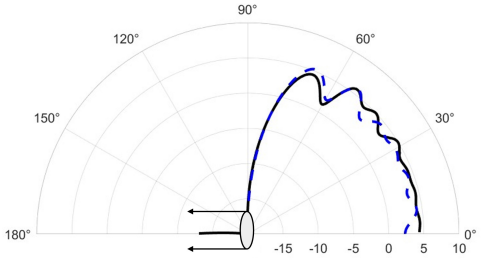

(G) Monopole $ka = 35, z_0/\lambda = 2$

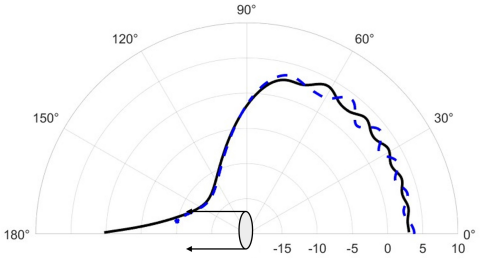

(H) Monopole $ka = 35, z_0/\lambda = 0.1$

FIGURE 5.20: Directivity $Q(\phi, ka)$ computed using COMSOL Multiphysics (blue dashed line) for point dipole and monopole source on the axis $r_0/a = 0$ of a semi-infinite duct at non-dimensional frequency $ka = 5$ and 35, for a source axial locations $z_0/\lambda = 2$ and 0.1, in dB.

Good agreement generally to within 1 dB and at certain angles 3 dB can be observed between the numerical and theoretical modes for all cases investigated in *figure 5.20*. This is unsurprising as only small additions have been made to exisitng validated models have been used in this chapter. The main difference to the current and previous approaches are the addition of cut-off modes, which have the capability to radiate significantly when the source is close to the open end of the duct. The observed good agreement between the numerical and theoretical model is unsurprising as the directivity factor function $D_{mn}(\phi, ka)$ of *Eq. 2.52* was validated in Gabard and Astley (2006) but only for propagating modes.

5.6 Summary

This chapter has presented a comparison between the acoustic radiation from free-field rotating point dipole and monopole sources, and incoherent distributions of axial dipole and monopole sources, to those inside a semi-infinite duct. By considering a single azimuthal order m, the concept of nil-shielding directions, first identified by Chapman (1996), has been demonstrated numerically. In the high frequency limit, as $ka \to \infty$, the sensitivity of the radiation to the axial location z_0 is weak, as the number of nil-shielding directions are shown to equate the free-field and ducted radiation for all source axial locations in the forward-arc. For the lower frequency cases, when the source is located at the open end of the duct, but not at the duct wall, good agreement is observed between free-field and ducted solutions.

Sources located close to the open end of semi-infinite ducts can have an increase in pressure radiation to the rear-arc $\phi > 90^\circ$, due to cut-off modes, by as much as 5 dB and a more general increase is observed of 3 dB accross a range of rear-arc angles. The total power increase due to cut-off modal radiation however, is marginal, as relative to the forward-arc radiation the overall level increase is small.

Ducted dipole sources located at the wall of the duct $r_0/a = 1$ are shown to have a large increase in the radiated pressure at all radiation angles $\phi \gtrsim 30^\circ$. This behavior is a result of the pressure doubling due to the interaction of he source and the duct hard wall. The resultant directivity for the case of a dipole source located at $r_0/a = 1$ is approximately omni-directional.

Chapter 6

Acoustic radiation from sources inside ducts of finite length

The previous chapter was concerned with a comparison of the radiation from free-field sources to those placed inside a semi-infinite duct. In this chapter the derivation for the radiation from a duct of finite length is provided. This model is applicable to radiate noise from all source type previously investigated in this thesis.

Approximate expressions for the radiation from sources inside ducts of finite length have been developed by 3 authors, Doak (1973b), Johnston and Ogimoto (1980b) and Hewlett et al. (1997). An exact expression was developed by Hamdi and Ville (1982), which is valid for propagating modes only. This restriction limits the solution to sufficiently long ducts.

In this thesis radiation from a finite length duct is approximated from two semi-infinite duct models using the method first derived by Hewlett et al. (1997). In their work, it was assumed the radiation from one open end of a finite length duct is independent of the radiation from the other and can be approximated by that from a semi-infinite duct. The model presented here extends their work to include any source type that can be assumed to have a modal amplitude term $a_{S,mn}(\omega)$.

6.1 Modal amplitudes from a finite length duct

This section presents an approximate expression to predict acoustic source radiation from a finite length duct using a modified modal pressure amplitude at the open ends of the duct which accounts for repeated reflections due to interaction with the open end of the duct.

For application to the existing pressure radiation model of *Eq. 2.51*, a modal amplitude at both the left and right open ends of the duct is required $a_{mn}^{(r)}(\omega)$ and $a_{mn}^{(l)}(\omega)$ respectively. Consider a source located inside a finite duct of length L at a distance z_0 from the right open end. It is assumed the source excites a mode which propagates in both directions denoted the right and left direct wave respectively, each of which contribute to the modal amplitude at the right open end of the duct $a_{mn}^{(r)}(\omega)$ as sketched in *figure 6.1*.

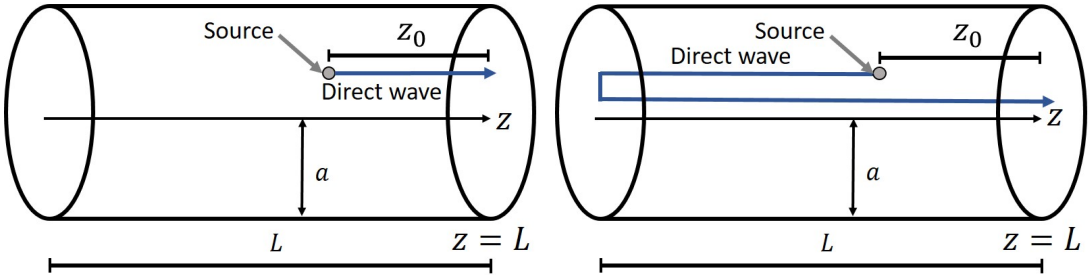

(A) The right going direct wave

(B) The left going direct wave

FIGURE 6.1: Finite duct and associated coordinates for two direct waves contributing to the total modal amplitude at the right open end.

Each mode of azimuthal order m reaching the open is scattered into all radial modes of the same azimuthal order m, as discussed in *Chapter 2* and *3*. The modal amplitude at each open end of the duct can therefore be written in terms of the scattering matrices where the modal amplitude of all modes of the same azimuthal order m are considered simultaneously.

The matrix equation of modal amplitudes at the right open end of the duct due to a single azimuthal order m and for all radial modes n can be written in the form,

$$\boldsymbol{a}_m^{(r)}(\omega) = \boldsymbol{\mathcal{P}}_m^{(r)}(\omega)\boldsymbol{a}_{S,m}(\omega) + \boldsymbol{\mathcal{P}}_m^{(l)}(\omega)\boldsymbol{b}_{S,m}(\omega)\,, \tag{6.1}$$

where the modal amplitudes $\boldsymbol{a}_{S,m}(\omega)$ and $\boldsymbol{b}_{S,m}(\omega)$, are column vectors of the right and left going modal amplitudes *at the source plane* respectively, each defined as,

$$\boldsymbol{a}_{S,m}(\omega) = \begin{bmatrix} a_{S,m1}(\omega) \\ a_{S,m2}(\omega) \\ \vdots \\ a_{S,mn'}(\omega) \end{bmatrix}, \qquad \boldsymbol{b}_{S,m}(\omega) = \begin{bmatrix} b_{S,m1}(\omega) \\ b_{S,m2}(\omega) \\ \vdots \\ b_{S,mn'}(\omega) \end{bmatrix} \tag{6.2}$$

truncated at $n = n'$ chosen to ensure convergence. The modal amplitudes for incoherent distributions of axial dipole and monopole sources as well as rotating point dipole and monopole sources is derived in *Chapter 4* for infinite ducts.

The term $\boldsymbol{\mathcal{P}}_m^{(r)}(\omega)$ in *Eq. 6.1* represents the sum of the phase factors that are evaluated each time a mode reaches the duct open end which are due to the right going direct wave shown in *figs 6.1a* and is defined by,

$$\boldsymbol{\mathcal{P}}_m^{(r)}(\omega) = \sum_{s=0}^{\infty} \boldsymbol{E}_{m,s}^{(r)}(z,\omega)\,, \tag{6.3}$$

where z is the displacement propagated by the mode between initial excitation at the source plane and the right open end of the duct evaluated for a mode that has experienced reflection due to interaction with the right open end s times (a total of $2s$ reflections). Each term of the phase factor $\boldsymbol{E}_{m,s}^{(r)}(z,\omega)$ is calculated using,

$$\boldsymbol{E}_m(z,\omega) = \begin{bmatrix} \mathrm{e}^{jk_{z,m1}z} & \dots & 0 \\ \vdots & \mathrm{e}^{jk_{z,m2}z} & \\ 0 & & \mathrm{e}^{jk_{z,mn'}z} \end{bmatrix}. \tag{6.4}$$

The sum of the phase accumulated by each mode that arrives at the *right* open end of the duct due to the excitation of the *left* going direct wave, shown by *figure 6.1b* is denoted $\boldsymbol{\mathcal{P}}_m^{(l)}(\omega)$ and can be calculated using,

$$\boldsymbol{\mathcal{P}}_m^{(l)}(\omega) = \sum_{s=0}^{\infty} \boldsymbol{E}_{m,s}^{(l)}(z,\omega)\,, \tag{6.5}$$

Consider the direct wave radiated by a source inside a finite length duct a distance z_0 from the right open end as shown in *figure 6.1a*. Upon reaching the right open end, the direct wave experiences reflection defined by a factor $\boldsymbol{R}_m(ka)$ of *Eq. 2.55*, and propagates back into the duct. The wave then reaches the left open end, reflects once more before reaching the right open end a second time. The propagation of the wave that has experienced reflections once from the right open end has a cumulative distance traveled $z = z_0 + 2L$. In general, a wave that has experienced reflection due to interaction with the right open end of the duct s times has phase factor of the form,

$$\boldsymbol{E}_{m,s}^{(r)}(z,\omega) = \boldsymbol{R}_m^{2s}(ka)\boldsymbol{E}_m(z_0 + 2sL,\omega)\,, \tag{6.6}$$

which can be substituted into *Eq. 6.5* to show,

$$\boldsymbol{\mathcal{P}}_m^{(r)}(\omega) = \sum_{s=0}^{\infty} \boldsymbol{R}_m^{2s}(ka)\boldsymbol{E}_m(z_0 + 2sL,\omega)\,, \tag{6.7}$$

which can be solved noting that *Eq. 6.7* is a geometric progression,

$$\boldsymbol{\mathcal{P}}_m^{(r)}(\omega) = \boldsymbol{E}_m(z_0)\mathrm{Inv}\left\{\left[\boldsymbol{I} - \boldsymbol{R}_m^2(ka)\boldsymbol{E}_m(2L)\right]\right\}\,. \tag{6.8}$$

Consider the radiation now from the left going direct wave and its modal contribution at the right open end shown in *figure 6.1b*. The direct wave will reach the left open end first, experience reflection, propagate back into the duct and reach the right open end. The first contribution at the right open end from the left going wave will have propagated a total distance $z = 2L - z_0$, as clearly indicated by the figure. The remaining reflected waves will behave in the same way as the right going waves, therefore the sum of the phase factors for the left going direct wave is of the form,

$$\boldsymbol{\mathcal{P}}_m^{(l)}(\omega) = \sum_{s=0}^{\infty} \boldsymbol{R}_m^{2s+1}(ka)\boldsymbol{E}_m(2L - z_0 + 2sL)\,, \tag{6.9}$$

which can be solved by noting that *Eq. 6.9* is a geometric progression,

$$\boldsymbol{\mathcal{P}}_m^{(l)}(\omega) = \boldsymbol{R}_m(ka)\boldsymbol{E}_m(2L - z_0)\mathrm{Inv}\left\{\left[\boldsymbol{I} - \boldsymbol{R}_m^2(ka)\boldsymbol{E}_m(2L)\right]\right\}\,. \tag{6.10}$$

For simplicity it is now assumed the source radiates equally in free-field in both directions,

$$\boldsymbol{a}_{S,m}(\omega) = \boldsymbol{b}_{S,m}(\omega)\,. \tag{6.11}$$

Substituting *Eq. 6.8*, *Eq. 6.10* and *Eq. 6.11* into *Eq. 6.1* leads to,

$$\boldsymbol{a}_m^{(r)}(\omega) = \boldsymbol{\mathcal{R}}_m(z_0,\omega)\boldsymbol{a}_{S,m}(\omega)\,, \tag{6.12}$$

where $\boldsymbol{\mathcal{R}}_m(z_0,\omega)$ is of the form,

$$\boldsymbol{\mathcal{R}}_m(z_0,\omega) = [\boldsymbol{E}_m(z_0) + \boldsymbol{R}_m(ka)\boldsymbol{E}_m(2L-z_0)]\text{Inv}\left\{\left[\boldsymbol{I} - \boldsymbol{E}_m(2L)\boldsymbol{R}_m^2(ka)\right]\right\}\,. \tag{6.13}$$

Following the same procedure to obtain the modal amplitude at the left open end of the duct $\boldsymbol{a}_m^{(l)}(\omega)$, noting the effective distance z_0 for the right open end of the duct becomes $L - z_0$ for the left open end, it can be shown that,

$$\boldsymbol{a}_m^{(l)}(\omega) = \boldsymbol{\mathcal{R}}_m(L-z_0,\omega)\boldsymbol{a}_{S,m}(\omega)\,, \tag{6.14}$$

The approximate radiation from a finite length duct due to a single azimuthal mode m is of the form,

$$\begin{aligned} p_m^{(D)}(R,\phi,\theta,\omega) \approx \Big(\boldsymbol{D}_m^T(\phi,ka)\boldsymbol{\mathcal{R}}_m(z_0,\omega) + \boldsymbol{D}_m^T(\pi-\phi,ka)\boldsymbol{\mathcal{R}}_m(L-z_0,\omega)\Big) \\ \boldsymbol{a}_{S,m}(\omega)\left(\frac{a}{R}\right)\mathrm{e}^{-j(kR+m\theta)}\,, \end{aligned} \tag{6.15}$$

where $\boldsymbol{D}_m^T(\phi,ka)$ and $\boldsymbol{D}_m^T(\pi-\phi,ka)$ are row vectors of directivity factors calculated from *Eq. 2.52* for each radial mode n. Following the analysis in *Chapter 4*, the mean square pressure can be predicted for rotating point sources using,

$$\overline{p^2}^{(D)}(R,\phi,\omega) = \frac{1}{2}\sum_{m=-\infty}^{\infty}\left|p_m^{(D)}(R,\phi,\theta)\right|^2. \tag{6.16}$$

6.1.1 Distribution of incoherent sources

The modal amplitude at the open end of a finite duct of *Eq 6.12* can be generalised to source distributions. Multiplying by the complex conjugate in *Eq. 6.12*,

$$E\{|\boldsymbol{a}_m^{(r)}(\omega)|^2\} = \boldsymbol{\mathcal{R}}_m(z_0,ka)E\{\boldsymbol{S}_{aa,m}(\omega)\}\boldsymbol{\mathcal{R}}_m^H(z_0,\omega)\,, \tag{6.17}$$

where the superscript ^{H} is the Hermitian Transpose and $E\{\boldsymbol{S}_{aa,m}(\omega)\}$ is the cross spectral matrix of modal pressure amplitude of the form,

$$E\{\boldsymbol{S}_{aa,m}(\omega)\} = \begin{bmatrix} E\{|a_{S,m11}(\omega)|^2\} & \dots & 0 \\ \vdots & E\{|a_{S,m22}(\omega)|^2\} & \\ 0 & & E\{|a_{S,mn'l'(\omega)}|^2\} \end{bmatrix}. \tag{6.18}$$

To ensure the incoherence of the modes, the coupling terms $E\{\boldsymbol{S}_{aa,m}(\omega)\}$, for modes of different radial order n and l, for $n \neq l$ (the off diagonal elements) are set to 0. Repeating the above analysis to form an expression for $E\{|\boldsymbol{a}_m^{(l)}(\omega)|^2\}$ shows that the mean square pressure for source distributions inside finite lengths ducts is of the form,

$$\begin{aligned}\overline{p^2}(R,\phi,\omega) = &\left(\frac{a}{R}\right)^2 \\ &\sum_{m=-\infty}^{\infty}\Big(\boldsymbol{D}_m(\phi,ka)\boldsymbol{\mathcal{R}}_m(z_0,\omega)E\{\boldsymbol{S}_{aa,m}(\omega)\}\boldsymbol{\mathcal{R}}_m^H(z_0,\omega)\boldsymbol{D}_m^H(\phi,ka)+ \\ &\boldsymbol{D}_m(\pi-\phi,ka)\boldsymbol{\mathcal{R}}_m(L-z_0,\omega)E\{\boldsymbol{S}_{aa,m}(\omega)\}\boldsymbol{\mathcal{R}}_m^H(L-z_0,\omega)\boldsymbol{D}_m^H(\pi-\phi,ka)\Big),\end{aligned} \tag{6.19}$$

6.1.2 Investigation of pipe axial standing waves

From classical theory resonant frequencies are observed due to axial standing waves in a finite length duct when the length of the pipe and wavelength of the frequency are approximately, $L/\lambda \approx 0.5, 1.5, 2.5...$, this corresponds to $kL = \pi, 3\pi, 5\pi....$ Furthermore an anti resonance occurs for $kL = 2\pi, 4\pi, 6\pi....$ Both of these expressions assume perfectly rigid ends.

Analysis of $\boldsymbol{\mathcal{R}}_m(z_0,\omega)$ from *Eq. 6.13*, which is used in calculation for all source types discussed, reveals resonance occurs when,

$$\det\left(\left|\boldsymbol{I} - \boldsymbol{E}_m(2L)\boldsymbol{R}_m^2(ka)\right|\right) = 0, \tag{6.20}$$

To satisfy *Eq. 6.20* both the propagation factor $\boldsymbol{E}_m(2L)$ and reflection matrix $\boldsymbol{R}_m^2(ka)$ must equal the identity matrix $\boldsymbol{I}$. However, in practise neither term can. Pipe resonance therefore occurs when $\boldsymbol{E}_m(2L)\boldsymbol{R}_m^2(ka)$ is a maximum. Due to the complexity of the Kernel K discussed in *Appendix A*, simple analysis of this condition cannot be achieved. A graphical example however, is presented in *Chapter 8*.

Chapter 7

Comparison between free-field and finite length ducted radiation

The previous chapter has derived expressions for the acoustic radiation from a finite length duct. This chapter uses this theory to perform predictions of the acoustic radiation from finite length ducts and compares them to the equivalent free-field radiation using the expressions derived in *Chapter 4*. These comparisons are used to identify the effect of the duct on free-field radiation. Specifically, an investigation with ducted radiation due to source radial and axial position, duct length and dipole orientation is conducted.

A comparison of the radiated power of free-field sources and those inside finite length ducts is also discussed. Finally, a COMSOL Multiphysics numerical validation study is presented to determine the accuracy of the approximations made to form the theoretical finite length duct radiation model.

7.1 Comparison between the directivity of free-field sources and those inside finite ducts

This section presents predictions of the radiation from free-field sources and those inside ducts of finite length. Computations of the radiation are presented for a distribution of incoherent axial dipole and monopole sources in a finite duct calculated by substituting *Eqs 4.67* or *4.76* respectively, *2.52* and *2.55* into *Eq. 6.19* and in free-field using *Eq. 4.37* or *4.45* respectively. Computations are also presented for rotating point dipole and monopole sources inside finite ducts calculated by substituting *Eqs 4.59* or *4.71* respectively, *2.52* and *2.55* into *Eq. 6.15* and in free-field calculated using *Eq. 4.28* or *4.41*. Four parameters are investigated, the effect of duct length, location of the sources axial plane, radii of rotation and dipole orientation to analyse the effect of the duct on source radiation.

7.1.1 A note on nil-shielding directions applied to the finite length duct model

Chapter 5 highlighted particular radiation angles ϕ_{mn} at the free-field and ducted radiation are equal for radiation due to a single azimuthal order m. At these angles, only a single duct radial mode n radiates, and all other modes have zero radiation. It was shown that in the high frequency limit when sufficient modes are present, each of which have a nil-shielding direction ϕ_{mn}, the radiation from semi-infinite ducts are in close agreement to the forward-arc of the radiation due to free-field sources.

For ducts of finite length, the radiation is the result of the superposition of the radiation from each open end of the duct. For radiation due to a single azimuthal order m, at ϕ_{mn}, where all but one mode would ordinarily have zero radiation, these angles are now masked by the radiation from the rear-arc. However, it is shown in *chapter 5* that the rear-arc radiation from a semi-infinite duct is small compared to the forward-arc at high frequencies. It is now investigated to determine if in the high frequency limit the radiation from a finite length duct matches the free-field radiation.

7.1.2 Effect of duct length on the directivity of free-field and ducted sources

This section compares the far-field directivity due to free-field sources and those from ducts of varying length. A duct length of $L/\lambda = 5$ and $L/\lambda = 0.02$, is now investigated for incoherent axial dipole and monopole sources, shown in *figure 7.1*, and rotating point dipole and monopole sources, shown in *figure 7.2*.

The mean square pressure $\overline{p^2}(R, \phi, \omega)$ for the four source types are simulated at $ka = 5$ and 35. The axial source location is assumed to be located at the centre of the duct $z_0 = L/2$, therefore only the directivity between $\phi = 0^\circ$ and 90° is shown. The point sources are assumed to rotate at $r_0/a = 0.5$ and the dipole orientation is axial ($\gamma = 0^\circ$).

Simulations are conducted for unit source strengths $\overline{F^2}(\omega)$, $\overline{Q^2}(\omega)$, $\overline{f^2}$ and $\overline{q^2}$ and observer radius $R = 1$. Clearly, the radiation due to free-field sources does not change with duct length.

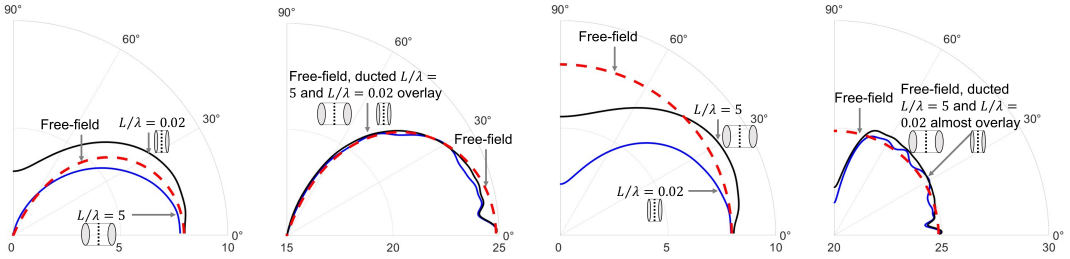

(A) Dipole $ka = 5$ (B) Dipole $ka = 35$ (C) Monopole $ka = 5$ (D) Monopole $ka = 35$

FIGURE 7.1: Directivity of free-field distributions of incoherent sources and sources located in the center $z_0 = L/2$ of a ducts of varying lengths. In dB re 1 Pa.

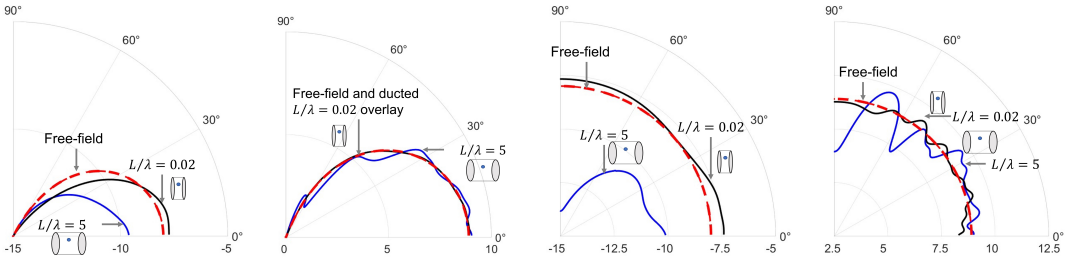

(A) Dipole $ka = 5$ (B) Dipole $ka = 35$ (C) Monopole $ka = 5$ (D) Monopole $ka = 35$

FIGURE 7.2: Directivity of free-field rotating point sources and sources located at the center $z_0 = L/2$ of ducts of various lengths. The radius of rotation is $r_0/a = 0.5$ and for the dipole source an orientation of $\gamma = 0°$ (axial) is simulated. In dB re 1 Pa.

At the relatively high non-dimensional frequency of $ka = 35$, plotted in *figs 7.1b, 7.1d, 7.2b* and *7.2d*, changing the duct lengths from $L/\lambda = 5$ to $L/\lambda = 0.02$ is seen to have a small effect on the ducted radiation. For the monopole sources this effect is shown to be less than 3 dB and the dipole sources less than 1 dB. As the excitation frequency is increased the number of propagating modes increases, each exhibiting a nil-shielding direction ϕ_{mn}. In the high frequency limit there are a continuum of nil-shielding directions where the forward-arc matches the free-field radiation. The rear-arc from the other open end is known to decrease with increasing frequency. This explains why *figs 7.1b, 7.1d, 7.2b* and *7.2d* show similar free-field and ducted radiation.

At $ka = 35$, the most notable differences between the radiation due to free-field and ducted sources are observed in the sideline directions, which as discussed in *Chapter 5* is due to reflection of near cut-off modes where nil-shielding directions are close to the sideline directions, causing a reduction and 'shielding' effect by the duct.

For the higher frequency cases shown in *figs 7.1b, 7.1d, 7.2b* and *7.2d*, the ducted radiation can be seen to oscillate around the free-field directivity. This phenomenon was first noted for the semi-infinite duct radiation model in *Chapter 5*, where it is shown that this is caused by modal interference between the radial modes n of the same azimuthal order m.

The effect of the duct length is seen to significantly affect the directivity of ducted radiation for the relatively low frequency case corresponding to $ka = 5$, shown in *figs 7.1a, 7.1c, 7.2a* and *7.2c*. In general decreasing the duct length from $L/\lambda = 5$ to $L/\lambda = 0.02$ is seen to increase the ducted radiation. For the case of the rotating point sources in *figs 7.2a* and *7.2c* the decrease in duct length causes the ducted radiation directivity to better match free-field radiation. However, decreasing the duct length from $L/\lambda = 5$ to $L/\lambda = 0.02$ for the distribution of incoherent axial dipole sources at the lower frequency investigated, shown in *figure 7.1c*, increases the ducted radiation above the free-field radiation.

Intuitively as $L/\lambda \to 0$ the effect of the duct on the radiation diminishes, as effectively the duct vanishes. This is not observed for all of the simulations presented in *figs 7.1* or *7.2*. This may be the result of the limitations in the assumption made in forming of the ducted radiation, where it is assumed that the radiation from each open end of the finite length duct is independent, and can be computed using $D_{mn}(\phi, ka)$, of *Eq. 2.52*, which was derived for a semi-infinite duct (one open end). Deviations between free-field and ducted directivities are shown in *figs 7.1* and *7.2* for the $L/\lambda = 0.02$ case to be up to 3 dB. Further work is required to determine if this a real effect or occurs due to the approximations made in calculations of the finite duct directivity.

Figures 7.1 and *7.2* reveal that the largest difference between the free-field and ducted radiation for ducts of negligible lengths is in the sideline direction $\phi \approx 90^\circ$, where the radiation from both the forward and rear-arc can contribute significantly. This disagreement is seen to be largest for the monopole sources, where for the dipole radiation the free-field and ducted radiation both tend to zero at $\phi = 90^\circ$ as shown by *figs 7.1b* and *7.2b*.

7.1.3 Effect of source axial location on the directivity of free-field and ducted sources

This section investigates the effect of the axial distance z_0 on the ducted source directivity considering finite length ducts and these are compared to the free-field directivity. The sources axial location inside a duct determines the phase of the pressure amplitude of the cut-on modes at the open ends of the duct. The sources axial location z_0 also determines the significance of the radiation due to cut-off modes. In *Chapter 5* it is discussed that cut-off modes radiate most strongly into the rear-arc, but have negligible radiation at the higher frequencies.

Figure 7.3 shows the radiated pressure at the non-dimensional frequencies of $ka = 5$ and 35, duct length $L/\lambda = 5$ and two axial source locations $z_0/\lambda = 2.5$, and $z_0/\lambda = 0.01$ due to a distribution of incoherent axial dipole and monopole sources, using the same parameters as in *figure 7.1*. The directivities are also presented in *figure 7.4* for rotating point dipole and monopole sources with the remaining parameters the same as those used in *figure 7.2*. Clearly the radiation of free-field sources does not change with axial location.

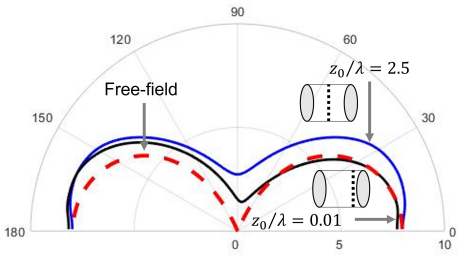

(A) Dipole $ka = 5$

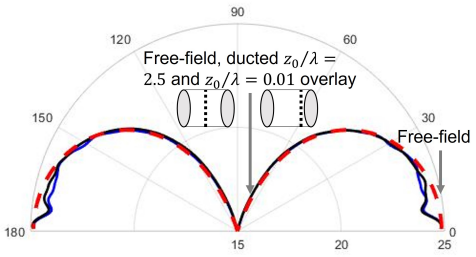

(B) Dipole $ka = 35$

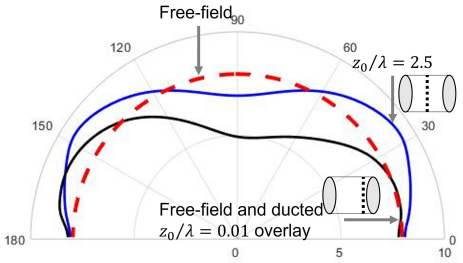

(C) Monopole $ka = 5$

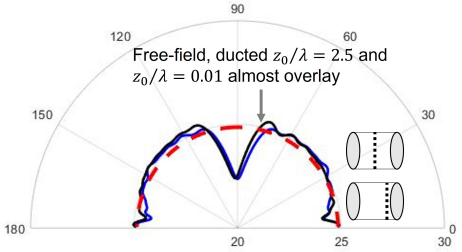

(D) Monopole $ka = 35$

FIGURE 7.3: Directivity of free-field source distributions and those shrouded inside a duct of length $L/\lambda = 5$ at various axial locations. In dB re 1 Pa.

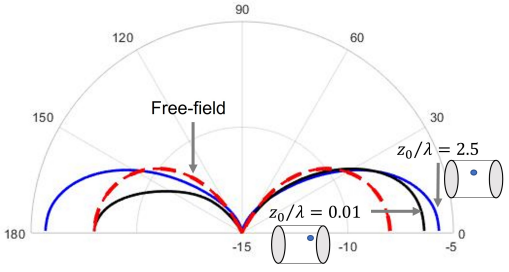

(A) Dipole $ka = 5$

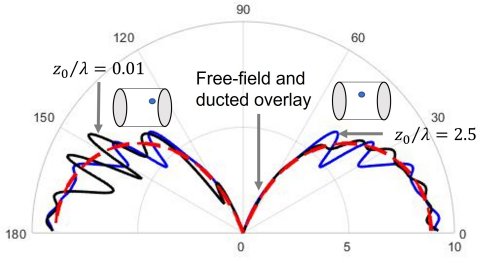

(B) Dipole $ka = 35$

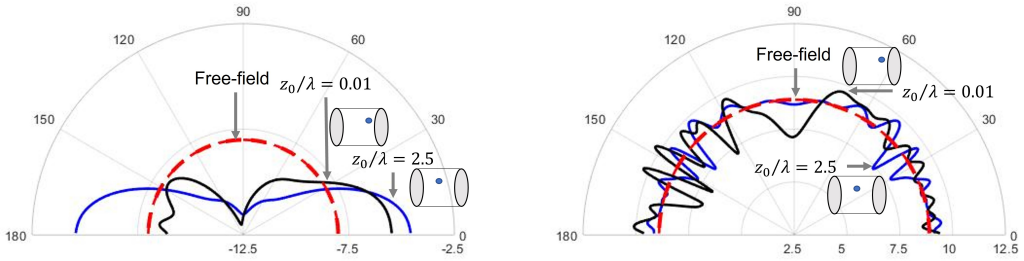

(C) Monopole $ka = 5$ (D) Monopole $ka = 35$

FIGURE 7.4: Directivity of free-field rotating point sources and those located inside ducts of length $L/\lambda = 5$ at varying axial location. The radius of rotation is $r_0/a = 0.5$ and for the dipole source an orientation of $\gamma = 0^\circ$ (axial) is simulated. In dB re 1 Pa.

For source distributions at the relatively high frequency of $ka = 35$, the effect of the source location on the far-field radiation is shown in *figs 7.3b* and *7.3d* to have an effect on the directivity of less than 0.5 dB. However, at the relatively low non-dimensional frequency of $ka = 5$, this effect is significantly larger, which is seen most strongly in the sideline directions, $\phi \approx 90^\circ$. In general, therefore, the acoustic radiation from ducts of finite length (also semi-infinite ducts as discussed in *Chapter 5*) is not sensitive to source axial location at high frequencies $ka \to \infty$.

Also shown in *figure 7.3*, for sources at the open end of the duct the directivity is shown to be roughly similar for the free-field and ducted sources over a large region of the forward-arc at the higher frequency of $ka = 35$. The same behavior is observed at $ka = 35$ for the rotating point sources, shown in *figs 7.5b* and *7.4d*. However, this behavior is not observed for the rotating point sources at the relatively low non-dimensional frequency of $ka = 5$, unlike the semi-infinite ducted case presented shown in *figs 5.6b* and *5.6d*. This difference, therefore, must be caused by the interference between the radiation from the forward-arc of the right open end and rear-arc from the left open end.

In *Chapter 5* it is shown that the directivity due to rotating point sources inside semi-infinite ducts and in free-field are similar over a range of angles where a direct 'line of sight' can be observed. The principle of direct line of sight applied to *figure 7.4* shows that this region does not exist for radiation from a finite length duct, due to modal interference between all of the reflected waves from each open end of the duct.

Analysis of the individual contribution of cut-on and cut-off modes is shown in figure 7.5 for the radiation from a finite length duct in *figure 7.4*, for the source near the open end case $z_0/\lambda = 0.01$. It is revealed that the cut-off modes make a contribution of less than 1 dB to the ducted directivity. This is unsurprising as the rear-arc radiation from a semi-infinite duct was significantly lower than the forward-arc radiation, especially at high frequency i.e. as shown by example in *figure 5.5*.

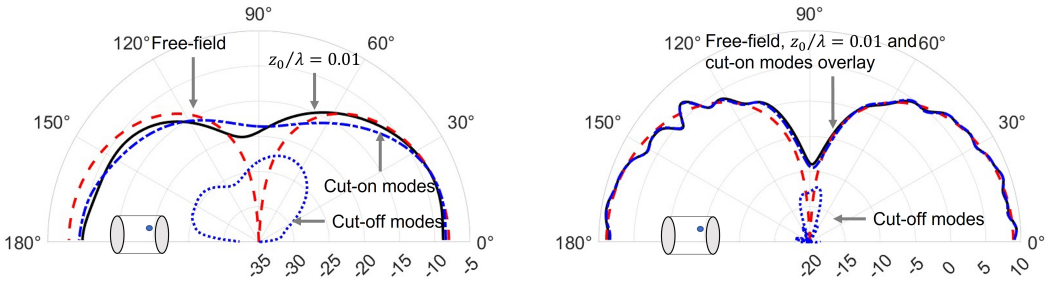

(A) Dipole $ka = 5$

(B) Dipole $ka = 35$

FIGURE 7.5: Directivity of free-field rotating point sources and those located inside ducts of length $\boldsymbol{L/\lambda = 5}$ near the open end $z_0/\lambda = 0.01$. The radius of rotation is $r_0/a = 0.5$ and for the dipole source an orientation of $\gamma = 0°$ (axial) is simulated. The contribution due to the cut-on and cut-off modes is shown. In dB re 1 Pa.

7.1.4 Effect of radius of rotation on the directivity of free-field and ducted sources

This section investigates the effect of source radius of rotation on the directivity of free-field sources and sources inside ducts of finite length. Analysis is conducted for sources inside both long and short ducts relative to the wavelength λ. It is shown in *chapter 5* that sources located near the wall of the duct $r_0/a \to 1$ produce an increase in ducted radiation, which is seen most strongly for dipole sources. This effect increases as the source moves closer to the open end $z_0/\lambda \to 0$.

To confirm this behavior for a finite length duct, *figure 7.6* shows the directivity of free-field and ducted sources at the two radii of rotations $r_0/a = 0$ and 1. The remaining parameters are the same as those used in *figure 7.2*. Note that the radiation of free-field sources does not change with radial location.

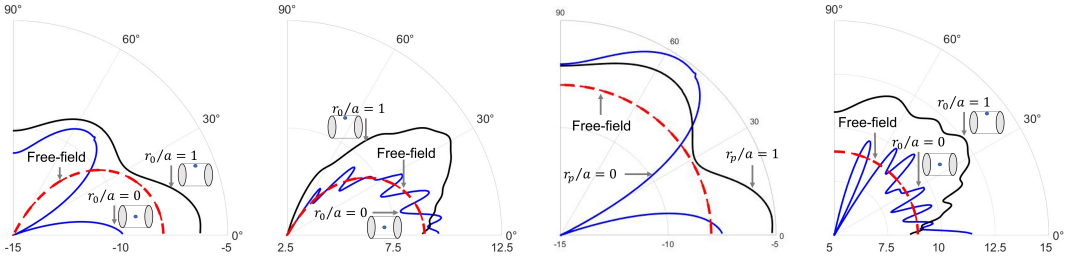

(A) Dipole $ka = 5$, $L/\lambda = 5$

(B) Dipole $ka = 35$, $L/\lambda = 5$

(C) Monopole $ka = 5$, $L/\lambda = 5$

(D) Monopole $ka = 35$, $L/\lambda = 5$

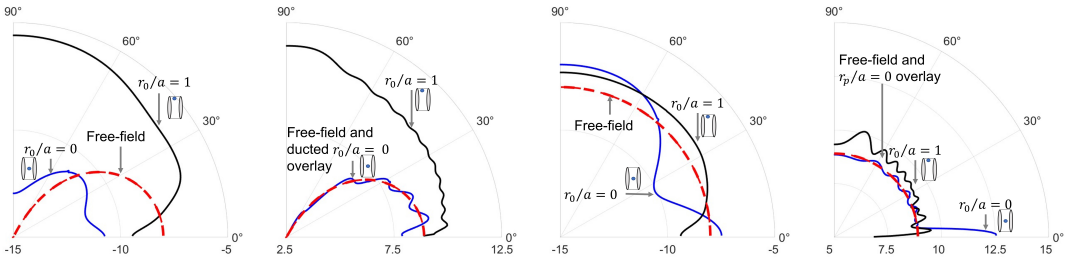

(E) Dipole $ka = 5$, $L/\lambda = 0.02$

(F) Dipole $ka = 35$, $L/\lambda = 0.02$

(G) Monopole $ka = 5$, $L/\lambda = 0.02$

(H) Monopole $ka = 35$, $L/\lambda = 0.02$

FIGURE 7.6: Directivity of free-field rotating point dipole and monopole sources and those at the center $z_0 = L/2$ of ducts of length $L/\lambda = 5$ and $L/\lambda = 0.02$, for the dipole source the orientation is simulated to be $\gamma = 0°$ (axial), for various radii of rotation. In dB re 1 Pa.

Figure 7.6 confirms that rotating sources at the wall, $r_0/a = 1$, of finite length ducts can produce a higher radiation than sources not at the duct wall. This behavior is observed over a wide range of far-field angles, $10° < \phi < 170°$ (note the figures are symmetric about $\phi = 90°$). The radiation at these angles is observed to be larger than the radiation of equivalent sources in free-field.

The increase in free-field source radiation due to the inclusion of the duct for sources located at the duct wall $r_0/a = 1$ was seen previously in *Chapter 5* for the semi-infinite ducted case, where a pressure doubling is observed. For the source on the duct rim cut-of modes were shown to radiate strongly causing the ducted radiation to be greater than free-field. The increase in ducted radiation due to increasing radii of rotations is seen to have greater effect for dipole than monopole sources, also noted from *Chapter 5*

For the relatively long duct of length $L/\lambda = 5$, at the relatively low frequency investigated corresponding to $ka = 5$, shown by *figs 7.6a* and *7.6c*, the radius of rotation is seen to affect the shape of the directivity, where at the higher non-dimensional frequency investigated $ka = 35$, shown by *figs 7.6b* and *7.6d* the shape follows a similar pattern to the free-field radiation.

7.1.5 Effect of dipole orientation on the directivity of free-field and ducted sources

This final section compares the directivity of free-field and ducted sources with varying dipole orientation γ. *Figure 7.7* shows the directivity of free-field and ducted rotating point dipole sources for two dipole orientations $\gamma = 45°$ and $90°$. The remaining parameters are the same as in *figure 7.2*.

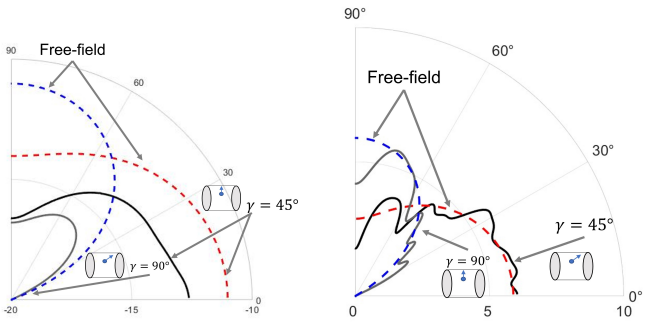

(A) Dipole $ka = 5$ (B) Dipole $ka = 35$

FIGURE 7.7: Directivity of rotating point dipole sources in free-field and inside a finite length ducts of length $L/\lambda = 5$ at the center $z_0 = L/2$ and radius of rotation $r_0/a = 0.5$ with varying dipole orientations. In dB re 1 Pa.

Much of the same conclusions can be drawn from *figure 7.7* as is discussed for *figure 5.10* for the semi-infinite duct case, where it is shown that increasing the dipole orientation shifts the mean square pressure radiation towards the sideline directions for both free-field and ducted sources. The conclusions regarding duct length L, axial location z_0 and radial location r_0 discussed earlier in this chapter are not affected by dipole orientation γ.

7.1.6 Summary of the differences between semi-infinite and finite length duct radiation

This section has compared the directivity of free-field sources to those inside ducts of finite length. This analysis is conducted for sources inside semi-infinite ducts in *Chapter 5*.

For both the semi-infinite and finite length duct cases the sources axial location is shown to have a diminishing effect as the frequency increases. This is due to the increase of the number of propagating modes as discussed in *Section 5.3*. Furthermore the radiation of sources from both duct types is similar to free-field radiation (except in the rear-arc of the semi-infinite duct case). Largest differences between free-field and ducted radiation are observed in the sideline directions, $120° < \phi < 60°$ where the relatively large reflection effect of near cut-off modes (which radiate strongest in the sideline directions) incident upon the open end of the duct decreases there radiation.

As the radius of rotation is increased $r_0/a \to 1$, the radiation from the duct increases, which is a larger effect for dipole sources compared to monopole sources. This effect is seen strongest for the dipole sources and sources near the open end of the duct and this has been shown to be true for both finite and semi-infinite ducts.

7.2 Sound power radiated by free-field and ducted sources

This section examines the effect of the sound power radiated by free-field and ducted sources. Three major aspects are discussed here. Firstly, a discussion of duct length and source axial location on the ducted power radiation is presented. An investigation of source radial location is then undertaken to confirm that r_0 has a dominating effect on ducted sound power which was noted for the semi-infinite case from *Chapter 5*.

It is shown in *Section 7.1.2* that the dependence on duct length L for ducted radiation is shown to be high at relatively low frequency, ka. Similarly, *Section 7.1.3* shows that source axial location also has a strong effect on the directivity of ducted sources at relatively low frequencies. Conversely, at relatively high frequencies, the effect of both L and z_0 was shown to be small, causing a difference of typically 1 dB at $ka = 35$. The most significant effect of changing duct length and source axial location is to alter the relative phase of the modal amplitude at the open end of the duct. At high frequencies where there are a sufficient numbers of modes, the relative phase, from *Eq. 6.15*, change between them becomes less significant, . In this section the sound power radiated by sources inside ducts of varying length and at varying axial location are investigated to determine their behavior at low frequency and confirm that only a small effect is observed at high frequency with varying L and z_0.

Computations of free-field and ducted sound power are presented for a distribution of incoherent axial dipole and monopole sources in a finite duct calculated by substituting *Eqs 4.67* or *4.76* respectively, *2.52*, *2.55* and *6.19* into *Eq. 2.57*, and in free-field using *Eq. 4.49* or *4.50* respectively. Computations are also presented for rotating point dipole and monopole sources inside finite ducts calculated by substituting *Eqs 4.59* or *4.71* respectively, *2.52*, *2.55* and *6.15* into *Eq. 2.57* and in free-field calculated using *Eq. 4.47* or *4.48*.

7.2.1 Effect of sound power due to duct length

This section investigates the effect of duct length on the sound power radiated from ducted sources relative to those in free-field using,

$$\Pi(\omega) = \frac{W^{(D)}(\omega)}{W^{(ff)}(\omega)}. \tag{7.1}$$

Figure 7.8 shows $\Pi(\omega)$ for distributions of incoherent axial dipole, and monopole sources, as well as rotating point dipole and monopole sources plotted against L/λ for a fixed frequency of $ka = 5$. A radius of rotation and dipole orientation are assumed to be $r_0/a = 0.5$ and $\gamma = 0^\circ$ (axial) respectively. Clearly, the free-field sound power is not affected by duct length. The theoretical pipe resonances, discussed in *Chapter 6*, $(L/\lambda = 0.5, 1.5, 2.5...)$ are also indicated in the figure for ducts with a rigid termination.

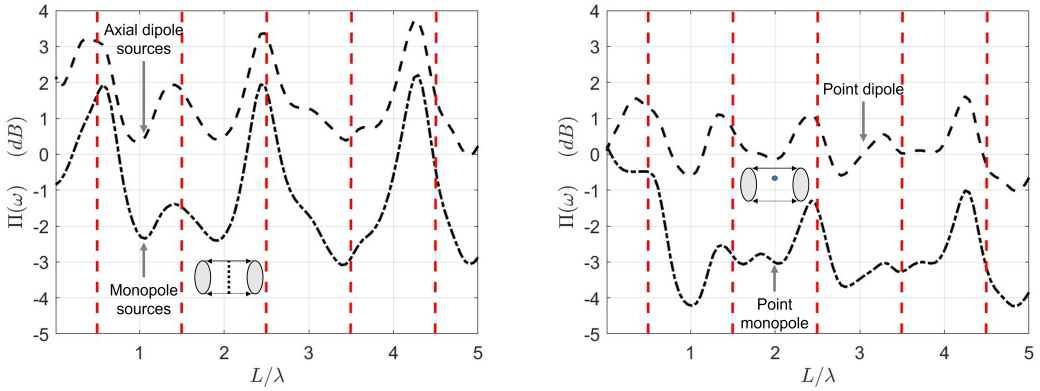

(A) Source distributions (B) Rotating point sources

FIGURE 7.8: Free-field to ducted power ratio at the non-dimensional frequency $ka = 5$ for incoherent source distributions and rotating point sources considering sources at the center of finite length ducts with a radius of rotation $r_0/a = 0.5$ and dipole orientation $\gamma = 0°$ (axial). Theoretical pipe resonances are shown (red dashed lines).

Figure 7.8 reveals a periodic variation of sound power with increasing duct length. In general the power ratio $\Pi(\omega)$ is larger than 0 dB for dipole sources, implying that at this frequency there is a small amplification in power due to the inclusion of the duct. The point monopole sources however, are shown to have a clear reduction in radiated power by the inclusion of the duct, $\Pi(\omega) < 0\ dB$. The duct length, for this relatively low frequency of $ka = 5$ has been shown to vary the power radiated by the ducted source by as much as 4 dB. A physical interpretation for this behavior is provided in Section 7.2.4.

The periodic behavior can be observed to coincide with the nodes and anti-nodes of low order duct resonances, which can be seen most strongly for the source distributions. As the duct length increases, the simple prediction of pipe resonances $kL = \pi, 3\pi, 5\pi...$ loses accuracy and the predictions of pipe resonances deviate. This can also be observed in the figure, as for example all sources investigated have a pipe resonance at approximately $L/\lambda \approx 4.2$, narrowly avoiding the predicted pipe resonance at $L/\lambda = 4.5$.

The same procedure used to produce *figure 7.8* is now repeated for the higher non-dimensional frequency of $ka = 35$ as shown in *figure 7.9*. The same oscillatory behavior is observed with a much smaller fluctuation amplitude of, $-1\,dB < 10\log(\Pi(\omega)) < 1\,dB$.

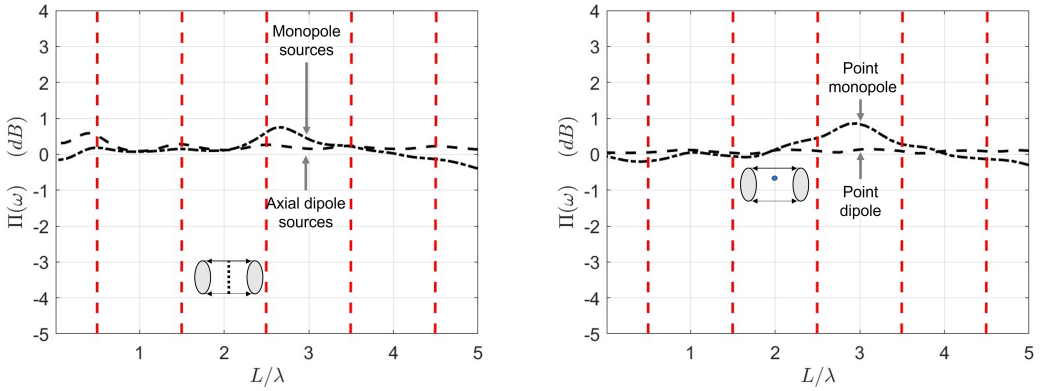

(A) Source distributions (B) Rotating point sources

FIGURE 7.9: Free-field to ducted power ratio at the non-dimensional frequency $ka = 35$ for incoherent source distributions and rotating point sources considering sources at the center of finite length ducts with a radius of rotation $r_0/a = 0.5$ and dipole orientation $\gamma = 0°$ (axial). Theoretical pipe resonances are shown (red dashed lines).

7.2.2 Effect of sound power due to source axial location

This section investigates the dependence of the sources axial location z_0 on the radiated sound power of ducted sources.

The power ratio $\Pi(\omega)$ is now used to investigate the effect of the sources axial location on the ducted radiation relative to free-field sources. *Figure 7.10* shows $\Pi(\omega)$ for distributions of incoherent axial dipole, and monopole sources, as well as rotating point dipole and monopole sources plotted against z_0/L for a fixed duct length of $L/\lambda = 5$ and a non-dimensional frequency of $ka = 5$. The remaining parameters are the same as in *figure 7.12*.

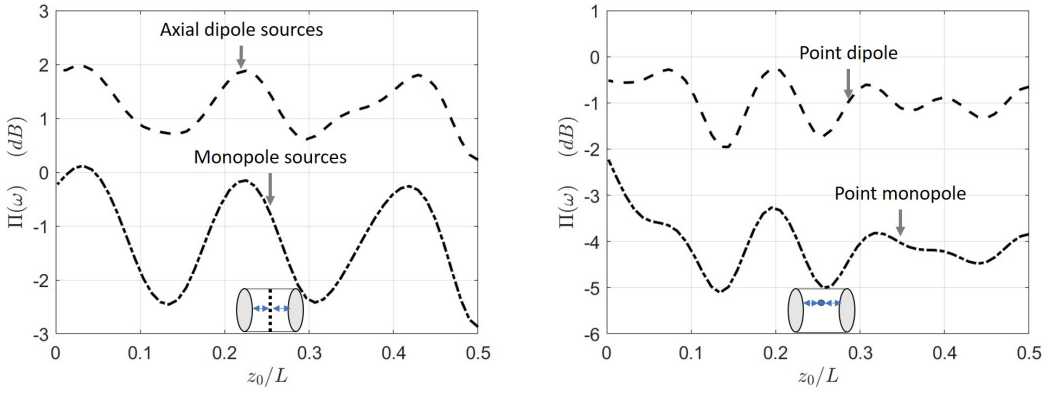

(A) Source distributions (B) Rotating point sources

FIGURE 7.10: Free-field to ducted power ratio at the non-dimensional frequency $ka = 5$ for incoherent source distributions and rotating point sources plotted against axial location z_0/L for a fixed duct length of $L/\lambda = 5$ with a radius of rotation $r_0/a = 0.5$ and dipole orientation $\gamma = 0°$.

Similar oscillatory behavior is observed in *figure 7.10* which has been observed previously in all figures of this section. The location of the source is shown to vary the sound power from the duct by up to 3 dB. Distributions of incoherent axial dipole sources are observed to have an increase in radiation due to the inclusion of the duct for the source at all axial locations. Contrarily the other sources investigated in *figure 7.10* have a consistent reduction in sound power due to the inclusion of the duct. A physical interpretation of these results is provided in Section 7.2.4.

The same analysis shown in *figure 7.10* is now repeated for the higher non-dimensional frequency of $ka = 35$ in *figure 7.11*. The same oscillatory behavior is observed with a much smaller fluctuation amplitude of, $-0.5\,dB < \Pi(\omega) < 0.5\,dB$. In both cases the dipole sources are shown to have a small increase in sound power due to the inclusion of the duct where the monopole sources exhibit a small reduction in sound power.

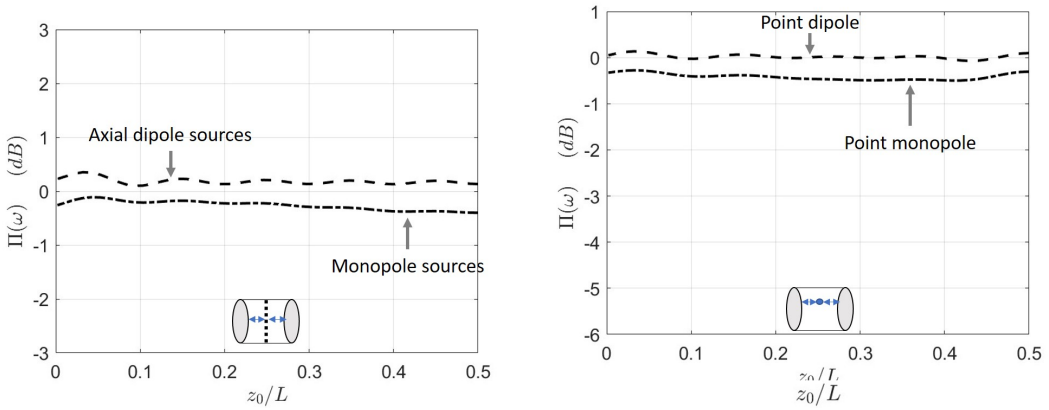

(A) Source distributions (B) Rotating point sources

FIGURE 7.11: Free-field to ducted power ratio at the non-dimensional frequency $ka = 5$ for incoherent source distributions and rotating point sources for a radius of rotation $r_0/a = 0.5$ and dipole orientation $\gamma = 0°$.

Further investigation into the effect of sound power due to source axial location is presented using the power split ratio $\eta(\omega)$, defined as the ratio between the sound power radiated to the forward-arc $0° \leq \phi \leq 90°$ to the total power. The ratio of sound power radiated to the rear-arc is therefore $1 - \eta(\omega)$. This term is investigated in *Chapter 3*, where only a single mode is considered only, unlike the multi-modal computations considered here.

Figure 7.12 shows the power split ratio $\eta(\omega)$ for distributions of incoherent axial dipole, and monopole sources, as well as rotating point dipole and monopole sources plotted against z_0/L for a fixed duct length of $L/\lambda = 5$. The point sources are assumed to have a radius of rotation of $r_0/a = 0.5$ and for the dipole sources and orientation of $\gamma = 0°$ (axial) is simulated.

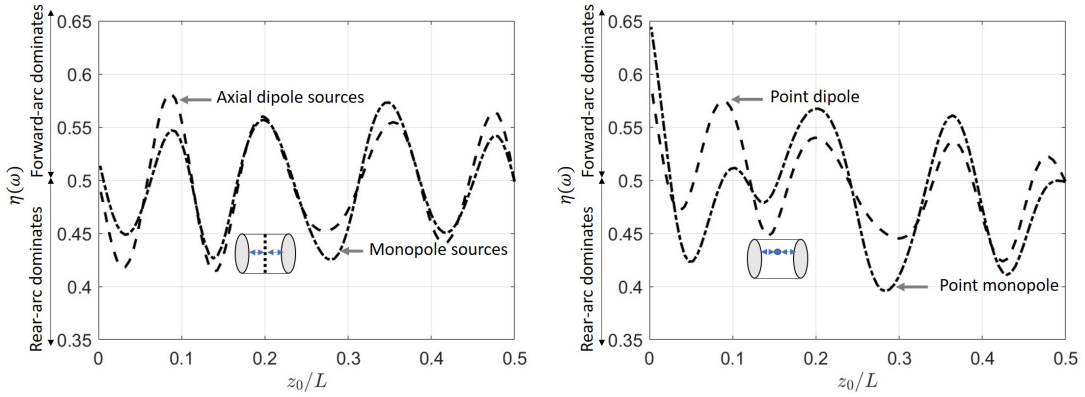

(A) Source distributions (B) Rotating point sources

FIGURE 7.12: Power split ratio of forward-arc to total sound power at the non-dimensional frequency $ka = 5$ for incoherent source distributions and rotating point sources for a radius of rotation $r_0/a = 0.5$ and dipole orientation $\gamma = 0°$.

Similar to the effect of the duct length, variation in the source axial location is seen to vary the sound power radiated from ducted sources periodically. For incoherent source distributions at one open end of the duct $z_0/L \approx 0$, the sound power split is $\eta(ka) \approx 0.5$, identifying equal forward and rear-arc power radiation. and for the rotating cases, the sound power split is shown to bias the forward-arc. This behavior identifies the increase of rear-arc radiation due to cut-off modes has no notable effect on the ducted power radiation for finite ducts.

The same analysis shown in *figure 7.12* is now repeated for the higher non-dimensional frequency of $ka = 35$ in *figure 7.13*. The same oscillatory behavior is observed with a much smaller fluctuation amplitude of, $0.45 < \mu(\omega) < 0.55$.

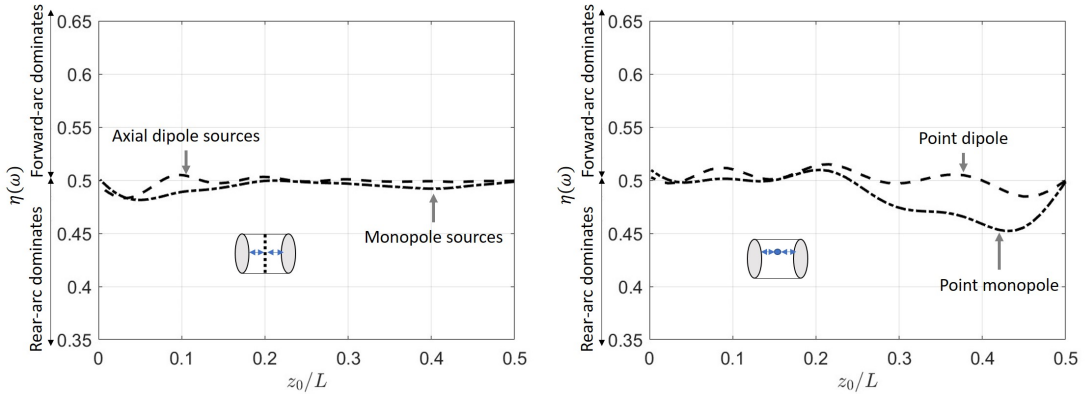

(A) Source distributions (B) Rotating point sources

FIGURE 7.13: Power split ratio of forward-arc to total sound power at the non-dimensional frequency $ka = 35$ for incoherent source distributions and rotating point sources for a radius of rotation $r_0/a = 0.5$ and dipole orientation $\gamma = 0°$.

7.2.3 Effect of sound power due to source radius of rotation

The sound power radiated by free-field and ducted sources with varying radii of rotation is now investigated. *Figure 7.14* shows the the power ratio $\Pi(\omega)$ of *Eq. 7.1* for free-field rotating point dipole and monopole sources and those inside ducts of length $L/\lambda = 5$ and $L/\lambda = 0.02$ for two radii of rotation, $r_0/a = 0$ and 1 at the duct centre $z_0 = L/2$ an axial dipole $\gamma = 0°$ is assumed. Note that the free-field sound power is not affected by source radial location r_0.

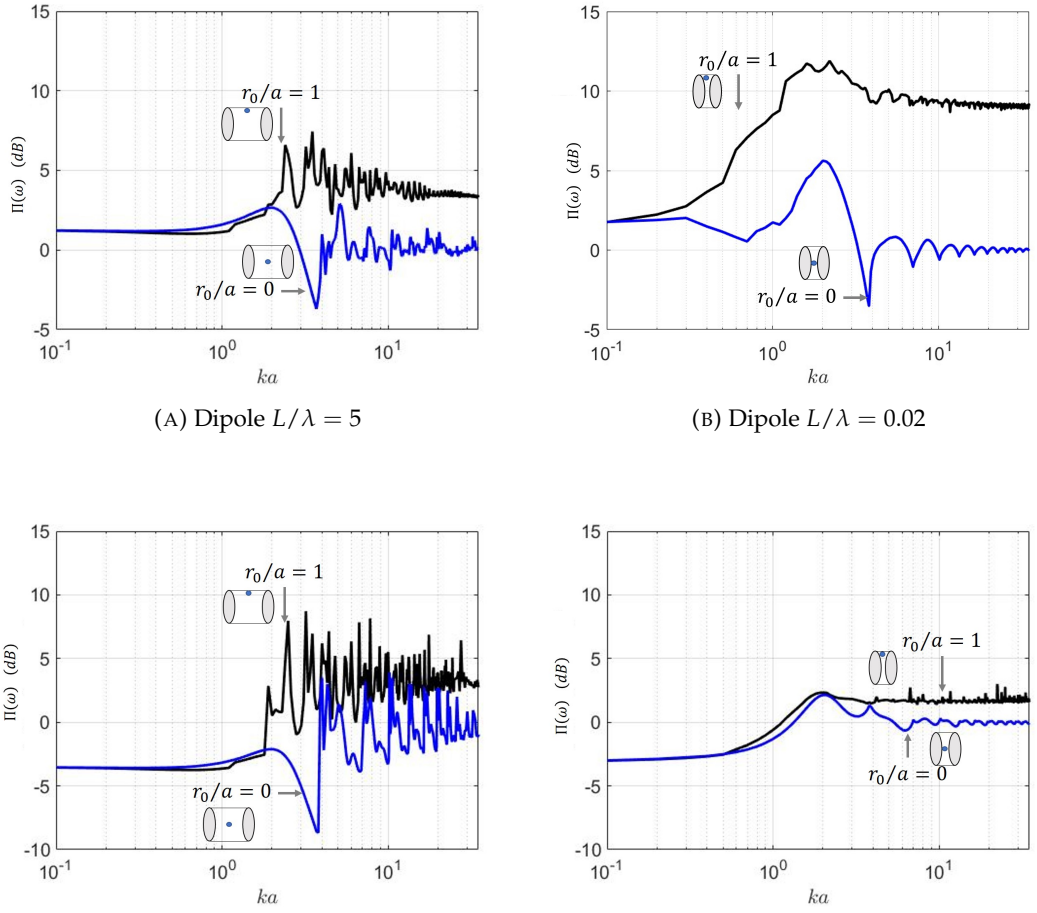

(A) Dipole $L/\lambda = 5$

(B) Dipole $L/\lambda = 0.02$

(C) Monopole $L/\lambda = 5$

(D) Monopole $L/\lambda = 0.02$

FIGURE 7.14: Ratio of free-field to ducted power for rotating point sources with $\gamma = 0°$ at the center $z_0 = L/2$ of ducts of varying length with and radii of rotation.

Figure 7.14 demonstrates that the source radius of rotation is an important parameter in determining overall sound power radiation from ducted sources. At the higher frequencies, sources on the duct axis $r_0/a = 0$ are shown to give equal free-field to ducted sound power radiation $\Pi(\omega) \approx 1$, which is the case for both source types and is shown to be the same for both duct lengths considered. However, for the source at the wall of the duct both the high frequency and the low frequency radiation is highly dependent on source type and duct length.

In *figure 7.14* the high frequency free-field to ducted power ratio is observed to increase $\Pi(\omega)$ for the sources at the wall, $r_0/a = 1$, for rotating point dipole and monopole sources inside ducts of length $L/\lambda = 5$ and $L/\lambda = 0.02$, are shown in *Table 7.1* below. These can be noted to be effectively double the radiated power from the semi-infinite cases shown in *Table 7.1*

Length / Source	$L/\lambda = 5$	$L/\lambda = 0.02$
Dipole	$\approx 3\ dB$	$\approx 9\ dB$
Monopole	$\approx 3\ dB$	$\approx 2\ dB$

TABLE 7.1: High frequency free-field to ducted power ratio for the source at the duct wall $r_0/a = 1$

Considering low frequencies, a frequency region exists $ka \lesssim 1.8$ where only the plane wave radiates efficiently from the ducted sources. The source distributions are shown to have a higher ducted than free-field power *figs 7.14a, 7.14b* and the point source is shown to have a lower ducted than free-field power *7.14d*, except for the dipole source located at the duct rim $(r_0/a, z_0/\lambda) = (1, 0)$, where the radiation is shown to be higher than the source on the duct axis $r_0/a = 0$, due to the radiation of cut-off modes, which is noted from *Chapter5*.

Finally, deep troughs are observed for the dipole power spectra case *7.14a* and sharp peaks are observed in the monopole power spectra *figs 7.14c*. These peaks are observed at modal cut-on frequencies, as detailed in Snakowska and Jurkiewicz (2010), where for the monopole source amplitude a mode just cut-on (or cut-off), $a_{mn} \propto 1/k_{z,mn}$ from *Eqs. 4.71* and *4.76* and at cut-on $k_{z,mn} = 0.02$. For the dipole source amplitude, modal reflections are known to locally decrease the radiated ducted power near the modal cut-on frequencies, which explains the troughs in the spectra of *figure 7.14a*. These phenomenon are not observed as strongly for the duct of negligible length cases $L/\lambda = 0.02$.

7.2.4 Interpretation of sound power results

The variation of radiated sound with duct length and its position within the duct may be explained by the variation in radiation resistance 'seen' by the sources. This concept is mostly easily explained for point sources. For point axial dipole ($\gamma = 0°$) and monopole sources the radiated sound power $W(\omega)$ at a single frequency can be computed from,

$$W(\omega) = \begin{cases} \frac{1}{2}\,\mathrm{Re}\{u_z(\boldsymbol{X}_0, \omega) f^*(\omega)\}, & \text{Dipole,} \\ \frac{1}{2}\,\mathrm{Re}\{p(\boldsymbol{X}_0, \omega) q^*(\omega)\}, & \text{Monopole,} \end{cases} \tag{7.2}$$

where $\boldsymbol{X}_0$ is the source plane location, and $u_z(\boldsymbol{X}_0, \omega)$ and $p(\boldsymbol{X}_0, \omega)$ are the particle velocity and acoustic pressure *inside* the duct at the source plane. The radiated sound power *outside* the duct due to dipole and monopole sources is therefore determined respectively by the amplitude and phase relationship between the source strength $f(\omega)$ or $q(\omega)$ and the particle velocity $u_z(\boldsymbol{X}_0, \omega)$ or acoustic pressure $p(\boldsymbol{X}_0, \omega)$.

7.2.4.1 Radiation impedance

The particle velocity $u_z(\boldsymbol{X}_0, \omega)$ is related to the source strength $f(\omega)$ by $f(\omega) = Z(\omega)u_z(\boldsymbol{X}_0, \omega)$, where $Z(\omega)$ is the radiation impedance and quantifies the effect of the environment on the ability of the source to radiate acoustic pressure. Similarly, the pressure $p_{mn}(\boldsymbol{X}_0, \omega)$ is related to the source strength $q(\omega)$ via $p_{mn}(\boldsymbol{X}_0, \omega) = Zq(\omega)$, from Rienstra and Hirschberg (2004). The sound power may therefore be written as,

$$W(\omega) = \begin{cases} \frac{1}{2}|f(\omega)|^2 \mathrm{Re}\{Z(\omega)\}, & \text{Dipole,} \\ \frac{1}{2}|q(\omega)|^2 \mathrm{Re}\{Z(\omega)\}, & \text{Monopole,} \end{cases} \tag{7.3}$$

where $\mathrm{Re}\{Z(\omega)\}$ is referred to as the radiation resistance. The source radiation impedance can be written as the sum of its values in free field $Z^{(ff)}(\omega)$ (i.e., in the absence of the duct) and the contribution due to the effect of the duct $\Delta Z^{(D)}(\omega)$ to account for the effect of duct modes and their reflections from the open end,

$$Z(\omega) = Z^{(ff)}(\omega) + \Delta Z^{(D)}(\omega) \tag{7.4}$$

Similarly, the sound power from the duct can also be expressed in the form,

$$W(\omega) = W^{(ff)}(\omega) + \Delta W(\omega)^{(d)}(\omega) \tag{7.5}$$

7.2.4.2 Variation due to duct length

The analysis above demonstrates that the efficiency of sound power radiation for dipole and monopole sources is directly linked to the particle velocity and acoustic pressure in phase with the source strength, respectively. *Figures 7.8* and *7.9* reveal that the radiated sound power from the duct is greatest at the axial resonance frequencies, which are approximately $kL \approx \pi, 3\pi, 5\pi...$, as indicated in the figures. For these conditions on kL, the phase differences between the source strength and pressure or velocity is smallest. Similarly at a fixed frequency the pressure and particle velocity will vary periodically along the duct due to axial standing waves. Maximum and minimum sound power is therefore radiated when the source plane is located at pressure (particle velocity) nodes and anti-nodes, respectively.

7.2.4.3 Variation due to location relative to the open end

One of the most important results of this thesis is that the sound power radiated by axial dipole sources tends to infinity as it is brought increasingly closer to the duct open end. *Equation 7.3* suggests that this behaviour must be because the in-phase component of axial velocity at the source plane must also tend to infinity as is it introduced increasingly closer to the duct open end so that $\Delta Z^{(d)}(\omega) \rightarrow \infty$ as $z_0/\lambda \rightarrow 0$. Since the number of propagating modes at any given frequency must be finite, the cause of the progressively increasingly sound power as $z_0/\lambda \rightarrow 0$ must be due to the contribution to the radiated sound power from cut-off modes, as demonstrated separately in the convergence study of *Section 4.3.2*. In an infinite duct, cut-off modes transmit zero energy. However, in the limit of $z_0/\lambda \rightarrow 0$, whilst the pressure amplitude at the source plane is identical $a_{mn}(\omega) = 1/(2S)\Psi^*_{mn}(r_0, \tilde{\theta}_0)$ for all modes (cut-on and cut-off) from *Eq. 4.59*, the amplitude of the modal axial particle velocity for cut-off modes tends to infinity since $v_{mn}(\boldsymbol{X}_0, \omega) = -a_{mn}(\omega)k_{z,mn}/(\rho\, c\, k)$, from *Eq. 2.34*, and $k_{z,mn} \approx j\kappa_{mn}$ for increasingly cutoff modes $\zeta_{mn} \rightarrow 0$.

In an infinite duct the acoustic pressure and particular velocity are in quadrature and hence transmit zero sound power. At the open end of a duct however, the phase, between pressure and particle velocity is altered, so that cut-off modes are able to radiate to the far-field, as discussed in detail in *Chapter 4*. As $z_0 \rightarrow 0$, therefore, the radiated sound pressure tends to infinity.

It is important to recognise that this unrealistic finding is mostly likely a consequence of the assumption of point sources used to represent the source distributions under investigation in his thesis, which is therefore an unrealistic representation of real sources of finite size. Nevertheless, this analysis is valid in highlighting most of the important physics underlying the radiation from ducted sources.

7.3 Numerical validation for the finite length duct radiation model

This section presents the results of numerical simulations conducted using COMSOL Multiphysics to predict the far-field radiation from point sources inside ducts of finite length. The purpose of these simulations is to validate the theoretical results presented in the previous sections of this chapter. The free-field source is not validated here, as this formulation is mostly classical, and well validated in the literature, by for example McAlpine et al. (2015).

Figure 7.15 shows a 2 dimensional axi-symmetric model for a finite length duct created using COMSOL Multiphysics.

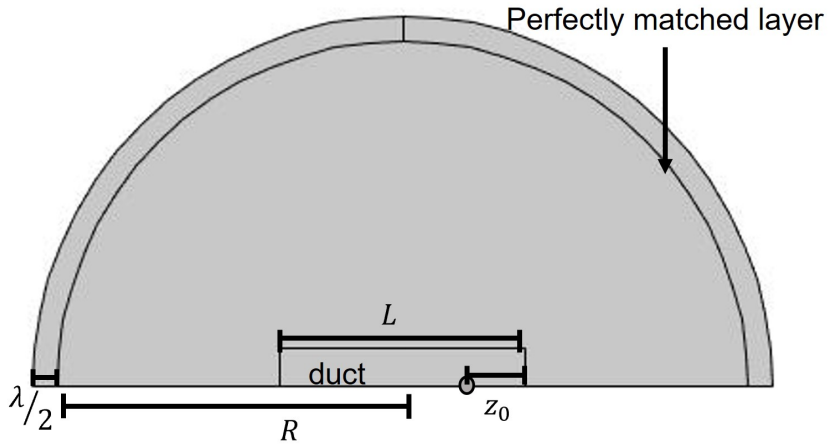

FIGURE 7.15: Geometry of the COMSOL 2 dimensional model

The geometry was generated in 2 dimensions and a revolution about the lower axis is applied. The 2 dimensional model was made from an oblong and a semi-circle, which when revolved represent the duct and computational domain respectively. The computational domain has a radius R, which has a chosen value to ensure the far-field criteria is observed to within 0.5 dB. A point source is modeled in the duct at a distance z_0 from one of the open ends. The edge of the domain at R is terminated in a perfectly matched layer, modeling a free-field. The perfectly matched layer was arbitrarily chosen to have a thickness of $\lambda/2$, and it was verified with simulations that the solution is not sensitive to this variable. A structured triangular mesh was used with a maximum distance between adjacent nodes chosen to ensure convergence to within 0.5 dB. Note this 2 dimensional axi-symmetric model allows for predictions of sources on the duct axis only $r_0/a = 0$.

Before validation simulations can be conducted using COMSOL Multiphysics it is necessary to determine the minimum distance R and number of nodes per wavelength required to ensure the solution is converged to less than 0.5 dB.

Figure 7.16 shows a plot of the directivity $Q(\phi, ka)$ of *Eq. 4.79* for a point axial dipole source $\gamma = 0°$ computed using COMSOL Multiphysics for non-dimensional frequency $ka = 5$, duct length $L/\lambda = 5$, source axial location $z_0 = L/2$. The simulations are conducted for 4 to 7 nodal points per wavelength at a far-field distance of $R = 8L$ and at a far-field radiated distance $R = 5L$ to $8L$ at 7 nodal points per wavelength. Note due to the normalisation property of $Q(\phi, ka)$ the distance R, in the far-field, does not alter the far-field directivity.

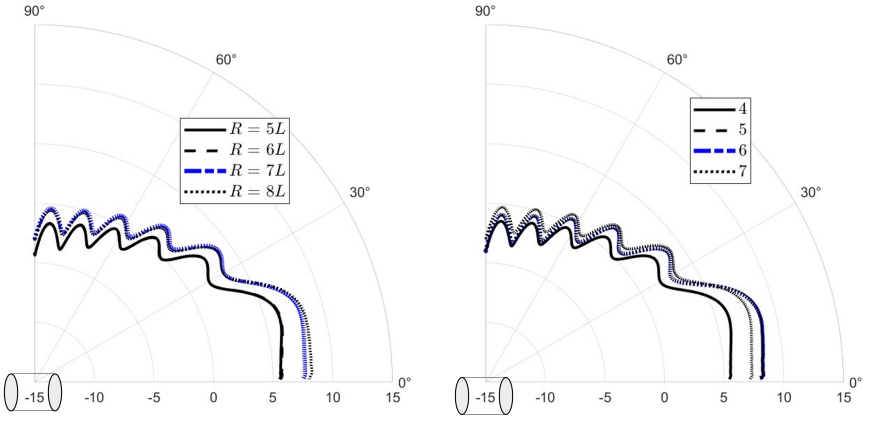

(A) Mesh study (B) Domain study

FIGURE 7.16: Directivity $Q(\phi, ka)$ computed using COMSOL Multiphysics for point dipole source on the axis $r_0/a = 0$ of a duct of length $L/\lambda = 5$ at non-dimensional frequency $ka = 5$, for a source axial location $z_0 = L/2$, varying points per wavelength and far-field radial distances, in dB.

Figure 7.16 shows the model is sufficiently converged, to within 0.5 dB at a far-field distance of $R = 7L$ with 6 points per wavelength.

7.3.1 Comparison between theoretical and numerical model

Figure 7.17 shows a comparison between the directivity $Q(\phi, ka)$ calculated using the theoretical model and using COMSOL Multiphysics. Comparisons are made for non-dimensional frequencies $ka = 5, 10$ and 35, duct length $L/\lambda = 5$, source location $(r_0/a, z_0/\lambda) = (0, 2.5)$, for a point axial dipole, $\gamma = 0°$, and monopole source. In each case only the forward-arc is shown as the directivity exhibits forward and rear-arc symmetry about $\phi = 90°$.

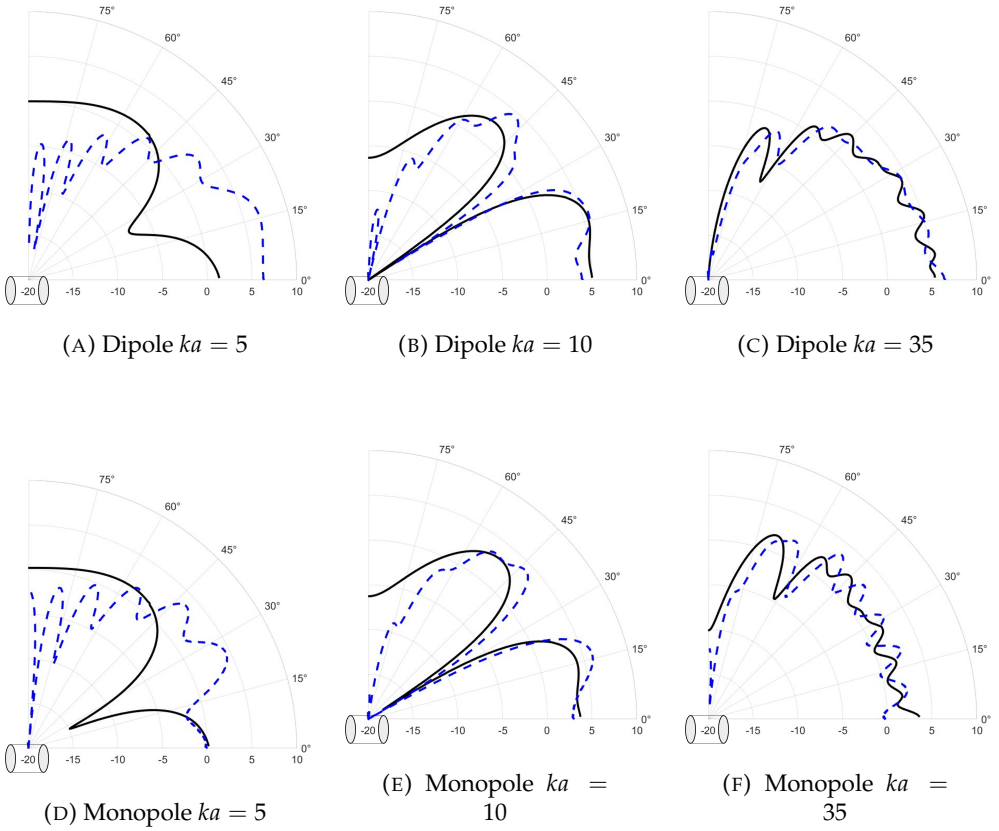

(A) Dipole $ka = 5$ (B) Dipole $ka = 10$ (C) Dipole $ka = 35$

(D) Monopole $ka = 5$ (E) Monopole $ka = 10$ (F) Monopole $ka = 35$

FIGURE 7.17: Directivity $Q(\phi, ka)$ computed using COMSOL Multiphysics (blue dashed line) and the theoretical model (solid black line) for point sources on the duct axis $r_0/a = 0$ at the center $z_0 = L/2$ of a duct of length $L/\lambda = 5$, in dB.

The agreement between the models is shown to vary significantly with frequency ka. Best agreement is observed for the $ka = 35$ case, considering the point dipole, agreement is observed to within 1 dB and approximately 3 dB (except in the sideline directions $\phi \approx 90°$) for the monopole shown in *figs 7.17c* and *7.17f* respectively. This finding implies that the theoretical model has good accuracy at high frequencies.

Reasonable agreement is observed for the $ka = 10$ cases shown in *figs 7.17b* and *7.17e*, typically to within 5 dB (although much worse agreement is observed in the sideline directions $\phi \approx 90°$). For both sources at $ka = 10$ both models predict two lobes in the forward-arc.

At the relatively low non-dimensional frequency of $ka = 5$, very poor agreement is observed as shown in *figs 7.17a* and *7.17d*. The differences at the lower frequencies are believed to occur because the theoretical predictions are based on the semi-infinite duct directivity, which for a relatively short duct of finite length disagreements are expected. It is shown in *figure 7.1*, in which the duct length is varied, that the dependence of the directivity of ducted sources on duct length is very high at the lower frequencies. This agreement between the models is now investigated for longer ducts.

7.3.2 Investigation of duct length

It is shown in *figure 7.17* that the theoretical duct radiation model does not agree with numerical COMSOL Multiphysics simulations at the non-dimensional frequency of $ka = 5$ and duct lengths of $L/\lambda = 5$. This section investigates the agreement between the theoretical and numerical models for longer ducts to observe if the agreement improves. *Figure 7.18* shows a comparison between the mathematical and numerical models for the directivity $Q(\phi, ka)$ of *Eq. 4.79* with three duct lengths $L/\lambda = 10, 20$ and 30 at the relatively low non-dimensional frequency $ka = 5$. The remaining parameters are the same as in *figure 7.17*.

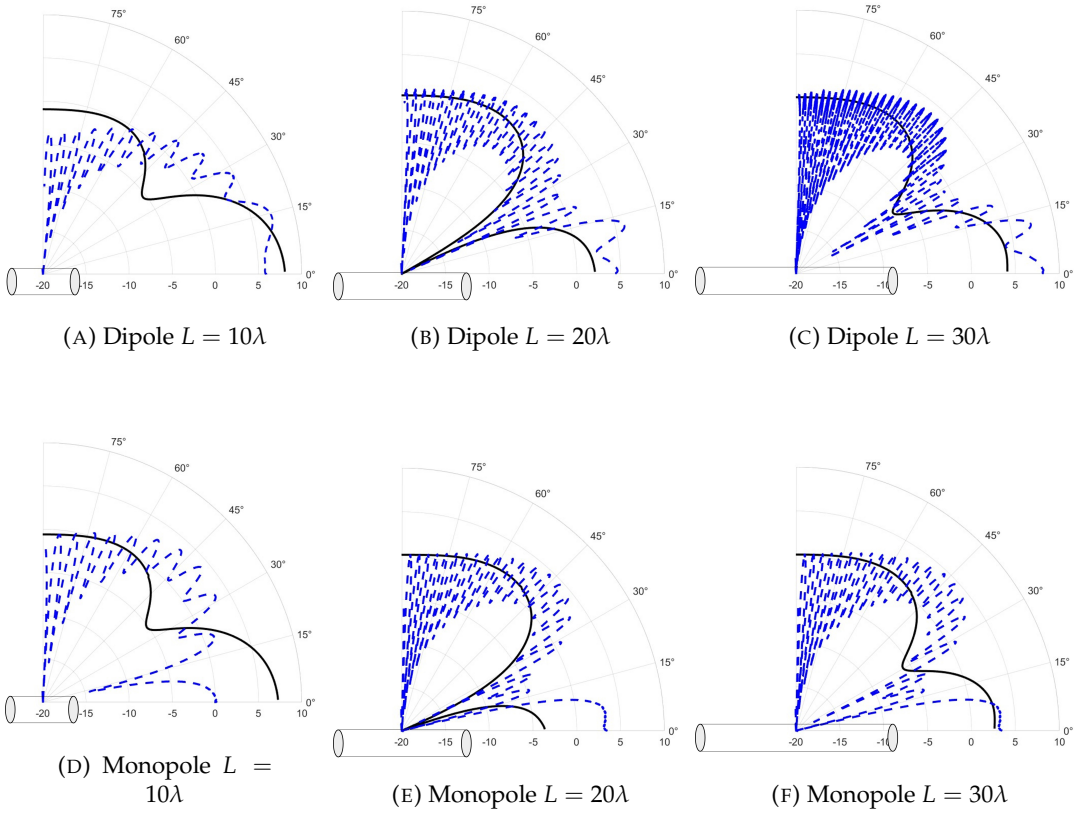

(A) Dipole $L = 10\lambda$ (B) Dipole $L = 20\lambda$ (C) Dipole $L = 30\lambda$

(D) Monopole $L = 10\lambda$ (E) Monopole $L = 20\lambda$ (F) Monopole $L = 30\lambda$

FIGURE 7.18: Directivity $Q(\phi, ka)$ computed using COMSOL Multiphysics (blue dashed line) and the theoretical model (solid black line) for point sources on axis $r_0/a = 0$ at the center $z_0 = L/2$ of a duct of varying length, in dB.

Figure 7.18 shows that the agreement between the models is improved by increasing the duct length from $L/\lambda = 10$ to 20. In all cases, the theoretical model predicts two directivity lobes in the forward-arc which is matched by COMSOL Multiphysics predictions for duct lengths of $L/\lambda = 20$ and 30. However, what is very noticeable from *figure 7.18* is the degree of oscillation in the directivity curve predicted by COMSOL Multiphysics. This is believed to be a direct consequence of increasing the domain size, noting $R = 7L$ with 6 points per wavelength is kept constant, which increases computation time from seconds (to produce *figure 7.17*) to hours.

7.3.3 Investigation of source location

This final section of the numerical validation considers the ducted radiation from sources at varying axial location. Simulations are considered at the relatively high non-dimensional frequency of $ka = 35$, where for the source in the centre $z_0 = L/2$ *figure 7.17* shows good agreement between the theoretical model and COMSOL Multiphysics simulations. *Figure 7.19* shows a comparison between the directivity $Q(\phi, ka)$ of *Eq. 4.79* between the theoretical and numerical model for source axial locations z_0/λ = 0.5 and 0.1 at frequency $ka = 35$ for a point axial dipole, $\gamma = 0^\circ$ and monopole source. The remaining parameters are the same as in *figure 7.17*.

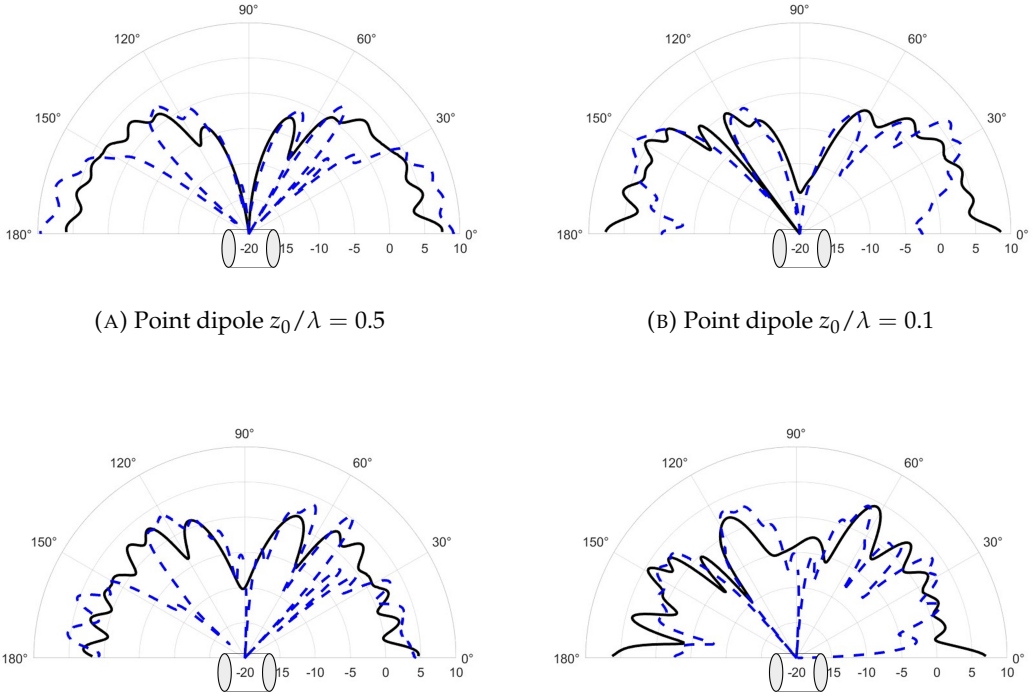

(A) Point dipole $z_0/\lambda = 0.5$

(B) Point dipole $z_0/\lambda = 0.1$

(C) Point monopole $z_0/\lambda = 0.5$

(D) Point monopole $z_0/\lambda = 0.1$

FIGURE 7.19: Directivity $Q(\phi, ka)$ computed using COMSOL Multiphysics (blue dashed line) and the theoretical model (solid black line) for point sources on axis $r_0/a = 0$ of a duct of length $L/\lambda = 5$ at varying axial locations, in dB.

Figure 7.19 shows broad agreement between the shape made by the two predicted directivities for both sources. The agreement is better for the source nearer the open end $z_0/\lambda = 0.1$ shown in *figs 7.19b* and *7.19d*. At certain angles, however, such as $\phi \approx 140^\circ$ in *figs 7.19a* and *7.19c*, disagreements are observed, where the numerical model predicts a null, which is not observed from the theoretical predictions.

This section has recorded that the theoretical model produces relatively good agreement with COMSOL Multiphysics simulations for sources at the centre of the duct $z_0 = L/2$ and at high frequencies. Poor agreement is observed at low frequencies and short ducts.

7.4 Summary

This chapter has presented a comparison between the acoustic radiation from free-field rotating point dipole and monopole sources, and incoherent distributions of axial dipole and monopole sources to those inside a finite length duct. Similarly to the findings presented in *Chapter 5*, it has been shown in the high frequency limit $ka \to \infty$ source axial location is unimportant. Furthermore, dipole sources located at the duct wall $r_0/a = 1$ have a large increase in ducted radiation, especially when located on the duct rim.

The radiation from a duct at high frequency is not sensitive to the duct length. However, at low frequency duct length plays a governing role in both the shape and level of the ducted radiation. Pipe resonance effects were shown to cause differences in the power radiated by the ducted sources of up to 4 dB.

Attempts to validate the theoretical model proposed in *Chapter 6* have been relatively successful at high frequency using COMSOL Multiphysics simulations. However, at low frequency large differences have been observed between the COMSOL Multiphysics simulations and theoretical predictions. As the length of the duct was increased the similarities between the models increased, implying the theoretical model may be invalid for short ducts at low frequency. This is believed to be a result of deriving the finite length duct model using semi-infinite duct directivity.

Chapter 8

Experimental investigation into acoustic radiation from sources inside semi-infinite ducts

In this chapter the results of an experimental investigation into the acoustic radiation from ducted sources is presented by way of validation of previous chapters. An approximate semi-infinite duct was constructed by blocking one open end of a relatively long duct of length 3.3 m with an anechoic termination. A loudspeaker driven by broadband signals was placed inside the duct at a measured radial and axial position (r_0, z_0) and 13 microphones were placed 3.5 meters away from the duct to measure directivity.

The free-field properties of the loudspeaker reveal radiation similar to a dipole source, approximately $\cos\phi$. The duct is shown to have largest effect where the free-field radiation exhibits a null. Moving the source closer to the open end of the duct is shown to reduce the effect of the duct on the forward-arc radiation. Furthermore, sources located closest to the duct wall are shown to give the highest ducted radiation.

8.1 Methodology

By means to validate the conclusions from previous chapters, experimental data was recorded to predict the directivity $Q(\phi, \theta, \omega)$ of *Eq. 8.1* and the open-to-ducted transfer function $\mathcal{T}(\phi, \theta, \omega)$ of *Eq. 8.2*. For stationary sources, an azimuthal observer angle dependence θ is introduced in *Eqs 8.1* and *8.2*, although this was not varied in the experiments. The azimuthal angle was consistent at $\theta = 90°$, as this was the most secure position to mount the loudspeaker.

To measure the acoustic pressure radiated from free-field and ducted sources, an array of 13 microphones were mounted on a rigid wire inside an anechoic chamber, as shown in *figure 8.1*, for two scenarios:

1. The loudspeakers radiation was measured by placing the source in free-field.
2. A Semi-infinite duct was formed from a plastic pipe of length $L = 3.3\ m$, radius $a = 0.15\ m$ and blocked at one end by anechoic wedges.

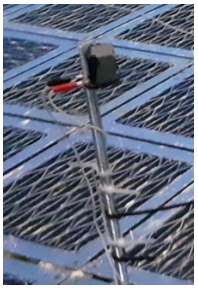

(A) Free-field

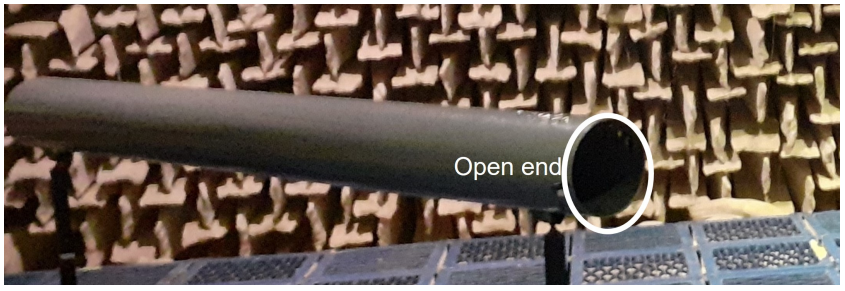

(B) Semi-infinite duct forward-arc

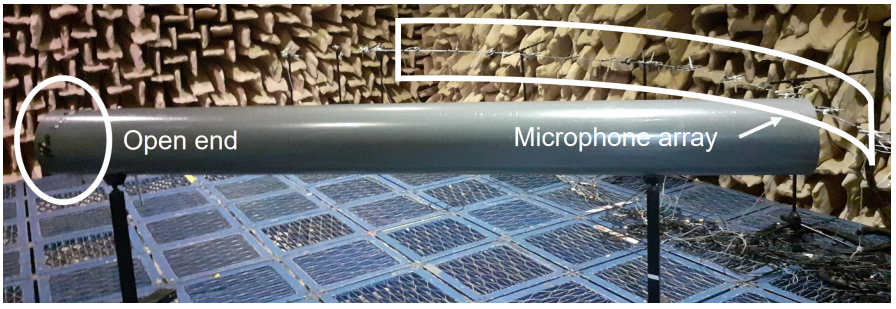

(C) Semi-infinite duct rear-arc

FIGURE 8.1: Photographs of the free-field and ducted experiments

The microphone array consisted of 13 FG-3329-P07 microphones from Knowles Electronics. As sketched in *figure 8.2* separate measurements of the forward and rear-arc were utilised, to create a total array of 25 data points for each measurement. The radiation at 90° was measured twice to ensure consistency between forward and rear-arc data. To obtain the data, the acoustic pressure was recorded for 10 seconds.

A sketch of the experimental set up is shown in *figure 8.2*.

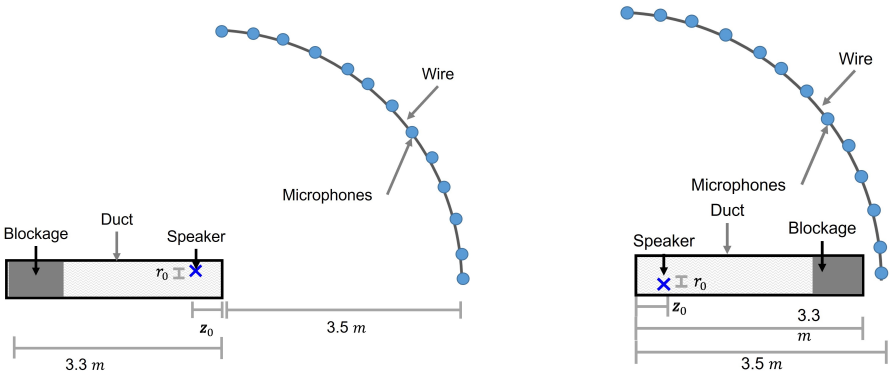

(A) Forward-arc (B) Rear-arc

FIGURE 8.2: Sketch of experimental setup to measure directivity from a loudspeaker source inside a semi-infinite duct

The radius of the microphone array was $R = 3.5\ m$ from the front face of the loud speaker and the duct open end for the free-field and semi-infinite duct radiation case respectively. *Chapter 5*, presents numerical simulations for acoustic radiation from a semi-infinite duct, where the far-field behavior is observed for $R = 4\lambda$, for which the longest wavelength is therefore $\lambda \approx 0.9\ m$, which corresponds to $ka \approx 1$.

For the semi-infinite duct, the principal idea of the acoustic termination was to prevent sound from leaking via the blocked end and minimise the reflections back into the duct. This was achieved by gradually decreasing the cross sectional area of the duct by filling it with sound absorbent fibre glass material. The fibre glass material was placed from the semi-infinite end of the duct to some axial location inside the duct, this distance was not explicitly measured although known to cover approximately half the length of the duct. It was clearly audible that there was minimal sound leakage from the semi-infinite end of the duct.

8.1.1 Source properties

The acoustic source used was a loudspeaker connected to a broadband signal generator, with a frequency range of $400\ Hz \lesssim f \lesssim 20000\ Hz$. This range corresponds to the non-dimensional frequencies $1 \lesssim ka \lesssim 55$. It was found that the signal to noise ratios at the higher frequencies were not sufficient (less than $0\,dB$ re background noise) to obtain accurate data. Photographs and dimensions of the source are shown in *figure 8.3*.

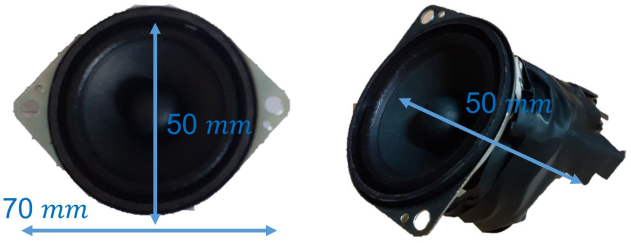

(A) Front view (B) Side view

FIGURE 8.3: Photograph of the source with dimensions labelled

The source location inside the duct (r_0, θ_0, z_0) is defined using the coordinate system shown in *figure 8.4*. The microphones were placed in a horizontal plane, in line with the $\theta = 0^\circ$ axis, as indicated in *figure 8.1*.

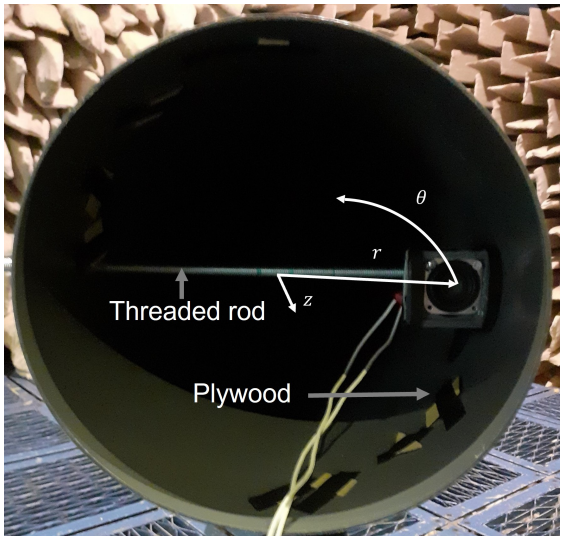

FIGURE 8.4: Coordinates of source inside duct for the experiments

To mount the loudspeaker inside the duct, as shown in *figure 8.4*, a threaded rod of radius 6 *mm* was placed through holes at opposite ends of the duct diameter. For each measurement the unused holes were covered from inside and outside of the duct, in an attempt to minimise sound leakage. The loudspeaker was attached to the rod using a magnet.

8.2 Measured radiation from the loudspeaker in free-field

This section presents the measured acoustic pressure radiation from the loudspeaker in free-field. This analysis is used in the next section when the measurements made using the semi-infinite duct are compared to those made in free-field. *Figure 8.5* shows the directivity $Q(\phi,\theta,\omega)$ of *Eq. 8.1* measured from the loudspeaker for the 2 non-dimensional frequencies $ka = 5$ and 15, where $a = 0.15$. Also shown in the figure for comparison is the directivity $Q(\phi,\theta,\omega) \propto \cos^2\phi$.

Throughout this chapter, in calculation of the denominator of the directivity, $Q(\phi,\theta,\omega)$, the free field pressure is used irrespective as to the pressure in the numerator,

$$Q(\phi,\theta,\omega) = \frac{\overline{p^2}(R,\phi,\theta,\omega)}{\frac{1}{2}\int_0^\pi \overline{p^2}^{(ff)}(R,\phi,\theta,\omega)\sin\phi d\phi}. \tag{8.1}$$

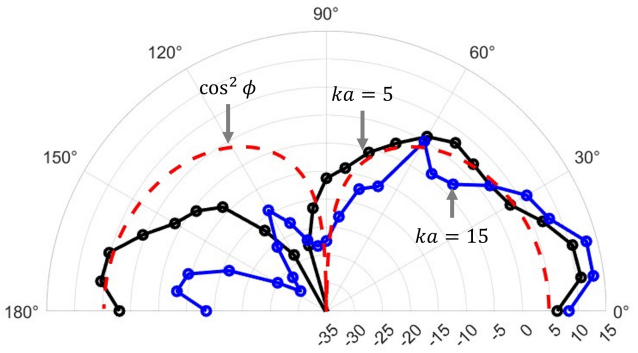

FIGURE 8.5: Directivity measured from the loudspeaker in free-field at varying frequency and for comparison $Q(\phi,\theta,\omega) \propto \cos^2\phi$ is also shown, in dB.

The free-field radiation of the loudspeaker has a high dependence on polar angle ϕ. Both frequencies presented in *figure 8.5* identify a null near $\phi = 120°$, this is likely a consequence of the casing structure of the loudspeaker, shielding the radiation at this angle. The radiation in the rear-arc is shown to be weaker, which is unsurprising, also due to the casing of the loudspeaker, further shielding the acoustic radiation.

The spectral variation of the loudspeaker measurements in free-field are now investigated in *figure 8.6*, which shows the sound pressure level measured from the loudspeaker in free-field plotted against non-dimensional frequency *ka* for the measured polar angles $\phi = 30°, 75°$ and $120°$.

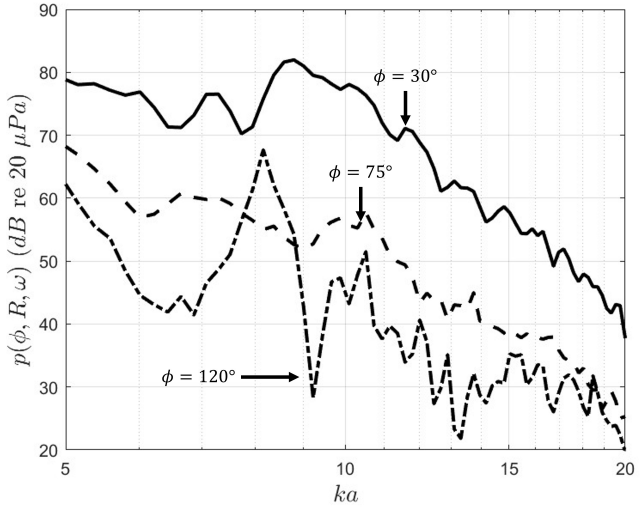

FIGURE 8.6: Sound pressure level measured from the loudspeaker in free-field at varying polar angle. In dB re 20 Pa.

The source level spectrum can be observed in *figure 8.6* to have a sharp decrease with frequency. Large differences in the source level are also observed between the angles investigated, where the radiation at 30 is typically 15 dB higher than the radiation at 75° and 120°. This further reinforces dipole like behavior of the free-field source, which exhibits a null near $\phi \approx 120°$ and lower radaition either side of this location.

8.3 Measured radiation from a semi-infinite duct

This section presents the measured radiation characteristics of the semi-infinite duct experiments. The signal to noise ratio is first analysed to identify the useful frequency range of the source. The effect of the source axial z_0 and radial r_0 location on the acoustic radiation from the semi-infinite duct is then investigated.

8.3.1 Signal to noise ratio

This section compares the background and experimental noise from measurements taken in the anechoic chamber, to measured results for the assumed quietest case, which is for the microphone in the rear-arc of the semi-infinite duct when the source is buried deepest inside the duct. For comparative purposes a forward-arc measurement is also shown.

Figure 8.7 shows the ratio of the pressure, $\overline{p^2}^{(D)}(R, \phi, \theta, \omega)$, radiated from the source at $(r_0/a, z_0/a) = (0.0, 2.0)$, measured from 1 microphone to the background pressure, $\overline{p^2}_B(\omega)$, recorded when the source was switched off. Two far-field polar angles are investigated, the representative forward-arc $\phi = 30^\circ$ and rear-arc $\phi = 150^\circ$ angles. Results are presented in dB.

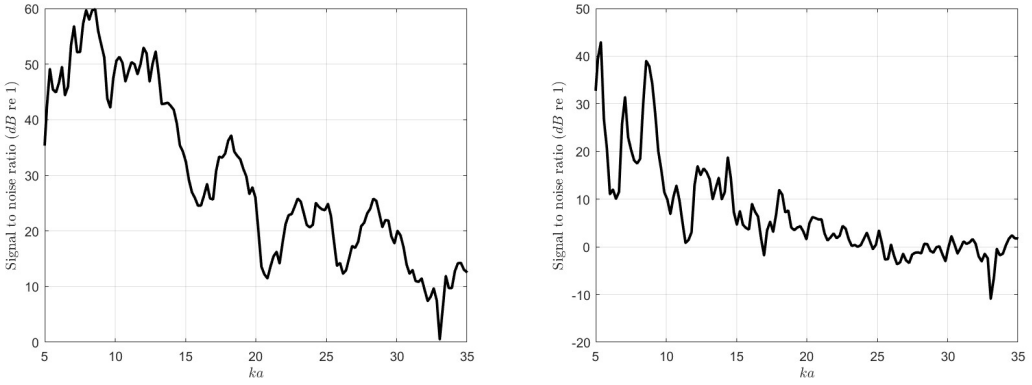

(A) $\phi = 30^\circ$ (B) $\phi = 150^\circ$

FIGURE 8.7: Signal to noise ratio between the ducted source and background noise for two polar angles, $\phi = 30^\circ$ and $\phi = 150^\circ$ for a source location $(r_0/a, z_0/a) = (0.0, 2.0)$

Figure 8.7a shows a good signal to noise ratio is observed of typically 10 dB or greater for $5 \lesssim ka \lesssim 35$ at $\phi = 30^\circ$. However, *figure 8.7b* shows that the range of frequencies with good signal to noise ratio in the rear-arc is very limiting. A signal to noise ratio of more than 0 dB is generally observed at frequencies $5 \lesssim ka \lesssim 20$ only. This behavior is unfortunate as any directivity investigation, considering the forward and rear-arc is hence limitted to this range. At both angles investigated in *figure 8.7*, a trough is observed at approximately $ka \approx 33$. This is believed to be a result of a disturbance in the background measurements of $\overline{p^2}_B(\omega)$.

8.3.2 Modal identification

To validate the experimental data, this section presents single microphone measurements of the sound pressure level from the ducted source, which is used to identify the modal cut-on frequencies.

Figure 8.8 shows the sound pressure radiation measured by a single microphone at $\phi = 45°$, for the source deep inside the semi-infinite duct with a source location $z_0/a = 2.0$. From theoretical studies, at this location, cut-off modes can be neglected. Two radial locations are investigated, $r_0/a = 0.0$ (where only the axi-symmetric, $m = 0$ modes radiate) and $r_0/a = 0.77$ (where all propagating modes have the potential to radiate efficiently). In each plot the associated cut-on frequencies $ka = \kappa_{mn}a$ are shown as the red dashed lines for each radial location, with the associated modal indices m and n shown.

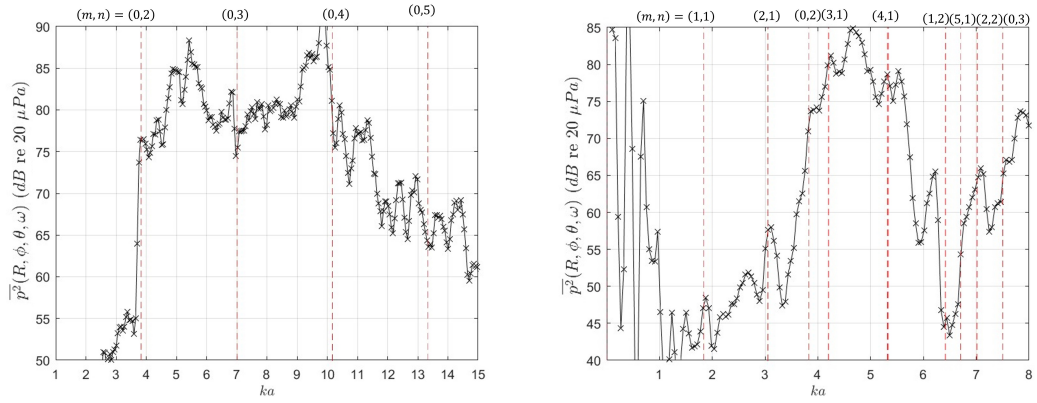

(A) $r_0/a = 0.0$ (B) $r_0/a = 0.77$

FIGURE 8.8: Sound pressure radiation measured at $\phi = 45°$ for the source located at $z_0/a = 2.0$ inside the semi-infinite duct at two radial locations $r_0/a = 0.0$ and 0.77. The cut-on frequencies ka are shown as the red dashed line.

Some modal cut-on frequencies are shown in *figure 8.8* to have a significant effect on the measured pressure level. To give examples, *figure 8.8a*, showing the data for the source on the duct axis $r_0/a = 0.0$ shows an increase of approximately 15 dB at $ka \approx 3.8$ is observed, which is the modal cut-on frequency for the mode $(m, n) = (0, 2)$. Significant decreases in pressure level are also observed at the modal cut-on frequencies for the $(0, 3)$ and $(0, 4)$ modes, at $ka \approx 7.0$ and 10.2 respectively.

For the radial location $r_0/a = 0.77$ investigated, shown in *figure 8.8b*, significant changes in measured pressure are observed at the cut-on frequencies for the modes $(m, n) = (1, 1)$ and $(2, 1)$ at the non-dimensional frequencies $ka \approx 1.8$ and 3.1 respectively. At the cut-on frequencies for modes of higher order however, no significant changes are observed at the modal cut-on frequencies, which is likely due to the relative contribution of each mode decreasing when more modes are present.

8.3.3 Investigation of source axial location on the acoustic radiation from semi-infinite ducts

This section investigates experimentally the effect of source axial location on the acoustic radiation from semi-infinite ducts. Experimental results are compared to the theoretical predictions. From *figure 8.5*, the free-field radiation is comparable to a dipole source which has radiation proportionality $p^{(ff)}(R,\phi,\theta,\omega) \propto f(\omega)\cos\phi\,/R$. The theoretical radiation of a stationary point dipole source inside a semi-infinite duct is formed from a coherent summation of modes, using *Eq. 2.53*, where each modal solution is formed by substitution of *Eqs. 2.52* and *4.59* into *Eq. 2.51*.

Figure 8.9 shows the directivity $Q(\phi,\theta,\omega)$ of *Eq. 8.1* at the two non-dimensional frequencies $ka = 5$ and 15 for the source located on the duct axis $r_0/a = 0.0$, with $\theta = 90°$ and at two axial locations $z_0/a = 0.07$ and 2.0.

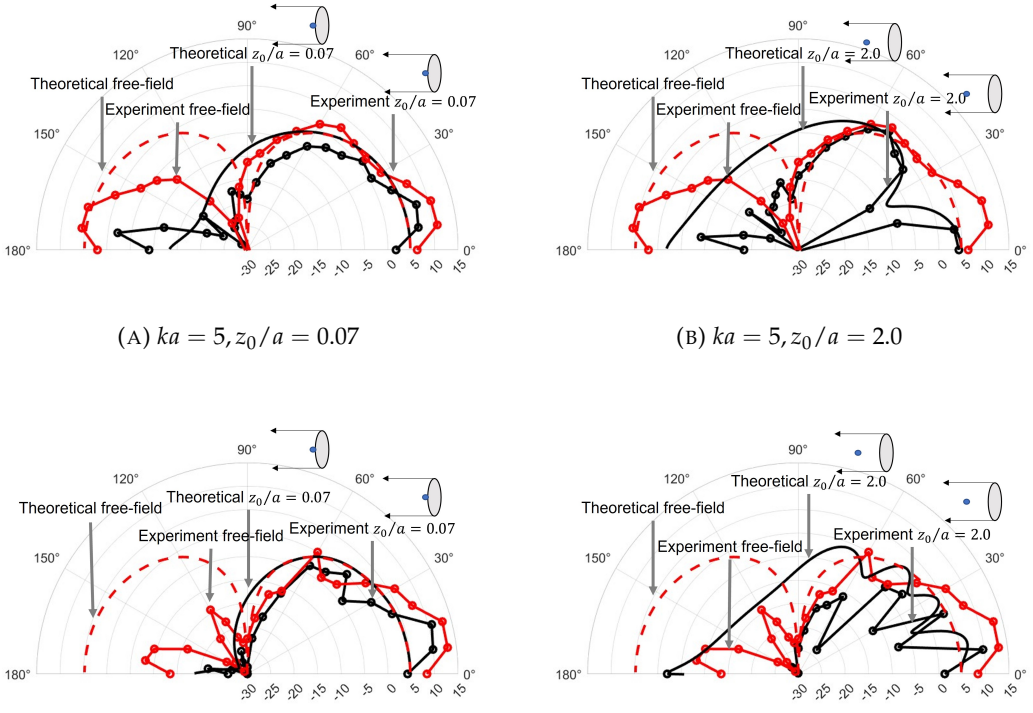

(A) $ka = 5, z_0/a = 0.07$

(B) $ka = 5, z_0/a = 2.0$

(C) $ka = 15, z_0/a = 0.07$

(D) $ka = 15, z_0/a = 2.0$

FIGURE 8.9: Directivity $Q(\phi,\theta,\omega)$ computed using experimental data and theoretical formulations for a source on the axis $r_0/a = 0$ of a semi-infinite duct at two non-dimensional frequencies $ka = 5$ and 15 with varying axial location, in dB.

Figure 8.9 shows that for sources near the open end of the duct $z_0/a = 0.07$, shown by *figs 8.9a* and *8.9c* the experimental data shows the ducted radiation is similar to the free-field, generally to within 3 dB for the $ka = 5$ case and 5 dB for the $ka = 15$ case in the forward-arc $\phi < 90°$. This behavior can also be observed from the theoretical predictions for dipole radiation. The theoretical predictions and experimental results generally follow the same trend, of a smooth $\cos\phi$ like directivity in the forward-arc.

For the source buried deep inside the duct, especially at the higher non-dimensional frequency investigated of $ka = 15$, shown by *figure 8.9d* the experimental results show a more 'spiky' directivity is observed with a large number of lobes and nulls. The location of the lobes are, in general, matched by the theoretical prediction. From the theory this behavior is likely an indication of modal interference between the cut-on modes caused by the phase differences of the modes arriving at the duct open end. The experiments show the nulls to be much deeper than the predictions.

For the low frequency case with the source buried deep inside the duct shown by *figure 8.9a*, the theoretical predictions and experimental results both indicate a null at $\phi \approx 20°$, although as previously noted the experimental data predicts the null to be much deeper and observes a reduction of 20 dB, where the theory predicts a reduction of less than 10 dB.

The effect of axial location from ducted source radiation is now explored over a broader range of frequencies using the open-to-ducted transfer function representing the ratio of free-field to ducted pressure radiation defined,

$$\mathcal{T}(\phi, \theta, \omega) = \frac{\overline{p^2}^{(D)}(R, \phi, \theta, \omega)}{\overline{p^2}^{(ff)}(R, \phi, \theta, \omega)}. \tag{8.2}$$

Figure 8.10 shows a colour map of the open-to-ducted transfer function $\mathcal{T}(\phi, \theta, \omega)$ of *Eq. 8.2* plotted against far-field angle ϕ and non-dimensional frequency ka for the source near the wall of the duct $r_0/a = 0.77$, at four axial locations $z_0/a = 0.07, 0.20, 1.7$ and 2.0, with $\theta = 90°$. Also shown in the figure on top of the colour map, is the corresponding source location z_0/λ.

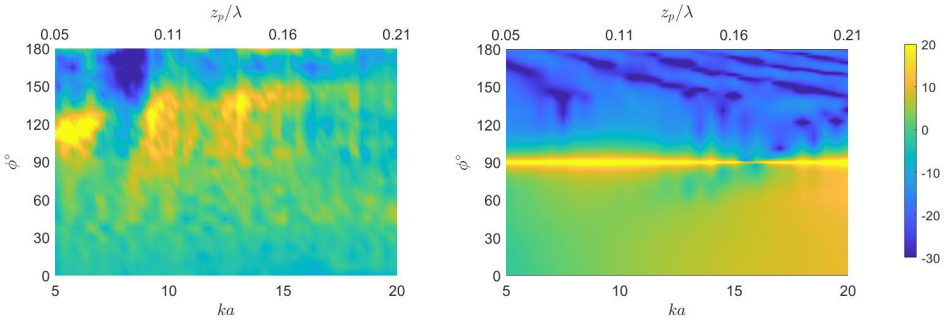

(A) Experiment $z_0/a = 0.07$ (B) Dipole $z_0/a = 0.07$

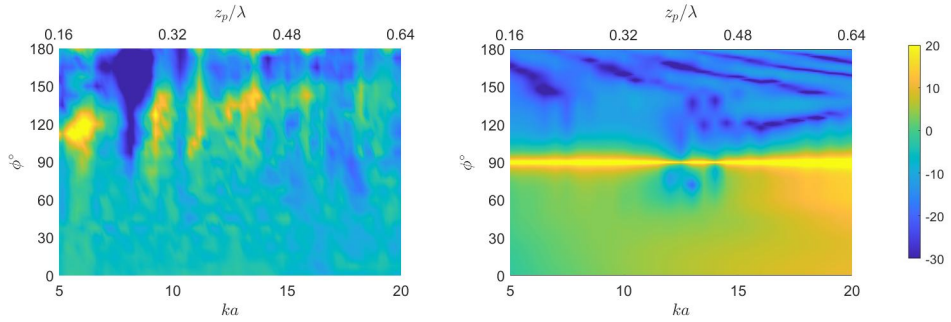

(C) Experiment $z_0/a = 0.20$ (D) Dipole $z_0/a = 0.20$

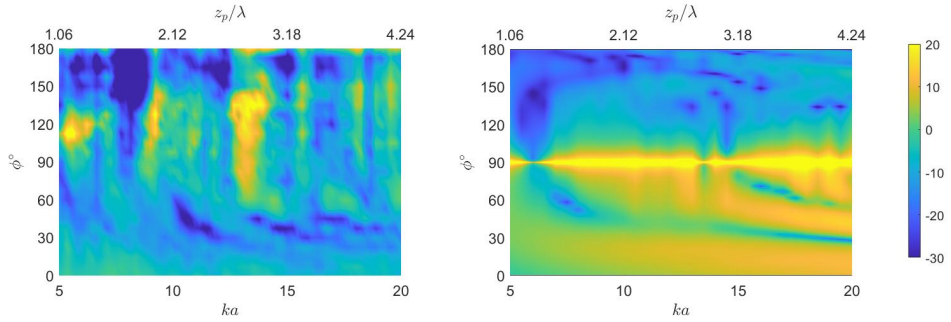

(E) Experiment $z_0/a = 1.3$ (F) Dipole $z_0/a = 1.3$

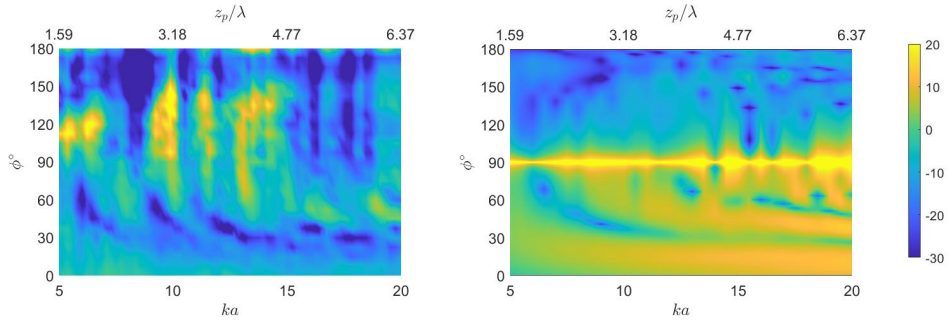

(G) Experiment $z_0/a = 2.0$ (H) Dipole $z_0/a = 2.0$

FIGURE 8.10: Open-to-ducted transfer function $\mathcal{T}(\phi, \theta, \omega)$ calculated using theoretical predictions and experimental data a source located near the wall $r_0/a = 0.77$, of a semi-infinite duct, with $\theta = 90°$, at varying axial locations, in dB.

In the sideline directions, especially at the lower frequencies the duct is shown to largely increase the pressure radiated by more than 20 dB at for example $z_0/a = 1.3$, $ka = 13$ and $\phi = 125°$. This effect is observed to be strongest for the $z_0/a = 0.07$ case and appears weaker as the source moves deeper inside the duct $z_0/\lambda \to \infty$, which is an indication of cut-off mode radiation. The theoretical analysis shows a large ducted radiation vs free-field in the sideline directions $\phi \approx 90°$, which is a result of the explicit null of 0 radiation from the free-field dipole source. This region is also seen in the ducted measurements for the far-field angle of $\phi \approx 120°$, indicating the loudspeaker has similar behavior in free-field to a dipole source, and the duct smooths the null.

Observe the cases of the source buried relatively deep inside the duct *figs 8.10e* to *8.10h* where $z_0/a = 1.3$ or 2.0. Both the theoretical predictions and experimental results show 'banana' shapes in the forward-arc $\phi \leq 90°$. This behavior is likely an indication of nulls in the ducted radiation directivity which can be seen to move towards the duct axis as frequency is increased. This is caused by the different amounts of modal interference between the cut-on modes at the open end of the duct, as the axial location of the source changes with frequency relative to the wavelength, z_0/λ.

More detailed analysis of the open-to-ducted transfer function $\mathcal{T}(\phi, \theta, \omega)$ of *Eq. 8.2* is now presented at the non-dimensional frequency of $ka = 5$. *Figure 8.11* shows $\mathcal{T}(\phi, \theta, \omega)$ computed using the theoretical predictions and experimental results for the source on the duct axis $r_0/a = 0.0$, with $\theta = 90°$ and two axial locations $z_0/a = 0.07$ and 2.0.

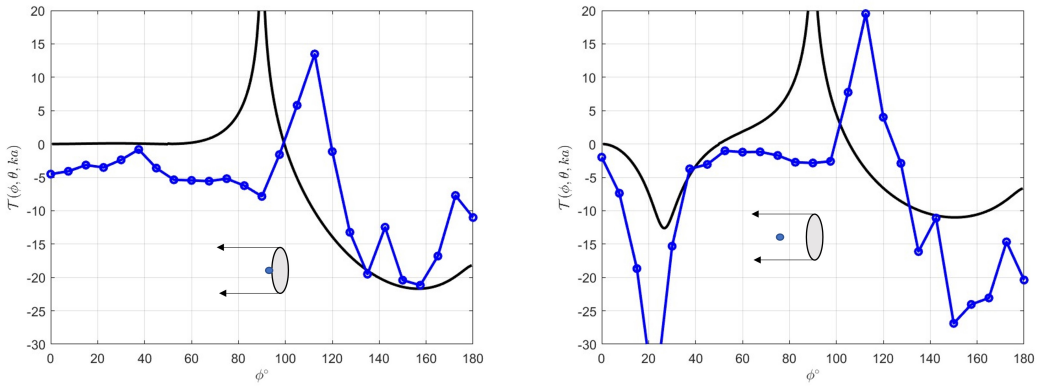

(A) $z_0/a = 0.07$ (B) $z_0/a = 2.0$

FIGURE 8.11: Open-to-ducted transfer function $\mathcal{T}(\phi, \theta, \omega)$ calculated using theoretical predictions (black line) and experimental data (blue dots and line) for a source located on the axis $r_0/a = 0.0$ of a semi-infinite duct, with $\theta = 90°$ and $ka = 5$, at varying axial locations, in dB.

Figure 8.11 shows the general shape of the directivity is consistent between the theoretical predictions and experimental results. In both plots, a large ducted radiation relative to the free-field is predicted which for the dipole source is $\phi = 90°$ and the experimental results $\phi = 120°$. In *figure 8.11b* both the experimental results and theoretical predictions show a null at $\phi \approx 25°$, but this is shown to be much deeper for the experimental results, which show a reduction of more than 30 dB at this angle, whereas the theoretical prediction shows this to be only a 10 dB reduction. These observations are also noted from *figure 8.9*.

For the theoretical predictions *figure 8.11a* identifies that for a large region of the forward-arc $\mathcal{T}(\phi, \theta, \omega) \approx 0\,dB$. This behavior is discussed in *Chapters 5* and *7* and was shown to be result of the small phase difference between cut-on modes. The experimental results shows the radiation from the free-field and ducted source is to within 5 dB for the low angles of the forward-arc $\phi < 60$.

8.3.4 Investigation of source radial location on the acoustic radiation from semi-infinite ducts

This section presents comparisons between the experimental results and theoretical analysis for the source at varying radial locations. From the theoretical analysis discussed in *Chapter 5* increasing the radial location of a source, especially when near the open end of the duct, causes the ducted radiation to be greater than free-field.

Figure 8.12 shows the directivity, $Q(\phi, \theta, \omega)$ of *Eq. 8.1* computed using experimental results and theoretical predictions at the two non-dimensional frequencies $ka = 5$ and 15 for the source located near the open end of the duct $z_0/a = 0.07$, with $\theta = 90°$ and at two radial locations $r_0/a = 0.50$ and 0.77. The free-field source is unaffected by the source radial location.

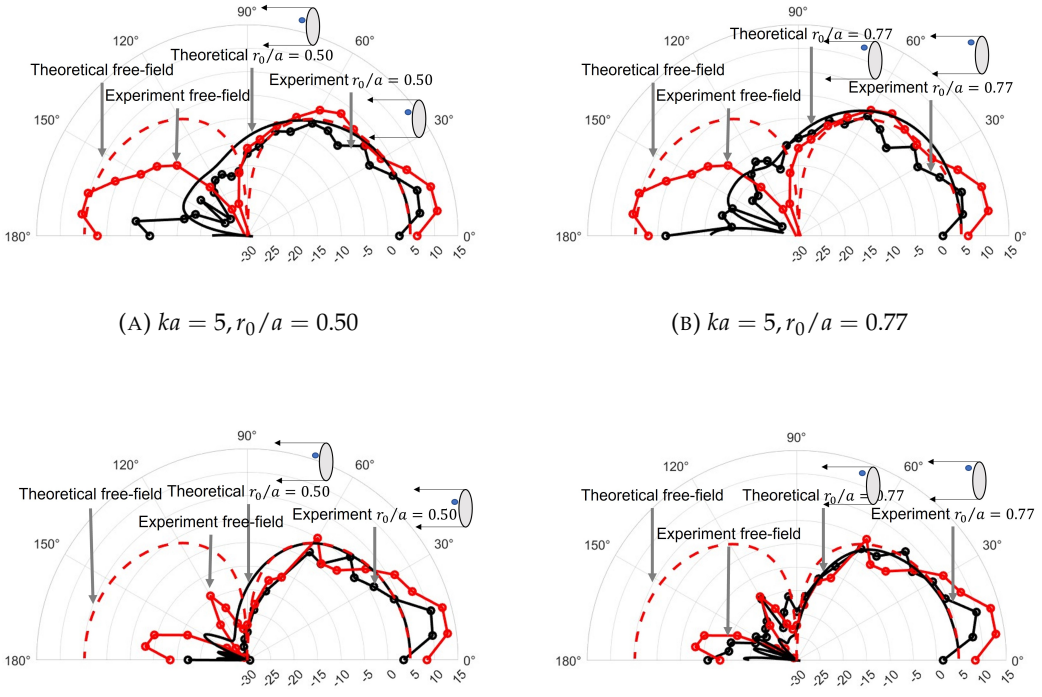

(A) $ka = 5, r_0/a = 0.50$

(B) $ka = 5, r_0/a = 0.77$

(C) $ka = 15, r_0/a = 0.50$

(D) $ka = 15, r_0/a = 0.77$

FIGURE 8.12: Directivity $Q(\phi, \theta, \omega)$ computed using experimental data and theoretical formulations for a source near the open end $z_0/a = 0.07$ of a semi-infinite duct at two non-dimensional frequencies $ka = 5$ and 15 with varying radial location, in dB.

Comparison between the source radial locations of $r_0/a = 0.50$ and 0.77 indicates higher radiation for the source located closer to the wall of the duct for the high frequency investigated in *figure 8.9c* and *8.9d* and is shown from the experimental data and theoretical predictions. This behavior is not observed for either the theoretical predictions or experimental results at the lower non-dimensional frequency shown in in *figure 8.9a* and *8.9b*.

Comparison between the theoretical predictions and experimental results show general agreement between the shape of all directivities, with radiation similar to $\cos\phi$ in the forward-arc. The experimental data shows the forward-arc is consistent between free-field and ducted measurements, typically to within 3 dB, this was discussed in the previous section and is shown for sources near the duct open end, $z_0/a = 0.07$.

Figure 8.14 shows a colour map of the open-to-ducted transfer function $\mathcal{T}(\phi, \theta, \omega)$ of *Eq. 8.2* plotted against non-dimensional frequency ka and far-field angle ϕ for the source buried deep inside a semi-infinite duct $z_0/a = 2.0$, with $\theta = 90°$, at four radial locations $r_0/a = 0.0, 0.26, 0.50$ and 0.77.

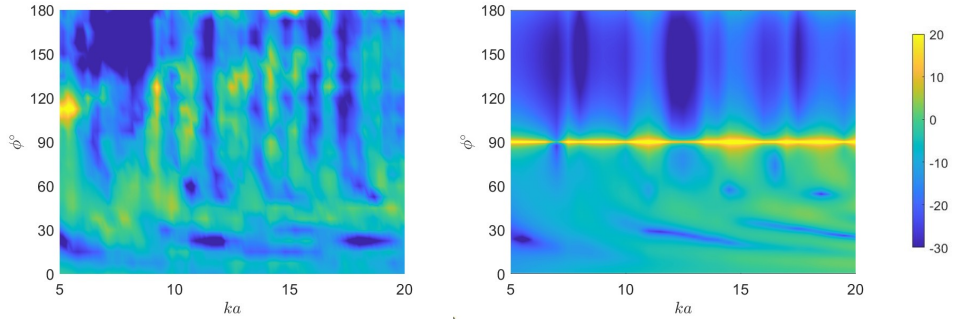

(A) Experiment $r_0/a = 0.0$ (B) Dipole $r_0/a = 0.0$

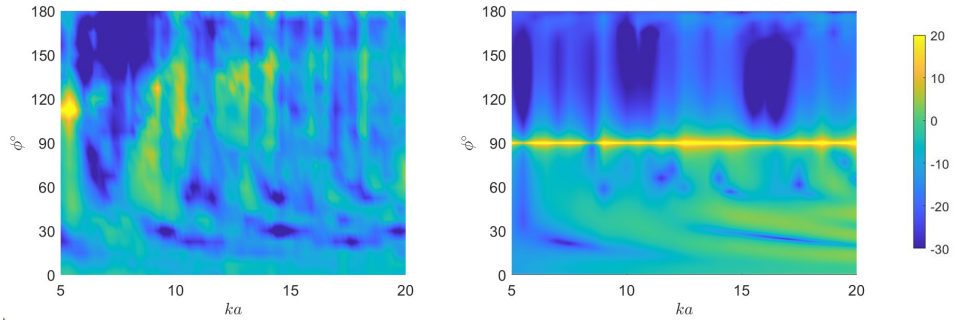

(C) Experiment $r_0/a = 0.26$ (D) Dipole $r_0/a = 0.26$

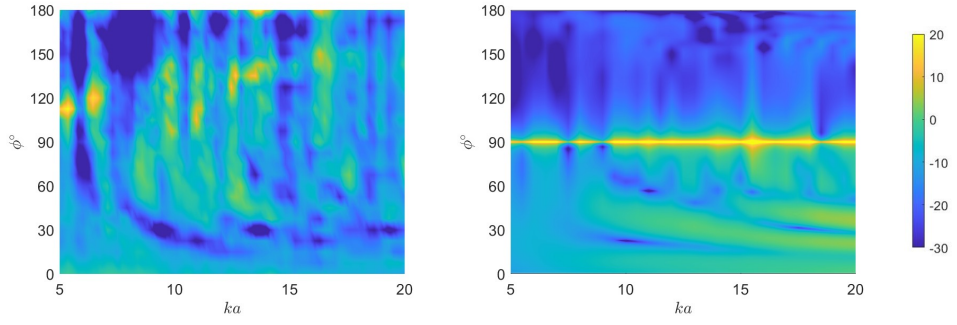

(E) Experiment $r_0/a = 0.50$ (F) Dipole $r_0/a = 0.50$

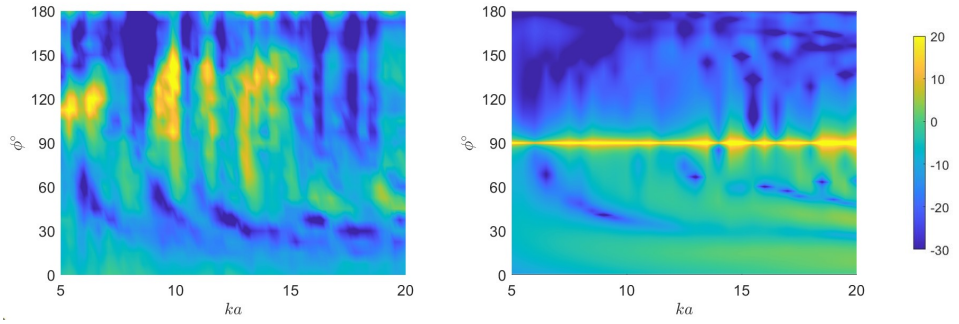

(A) Experiment $r_0/a = 0.77$ (B) Dipole $r_0/a = 0.77$

FIGURE 8.14: Open-to-ducted transfer function $\mathcal{T}(\phi, \theta, \omega)$ calculated using theoretical predictions and experimental data for source located deep inside a semi-infinite duct $z_0/a = 2.0$, with $\theta = 90^\circ$, at varying radial location, in dB.

Figure 8.14 further indicates that increasing the source radial location increases the ducted radiation, where a darker yellow pattern is observed for the experimental data as the source is located closer to the duct wall $r_0/a \to 1$. This behavior is observed most strongly in the sideline directions in the rear-arc $90^\circ < \phi < 150^\circ$ and the effect of radial location is shown to be relatively small at low radiation angles $\phi \lesssim 30^\circ$.

Comparison between the theoretical predictions and experimental data in *figure 8.14* shows conceptual agreement with a number of similar features. Both methods of calculation the transfer function shows of $\mathcal{T}(\phi, \theta, \omega) > 20\,dB$ in the sideline directions which is due to the null in the free-field radiation. Banana shapes are observed in both the experimental and theoretical directivities, which indicate a null moving towards the duct axis as frequency is increased.

Single frequencies are now investigated to perform a more detailed analysis using the open-to-ducted transfer function $\mathcal{T}(\phi, \theta, \omega)$ of *Eq. 8.2*. *Figure 8.15* shows $\mathcal{T}(\phi, \theta, \omega)$ computed using the theoretical predictions and experimental results for a non-dimensional frequency of $ka = 15$, with the source near the open end $z_0/a = 0.07$ of a semi-infinite duct, with $\theta = 90^\circ$ and two radial locations $r_0/a = 0.0$ and 0.77.

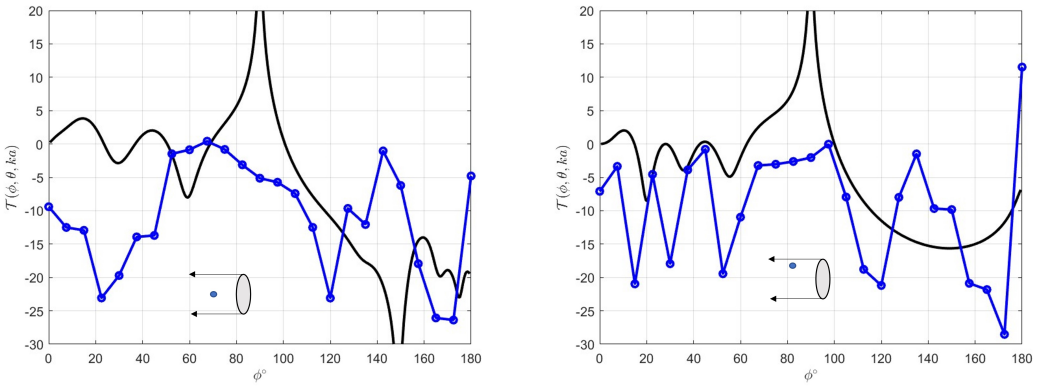

(A) $r_0/a = 0.0$ (B) $r_0/a = 0.77$

FIGURE 8.15: Open-to-ducted transfer function $\mathcal{T}(\phi, \theta, \omega)$ calculated using theoretical predictions (black line) and experimental data (blue dots and line) for a source located deep inside $z_0/a = 2.0$ of a semi-infinite duct, with $\theta = 90^\circ$ and $ka = 15$, at varying radial locations, in dB.

Figure 8.11a shows general agreement between the shape of the directivities between the theoretical predictions and experimental results. Both models predict 3 nulls in the forward-arc, although the experimental results predict these to be much deeper which is consistent with other analysis in this chapter. *Figure 8.11b* shows large differences between the experimental results and theoretical predictions. One cause for this is the differences between the free-field radiation of the loudspeaker and a dipole source as indicated in *figure 8.5*.

This chapter has presented experimental results to validate the theoretical predictions. Some of the main conclusions of the predictions have been observed such as sources near the open end of semi-infinite ducts $z_0/\lambda \approx 0$ having equal free-field and ducted radiation, as shown in *figure 8.9*. It has also been shown that the ducted radiation generally increases as the source moves closer to the duct wall $r_0/a \to 0$, which can be concluded from *figure 8.14*. However, a more detailed analysis has revealed large differences between the experimental data and theoretical predictions, such as *figure 8.15b*.

Chapter 9

Application of findings

This chapter relates the findings of this thesis to the applications of this work detailed in *Chapter 1.2*. To apply the analysis presented in this thesis, an open-to-ducted transfer function can be applied 'blindly' to any situation where an acoustic prediction has been made without considering the effect of a duct. Alternatively, for certain applications, the noise generating mechanisms can be identified and constructed from ideal sources. Using numerical simulation software to solve for the source strengths the theoretical duct model can be applied directly to predcit the acoustic radiation.

9.1 Application of an open-to-ducted transfer function

This section identifies how an open-to-ducted transfer function method can be applied to solve acoustical engineering problems.

To modify free-field source radiation to account for a hard-walled boundary of a duct likely requires re-derivation of the fundamental equations in the analysis, making simple modification impossible. The ducted radiation model predictions in this thesis can be divided by the free-field predictions to form a transfer function, which can be used to quantitatively identify the effect of placing an acoustic source inside a duct, without specific detail of the noise generating mechanism. The transfer function approach follows the schematic detailed in *figure 9.1*.

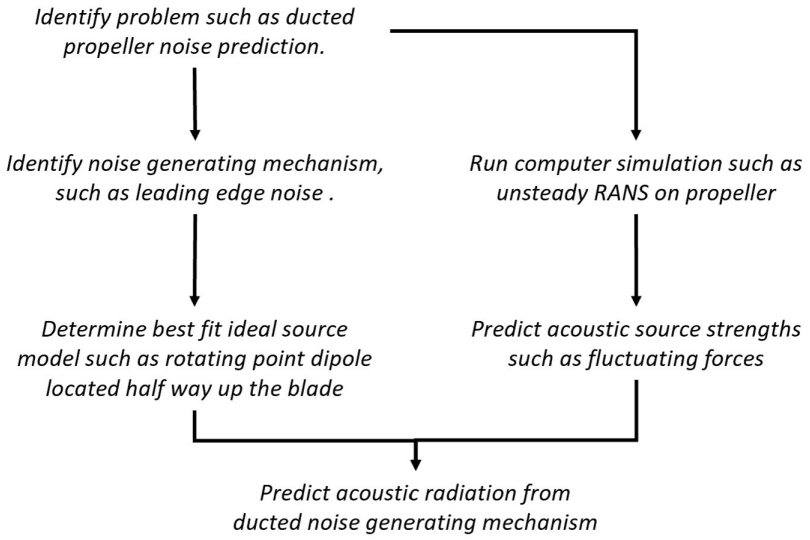

FIGURE 9.1: Schematic of incorporating open-to-ducted transfer function model into ducted acoustic source predictions

The findings of this thesis allow existing literature for free-field sources, such as propeller noise predictions, to be modified to include a duct, without manipulation of the fundamental analysis for each source mechanism of noise.

One potential issue with this method is the inclusion of explicit nulls in either the free-field or ducted prediction. Particularly for the dipole sources, the free-field pressure exhibits zero radiation at the dipole null, where the ducted model typically predicts relatively small, but non-zero radiation. The transfer function of a dipole source approaches infinity at the null angle of the dipole and hence an appropriate interpretation of this must be incorporated.

The advantages of this method are that it allows direct application of the theoretical model detailed in this thesis without further work. This method however, carries a certain degree of inaccuracy, as it does not consider much detail of the acoustic source.

9.2 Constructing a propeller from ideal sources

Alternatively, and more accurately, the theoretical model proposed in this thesis could be applied to propeller noise by; identifying the noise generating mechanisms, modelling them as ideal sources and using numerical simulations to determine the source strength. An example implementation of this is shown in *figure 9.2*.

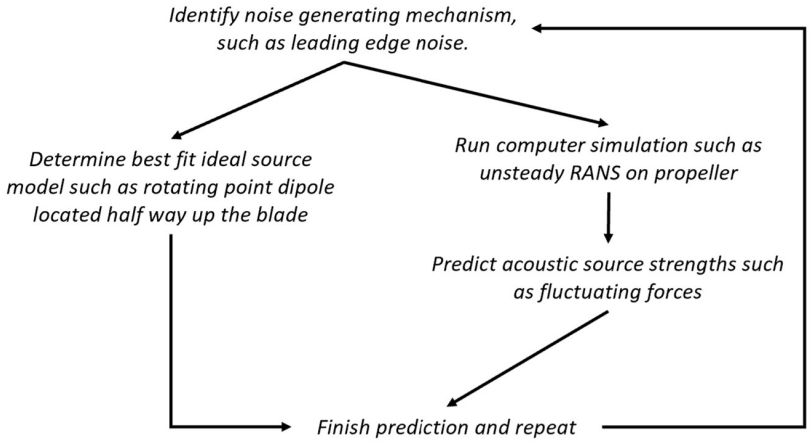

FIGURE 9.2: Schematic of constructing a propeller noise as ideal sources for use in the theoretical duct model

This thesis has investigated monopole and dipole sources which require a volume velocity and fluctuating force component. These parameters are readily available from unsteady flow simulations and can be used to determine the values f, F, q and $\mathcal{Q}$, which are required to predict the acoustic radiation from ducted sources using the theoretical models presented in this thesis (*Chapter 4* and *6*).

This method of application is likely more accurate than the transfer function method but requires an unsteady simulation. This increases the complexity of the solution, as well as the computation time.

9.3 Discussion of results to applications

This final section relates the usefulness of the findings from this thesis back to the applications discussed in *Chapter 1.2*.

This thesis has shown that at low frequencies ducts have a large effect on both the power level and directivity of acoustic sources. Low frequencies are of primary interest to marine ducted propellers, therefore this work remains highly applicable. Furthermore the effect of cut-off modes have been shown to be largest at low frequency.

Conversely, this thesis has also shown that for sources close to the duct open end relative to the source wavelength the duct is effectively transparent, having no effect. This means for a certain frequency range a short duct will have no effect and can be omitted in acoustic modelling, which is most applicable to marine ducted propellers whose radiation characteristics are typically at low frequency.

In practice, the higher frequency range of broadband propeller radiation is likely to be affected heavily by the inclusion of the duct. However, the lower frequency range will be largely unaffected due to the source being located only a fraction of a wavelength from the duct open end.

The effect of cut-off modes were shown to be relatively large in the rear-arc for the semi-infinite duct case but for the finite length duct case, in general very small effects were observed. One interpretation of this is that cut-off modes can be neglected (for sources not located at the duct wall). Furthermore the number of cut-off modes required to accurately predict acoustic radiation was shown to substantially increase the total number of modes required, therefore it is convenient to ignore cut-off modes if possible to reduce computation time.

One important finding from this thesis is that dipole sources near the duct wall have much higher radiation than sources elsewhere. This is especially concerning for tip gap noise, which is a prominent noise generating mechanism in propeller noise. It is believed that this large increase is due to the interaction of the source with the duct hard wall. Potentially, by omitting the hard wall of the duct, i.e. by using liners, the effect of tip gap noise can be significantly reduced.

For large computations involving the addition of cut-on and cut-off modes the scaling law of cut-off modes can be utilised to reduce computation time. This may be especially important when considering the cases when cut-off modes where shown to be most important such as for sources near the duct rim.

Chapter 10

Conclusion and suggestions for further work

This section summarises the main conclusions of the work presented in this thesis. Three distinct areas of research have been addressed, which are the three objectives stated in *Chapter 1*, which are:

1. To understand the far-field acoustic radiation characteristics of cut-off modes highlighting the differences between propagating acoustic cut-on and cut-off modes, *Chapter 3*.

2. To identify the significance of cut-off modes in calculations of multi-modal acoustic radiation from sources close to the open end of a duct, *Chapters 5, 7* and *8*.

3. Compare the ducted radiation prediction to an equivalent free-field source radiation prediction, to identify the effect of the duct, *Chapters 5, 7* and *8*.

Some aspects of this work could be further developed. These points are also noted in this chapter.

10.1 Conclusion

This Thesis has compared the radiation of acoustic sources in free-field and from hard-walled circular ducts, with emphasis on sources close to an open end of a duct. The study was motivated by the need to identify the effect on far-field radiation due to sources in a duct. The conclusions are now split accordingly to the three objectives mentioned above:

10.1.1 Cut-off modal radiation

1.1 Modes excited just below their Cut-on frequency radiate most strongly to the rear-arc.

1.2 Cut-off modes exhibit a major lobe whose radiation angle is determined by m. A number of side lobes are also present above a threshold frequency of $\xi_m > 1$.

1.3 The directivity of sufficeintly cut-off modes is roughly symmetric about 90° at the sufficiently low frequencies of $\xi_m < 1$. In this low frequency limit, therefore, the total sound power is equally distributed between the forward and rear-arcs.

1.4 Whilst the behaviour of well cut-off modes is mainly governed by m, their sensitivity to the radial mode index n increases as the frequency approaches cut-on from below. The transition from cut-off to cut-on is therefore gradual.

1.5 At a constant frequency and azimuthal mode order m the directivity of cut-off modes for un-flanged ducts has been shown to vary as $D_{mn}(\phi, ka) \propto \sqrt{1/\kappa_{mn}}$.

1.6 At a constant frequency and azimuthal mode order m the directivity of cut-off modes for flanged ducts has been shown to vary as $D_{F,mn}(\phi, ka) \propto 1/\kappa_{mn}$, excluding the effect of reflections.

1.7 For sufficiently well cut-off modes radiating from an un-flanged duct, the radiation efficiency τ_{mn} is predominantly dependent on the azimuthal mode index m and has dependency $\tau_{mn} \propto (ka)^{2m+2}$, agreeing with the flanged formulation first investigated by Morfey (1969). In general, therefore, modes of increasing order m, excited below cut-off $k < \kappa_{mn}$, are less significant to overall radiation in multi-mode calculations.

1.8 The equivalent radiation velocity distribution for cut-off modes has been shown to be predominantly located beyond the sonic radius at which the azimuthal phase speed equals the speed of sound.

10.1.2 Significance of cut-off modes in multi-modal radiation

1.1 Multi-modal directivity for sources close to the open end requires a large number of cut-off modes relative to the number of cut-on modes.

1.2 For dipole sources exactly at the open end of the duct, $z_0/\lambda = 0$, the contribution due to cut-off modal radiation dominates that from the cut-on modes.

1.3 Using an asymptotic approach the radiated field has been predicted for dipole sources exactly at the duct open end confirming the convergence behavior identified in *2.2*

1.4 The directivity pattern has been predicted for distributions of incoherent axial dipole sources at the open end of the duct and point dipole sources at the rim of the duct to be of the form $\sin^2(\phi/2)$.

1.5 The far-field mean square pressure in the rear-arc has been shown to increase by as much as 5 dB when locating the source close to the open end of the duct. Furthermore, an increase of at least 1 dB has been observed for sources located less than 0.5 wavelengths from the duct open end.

10.1.3 Comparisons between free-field and ducted radiation

1.1 The concept of nil-shielding directions ϕ_{mn}, first proposed by Chapman (1996), has been investigated numerically, in which the far-field directivity from a hard-walled duct is precisely equal at the mode-ray angles, to the free-field radiation.

1.2 For sources deep within the duct, such that only propagating modes radiate significantly, the number of nil-shielding directions increases as the frequency ka is increased. Agreement between the free field and ducted multi-mode solutions therefore tend to agree over all radiation angles and not just at ϕ_{mn} in the high frequency limit $ka \to \infty$.

1.3 When the source is located at the open end of the duct, but not at the duct wall, good agreement is observed even at low frequencies over all radiation angles between the free-field and ducted solutions, signifying the importance of cut-off modes for sources located close to the open end.

1.4 For dipole sources located exactly at the duct wall a doubling of the sound power occurs.

1.5 For dipole sources located on the duct rim the far-field directivity is fundamentally different from that of the free-field result, and more closely resembles that of monopole sources at frequencies above the first cut-off frequency.

10.2 Further Work

This section suggests further research that could be conducted to extend and improve the work conducted for this thesis.

10.2.1 Expansion of the theoretical model

The current theoretical model, proposed in this thesis, predicts the free-field and ducted acoustic radiation due to monopole and dipole sources. The model could be expanded to improve practical applicability by including:

- Axial flow
- Ducts with specified non-zero impedance condition at the wall
- Ducts with a negligible wall impedance (sound soft boundary)
- An annulus inside the duct
- Ducts with varying cross sectional area

For aircraft and drones the axial flow is likely to be an important contributor in the noise radiation. By inclusion of flow in the theoretical model the accuracy of the predictions when used for these applications would be increased.

It is very common for modern ducted systems to incorporate noise quietening techniques such as sound absorbing liners. This thesis has identified the effect of ducts on acoustic sources assuming a hard-walled boundary condition. For real applications this may not be the most realistic assumption and it would be desirable to incorporate a finite impedance at the duct wall in the modelling.

For propeller applications the rotor hub obstructs a proportion of the duct. To improve the accuracy of the predictions for real applications it may be desirable to include an annulus in the duct model. Furthermore, aircraft commonly utilise a bypass flow for their propulsion, where the outer bypass chamber could be modeled as an annular duct.

Finally, for aircraft applications, the outlet of the duct often incorporates a nozzle, which is used to increase the axial flow speed. Additionally, the inlet radius of the duct is often asymmetric to account for the range of flow angles entering the nacelle as the engine speed varies. The duct radiation model could include applicability for a duct with a varying cross sectional area to better represent aircraft.

10.2.2 More detailed simulations

At present it is largely unknown as to the degree of accuracy of the finite length duct model at low frequency for short ducts. This uncertainty was indicated by COMSOL Multiphysics simulations.

One suggestion for further work, is to produce a more general three dimensional COMSOL Multiphysics duct radiation model, which predicts radiation from sources at any radii inside the duct (not just $r_0/a = 0$ predictions available from the present model). This would allow more comparisons to be made between the theoretical model and COMSOL Multiphysics simulations, which could better identify the validity of the theoretical model.

A major finding is that ducted dipole sources located at the duct wall $r_0/a = 1$ exhibit a large increase in acoustic radiation. Using a more sophisticated, three dimensional COMSOL Multiphysics model, a secondary prediction for this case can be made. This will further identify the impact of locating a dipole source at a duct hard wall.

10.2.3 Experimental work

This thesis detailed an experimental investigation in to the effect of a semi-infinite duct on acoustic source radiation. This work could be extended to also consider a finite length duct, which could be used to better understand the applicability and limitations of the finite length duct model.

The experimental work conducted used a loudspeaker, which was shown to approximately exhibit 'dipole like' free-field behavior. The near-field behavior of the loudspeaker was not investigated. This means the radiation from the loudspeaker used *inside* the duct may not have been accurately represented by a dipole source, which is a cause for uncertainty in the results.

A broader experimental investigation could be conducted where a range of sources are used in attempt to best match an ideal source, such as a monopole or a dipole source. This would allow a more direct comparison between the theoretical model and experimental results. For example a more realistic dipole source could be created by placing two loudspeakers 180° out of phase (backwards facing). Additionally, an ideal monopole source could be created from an electrical spark plug, which could provide a more direct comparison to the theoretical results.

One finding from this thesis is that dipole sources located exactly on the duct rim radiate strongly into the rear-arc, which for the semi-infinite duct case has approximate directivity proportional to $\sin\phi/2$. An experiment could be designed specifically to determine how closely this result can be obtained. Observing low frequencies would relax the limit on how physically close the source can be located to the duct open end.

Appendices

Appendix A

Baddour's scaling-law for cut-off modes

This Appendix derives simple scaling laws for the directivities of cut-off modes in terms of their transverse wavenumber $\kappa_{mn}a$ for both un-flanged and flanged ducts. Here it is shown that the directivity of cut-off modes exhibit a particularly simple dependence on $\kappa_{mn}a$ and that their behaviour for flanged and un-flanged ducts are fundamentally different.

A.1 Scaling-law for un-flanged ducts

This analysis is conducted using the form of the solution of the un-flanged directivity factor derived by Gabard and Astley. Following Gabard and Astley (2006), the directivity for a hollow un-flanged circular hard-walled duct is of the form,

$$D_{mn}(\phi, ka) = \frac{(1-\cos\phi)}{\sin\phi H'_m(ka\sin\phi)} \frac{(k+k_{z,mn})}{(k_{z,mn}-k\cos\phi)\sqrt{(1-\frac{m^2}{\kappa_{mn}^2 a^2})}} \frac{K_m^-(k_{z,mn}a)}{K_m^+(\cos\phi)}, \tag{A.1}$$

where K_m^+, K_m^- are the positive and negative Kernel functions arising from the Wiener-Hopf solution of the form,

$$K_m^{\pm}(\Theta) = \mathrm{e}^{j\mathcal{K}_m(\Theta)\pm\frac{1}{2}K(\Theta)}, \tag{A.2}$$

where $\mathcal{K}$ is the complex phase factor,

$$\mathcal{K}_m(\Theta) = \frac{ka}{2\pi}\int_0^1 \left[\frac{K(ka\sqrt{1-v^2}) - K(\Theta)}{v-\Theta} - \frac{K(ka\sqrt{1-v^2}) - K(\Theta)}{v+\Theta}\right]\frac{dv}{d\eta}d\eta. \tag{A.3}$$

where $K(\Theta)$ is the function,

$$K(\Theta) = \ln\left[\frac{\Theta}{ka}\left(\frac{J_m(\Theta)}{J'_m(\Theta)} - \frac{H_m(\Theta)}{H'_m(\Theta)}\right)\right], \tag{A.4}$$

and v is the polynomial function,

$$v = \frac{\eta}{(1-\eta)^2} - 2\eta(1-\eta)^2 j \tag{A.5}$$

The function $K(\Theta)$ is a complex function of frequency whose phase is assumed to to be a continuous function and therefore 'unwrapped'. Note also that the second term in $K(\Theta)$ is singular at the turning points of $H'_m(\Theta)$, and following Gabard and Astley (2006), can be computed from the approximation,

$$\frac{H_m(\Theta)}{H'_m(\Theta)} \approx \frac{-8\Theta + (1-4m^2)j}{3+4m^2-8\Theta j}. \tag{A.6}$$

Consider the directivity factor $D_{mn}(\phi, ka)$ for the un-flanged duct, neglecting the terms that do not depend on radial mode n,

$$D_{mn}(\phi, ka) \propto \frac{(ka + k_{z,mn}a)}{(k_{z,mn}a - ka\cos\phi)\sqrt{(1-\frac{m^2}{\kappa_{mn}^2 a^2})}} \times \frac{1}{\sqrt{\kappa_{mn}}} \times \frac{e^{j\mathcal{K}_m(\kappa_{mn}a)}}{\sqrt{\frac{J_m(\kappa_{mn}a)}{J'_m(\kappa_{mn}a)} - \frac{H_m(\kappa_{mn}a)}{H'_m(\kappa_{mn}a)}}} \tag{A.7}$$

Equation A.7 is valid for both cut-on and cut-off modes. For sufficiently well cut-off modes, $ka < |k_{z,mn}a|$, the term $(k_{z,mn}a + ka)/(k_{z,mn}a - ka\cos\phi) \approx 1$ and $\sqrt{1 - m^2/\kappa_{mn}^2 a^2} \approx 1$, since $m/\kappa_{mn} < 1$. Finally, note from numerical studies that that as the mode becomes increasing cut-off ($\zeta_{mn} < 0.5$) the second term in *Eq. A.7* becomes increasing independent of the radial model index n and is therefore only dependent on m and frequency, which is denoted γ_m,

$$\frac{e^{\mathcal{K}_m(\kappa_{mn}a)}}{\sqrt{\frac{J_m(\kappa_{mn}a)}{J'_m(\kappa_{mn}a)} - \frac{H_m(\kappa_{mn}a)}{H'_m(\kappa_{mn}a)}}} = \gamma_m, \qquad \zeta_{mn} < 1, \tag{A.8}$$

Computations show the value of γ_m increases with m and is largely independent of frequency, taking smallest value $\gamma_m \approx 0.7$, for sufficiently cut-off modes, .

Incorporating the two approximations above leads to the scaling law for the directivity of cut-off modes in the form

$$D_{mn}(\phi, ka) \propto \frac{1}{\sqrt{\kappa_{mn}}} \qquad (\text{for} \quad \text{constant } m \text{ and } ka). \tag{A.9}$$

A.2 Scaling law for flanged ducts

Following a similar analysis on the expression for the directivity for a flanged duct as for the un-flanged duct above, omitting all terms that are independent of radial mode order n, gives,

$$D_{F,mn}(\phi, ka) \propto \frac{k_{z,mn}}{(\frac{\kappa_{mn}^2}{k^2} - \sin^2\phi)\sqrt{(1 - \frac{m^2}{\kappa_{mn}^2 a^2})}}, \tag{A.10}$$

Assuming sufficiently cut-off modes, $\kappa_{mn} >> k$ and hence making the approximations $\kappa_{mn}^2/k^2 >> \sin^2\phi$, $m/\kappa_{mn} < 1$ and $k_{z,mn} \approx j\kappa_{mn}$, which in *Eq. A.10* gives the following approximate scaling law for the directivity of cut-off modes,

$$D_{F,mn}(\phi, ka) \propto \frac{1}{\kappa_{mn}} \qquad (\text{for} \quad \text{constant } m \text{ and } ka), \tag{A.11}$$

which is a fundamentally different scaling law from that of *Eq. A.9* deduced for un-flanged ducts. Flanged ducts are therefore less efficient in radiating cut-off modes. Combining *Eq. A.9* and *Eq. A.11* reveals that the flanged and un-flanged radial mode n dependencies differ by $(\kappa_{mn}a)^{1/2}$. Note the effect of reflection at the open end is included in the un-flanged directivity of *Eq. A.1* but the formulation for the flanged duct of *Eq. 2.38* does not, which could explain this discrepancy.

Bibliography

RK Amiet. Noise produced by turbulent flow into a propeller or helicopter rotor. *AIAA Journal*, 15(3):307–308, 1977.

A Limited. Hoover h-upright 500 hu500ghm upright vacuum cleaner. https://www.ibtimes.com/dyson-supersonic-combines-vacuum-cleaner-fan-technology-435-hairdryer-2360229, 2021.

B Baddour. Isvr acoustics group coffee machine. not published, 2022.

B Baddour, P Joseph, A McAlpine, and R Leung. On the characteristics of modal radiation from ducts above and below cut-off. page 70001, 2020.

B Baddour, P Joseph, A McAlpine, and R Leung. Significance of cut-off modes in acoustic radiation from ducts. page 2299, 2021.

B Baddour, P Joseph, A McAlpine, and R Leung. Acoustic radiation characteristics of cutoff modes from ducts. *Journal of Sound and Vibration*, 541:117306, 2022a.

B Baddour, P Joseph, A McAlpine, and R Leung. Acoustic radiation from a finite length duct. 2022b.

B Baddour, P Joseph, A McAlpine, and R Leung. Open-to-ducted transfer function for point dipole sources. page 3083, 2022c.

W K Blake. *Mechanics of flow-induced sound and vibration, Volume 2: Complex flow-structure interactions*. Academic press, 2017.

CJ Chapman. Sound radiation from a cylindrical duct. part 1. ray structure of the duct modes and of the external field. *Journal of Fluid Mechanics*, 281:293–311, 1994.

CJ Chapman. Sound radiation from a cylindrical duct. part 2. source modelling, nil-shielding directions, and the open-to-ducted transfer function. *Journal of Fluid Mechanics*, 313:367–380, 1996.

Cheap Drones. Hbfpv dx40 40mm eva ducted 2-3s hd fpv racing drone caddx baby turtle f4 osd 12a 0803 motor. https://cheapdrone.co.uk/

hbfpv-dx40-40mm-eva-ducted-2-3s-hd-fpv-racing-drone-caddx-baby-turtle-f4-osd-12a-0803-mo
2022.

C Cutler. How does a turbofan engine work?
https://www.boldmethod.com/learn-to-fly/aircraft-systems/
how-does-a-jet-engine-turbofan-system-work-the-basics/, 2020.

E Doak. Excitation, transmission and radiation of sound from source distributions in hard-walled ducts of finite length (ii): The effects of duct length. *Journal of Sound and Vibration*, 31(2):137–174, 1973a.

PE Doak. Excitation, transmission and radiation of sound from source distributions in hard-walled ducts of finite length (i): The effects of duct cross-section geometry and source distribution space-time pattern. *Journal of Sound and Vibration*, 31(1):1–72, 1973b.

Industry Drive. Research conflicts on drone delivery costs, efficiency as parcel carriers scale operations. https://www.supplychaindive.com/news/
drones-energy-efficient-delivery-vans-experts-disagree/578418/, 2020.

R Duivis. Jet engine propulsion; the comparison of power between a car and an aircraft? https://blog.klm.com/
jet-engine-propulsion-the-comparison-of-power-between-a-car-and-an-aircraft/,
2020.

R Edwards. Marine propeller market overview:.
https://www.robedwards.com/2013/09/
the-corkscrew-seal-massacre-trying-to-tracking-down-the-culprits.html,
2020.

W Ernsthausen. The source of propeller noise. Technical report, 1937.

EASA Europa. Easa europa regulations.
https://www.easa.europa.eu/regulations, 2021.

JE Ffowcs Williams and DL Hawkings. Sound generation by turbulence and surfaces in arbitrary motion. *Philosophical Transactions for the Royal Society of London. Series A, Mathematical and Physical Sciences*, pages 321–342, 1969.

G Gabard and RJ Astley. Theoretical model for sound radiation from annular jet pipes: far-and near-field solutions. *Journal of Fluid Mechanics*, 549:315–341, 2006.

IE Garrick and Charles E Watkins. A theoretical study of the effect of forward speed on the free-space sound-pressure field around propellers. Technical report, NASA, 1953.

IS Gradshteyn, IM Ryzik, and A Jeffrey. *Table of Integrals, Series, and Products*. Section 3.248, p 294, 1980.

M Gunjan and M Sonia. The corkscrew seal massacre: trying to track down the culprits. https://www.alliedmarketresearch.com/marine-propeller-market, 2013.

L Gutin. On the sound field of a rotating propeller. *Physikalische Zeitschrit der Sowjetinion: Physical magazine of the Soviet Union volume 9 number 1*, 9 (NACA-TM-1195), 1948.

MA Hamdi and JM Ville. Development of a sound radiation model for a finite-length duct of arbitrary shape. *AIAA Journal*, 20(12):1687–1692, 1982.

DB Hanson. Compressible helicoidal surface theory for propeller aerodynamics and noise. *AIAA Journal*, 21(6):881–889, 1983.

D Hewlett, p Nelson, and c Morfey. The radiation from acoustic sources within a finite length circular duct immersed in water. *Proceedings of a meeting - Internoise*, 1997.

GF Homicz and JA Lordi. A note on the radiative directivity patterns of duct acoustic modes. *Journal of Sound and Vibration*, 41(3):283–290, 1975.

MS Howe. Installation effects on the production of blade-vortex interaction noise by a ducted rotor. *Journal of sound and vibration*, 156(1):61–78, 1992.

IBTimes. Dyson supersonic combines vacuum cleaner and fan technology. https://ao.com/product/hu500ghm-hoover-hupright-500-upright-vacuum-cleaner-green-72976-60.aspx, 2021.

GW Johnston and E Ogimoto. Sound radiation from a finite length unflanged circular duct with uniform axial flow. ii. computed radiation characteristics. *The Journal of the Acoustical Society of America*, 68(6):1871–1883, 1980a.

GW Johnston and K Ogimoto. Sound radiation from a finite length unflanged circular duct with uniform axial flow. i. theoretical analysis. *The Journal of the Acoustical Society of America*, 68(6):1858–1870, 1980b.

PF Joseph and CL Morfey. Multimode radiation from an unflanged, semi-infinite circular duct. *The Journal of the Acoustical Society of America*, 105(5):2590–2600, 1999.

L E Kinsler, A R Frey, AB Coppens, and J V Sanders. *Fundamentals of acoustics*. John wiley & sons, 2000.

H Levine and J Schwinger. On the radiation of sound from an unflanged circular pipe. *Physical review*, 73(4):383, 1948.

Qi D Mao Y, Gu Y and H Tang. An exact frequency-domain solution of the sound radiated from the rotating dipole point source. *The Journal of the Acoustical Society of America*, 132(3):1294–1302, 2012.

A McAlpine. *Mathematical Methods for Acoustics*. University of Southampton, 2018.

A McAlpine and MJ Kingan. Far-field sound radiation due to an installed open rotor. *International Journal of Aeroacoustics*, 11(2):213–245, 2012.

A McAlpine, AP Daymond-King, and AJ Kempton. Sound radiation from a flanged inclined duct. *The Journal of the Acoustical Society of America*, 132(6):3637–3646, 2012.

A McAlpine, Gaffney J, and Kingan MJ. Near-field sound radiation of fan tones from an installed turbofan aero-engine. *The Journal of the Acoustical Society of America*, 138 (3):1313–1324, 2015.

CL Morfey. A note on the radiation efficiency of acoustic duct modes. *Journal of Sound and Vibration*, 9(3):367–372, 1969.

RM Munt. The interaction of sound with a subsonic jet issuing from a semi-infinite cylindrical pipe. *Journal of Fluid Mechanics*, 83(4):609–640, 1977.

MK Myers and JH Lan. Sound radiation from ducted rotating sources in uniform motion. In *1993 15th AIAA Aeroacoustics Conference, pages*1 − −13, 1993.

S Nathan. Leading rolls-royce technology efforts: polishing the jewel in the crown. https://www.theengineer.co.uk/content/interviews/leading-rolls-royce-technology-efforts-polishing-the-jewel-in-the-crown/, 2018.

YK Nomura, I Yamamura, and S Inawashiro. On the acoustic radiation from a flanged circular pipe. *Journal of the Physical Society of Japan*, 15(3):510–517, 1960.

AB Parry and DG Crighton. Asymptotic theory of propeller noise. i-subsonic single-rotation propeller. *AIAA journal*, 27:1184–1190, 1989.

N Peake and ID Abrahams. Sound radiation from a semi-infinite lined duct. *Wave Motion*, 92:102407, 2020.

N Peake and DG Crighton. An asymptotic theory of near-field propeller acoustics. *Journal of Fluid Mechanics*, 232:285–301, 1991.

Promain UK LTD. Jotun safeguard universal es. https://www.promain.co.uk/jotun-safeguard-universal-es.html, 2020.

B Rayleigh. *The theory of sound*. New York Dover Publications, 1945.

E Rice and A Prydz. Multimodal far-field acoustic radiation pattern using mode cutoff ratio. *AIAA Journal*, 16(9):906–911, 1978.

SW Rienstra and A Hirschberg. An introduction to acoustics. *Eindhoven University of Technology*, 18:249, 2004.

J Schulten. Frequency-domain method for the computation of propeller acoustics. *AIAA journal*, 26(9):1027–1035, 1988.

A Snakowska and J Jurkiewicz. Efficiency of energy radiation from an unflanged cylindrical duct in case of multimode excitation. *Acta Acustica united with Acustica*, 96:416–424, 2010.

A Snakowska and J Jurkiewicz. A new approach to the theory of acoustic multi-port networks with multimode wave and its application to muffler analysis. *Journal of Sound and Vibration*, 490:115722, 2021.

A Snakowska, H Idczak, and B Bogusz. Modal analysis of the acoustic field radiated from an unflanged cylindrical duct–theory and measurement. *Acta Acustica united with Acustica*, 82(2):201–206, 1996.

Technology Co. 2020. https://www.made-in-china.com/products-search/hot-china-products/Camera_Drone.html, 2020.

G Throneberry, CM Hocut, and A Abdelkefi. Multi-rotor wake propagation and flow development modeling: A review. *Progress in Aerospace Sciences*, 127:100762, 2021.

J Tyler and T Sofrin. Axial flow compressor noise studies. Technical report, SAE, 1962.

KS Wang and TC Tszeng. Propagation and radiation of sound in a finite length duct. *Journal of Sound and Vibration*, 93(1):57–79, 1984.

AL Weinstein. The theory of diffraction and the factorization method: Generalized wiener-hopf technique. 1969.

WE Zorumski. Generalized radiation impedances and reflection coefficients of circular and annular ducts. *The Journal of the Acoustical Society of America*, 54(6): 1667–1673, 1973.